COUPLING TO A RECEIVING APERTURE FROM A RANDOM MEDIUM AT MILLIMETRIC WAVELENGTHS

by

ISMAIL A. MASHHOUR

A Thesis submitted for the Degree of
Doctor of Philosophy in the Faculty of Engineering,
University of London and the Diploma of
Membership of the Imperial College (DIC)

Department of Electrical Engineering
Imperial College of Science and Technology
Exhibition Road, London, S.W.7

June, 1979

بسم الله الرحمن الرحيم

الحمد لله
الذى هدانا لهذا
وما كنا لنهتدى لولا أن هدانا الله

In the name of God, Most Gracious,
Most Merciful

Praise be to God, who hath guided us to this,
never could we have found guidance, had it not
been for the guidance of God

ABSTRACT

Some aspects of the interaction between a turbulent clear air medium and narrow beam millimetric wave propagation circuits are investigated. Theoretical and experimental studies at a propagation frequency of 38 GHz are described.

The solution adopted for the wave equation governing the propagation of millimetric waves in a medium with weak refractive index inhomogeneities is the Parabolic Equation solution. On application of this solution, the propagation medium is shown to be equivalent to a spatial and temporal phase-modulation screen. Two types of media are considered; the first is one with a square law refractive index vertical profile. Estimates are presented for the signal gain or loss due to the focussing or defocussing effects of the medium. The second medium considered was one interspersed with refractive index inhomogeneities or blobs of randomly varying magnitude and size. A rigorous solution based on a Huygens' Principle approach provides information on the statistics of the amplitude and phase fluctuations and their probability distributions at the receiver site, as a function of the system and medium parameters.

The extension of the analysis to a strongly random medium is made possible by dividing the medium into a number of regions or slabs, each represented by an appropriate phase screen. An angular plane wave spectrum approach is used to determine the coherent and incoherent powers available at the receiver plane. The propagation of the angular power spectrum and its corresponding lateral coherence function, through a series of random phase screens, is studied. This approach leads to a general transmitter-to-medium-to-receiving aperture coupling formula. A system signal-to-noise ratio and efficiency are

defined in terms of the aperture sizes and the parameters of the random medium.

A description of a 38 GHz, continuous-wave 12 kilometre radio link is given, together with the data processing procedures used to analyse the data available from an interferometer receiver system. Results for the amplitude fluctuations and variations of the cross correlation coefficients are presented. Results of the phase difference and angle-of-arrival fluctuations are also reported. The response of different receiving aperture sizes and the difference in their efficiencies and "smoothing" properties are also investigated.

Some of the results obtained from the analysis and investigations carried out may prove to be useful in the efficient design and implementation of millimetre wave systems operating under different atmospheric conditions.

ACKNOWLEDGEMENTS

The author would like to thank a number of people who aided him throughout this project and in the preparation of the resulting thesis.

Foremost, he would like to acknowledge his gratitude to Dr. R. H. Clarke, who not only provided valuable assistance and guidance, but also provided constant encouragement and understanding.

The author is deeply indebted to the assistance provided by Mr. M. Inggs throughout the project, and to his enlightening discussions, and to the high technical skills of Mr. D. K. Sage. Without both their efforts, the experimental project would probably not have been realised.

He much appreciates the many interesting discussions and assistance provided by his former colleagues, Drs. M. Nicolaides and J. Kanellopoulos.

He is very grateful to Mrs. Helen Bastin for her proficient typing and to Mrs. Janet Hill for her skilful drafting.

The author is deeply grateful to his parents for their encouragement and support throughout the period of study.

Finally, the author would like to express his thanks to the Communications Department of the A.O.I. for support during part of the research.

TABLE OF CONTENTS

CHAPTER 1

INTRODUCTION

Ever increasing demand for radio-wave telecommunications is forcing radio system designers to operate at higher and less congested portions of the radio-wave spectrum. Nowadays, the maximum frequency of commercially available systems verges on 18 GHz and, very soon, frequencies of 30 GHz and above will be in demand. Millimetre wave frequencies are not just a necessity because of radio spectrum congestion; they are very attractive in their own right. Their attraction is due, amongst other things, to their compactness and simplicity of manufacturing of millimetre wave sub-systems. The compactness is also obvious in the small high gain millimetre wave antennas.

The areas of utilization of millimetre waves are wide and varied. For example, the 36 - 40 GHz has been allocated to fixed line-of-sight links, mobile and satellite communications systems[1].

In spite of the inevitable advent of millimetre wave systems and the increased amount of theoretical and experimental investigations of the behaviour of such systems, there remains a certain amount of misgiving amongst the system engineers when such frequencies are mentioned for utilization. The main causes of concern are the atmospheric effects on the propagating wave.

This report investigates both theoretically and experimentally some aspects of the atmospheric effects on millimetre wave propagation. In the following introductory discussion, the propagation medium with its different irregularities will be briefly considered. The system parameters which are affected by the medium are then discussed.

A review of the theoretical approaches utilized in estimating the effect of the medium on radio-waves will be presented. The

experimental procedures undertaken to assess the theoretical predictions and to provide data which may be useful for future systems design will also be presented. These will be given together with the data processing techniques involved.

1.1 The Propagation Medium

The region of the atmosphere which affects line-of-sight millimetre wave propagation is the troposphere. This lowest atmospheric shell is characterized by a general decrease of temperature with altitude, with a lapse rate of $2^{o}C/Km$. Clouds are formed within this shell and convection due to wind forces is active. Experiments have indicated that the earth's troposphere occupies the space above the earth's surface to a height of 10 kilometres[2].

The meteorological factors which play a dominant role in the production of irregularities in the tropospheric propagation medium are temperature, humidity and pressure. These factors cause the variation of the refractive index across the propagation path, which directly affects the velocity of the propagating wave. The C.C.I.R. have adopted the following formula for the refractive index n[3]:-

$$n = 1 + \left[\frac{77.6}{T}\left(p + \frac{4.810\ e}{T}\right)\right] . 10^{-6} \qquad (1.1)$$

where T is the absolute temperature in degrees Kelvin and e and p are the water-vapour pressure and atmospheric pressure in millimetres.

Therefore, any changes in T, p or e produce a variation in n. The order of influence depends largely on the mechanisms involved as will be shown later.

The variations in the refractive index due to the varying meteorological factors may basically be divided into two categories

according to the temporal scales involved. Long-term, large-scale variations, e.g. over a period of a few hours and smaller size, short-term ones over a period of a few seconds will be considered.

1.1.1 Long Term Refractive Index Variations

The long term refractive index variations are those which occur in the vertical profile. These variations are usually diurnal or even monthly variations and they extend over a few tens of kilometres. Under normal atmospheric conditions, i.e. over dry inland paths, the refractive index decreases linearly with height and hence causes a downward tilt of the propagating beam. Such standard refraction conditions are accounted for by modifying the earth's radius by a factor K and the modified or effective earth's radius is used in the design of line-of-sight links[4, 5]. The K-factor is a function of the refractive index gradient and is defined as follows:-

$$K = \frac{a'}{a} = \frac{1}{1 + a \cdot \frac{dn}{dh}} \qquad (1.2)$$

where a' and a are the effective and true radii of the earth respectively, and h is the height above the ground.

The refractive index has been found to decrease sharply with height for the first few tens of metres and then the gradient becomes less negative as the height increases. Hence an exponentially decreasing profile is the preferred standard[6]. However, under some anomalous conditions the refractive index gradient deviates from the standard model. These deviations are a function of the underlying terrain and prevailing weather conditions.

Table 1.1 shows the values of K and the refractive index

gradient dn/dh for the first 100 metres above the earth's surface for various atmospheric conditions[7]. As shown in Fig. 1.1, the refractive index may assume varying vertical profiles which depend on the prevailing atmospheric conditions and on the underlying surface.

The modified earth's radius concept provides a method of estimating the linear first order effects of the refractive index variations. However, the second and higher order effects due to the inversions in the n-profile are not accounted for. These higher order variations induce a loss or gain in the signal level due to the de-focussing or focussing effects of the inversion layers.

Such refractive index profiles are likely to exist over a long period of time, e.g. a few hours. This is due to the fact that the mechanisms involved are long term processes, e.g. warm air blowing inland over coastal areas in the night-time. Therefore, the profiles may be considered to be stationary over a long period of time.

In Chapter 2 an analysis is undertaken to predict the effects of a medium characterized by a square-law refractive index profile on a propagating finite beam. The refractive index profile is assumed to be constant with time, i.e. a deterministic quantity. This is a reasonable assumption according to the above discussion.

1.1.2 Short Term Refractive Index Fluctuations

These fluctuations are the smallest sized ones produced by the atmospheric dynamics. They are due to the motion of blobs of varying refractive index, with scale sizes ranging from tens of metres to about 1 millimetre[8]. There are two main causes of small-scale refractive-index irregularities close to the surface of the earth[9]. The first acquires its energy from stable air layers moving close to the surface of the earth and the irregularities are produced by the stirring

TABLE 1.1

K-FACTORS AND REFRACTIVE INDEX GRADIENT VARIATIONS. (AFTER GTE LENKURT MANUAL)

K	$(dn/dh) \cdot 10^6$ per Km.	Prevailing Climate	Propagation
5/12 1/2 2/3	+ 220 + 157 + 80	Low ground humidity, advection fog over cold water, above normal low level temperature	Subrefraction
1	0	Homogeneous, uniform	Straight line ray
1.25 4/3 1.6	- 30 - 40 - 58	Dry, mountainous Typical inland. Humid, coastal	Standard refraction
2.75 ∞	- 100 - 157	High ground humidity, steam. Fog over warm water, below normal or rapid drop in low level temperatures	Super-refractive, flat earth propagation, ducting
- 1 - 1/2	- 314 - 470		Ducting, trapping

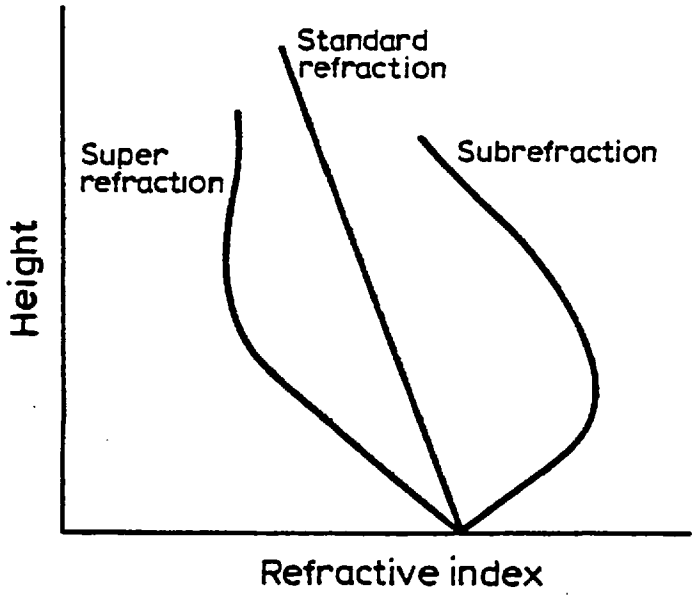

Fig. 1.1 Refractive index vertical profiles

action caused by obstacles along the path. The second source of turbulence originates from ground sources and the irregularities are carried into the surrounding atmosphere by thermal convection. The two causes of turbulence will be qualitatively discussed below.

(a) Refractive Index Irregularities Caused by Stirring Actions

Stably stratified layers of air are carried along the propagation path, with the wind velocity having a certain profile. Usually the wind velocity is lower at ground level and increases with height, thus possessing an orderly shearing motion. This motion is made disorderly if the laminar flow is obstructed by obstacles, which may be man-made, buildings, towers, etc., or natural, e.g. mountainous regions. Due to this stirring motion produced by the obstacles, parcels of air are carried from one level to another, thus causing temperature and hence refractive-index fluctuations amongst the originally stable layers. If the ground temperature is lower than the air temperature, then the temperature would increase with altitude for the first few metres and cool parcels of air would be stirred into the upper warmer layers. These air parcels would tend to sink downwards again due to the buoyancy forces; the opposite process is also true.

The size of the broken-down parcels of air depends to a large extent on the structure of the obstacles involved and on the temperature and wind velocity profiles. Furthermore, these parcels tend to break down into smaller eddies as they move from one layer to the next. This is due to the combined wind shear and buoyancy forces acting on the air parcel. Detailed and quantitative analysis of turbulence due to stirring motions may be found in the literature, e.g. Brunt[10].

(b) Refractive Index Irregularities Caused by Thermal Convection

Whenever thermal sources are found on the surface, the air above the sources is unstably stratified, i.e. becomes turbulent. Thermal sources may be man-made or natural. Chimneys, parking lots and heated buildings in general are some examples of man-made thermal sources. Natural sources occur when the ground is much warmer than the air above; an obvious example is desert terrain in the day-time. Generally, bare ground absorbing solar energy acts as a thermal source.

As a result of the presence of thermal sources, bubbles of hot air are discharged into the air above. The mechanisms of formation of the bubbles vary according to the dynamic and thermal conditions of the atmosphere. Eventually the bubbles ascend into the surrounding atmosphere under their buoyancy forces. The bubbles have been shown by Scorer and Ludlam[11] and Scorer and Ronne[12] to have a cap which is hemispherical in shape. As the bubble ascends, it leaves in its wake a trail of relatively cooler air and parts of the bubble are eventually eroded and washed in its wake. Thus as the bubbles ascend, they produce smaller eddies which circulate freely causing smaller refractive index irregularities.

As the bubbles rise, the temperature difference between the core and the surrounding air, namely, the excess temperature, decreases. Scorer[9] has shown that the excess potential temperature $\Delta\theta$ is proportional to $z^{-1/3}$ where z is the height above the ground. Whilst the excess temperature of the bubble decreases with altitude, its size increases. The variation of the size and temperature of a bubble as a function of altitude is given in Table 1.2, which is after Nicolaides[13] and Wulfson[14].

Therefore, it may be seen that a line-of-sight radio link

TABLE 1.2

Altitude (metres)	Mean Dimension of Bubble (metres)	Mean Temperature Excess (deg. cent.)
10	31	0.54
30	37	0.18
50	43	0.19
100	46	0.18
300	58	0.14
500	61	0.11
1000	64	0.10

encounters larger and less intense irregularities as the distance above the ground increases in an environment which contains thermal sources.

(c) Refractive Index Fluctuations due to Humidity Variations

So far, only the effects of temperature variations on refractive index irregularities have been considered. However, it may be seen from Equation (1.1) that humidity variations have a greater effect on the refractive index at microwave frequencies than temperature variations.

The density of water vapour is 0.62 times that of dry air. Hence, if two parcels of air have the same density but different humidities, they must have different temperatures. When those parcels are disturbed for any reason, the disturbance dies out only when the density becomes uniform along a horizontal surface. Therefore, the atmosphere is left with a patchy distribution which is only smoothed out by molecular diffusion over many hours[9].

Therefore, in propagation paths over warm water or vegetation,

or over water-laden chimney outlets, blobs of different refractive index are expected to be distributed in the medium. The prevailing wind conditions and hence the size of the blobs determine their effects on a propagating beam. Very large blobs which engulf the beam would act as lenses which would have a focussing effect, whereas many smaller and less intense blobs distributed randomly across the path would have a scattering effect. The time variations of the focussing or scattering effects is largely dependent on the prevailing wind conditions.

In conclusion it may be said that the propagation medium usually contains refractive index irregularities of one form or another, which vary in magnitude and spatial distribution. Anomalous propagation conditions are caused by irregular vertical refractive index profiles which have a very slow temporal variation, e.g. a few hours. The effect of such profiles is to tilt and focus or defocus a propagating beam.

Other types of irregular transmission media are those which contain a random spatial distribution of blobs of varying sizes and refractive indexes. The presence of such blobs is caused mainly by stirring motion due to obstacles or by thermal convection. It is worthwhile noting that both causes of blob-producing mechanisms previously discussed are present in an urban environment. The sizes of these blobs may vary from tens of metres down to 1 millimetre with the larger blobs further away from the surface than the smaller ones.

The presence of such blobs is likely to have a scattering effect on a propagating radio wave with the scattering becoming more pronounced as the propagating wave-length decreases. Very large blobs, e.g. tens of metres, are likely to have a lens-like effect on a propagating beam.

The rate of fluctuation of the scattered signal may be linked to that of the refractive index fluctuations if the blobs are considered

to be "frozen" in space and carried along by the wind flow, as postulated by Taylor[15]. From an analysis of the wave number spectra of the turbulence, which has been carried out by Kolmogoroff[16], and adopting Taylor's "frozen turbulence" hypothesis, the temporal spectra of the refractive index fluctuations may be obtained. There are also received-signal fluctuations due to internal rearrangements of the refractive index with time, as opposed to external whole-body shifts. The fluctuation spectra due to the internal mechanisms are deduced in this thesis. A detailed analysis of the variation of the temporal spectra of the refractive index and signal fluctuations as a function of various atmospheric parameters has been carried out by Nicolaides[13].

Having briefly considered the propagation medium, some of the millimetre-wave system parameters affected by the medium irregularities will be discussed in the next section.

1.2 System Design Considerations

Randomly varying refractive index inhomogeneities present in the medium cause a fluctuation in the mean value of the propagating signal. However, the medium effect most feared by millimetre wave system designers is complete loss of signal due to absorption, the main causes of which are rain and fog.

Fig. 1.2 shows the attenuation due to precipitation by rain and fog for different frequencies after C.C.I.R[7]. It may be seen from the figure that an acceptable system's value of 1 db/Km at 40 GHz is obtained at a moderate rainfall rate of 4.0 mm/hr, or under visibility conditions of 30 metres in fog. Higher rainfall rates may be tolerated due to the fact that high intensity rain cells seldom cover a propagation path of more than a few kilometres.

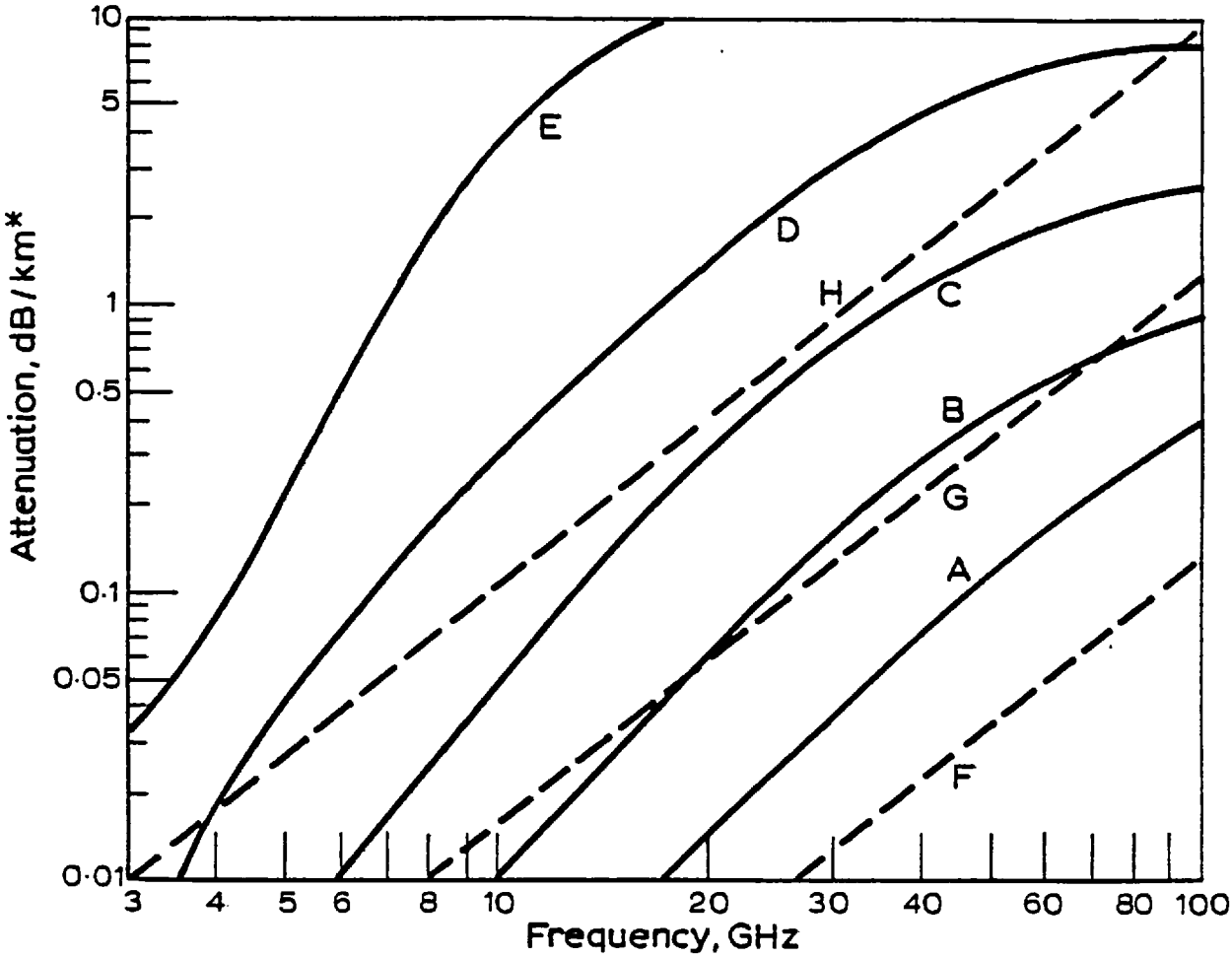

Attenuation in rainfall density of:

A. 0.25 mm/hr (drizzle) - 0.01 in/hr
B. 1·0 mm/hr (light rain) - 0·04 in/hr
C. 4·0 mm/hr (moderate rain) - 0·16 in/hr
D. 16 mm/hr (heavy rain) - 0·64 in/hr
E. 100 mm/hr (v. heavy rain) - 4·0 in/hr

Attenuation in fog or cloud:

F. 0·032 gm/m^3 (visibility greater than 600m.)
G. 0.32 gm/m^3 (visibility about 120m)
H. 2·3 gm/m^3 (visibility about 30m)

*Attn. - dB/mile = 1·61 x (Attn. in dB/km)

Fig. 1·2 Attenuation due to precipitation (after CCIR)

Apart from the attenuation effects due to rain and fog, or loss of signal due to antenna decoupling caused by variations in the refractive index profile, the clear air random medium poses a few problems. These are basically due to scattering and atmospheric multipath effects caused by the inhomogeneities in the medium. Some of the system design parameters affected by clear air turbulence are discussed below.

(a) Reliability of a Line-of-Sight Radio Link

Atmospheric multipath produced by the interaction of rays scattered from the random inhomogeneities causes fades in the received signal level. The duration and depth of the fades depend on the path length and on the nature of the inhomogeneities. Such fades may present serious problems if their magnitude and rate of occurrence are such that the signal is lost for an unreasonably long period of time.

Assuming the fades to be Rayleigh distributed, the annual outage probability, W, for a certain path is given by[7]:-

$$W = a \cdot b \cdot (2.5) \cdot 10^{-6} \cdot f \cdot D^3 \cdot 10^{-F/10} \qquad (1.3)$$

where: a is a terrain factor, values of which are equal to:-

4 : for very smooth terrain, including over water

1 : for average terrain with some roughness

1/4 : for mountainous, very rough or very dry

b is an atmospheric factor and is equal to:-

1/2 : Gulf coast or similar hot, humid areas

1/4 : normal interior temperate or northern

1/8 : mountainous or very dry

f is the frequency in GHz

D is the path length in miles

F is the fade margin, to the "minimum acceptable" point, in decibels

The above equation takes into consideration atmospheric and surface caused multipath. The reliability of the system A is then given by:-

$$A = (1 - W) \cdot 100 \text{ per cent}$$

Therefore, for a 20 mile, 40 GHz radio link, over average terrain and normal interior temperate, i.e. a = 1 and b = 1/4, the reliability A for a system with a 40 db fade margin is predicted to be 99.998%, which corresponds to an average outage time of 10.5 minutes per year.

If higher reliability figures are required to meet stringent performance values, or for adverse propagation conditions, therefore, diversity must be considered.

Different forms of diversity may be possibly used, e.g. frequency, space, cross polarization or hybrid diversity techniques. Probably the most convenient diversity technique for millimetre wave propagation is space diversity. This is due to the small antenna sizes involved and for the small correlation distances across the receiver plane. A spatial diversity improvement factor I has been defined[7] as follows:-

$$I = (1 - r^2) \cdot 10^{F/10} \qquad (1.4)$$

where r is the correlation coefficient and F is the fade margin. Hence predictions and experimental investigations of the variation of the correlation length across the receiver plane, under various atmospheric conditions, are necessary for effective planning of spatial diversity systems. Results of such experimental investigations are reported in Chapter 8 for a 38 GHz radio link.

(b) Medium Scattering Effects on System Signal-to-Noise Ratio and Antenna Efficiency

The fluctuations in the received signal due to the random scattering by the medium inhomogeneities is effectively a noise contribution by the medium. This noise is added to the inherent receiver noise and could prove to be detrimental in the implementation of systems with particularly high signal-to-noise ratio requirements. Such systems are becoming increasingly popular to-day and are mainly digital data transmission systems, hence a deterioration in the signal-to-noise ratio is reflected as an increase in the bit-error rate. A high band rate data system requires bit-error probabilities less than 10^{-7}.

Fig. 1.3 shows the relationship between the bit-error rate probability and the signal-to-noise power ratio in decibels for different modulation schemes, taken after Garner[17]. The curves are calculated under the assumption that the noise is Gaussian distributed.

Atmospherically contributed noise may be "smoothed" out by using large aperture size receiving antennas. Such a choice is particularly relevant to achieve the bit-error probability requirements for high speed data transmission systems.

The other aspect of beam scattering by small refractive index

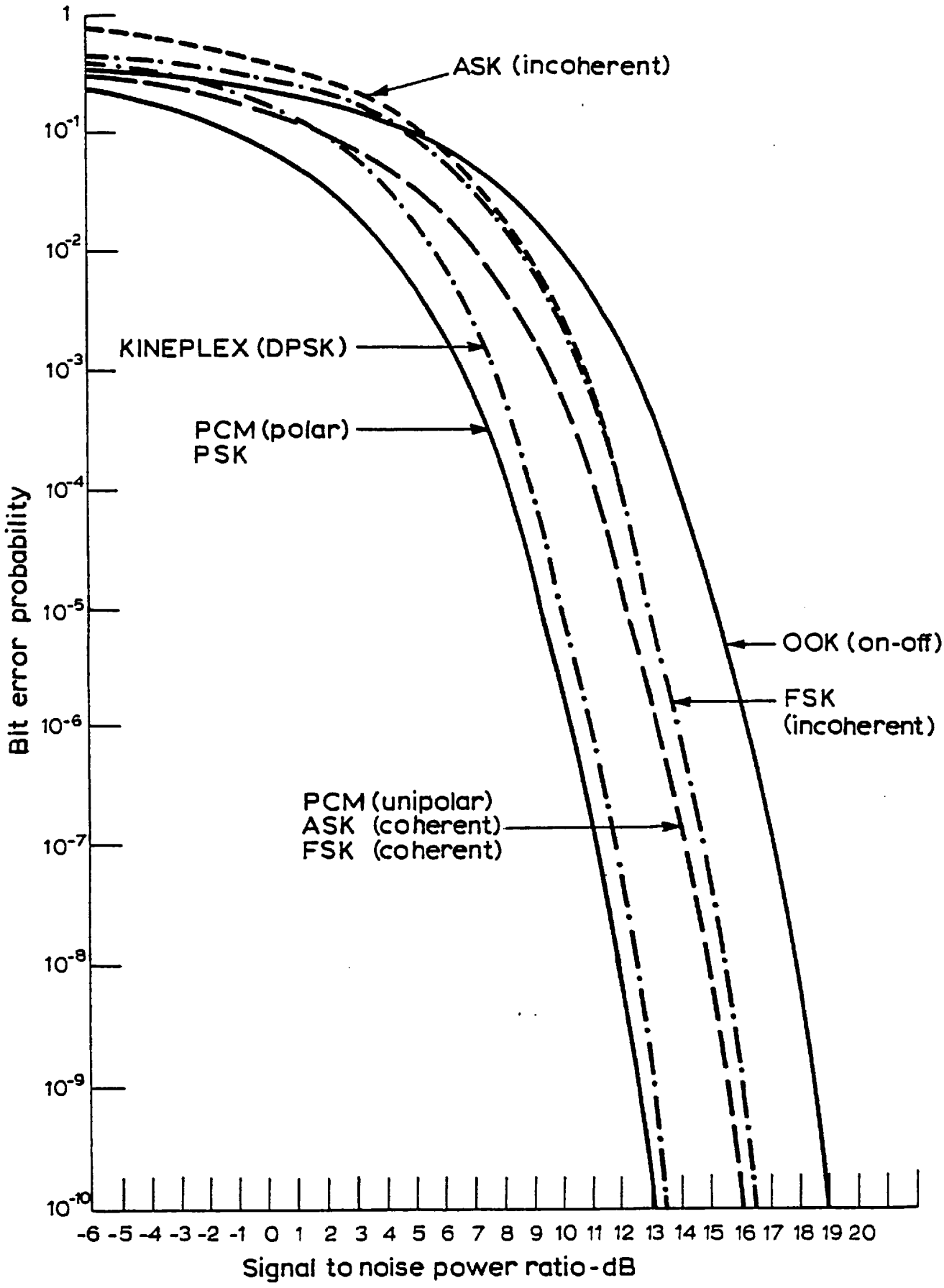

Fig. 1·3 (After Garner)

inhomogeneities is a drop in receiving aperture efficiency. This drop is due to the fact that the scattered portions of the incident wave correspond to off-axis incident power. Therefore, if the magnitude of the scattered power and the random scattering angles are relatively large, a large aperture size receiving aperture with a very narrow beam would be "insensitive" to off-axis incident energy. Therefore, very high gain aperture would have a lower receiving efficiency than the wider beam width smaller apertures. Gain degradation on loss of efficiency of large apertures in turbulent media has been theoretically investigated and some experimental evidence is available[18]. A drop in aperture efficiency is effectively a drop in the system efficiency, which is an important design factor in low power propagation over long distances, which is the case for millimetre wave systems.

Therefore, a proper choice of the transmitting and receiving apertures is necessary to obtain the desired signal-to-noise ratios and efficiencies for a millimetre wave system. An analysis of the variation of both the signal-to-noise ratio and efficiency as a function of the aperture dimensions and the nature of the medium inhomogeneities is given in Chapter 5. Results of experimental investigations of the variation of the magnitude of the fluctuations and the gains of different size receiving apertures are given in Chapter 3.

(c) Angle-of-Arrival Fluctuations

Large scale size blobs of varying refractive index tend to refract narrow beams as a whole. Due to the random motion of the blobs, the angle of incidence of the beam at the receiver site would then fluctuate about the on-axis direction. Such large scale angle-of-arrival fluctuations would cause a fluctuation in the received signal due to the off-axis reception by narrow beam receiving antennas. These fluctuations

may be decreased by using adaptive reception techniques, where the receiving antenna would track the incident beam and adjust its pointing angle for maximum reception. Modern designs of antenna arrays facilitate the implementation of such adaptive systems due to the electronic beam steering techniques used. Adaptive receiving systems using pilot laser beams, assuming the medium to be reciprocal, have been considered in some detail by Fanté[19]. Therefore, under turbulent atmospheric conditions with drastic angle-of-arrival fluctuations, costly large aperture antennas may be replaced by smaller and cheaper ones arranged in a more efficient adaptive array system.

Implementation of such adaptive receiving systems requires detailed knowledge of the magnitude and rate of the angle-of-arrival fluctuations. Experimental investigations of the magnitude and rate or temporal spectra of the fluctuations have been carried out by means of an interferometer receiver, with the results given in Chapter 8.

Such investigations are also very useful for radio systems which are affected by any small variation in the angle-of-arrival caused by the atmosphere. An example of such systems is monopulse radar, which derives target information by null reception from two or more offset apertures[20]. Therefore, any slight atmospherically caused variation would produce errors in target location or definition. Such errors may be accounted for if medium effects are known in detail.

The theoretical and experimental approaches, applied in this thesis, to investigate some of the medium effects on a propagating millimetric wave will be discussed below.

1.3 Review of Theoretical Approaches

The purpose of the theoretical investigations carried out in the following chapters is to understand, in physical terms, the effects

of a random medium on a narrow propagating beam. An attempt has been made to formulate some of the relevant system parameters in terms of measurable or predictable medium parameters.

The interaction between the medium and the propagating wave is obtained by solving the wave equation in a medium with refractive index variations. The solution applied in the investigations is the Parabolic Equation (PE) solution, which is an approximate solution. The conditions for reducing the scalar wave equation to a parabolic form are:-

(i) The wave length of the propagating wave is small compared to the dimensions of the medium inhomogeneities, and,

(ii) The variations in the refractive index are much smaller than unity.

The solution as described in Chapter 2 is split into two parts, the first allowing for diffraction under free space conditions and the second neglecting diffraction but taking the refractive index variations into account. For narrow beams, the "split-step" solution shows that the effect of weak refractive index variations is to contribute a phase variation, the characteristics of which are determined from the characteristics of the refractive index variations. This leads to the notion of collapsing the tenuous medium into a phase screen representative of the medium. The PE solution becomes inaccurate in media with strong variations in the refractive index. In such cases, the path length may be partitioned into several slabs such that the refractive index variations may be considered to be weak within each slab. Therefore, each slab may be collapsed into an appropriate phase screen and the medium is represented by a series of phase screens normal

to the direction of propagation.

Parabolic variations in the refractive index profile are treated in Chapter 2. Since atmospheric conditions producing such profiles are usually very slow time varying processes, the refractive index variations are considered to be deterministic. As previously mentioned, the medium is represented by an appropriate phase screen and for strong parabolic gradients, multiple phase screens are applied. A computer adaptable recursive formula is obtained to calculate the waist and radius of curvature of the beam as it propagates through a number of phase screens. The amount of focussing or defocussing of the diffracting beam is estimated for various gradients. The effects of localized regions, with a parabolic gradient, of varying thickness and location along the propagation path are also studied.

A rigorous solution for the on-axis electric field fluctuations in a random medium is presented in Chapter 3. The medium statistics are defined and the appropriate random phase screen is imposed at the transmitter plane. The transmitter aperture field is broken down into a set of Huygens' sources and the on-axis random field is then taken as the summation of all the elemental fields radiated by the random phase modulated Huygens' sources. The percentage field fluctuations observed by an on-axis point aperture are obtained in the near and far fields of the transmitting aperture, as a function of the transmitter aperture size and the medium parameters. Individual second-order statistics and distributions of the amplitude and phase fluctuations may be obtained by adopting a "Hoyt vector" type of representation of the fluctuating field. This is achieved by resolving the fluctuating field into its real and imaginary components and then obtaining the statistics of their fluctuations.

Extending the analysis to a strongly random medium, i.e.

imposing further phase screens on the propagating wave is not practical with a Huygens' Principle approach. This is due to the complexity of the equations involved, as will be shown later. Another drawback for this rigorous approach is the difficulty in introducing the effects of a finite receiving aperture with a finite beam width as opposed to an omnidirectional point receiver.

To overcome the above-mentioned difficulties, an angular spectrum approach is then applied to investigate the coupling of a wave to a finite receiving aperture after propagation through a strongly random medium. Although detailed field statistics are not easily obtained by this method, yet its physical significance and ease of manipulation make it a very useful analytical tool.

A brief introduction to the angular plane wave spectrum representation of propagating fields is given in Chapter 4. The imposition of a random phase screen has the effect of reducing the coherent power propagating and introducing an incoherent angular power. The magnitude and angular spread of the coherent and incoherent angular powers are studied as they propagate through a series of random phase screens, representing a strongly random medium. These are obtained as a function of the transmitter aperture size and the medium parameters.

Having obtained the coherent and incoherent angular powers available at the receiver plane, the next step is to calculate the amount of power coupled to a finite receiving aperture. A general transmitter-to-random medium-to-receiving aperture is obtained in Chapter 5. The coherent and incoherent coupled powers are obtained as a function of the transmitter and receiver aperture sizes and of the random medium parameters. A system efficiency and signal-to-noise ratio are defined in terms of the system and medium parameters.

The incorporation of the transmitter aperture size in the

analysis seems to be of some importance since most of the analysis present in the literature deals with plane wave propagation in a random medium. It has been suggested[21] that there exists "serious deficiencies of the general understanding of transmitter effects on scintillation". Under some medium conditions, which will be shown in the text, the transmitter aperture size has a more dominant effect on the system signal-to-noise ratio and efficiency, than the receiver aperture size.

To complement the theoretical analysis and to provide further insight into the random atmospheric effects on millimetre wave propagation, some experimental investigations have been carried out.

1.4 Review of Experimental Investigations

A 38 GHz (8 millimetre) continuous wave radio link was set up over a 12 kilometre path across South London. The main purpose of the link was to investigate the medium-induced amplitude and phase distortions across the receiver plane. This necessitated the joint construction of a variable spacing interferometer receiver system, with amplitude and phase difference detectors. Various climatological conditions were monitored at the receiver site and a synoptic data record was simultaneously available with the signal fluctuations. Detailed information for the radio link and the associated systems are given in Chapter 6.

The amplitude fluctuations available from the dual channel detectors and the phase difference information were simultaneously recorded for off-line data processing and analysis on a digital computer. The data handling and processing techniques used and the relevant programs are given in Chapter 7.

The results presented in Chapter 8 are divided into three sections, namely, they are those dealing with amplitude fluctuations,

phase difference fluctuations and different aperture size effects. The amplitude fluctuations were observed to be very low, e.g. 1%; this seems to agree to a large extent with the theoretical predictions based on the coupling formula derived in Chapter 5. Measurements of the spectra of the amplitude fluctuations seem to agree with those obtained from other experimental links over London[22] and with theoretical predictions made in the literature. Amplitude cross-correlation coefficients were measured at various horizontal and at one vertical spacing, under different atmospheric conditions. These were generally found to be quite low, i.e. less than 0.5 at spacing larger than 0.8 metres, which gives some confidence in the design of spatial diversity systems with small receiver separations.

Phase difference measurements were simultaneously carried out at various spacings and again, these were also found to be very small, e.g. ± 5 degrees. Angle-of-arrival fluctuations were rarely observed under the different atmospheric conditions which prevailed over the measurement periods. These results were also found to be in agreement with those predicted from the phase screen approach.

Three different aperture sizes were used to investigate the variation in reception as a function of the receiver aperture size. Experiments were carried out to estimate the aperture smoothing effect, i.e. the enhancement of the signal-to-noise ratio due to the larger aperture size. The variation in the mean signal level was taken as a variation in the aperture efficiency, after taking into account the signal level variations due to other factors. The variations in the behaviour of the aperture sizes used were negligible, which was predicted by the coupling formula, for the aperture sizes under consideration.

CHAPTER 2

WAVE PROPAGATION THROUGH A SQUARE LAW MEDIUM

In this chapter, the randomness of the medium is set aside and the effect of a deterministic inhomogeneous medium is investigated. Linear vertical gradients of the refractive index are known to cause a bending of the propagating wave, which affects the propagation distance covered and are accounted for by modifying the earth's radius.

The second order effects of a quadratic vertical gradient of the refractive index on a propagating Gaussian wave are investigated. The medium is assumed to be uniform in the lateral y-direction and independent of z, the direction of propagation.

The propagating wave under consideration is one radiated by an on-axis aperture with Gaussian amplitude and zero phase distribution, i.e. the rays' input to the medium are parallel with a zero launch angle.

As a consequence of the focussing or defocussing, the spot-size or "1/e" waist of the Gaussian beam in the vertical direction, is different from that in the case of free space propagation. This may be interpreted as a gain or loss induced by the medium. As a result of the power concentration, long distance propagation can occur under ducting conditions.

The analytical approach used here is based on the solution of the parabolic wave equation, which is an approximate form of the wave equation in a medium with small magnitude and large scale-size variations in the refractive index. The problem is then reduced to that of estimating the focussing or defocussing of a cylindrical wave by a medium containing a series of on-axis concave or convex lenses of variable focal lengths.

2.1 Examples of Propagation Media with a Parabolic Refractive Index Gradient

2.1.1 The Exponential Refractive Index Model of the Atmosphere

The vertical gradient of the refractive index has been described by many models, each representing an average over some period of time for certain geographical locations.

The basic model is one which assumes a linear decrease of refractive index with height. Since the refractive index cannot decrease below unity, therefore, an indefinitely decreasing linear gradient cannot be a feasible representation. To overcome this problem, some authors[6] have recommended a linear decrease to some height, which is taken to be 1 kilometre, followed by an exponentially decreasing gradient.

The second model of the atmosphere is the exponential one and which has been recommended by the C.C.I.R.[3] and is of the form:-

$$n(x) = 1 + n_s \cdot e^{-0.136\,x}$$

where $n(x)$ is the refractive index as a function of the height x measured in kilometres. n_s is the value of the refractive index at ground level. The recommended value for sea level is $289 \cdot 10^{-6}$.

For small values of x, say, less than 1 kilometre, the above expression may be expanded in the quadratic form:-

$$n(x) \simeq 1 + 289 \cdot 10^{-6} \left[1 - 0.136 \cdot 10^{-3}\, x + \frac{(0.136 \cdot 10^{-3})^2\, x^2}{2}\right] =$$

$$= 1.000289 - 3.93 \cdot 10^{-8}\, x + 2.67 \cdot 10^{-12}\, x^2 \quad , \quad x \text{ is in metres}$$

The phase contribution of the different terms of the equation may be analysed individually. The zero order term represents a constant phase shift to the propagating beam, which is of no consequence. The first order term which is equivalent to the linear gradient has the effect of bending the propagating wave back towards the ground. This effect has been thoroughly investigated, and the concept of an increased earth's radius is used to account for the increase in the propagation distance.

The second order term has the effect of a defocussing lens in the case of an exponentially decreasing gradient. The medium in this case continuously defocusses the beam as it propagates along, with the equivalent continuous lens placed normal to the direction of propagation and its axis passing through the focal point of the parabola representing the refractive index profile.

The complex combination of simultaneous bending and defocussing will not be analysed since this requires a continuous shifting of the axis of the continuous lens with respect to the axis of the propagating wave. However, the individual effect of defocussing by a continuous lens-like medium is investigated.

Therefore, in addition to the increased distance of propagation due to the bending of the beam, there is an accompanying loss due to the diffusion of power caused by the continuous defocussing of the medium which enhances the continuous spreading due to free-space diffraction.

Under some inversion conditions, the refractive index increases up to some altitude after which the index begins to decrease again. This sort of profile gives rise to a negative parabolic gradient. Therefore, in this case, the medium focusses the propagating beam which counters the free space spreading of the wave. This additional

concentration of the beam is equivalent to an increase in the available power per unit solid angle and is thus a gain induced by the medium.

The propagation of radio waves under inversion conditions has been analysed and discussed by many authors[4, 20, 23, 24]. However, the medium induced gain or loss are not readily predictable and no numerical adaptations have been developed.

2.1.2 Localized Inversions and Large Spherical Inhomogeneities

In the previous section, the exponential model for the refractive index gradient was taken to represent an average propagation medium. However, many propagation paths are not necessarily represented by an average model since, for most practical situations, the underlying surface is not uniform.

Since the refractivity gradient is a function of the vertical distribution of atmospheric temperature, humidity and pressure, therefore, any localized variation in any of these parameters will cause a change in the refractivity gradient. Localized changes of the different parameters may be caused by any number of factors, a discussion of which is present in the literature, e.g. Bean and Dutton[25] and Gossard[26]. To cite a few of the possible cases for an urban environment, is propagation over relatively warm patches of ground, e.g. parking lots, or over sources of hot air and high water vapour content, e.g. outputs of large chimneys.

The effect of the localized inhomogeneities may be to create an inversion layer at a very low altitude, e.g. a few tens of metres, which possibly lies on the propagation axis of a radio link (Fig. 2.1).

Examples of different parabolic gradients may be obtained by fitting a polynomial to various practically measured refractivity

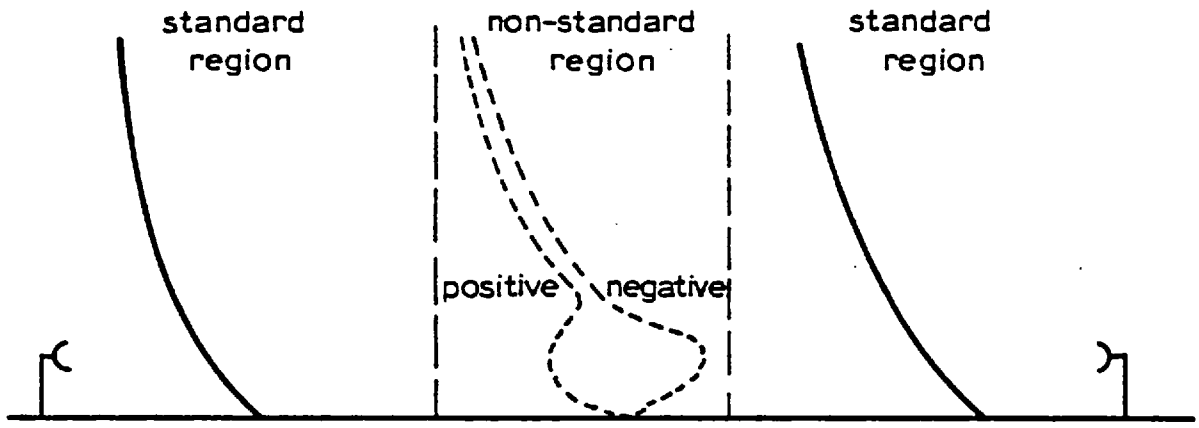

Fig. 2.1 Localized refractive index profiles along the propagation path

profiles, e.g. over Colorado, USA[25]. The refractivity for the first 80 metres is given by:-

$$n(x) = 1.000295 + 5.44 \cdot 10^{-7} \cdot x - 6.61 \cdot 10^{-9} \cdot x^2$$

where x is the height in metres. This indicates a negative parabolic gradient for the refractivity profile; the inflection point was at a height of 40 metres.

The width of the localized non-standard region obviously depends on the underlying medium. In some cases, the propagation path may be divided into two portions, each of different refractivity gradients, e.g. on propagation between sea and land or vice versa.

In other cases, the localized portion may be represented ideally by a spherical blob, e.g. in the case of organized thermal cells or convective bubbles of hot humid air. The refractivity within the

spherical blob may be assumed uniform and different from the surrounding atmosphere. It will be shown that this situation is analogously represented by a slab of the medium with a different parabolic gradient, the magnitude of which depends on the radius of the spherical blob and on the difference in the refractivity between the blob and the surrounding medium.

As an example, consider a medium with a temperature of $15^{o}C$, pressure of 1,000 mbar and a relative humidity of 10%, and a puff of saturated hot air at the same atmospheric pressure, but with a temperature of $45^{o}C$. The difference in refractivity is $320 \cdot 10^{-6}$ n-units.

To simplify the analysis, the centre of the spherical blob will be assumed to lie on the propagation axis (Fig. 2.2).

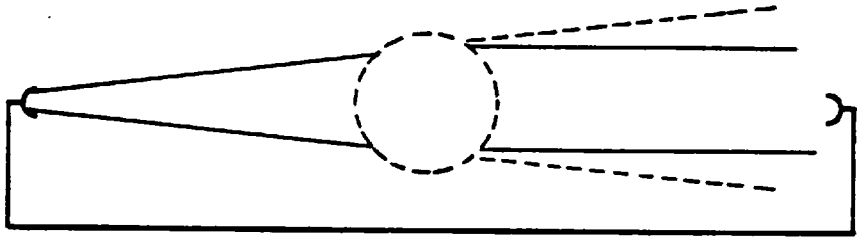

Fig. 2.2 Focussing effect of a spherical blob

The position of the localized region with respect to both the transmitter and the receiver plays an important part in the amount of focussing or defocussing of the diffracting beam, and will be investigated for various positions and widths of the localized region along the propagation path.

2.1.3 Self-Focussing Optical Fibres

The application of optical fibres for optical signal communications has been enhanced by the introduction of self-focussing fibres. These tend to contain the propagating wave and thus decrease the losses due to leakage of the diffracting beam from the fibre walls.

The subject of wave propagation through either a continuous lens-like medium, or a medium with periodic thin lenses has been studied by many researchers. For example, Kogelnik[27] formulates the laws governing the propagation of a light beam in terms of a complex valued beam parameter; Tien et al[28] obtain an equation for the beam radius using a ray optics approach, and Marcuse[29] treats the propagation of a Gaussian beam in a lens wave guide and obtains ray transformation matrices.

In the present treatment, the waist and radius of curvature of a Gaussian beam are traced through a medium with discreet periodic lenses, which in the limit, as the separation between them decreases, may be considered to be continuous without any significant error.

It will be shown that for a certain critical value of the parabolic gradient, the diffraction of the Gaussian beam is totally overcome and the beam is periodically focussed as it propagates along the guide. It is in this mode that the wave could propagate for very long distances through the guide without any leakage.

2.2 Application of the Parabolic Equation Solution of the Wave Equation to a Tenuous Inhomogeneous Deterministic Medium

In order to study the effect of a parabolic or square-law variation in the refractive index on the properties of a propagating Gaussian wave, a diffraction approach will be considered, and is based on an approximate solution of the wave equation known as the parabolic equation (PE) approximation.

The refractive index n, may be written in cartesian co-ordinates as follows:-

$$n(x,y,z,t) = 1 + \Delta n(x,y,z,t) \tag{2.1}$$

where $\Delta n(x,y,z,t)$ is the variation of the refractive index from its nominal value of unity, at a time t.

The scalar electric field E of a quasimonochromatic beam is thus determined from the solution of the wave equation:-

$$\nabla^2 E + k^2 (1 + \Delta n)^2 E - \nabla (\nabla . E) = 0 \tag{2.2}$$

The last term in the above equation represents depolarization effects, which can be shown[19] to be negligible for microwave frequencies and, hence, will be neglected.

The variations of the refractive index, Δn, will be considered to be much less than unity. This assumption is true for media with inherently weak variations, or over small distances of a medium with strong variations, such that the departure from a mean or nominal value is small.

In this case, the scalar wave equation reduces to:-

$$\nabla^2 E + k^2 (1 + 2\Delta n) E = 0 \tag{2.3}$$

For the time being, we shall consider the electric field E to be propagating essentially in the forward direction along the z-axis. The magnitude u of this field is a relatively slowly varying function of both position and time due to the variations $\Delta n (\underset{\sim}{r},t)$ of the refractive index, where $\underset{\sim}{r}$ is an abbreviation for (x,y,z) and, therefore:-

$$E\ (\underset{\sim}{r},t) = u\ (\underset{\sim}{r},t)\ .\ e^{-jkz} \tag{2.4}$$

Substituting in the wave equation, and assuming that the longitudinal scale size of the variations is much larger than the wavelength, i.e.:-

$$\frac{\partial^2 u}{\partial z^2} << 2k\ \frac{\partial u}{\partial z} \tag{2.5}$$

The wave equation is thus reduced to a differential equation of a parabolic form, which is known in the literature as the parabolic equation (PE) approximation:-

$$\frac{\partial^2 u}{\partial x^2} + \frac{\partial^2 u}{\partial y^2} - j2k\ \frac{\partial u}{\partial z} + 2k^2\ \Delta n\ .\ u = 0 \tag{2.6}$$

For simplicity, the two-dimensional form of the parabolic equation will be discussed, i.e. uniformity in the y-direction will be assumed. However, the same development principles apply in the three-dimensional case.

The solution of the parabolic approximate form of the wave equation for a diffracting wave in an irregular medium is a difficult task. However, to circumvent this difficulty, it has been shown[30] that the solution process may basically be split into two parts, by means of the so-called "Split-Step Fourier Algorithm".

The first part is the solution of the parabolic equation for a diffracting wave in a medium with no refractive index variations. The second step in the overall solution is the further assumption of large lateral scale sizes of the irregularities which allows for further simplification of the parabolic equation.

First, in the absence of refractive index irregularities, the scalar electric field in the right half plane $z \geq 0$ may be represented by a series or spectrum of plane waves. The relationship between the electric field distribution $E(x,z)$ and the angular plane wave spectrum $F(s)$ being a Fourier transform relationship. (This topic will be discussed in more detail in Chapter 4).

$$E(x,z) = \int_{-\infty}^{+\infty} F(s) \cdot e^{-jk\,(xs + zC)}\, ds \qquad (2.7)$$

The plane-wave spectrum function $F(s)$ is expressed in terms of the angle variable $s = \sin\theta$, where θ is the angle that each plane-wave direction makes with the z-axis, and $C = \cos\theta$. For the case of a narrow diffracting beam, e.g. the angular plane-wave spectrum is limited within the range $|s| \leq 0.2$, i.e. $|\theta| \leq 12^{0}$, then the cosine may be approximated by $C \simeq 1 - \frac{1}{2} s^2$, and, therefore, the field at a plane distance d may be approximately given by:-

$$E(x,d) \simeq e^{-jkd} \int_{-\infty}^{+\infty} F(s) \cdot e^{-jkxs} \cdot e^{\frac{1}{2} jkds^2}\, ds \qquad (2.8)$$

Substituting the above expression for the electric field in the parabolic equation and noting that u is denoted by the integral in the above expression:-

$$-k^2 \cdot s^2 \cdot u + k^2 \cdot s^2 \cdot u + 2k^2 \cdot \Delta n \cdot u = 0 \qquad (2.9)$$

This confirms that the parabolic equation is valid for narrowly confined propagating fields in a medium with no refractive

index irregularities, i.e. $\Delta n = 0$.

The next step in the solution of the parabolic equation in an irregular medium is to neglect diffraction and to make the further assumption that the lateral scale sizes of the irregularities are much larger than the wavelength. In view of this assumption, it is reasonable to omit the remaining second order derivatives and, hence, the solution of the remaining first order differential equation is:-

$$u(x,t;d) = u(x,t;0) \cdot e^{j\phi(x,t;d)} \qquad (2.10)$$

where:-

$$\phi(x,t;d) = - k \int_0^d \Delta n(x,z,t)\, dz$$

The above solution indicates that the modification imposed by an irregular medium is purely a phase contribution. The electric field distribution on a normal observation plane at a distance d is the initial field distribution projected forward with its phase modified. The characteristics of the phase contribution are determined by the characteristics of the refractive index irregularities $\Delta n(x,z,t)$ along the propagation path.

Having established the two parts of the solution, first allowing for narrow spreading of the wave in a uniform free space medium, and the second allowing for the presence of irregularities but suppressing diffraction, the two parts of the solution may be combined, and the scalar field E at a distance d in a medium with refractive index variations $\Delta n(x,z,t)$ may be written as:-

$$E(x,t;d) = E_0(x;d) \cdot e^{j\phi(x,t;d)} \tag{2.11}$$

where $E_0(x;d)$ is the free space field at the observation plane $z = d$, and $\phi(x,t;d)$ is the phase contribution of the medium given by Equation (2.10).

$E_0(x;d)$ is the free space field at $z = d$ and is given by the Fourier transform relationship of Equation (2.7). By applying the convolution theorem to Equation (2.7), it may be shown that the electric field is alternatively given by:-

$$E(x;d) = \frac{e^{-jkd}}{\sqrt{j\lambda d}} \cdot \int_{-\infty}^{+\infty} E(x',0) \cdot e^{-j\frac{k}{2d}(x - x')^2} dx' \cdot e^{j\phi(x,t;d)} \tag{2.12}$$

which is Fresnel's diffraction formula.

The procedure to be followed in calculating the field distribution after propagation through a medium of refractive index irregularities is to divide the total path length involved into regions or slabs, each of thickness d. The refractive index variations Δn within each region are then small enough to allow for the application of the parabolic equation approximation.

Having calculated the field distribution at the end of the first region at $z = d$, the process is repeated to calculate the field distribution at $z = 2d$, with the initial field in this case being that calculated at $z = d$. Repeating this procedure for the total number of slabs, the field distribution at the final observation plane may be observed.

The above outlined approximate method for the solution of the wave equation in an irregular medium was used and proven to be satisfactory in such applications, e.g. Tappert and Hardin[31], who have applied this technique to obtain algorithms used mainly in under-

water acoustic propagation.

The mathematical simplicity and physical justification involved in its application make this method a powerful tool to use.

The refractive index variations to be considered in this chapter are of a deterministic nature and as previously mentioned, are of the form $n(x) = 1 - px^2$, where p is the strength of the parabolic gradient. Time variations are not considered.

The aperture electric field distribution will be arbitrarily taken as a uniform phase and Gaussian amplitude distribution, with a "1/e" waist w_o. Therefore, the aperture electric field at z = 0 is:-

$$E(x,0) = e^{-x^2/w_o^2}$$

To trace the "1/e" waist point or spot size of the beam through the medium, the total path of length L will be divided into n slabs or regions, each of thickness d. The contribution of each region is to add a phase which is dependent on the refractive index variation within the slab, and is given by Equation (2.10). Therefore, the phase ϕ is given by:-

$$\phi(x;d) = -k \int_0^d (1 - px^2)\, dz = -kd + kpx^2d$$

The procedure is to add the effect of each slab to the electric field distribution at the beginning of the slab, and then allow the phase modulated field to diffract to the next slab in a free space manner. This process will be repeated for n successive slabs.

The initial field at z = 0 is modified by the phase contribution of the slab from z = 0 to z = d. Therefore:-

$$E(x;0) = e^{-x^2/w_o^2} \cdot e^{+ jkpx^2d}$$

The complex electric field distribution at the next plane, $z = d$ is calculated using Fresnel's diffraction formula. Substituting for $E(x',0)$ and after some manipulation, the field distribution at $z = d$ is:-

$$E(x;d) = C \cdot e^{-x^2/w_1^2} \cdot e^{-j \frac{k}{2R_1} x^2} \qquad (2.13)$$

where:-

$$w_1^2 = w_0^2 \left[a_0^2 + (2pd^2 - 1)^2\right]$$

and:-

$$R_1 = d \left[\frac{a_0^2 + (2pd^2 - 1)^2}{a_0^2 + 2pd^2 (2pd^2 - 1)}\right]$$

$a_0 = \frac{\lambda d}{\pi w_0^2}$, C is a constant term

The above expression for the "1/e" waist and radius of curvature are reduced for free space propagation (i.e. $p = 0$) to those obtained by Siegman[32].

At $z = d$, the effect of the medium from $z = d$ to $z = 2d$, i.e. the phase contribution $\phi(x,d) = kpx^2d$, is added. Therefore, the modified complex electric field distribution at $z = d$ is:-

$$E(x;d)\Big|_{\text{phase modified}} = C \cdot e^{-\frac{x^2}{w_1^2}} \cdot e^{-j \frac{k}{2R_1} x^2} \cdot e^{jkpx^2d}$$

This phase modified field distribution is allowed to diffract in a free space manner to the plane z = d, and may be shown to be:-

$$E(x;2d) = C \cdot e^{-\frac{x^2}{w_2^2}} \cdot e^{-j\frac{kx^2}{2R_2}}$$

$$w_2^2 = w_1^2 \left[\left(2pd^2 - 1 - \frac{d}{R_1}\right)^2 + a_1^2 \right]$$

$$a_1 = \frac{\lambda d}{\pi w_1^2}$$

and:-

$$R_2 = d \left[\frac{a_1^2 \left(2pd^2 - 1 - \frac{d}{R_1}\right)^2}{a_1^2 + \left(2pd^2 - \frac{d}{R_1}\right)\left(2pd^2 - 1 - \frac{d}{R_1}\right)} \right]$$

To calculate the complex electric field distribution at z = 3d, the effect of the medium from z = 2d to 3d is added onto the distribution at z = 2d. The modified field is then allowed to diffract to the plane z = 3d.

The above procedure may be shown to produce a recursive formula, by which the complex electric field distribution at a distance z = m . d may be obtained in terms of the field distribution at a previous slab at z = (m - 1) . d, i.e.:-

$$E(x;md) = C \cdot e^{-x^2/w_m^2} \cdot e^{-j\frac{kx^2}{2R_m}} \qquad (2.14)$$

$$w_m^2 = w_{m-1}^2 \left[\left(2pd^2 - 1 - \frac{d}{R_{m-1}}\right)^2 + a_{m-1}^2 \right]$$

$$a_{m-1} = \frac{\lambda d}{\pi w_{m-1}^2}$$

and:-

$$R_m = d\left[\frac{a_{m-1}^2 + \left(2pd^2 - 1 - \frac{d}{R_{m-1}}\right)^2}{a_{m-1}^2 + \left(2pd^2 - \frac{d}{R_{m-1}}\right)\left(2pd - 1 - \frac{d}{R_{m-1}}\right)}\right]$$

It is worthwhile noting here that a Gaussian beam propagating through a medium with a parabolic refractive index gradient, remains Gaussian. However, the "1/e" waist and radius of curvature of the modified Gaussian beam are a function of the parabolic gradient p as may be seen from the above equations.

In the previous analysis, the phase effect of each region was added to the field distribution at the beginning of the region. However, it may easily be shown that adding the phase modification due to each region at the end of the region, produces a similar result, except that the recursive formulae (2.14) fall back by a slab. Obviously if the regions or slab thickness are very small with respect to the path length, the difference is insignificant.

2.3 Propagation Through a Continuous Medium with a Parabolic Gradient

The availability of a recursive formula to determine the spot-size and the radius of curvature of the Gaussian wave, facilitates the computational process. A computer program has been written which determines both quantities for varying propagation distances, parabolic gradients and slab thicknesses.

The accuracy of the phase integral method deteriorates for increased slab thickness and/or increase in the parabolic gradient. An

example of this deterioration may be found in Table 2.1. The waist at 1,000 metres was calculated for a wavelength of 8 millimetres. The true waist at 1,000 metres is assumed to be that obtained by a slab thickness of 1 metre. The percentage error is defined as:-

$$\text{Percentage error} = \frac{W_{slab} - W_1}{W_1} \cdot 100$$

where: W_{slab} = waist at 1,000 metres calculated using a slab of thickness d metres

W_1 = waist at 1,000 metres calculated using a slab of thickness 1 metre.

It may be seen from the following table that the accuracy decreases as the slab thickness and the parabolic gradient are increased.

Fig. 2.3 shows the variation of the beam spot-size as a function of distance for a 12 kilometre path for various negative and positive parabolic gradients in a continuous medium. The wavelength considered is 8 millimetres, radiated by an aperture with Gaussian amplitude distribution with a "1/e" width of 0.3 metres. The slab thickness was taken as 10 metres.

The continuous focussing of the medium concentrates the beam in the vertical direction and thus the available electric field per unit solid angle is increased, which is equivalent to a gain.

On the other hand, the defocussing of the medium is equivalent to a loss induced by the medium.

Since the loss or gain are in the vertical direction only, and since the Gaussian beam is assumed to be uniform in the lateral and

TABLE 2.1

Slab Thickness in metres d	%age error		Slab Thickness in metres d	%age error	
	$p = 3 . 10^{-8}$	$p = 3 . 10^{-5}$		$p = 3 . 10^{-8}$	$p = 3 . 10^{-5}$
1	0	0	40	0	1.51
2	0	0	50	0	2.35
4	0	0.01	100	0.01	8.56
5	0	0.02	125	0.02	11.90
8	0	0.06	200	0.04	14.86
10	0	0.09	250	0.06	262.29
20	0	0.38	500	0.25	
25	0	0.59	1,000	1.01	

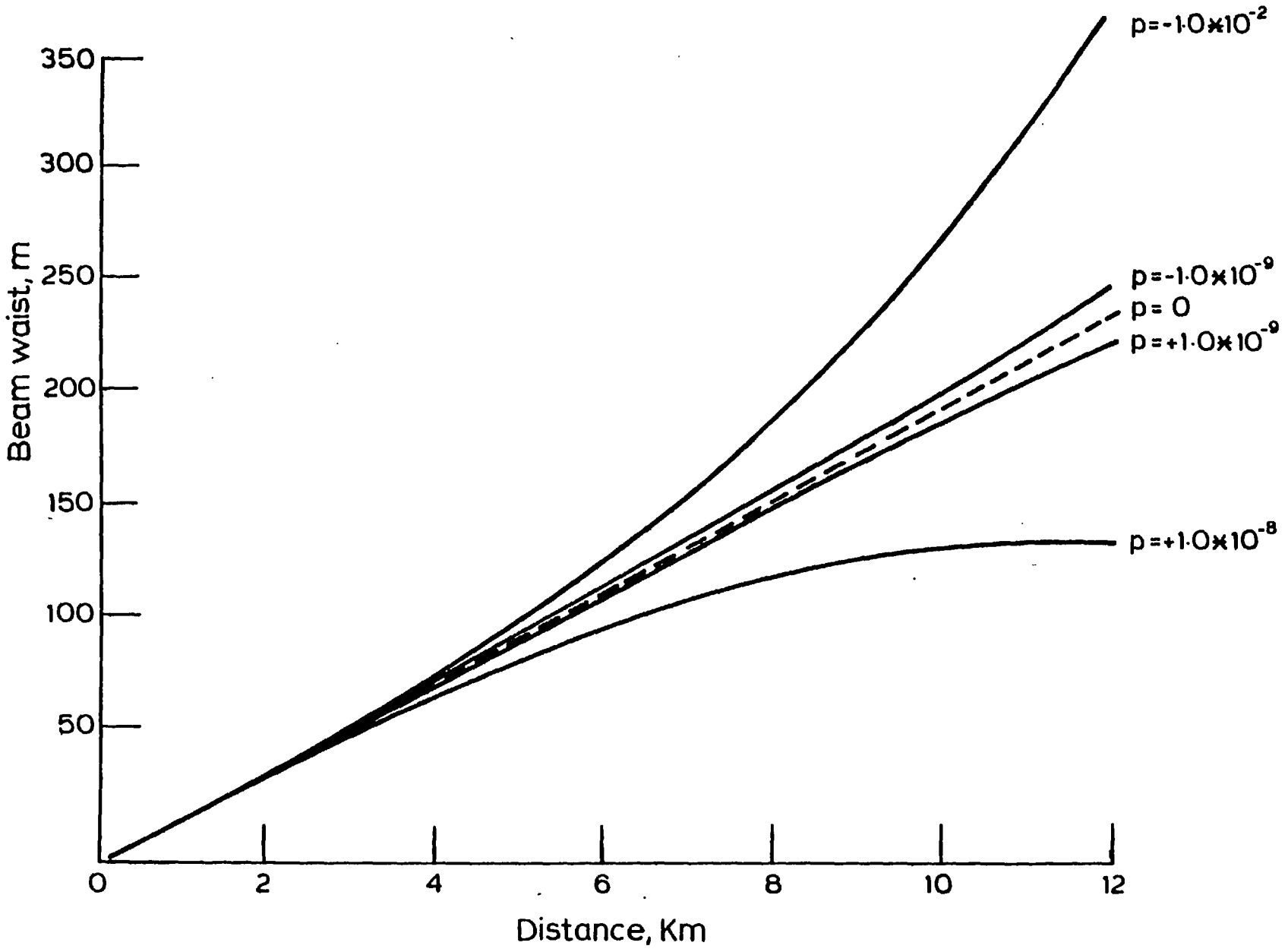
p=-1·0*10^-2
p=-1·0×10^-9
p= 0
p=+1·0×10^-9
p=+1·0×10^-8
Beam waist, m
350
300
250
200
150
100
50
0
2
4
6
8
10
12
Distance, Km

Fig. 2·3

vertical directions. Therefore, the beam cross-section is reduced from a circle in the free space case to an ellipse in the square law medium.

The equivalent gain or loss in the electric field may be defined as the ratio of the areas of the ellipse to the free space circle.

Table 2.2 shows the gain and loss induced by various gradients for the 12 kilometre path at a wavelength of 8 millimetres.

TABLE 2.2

Parabolic Gradient	Power Gain in dbs	Parabolic Gradient	Power Gain in dbs
$+ 3.0 \cdot 10^{-10}$	0.125	$- 3.0 \cdot 10^{-10}$	- 0.124
$+ 3.0 \cdot 10^{-9}$	1.289	$- 3.0 \cdot 10^{-9}$	- 1.216
$+ 3.0 \cdot 10^{-8}$	23.295	$- 3.0 \cdot 10^{-8}$	- 10.121

Continuous Self-Focussing

If the parabolic gradient is sufficiently increased, it may be shown that the beam may be totally contained by means of continuous focussing which completely overcomes the diffraction process.

Fig. 2.4 shows such a situation for a He-Ne laser of wavelength $6.328 \cdot 10^{-7}$ metres, with a "1/e" aperture size of 5 millimetres. Increasing the strength of the parabolic gradient may be seen to decrease the dimensions within which the beam may be contained.

2.4 Propagation Through Localized Thermals

As previously mentioned, the localized thermals may be regions of different parabolic gradients located within the propagation path.

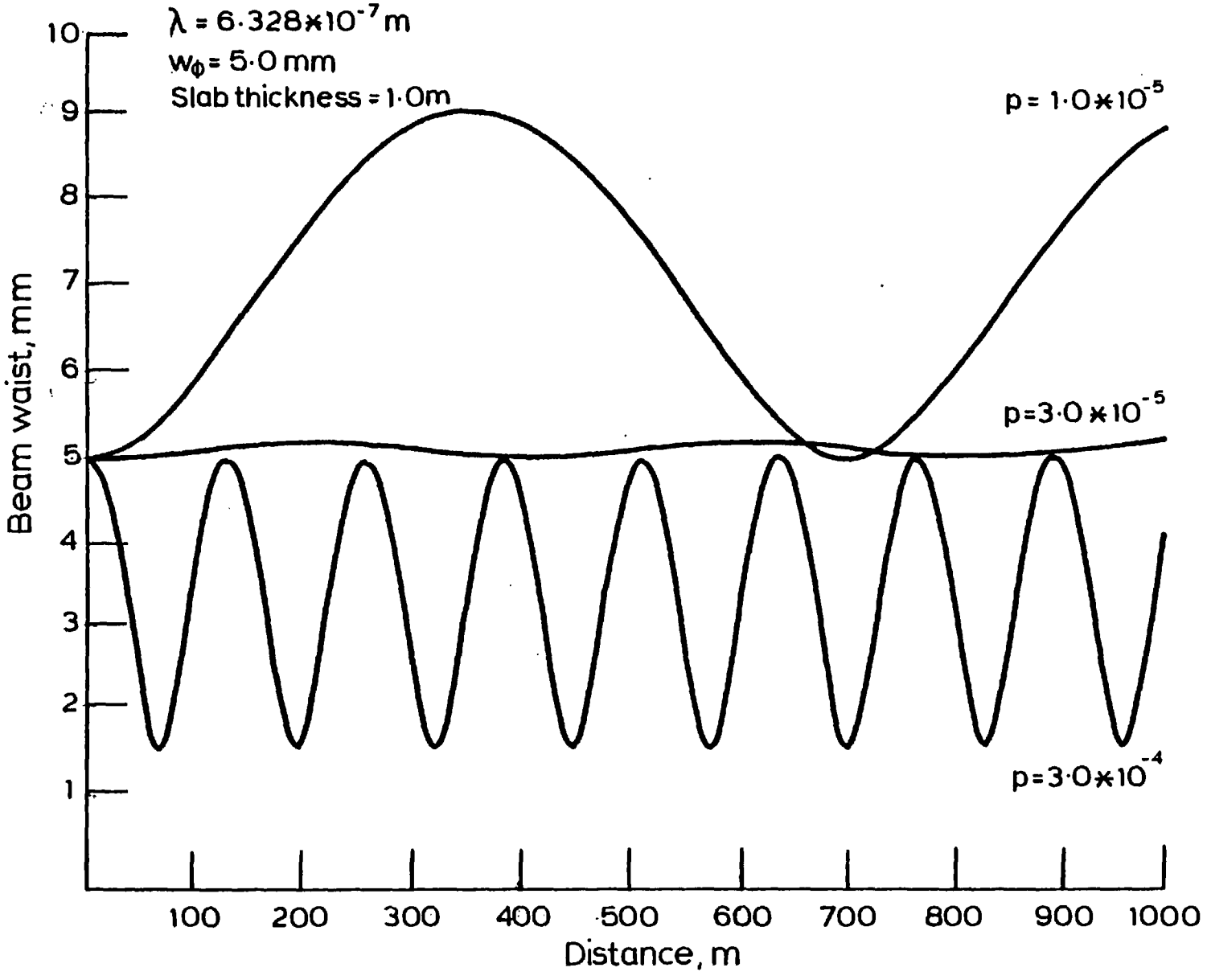
λ = 6·328*10⁻⁷m
w₀ = 5·0 mm
Slab thickness = 1·0m
p = 1·0*10⁻⁵
p=3·0*10⁻⁵
p=3·0*10⁻⁴
Beam waist, mm
Distance, m
10
9
8
7
6
5
4
3
2
1
100
200
300
400
500
600
700
800
900
1000

Fig. 2·4

Alternatively, the localized thermals may be due to spherical or cylindrical puffs of uniform refractive index within a medium of different refractive index.

Phase Modification Due to Spherical Blobs

Consider a spherical blob in two-dimensional form, or alternatively a cylinder of radius A, with a refractive index n_2 in a medium n_1, as shown below:-

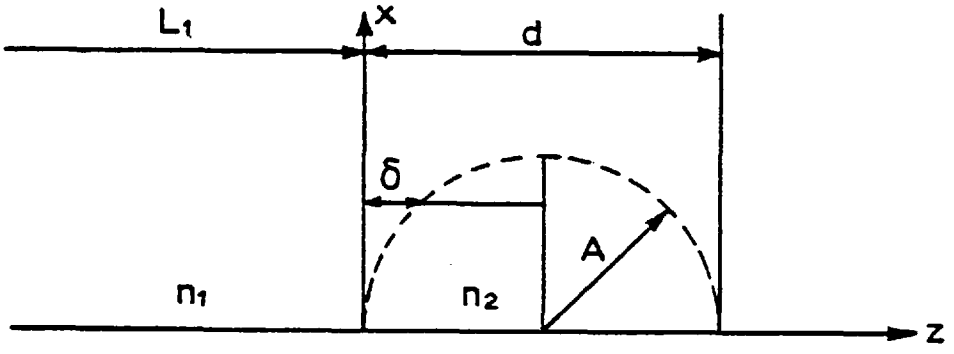

The phase change acquired by the propagating wave may be calculated according to Equation (2.10):-

$$\phi(x,L_1 + d) = 2 \left[- kn_1\delta - kn_2 (A - \delta) \right]$$

neglecting the linear phase component and substituting $\delta \simeq x^2/2A$:-

$$\phi(x,L_1 + d) \simeq k \cdot \frac{2 \cdot (n_2 - n_1)}{d^2} x \cdot d = kpx^2d \quad , \quad p = 2 \cdot (n_2 - n_1)/d^2$$

where p is the equivalent parabolic gradient mentioned previously. For $n_2 - n_1 = 320 \cdot 10^{-6}$ n-units, and a radius of 20 metres, therefore,

$p = 4.0 \cdot 10^{-7}$.

Effect of Varying the Location of the Localized Region

The presence of a localized parabolic region with a positive gradient, will focus the diffracting beam, the amount of focussing obviously being proportional to the thickness of the region along the direction of propagation, and on the magnitude of the parabolic gradient.

The amount of focussing is seen to be a function of the location of the parabolic medium with respect to both transmitter and receiver. This may clearly be seen in Figs. 2.5, 2.6 and 2.7. In all three cases, the region was taken to be 200 metres wide, with a gradient of $3.0 \cdot 10^{-7}$. In Figs. 2.5, 2.6 and 2.7, the regions are situated at distances from the transmitter of 200, 6,000 and 10,000 metres respectively.

The gain at a propagation distance of 12 kilometres is seen to be greatest for the mid-path location of the parabolic region. However, it may be observed that the rate of increase of the waist is positive for locations near the transmitter and becomes less so as the parabolic region is moved away. At some distance, the waist begins to decrease, i.e. focussing overcomes the diffraction process.

This may be attributed to the fact that the radius of curvature of a spherical (or cylindrical) Gaussian wave increases as the wave propagates further away. Therefore, the wave tends to become plane and, hence, may be focussed more readily by a lens-like region.

The above qualitative description obviously does not provide a means of determining the effects of a lens-like region of varying thickness, gradient and position on the spotsize or waist at various path lengths. However, the availability of a computational algorithm provides an easy means of prediction.

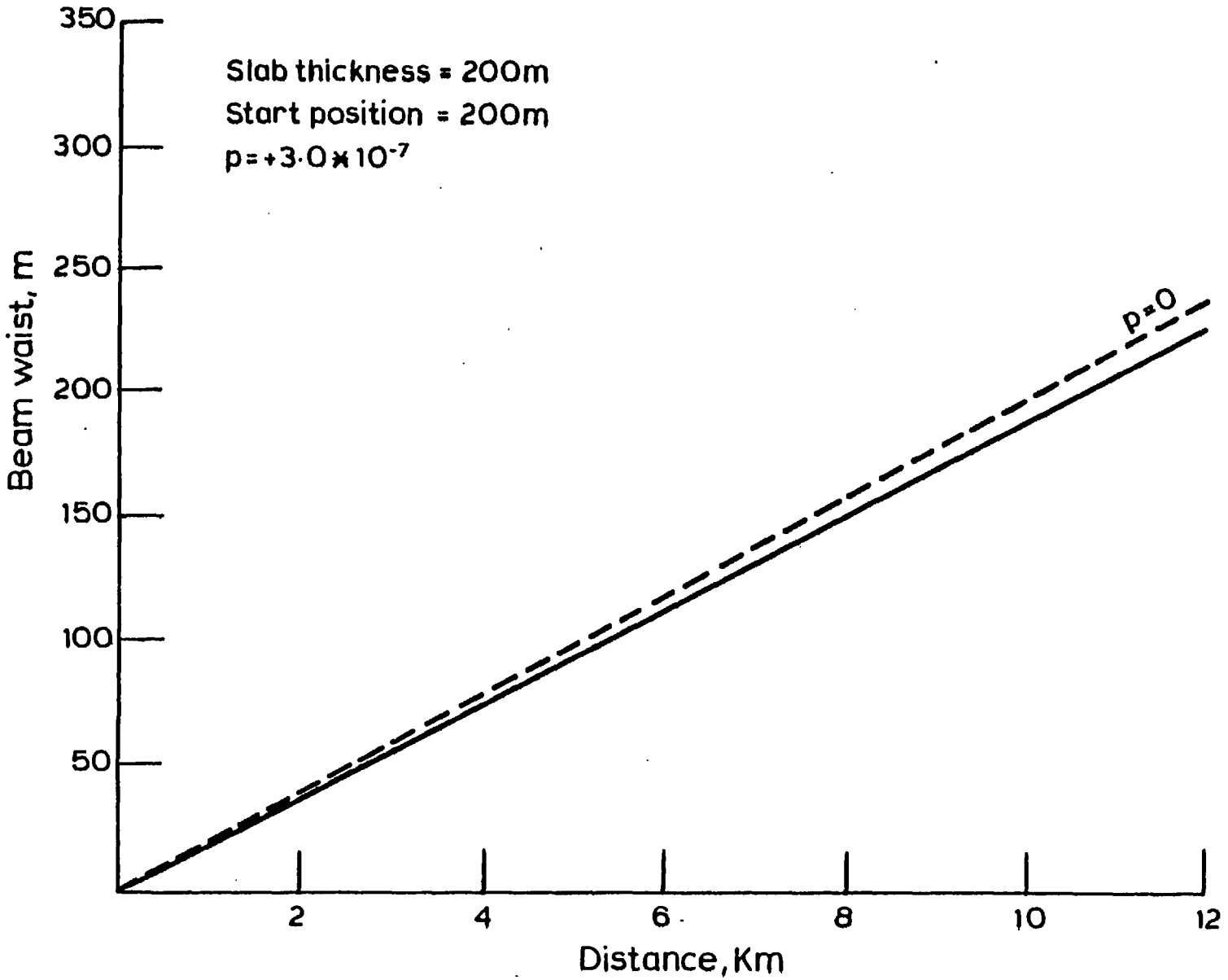
Slab thickness = 200m
Start position = 200m
p = +3·0 * 10⁻⁷
p=0
Beam waist, m
350
300
250
200
150
100
50
2
4
6
8
10
12
Distance, Km

Fig. 2·5

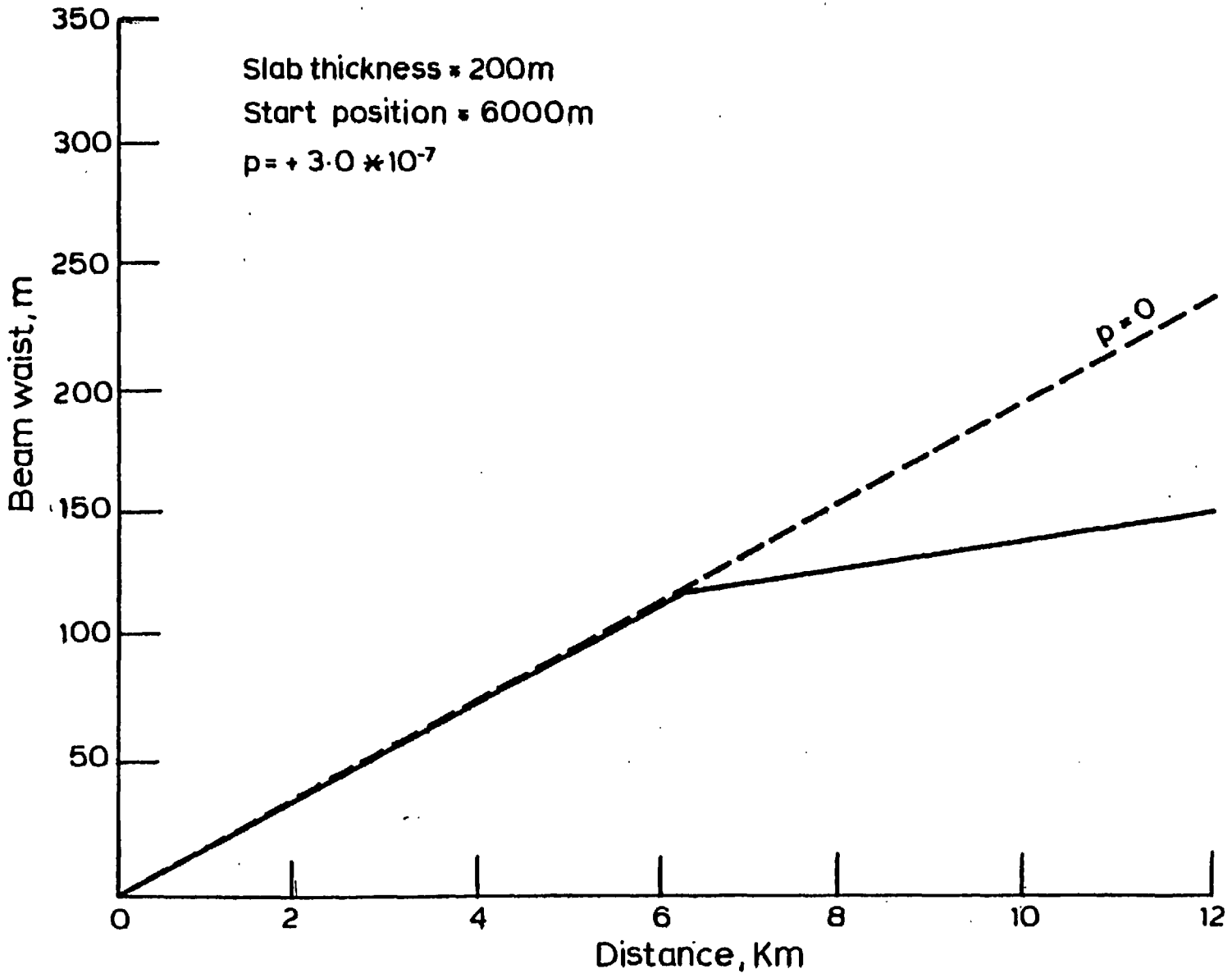
Slab thickness = 200m
Start position = 6000m
p = + 3·0 * 10⁻⁷
p=0
Beam waist, m
350
300
250
200
150
100
50
0
2
4
6
8
10
12
Distance, Km

Fig. 2·6

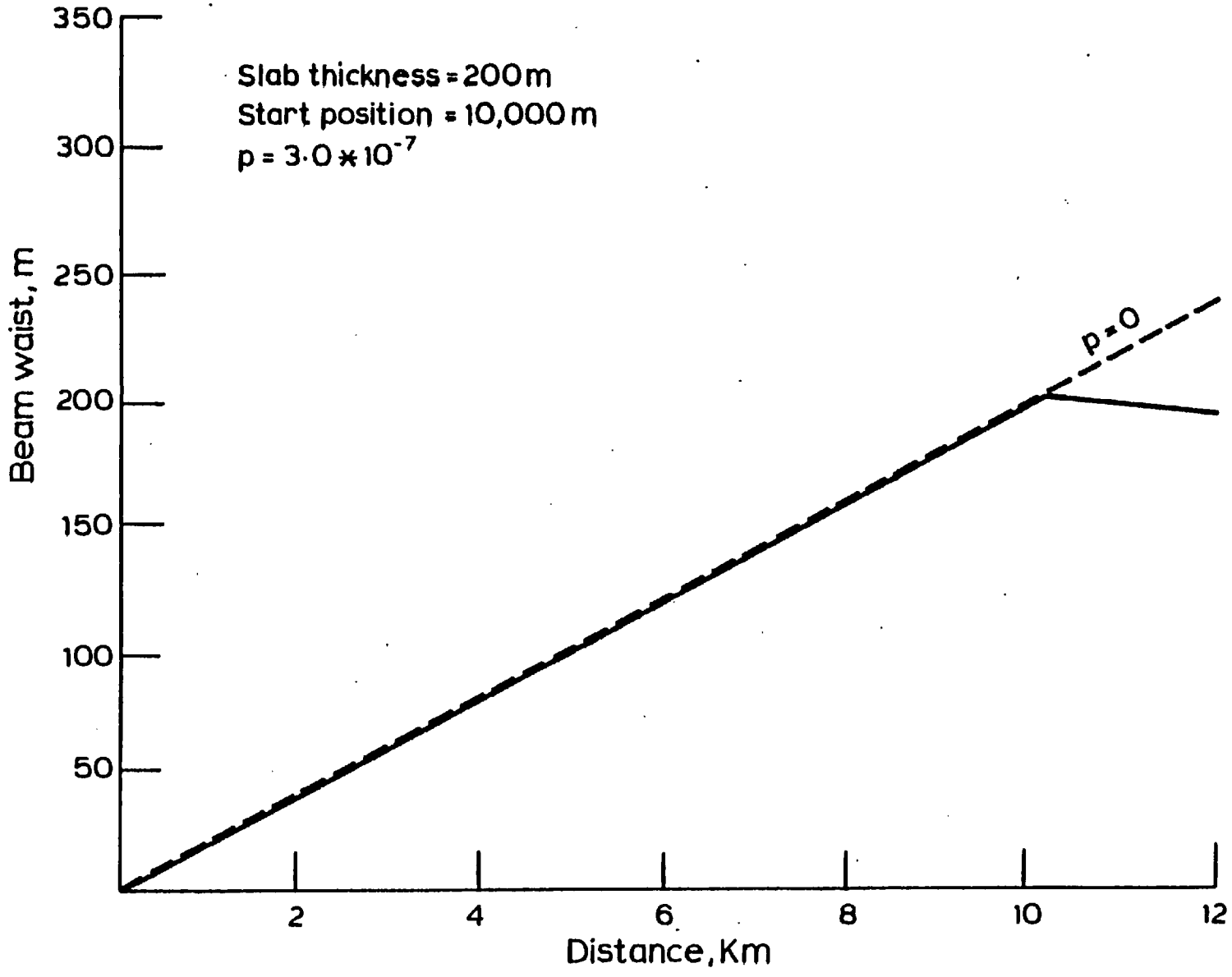
Slab thickness = 200 m
Start position = 10,000 m
p = 3·0 * 10⁻⁷
p=0
Beam waist, m
350
300
250
200
150
100
50
2
4
6
8
10
12
Distance, Km

Fig. 2·7

In conclusion, it may be seen that a square law medium focusses the propagating wave (or defocusses it for a negative gradient). This may explain such phenomena as anomalous propagation or signal enhancement at certain periods of the day when inversion layers are most likely to occur. For example, the refractivity profile discussed in Section 2.1.2 was obtained at 0250 hours; the parabolic gradient in this case would cause an increase of 2.95 decibels in the electric field over a propagation distance of 12 kilometres at a wavelength of 8 millimetres and a transmitting aperture with a Gaussian amplitude distribution with a "1/e" width of 0.3 metres. Such inversion conditions are likely to occur over relatively long periods of time, i.e. possibly a few hours, and would not appear as signal fluctuations of a random nature.

On the other hand, localized patches with parabolic gradients are mainly influenced by prevailing wind conditions, and are more likely to produce faster fluctuations. The amount of fluctuations has been seen to depend on the location of the parabolic region and the strength of the parabolic gradient, which is likely to vary over a period of a few seconds. For example, the magnitude of the field variations varies for a 20 metre spherical blob with a difference in refractive index of $320 \cdot 10^{-6}$ n-units from the surrounding atmosphere, from 0.07 decibels to 0.43 decibels for distances of 500 metres and 6,000 metres respectively from the transmitter end, for a radio link as described above.

The application of the split-step Fourier method in the solution of the parabolic equation has been seen to be a useful technique in determining the effects of a medium with small magnitude, large scale-size (compared to the wavelength) variations in the refractive index.

The consequent phase integral results are readily applied in

a medium with random variations of the refractive index, as will be shown in the following chapters.

CHAPTER 3

STATISTICS OF AN ELECTRIC FIELD PROPAGATING THROUGH A MEDIUM WITH WEAK RANDOM REFRACTIVE INDEX FLUCTUATIONS

The purpose of this chapter is to investigate the effects of a random medium characterized by uniform and homogeneous spatial variations of the refractive index throughout the propagation path.

The scale sizes of the variations considered are large compared to the wavelength involved, and the magnitude of the variations about a constant mean value is considered to be small with respect to the mean value. Under such conditions, the results obtained from the solution of the parabolic equation approximation of the wave equation, outlined in Chapter 2, namely, the phase integral solution, are applicable to the propagating wave.

The approach used is based on considering the radiating aperture as a set of Huygens' sources. It will be shown that the medium may be collapsed into an equivalent phase screen situated at the transmitter plane.

The statistics of the complex on-axis electric field are obtained, which give an insight into the individual amplitude and phase fluctuations, and into the probability distributions of the random field. The dependence of the field fluctuations on the properties of the random medium and on the system parameters are outlined.

3.1 The Parabolic Equation Solution of the Scalar Wave Equation in a Weakly Random Medium

It has been shown in Chapter 2 that the approximate solution of the parabolic equation in a medium with small refractive index variations, with scale-sizes much larger than the wavelength, is basically

a phase disturbance. The modification in phase due to the medium is determined by the characteristics of the refractive index variations as shown in Equation (2.10).

The refractive index variations considered here are of a random nature and, therefore, it is necessary to define their statistics.

3.1.1 Statistical Description of the Medium

The randomness of the medium is attributed to the presence of random variations or irregularities in the refractive index, which is assumed to be a real quantity. This is a valid assumption at microwave frequencies and, hence, absorption is not considered.

The refractive index fluctuations are assumed to be statistically uniform throughout the medium. The refractive index may be written in cartesian co-ordinate form as follows:-

$$n(x,y,z;t) = \langle n \rangle + \Delta n(x,y,z;t) \qquad (3.1)$$

where: $\langle n \rangle$ is the expected value of the refractive index which, for convenience, will be taken to be unity.

Δn is the random fluctuation around the mean value.

The analysis presented is concerned with the effects of the spatial variations of the refractive index and not the temporal ones, hence the time dependence will be dropped. Furthermore, the lateral spatial fluctuations of the refractive index $\Delta n(x,y)$ are considered to be independent, i.e. $\Delta n(x,y) = \Delta n(x) \cdot \Delta n(y)$ and, therefore, to make the analysis less cumbersome, the two-dimensional form of the fluctuations will be considered, i.e. $\Delta n = \Delta n(x,z)$.

The above reduction of the functional form of the refractive

index fluctuations does not affect the significance of the analysis since, as previously mentioned, the variations are considered to be independent and, therefore, it will be seen that their effect may be added in the final solution symmetrically.

Assuming spatial stationarity, the autocorrelation function of the refractive index fluctuations is defined as:-

$$R_n(\xi,\zeta) = \langle \Delta n(x,z) \cdot \Delta n(x+\xi, z+\zeta) \rangle = \sigma_n^2 \cdot r_n(\xi,\zeta)$$

where ξ and ζ are the lateral and longitudinal separations respectively and σ_n^2 is the variance of the refractive index fluctuations. $r_n(\xi,\zeta)$ is the normalized autocorrelation function.

The autocorrelation function can have various functional forms depending on the nature of the irregular medium. The form chosen in this treatment is the Gaussian one, i.e.:-

$$r_n(\xi,\zeta) = \exp\left[-\frac{\xi^2}{\xi_0^2} - \frac{\zeta^2}{\zeta_0^2}\right] \qquad (3.2)$$

The quantities "ξ_0" and "ζ_0" are called the scale-sizes of the irregularities and can be thought of as the size of an average "blob" or irregularity in the lateral and longitudinal directions respectively.

The Gaussian autocorrelation function has the advantage that it enables many results to be evaluated analytically. However, it is important to realise that this does not imply that the medium fluctuation has Gaussian statistics[33]. The form of the probability distributions governing n(x,z) and the form of the autocorrelation function are quite independent of each other. A function n(x,z) obeying non-Gaussian statistics may or may not have a Gaussian autocorrelation function and

vice versa.

3.1.2 Statistics of the Phase Contribution of the Medium

Having defined the necessary statistical properties of the medium, the resulting random phase contribution will now be studied.

Consider a bundle of parallel rays propagating as shown in Fig. 3.1. Applying the approximate solution of the parabolic equation, the rays will suffer a phase change determined by the intervening medium. In physical terms, the refractive index blobs may be considered to be randomly distributed lenses.

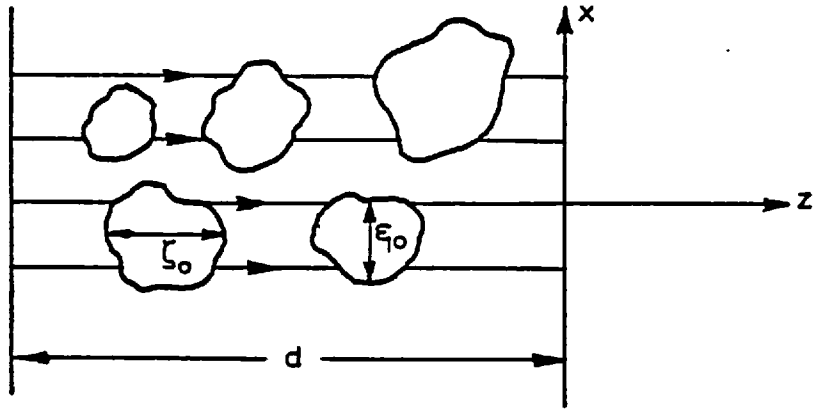

Fig. 3.1 Random distribution of refractive index blobs in a propagation path

The phase variation is calculated according to Equation (2.10) and is:-

$$\phi(x)\Big|_{z=d} = -k \int_0^d \Delta n(x,z)\, dz \qquad (3.3)$$

It may be shown[34] that the phase autocorrelation function at the plane z = d, in terms of the lateral separation ξ, is:-

$$R_\phi(\xi) = k^2 \cdot d \cdot \int_{-d}^{+d} \left[1 - \frac{|\zeta|}{d}\right] \cdot R_n(\xi,\zeta) \cdot d\zeta = \sigma_\phi^2 \cdot r_\phi(\xi)$$

where: σ_ϕ^2 is the variance of the phase fluctuations.

$r_\phi(\xi)$ is the normalized phase autocorrelation function.

Substituting for the refractive index autocorrelation function in its Gaussian form, the above integral is found to be:-

$$R_\phi(\xi) = k^2 \cdot d \cdot e^{-\xi^2/\xi_0^2} \left[\sqrt{\pi} \cdot \zeta_0 - \sqrt{\frac{\pi}{2}} \cdot \frac{\zeta_0^2}{d}\right] \cdot \sigma_n^2$$

which for $d >> \zeta_0$, reduces to:-

$$R_\phi(\xi) = \sqrt{\pi} \cdot k^2 \cdot d \cdot \sigma_n^2 \cdot \zeta_0 \cdot e^{-\xi^2/\xi_0^2}$$

Therefore:-

$$\sigma_\phi^2 = \sqrt{\pi} \cdot k^2 \cdot d \cdot \sigma_n^2 \cdot \zeta_0 \qquad (3.4)$$

and:-

$$r_\phi(\xi) = e^{-\xi^2/\xi_0^2}$$

which is of the same form as the autocorrelation function assumed for the refractive index fluctuations.

Having defined the random medium and its relevant statistical properties, the problem then is to investigate the effect of such a medium on a diffracting wave propagating through it.

The following analysis will add insight into the manner by which the field is coupled from a finite transmitting aperture into a random field. The dependence of the field fluctuations on the size of the aperture relative to the medium scale sizes will be determined. The behaviour of the random complex electric field is investigated in the near and far fields of a finite radiating aperture, i.e. the analysis is not limited to a plane wave propagation problem.

3.2 Random Field Calculations Using Huygens' Principle

In this section, the statistics of the electric field will be obtained using a Huygens' Principle approach. Although this method is more complicated than the lateral coherence approach outlined in Chapter 4, it is worthwhile to pursue due to the more detailed information it provides for the field statistics.

First, the complex field distribution is calculated in a plane normal to the propagation direction for a Guassian aperture field in a deterministic medium and the randomness is then imposed.

3.2.1 Fresnel Field Calculations in a Uniform Medium

Consider a radiating aperture of finite width, a. The aperture field is defined with respect to a lateral co-ordinate system ξ. This field may be assumed to be quantized into a large number of elemental sources $f_i(\xi)$.

The complex electric field distribution resulting from the combination of the elemental sources is calculated at the plane $z = d$ and at a point p whose x-coordinate is as shown in Fig. 3.2.

The complex electric field at the observation point p(x,d) due to the elemental source $f_i(\xi)$ is linearly polarized, with an x-component given by[35]:-

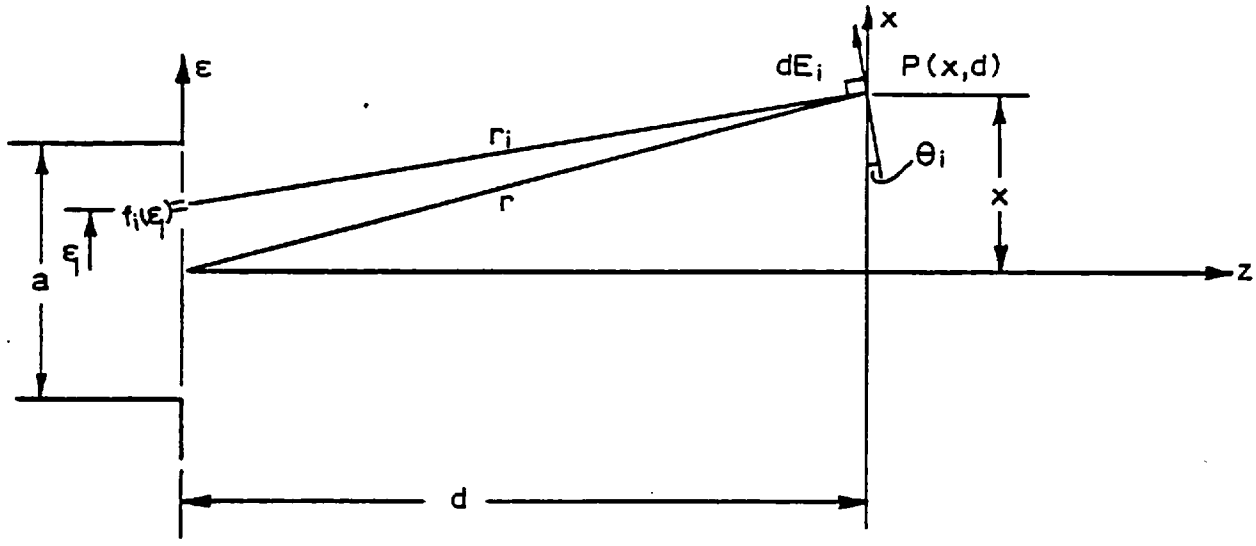

Fig. 3.2 Electric field radiated by an elemental source

$$dE_x(x;d) = \sqrt{\frac{j}{\lambda}} \frac{f_i(\xi)}{\sqrt{r_i}} e^{-jkr_i} \cdot \cos\theta_i \, d\xi \qquad (3.5)$$

Making use of the following approximations, which are the Fresnel approximations:-

(i) $\cos\theta_i \simeq 1$, which is a good approximation for narrow beam spreads.

(ii) $r_i \simeq d + \dfrac{(x - \xi_i)^2}{2d}$

(iii) assume that d is large enough for amplitude variations due to r_i changing to be negligible.

Therefore:-

$$dE_x(x;d) \simeq \sqrt{\frac{j}{\lambda d}} \cdot e^{-jkd} \cdot e^{-jk\frac{x^2}{2d}} \cdot f_i(\xi) \cdot e^{-jk\frac{x\xi_i}{d}} \cdot e^{-j\frac{k\xi_i^2}{2d}} d\xi$$

and, hence, the value of the electric field at the observation point p is the integral over the aperture:-

$$E_x(x;d) \simeq \sqrt{\frac{j}{\lambda d}} \cdot e^{-jkd} \cdot e^{-jk\frac{x^2}{2d}} \cdot \int_{-a/2}^{+a/2} f(\xi) \cdot e^{j\frac{kx\xi}{d}} \cdot e^{-j\frac{k\xi^2}{2d}} d\xi \qquad (3.6)$$

A reasonably practical analytical distribution for the aperture $f(\xi)$ is a uniform phase and Gaussian amplitude distribution, which is also simple to integrate, i.e.:-

$$f(\xi) = b \exp(-\xi^2/w^2)$$

where w is the "1/e" width of the radiating aperture field and will be taken as the effective aperture size.

Substituting this aperture field into Equation (3.6) and noting that the Gaussian field is a decaying one, so the limits of the integration can be taken to be $\pm \infty$, it may be shown that:-

$$E_x(x;d) = C_d \cdot e^{-\frac{x^2}{w_d^2}} \cdot e^{-j\frac{kx^2}{2R_d}} \qquad (3.7)$$

where:-

$$C_d = b \cdot e^{-jkd} \cdot \sqrt{\frac{1 + j(2d/w^2k)}{1 + (2d/w^2k)^2}}$$

$$w_d^2 = w^2 \cdot \left[1 + \left(\frac{2d}{w^2k}\right)^2\right]$$

$$R_d = d \cdot \left[1 + \left(\frac{wk}{2d}\right)^2\right]$$

w_d and R_d are the "1/e" waist and radius of curvature respectively of the Gaussian beam at the plane z = d.

It is worthwhile noting here that the expression for the Gaussian field distribution is identical to that obtained in Chapter 2 for the free space case (Equation (2.13) with p = 0).

The magnitude of the on-axis field, x = 0, is given by $|C_d|$. Therefore:-

$$|E_x(0;d)| = b \cdot \sqrt{\frac{k}{2d}} \cdot \frac{1}{4\sqrt{\left(\frac{1}{w^2}\right)^2 + \left(\frac{k}{2d}\right)^2}} \qquad (3.8)$$

3.2.2 Fresnel Field Calculations in a Random Medium

As previously mentioned, the effect of the random medium under consideration on a propagating bundle of rays is to contribute a random phase modulation given by Equation (3.3). Therefore, the elementary field at the observation point p(x,d) due to an elementary Huygens' source $f_i(\xi)$, will be modified by the random phase contribution along r_i and, hence, Equation (3.5) becomes:-

$$dE_x(x;d) = \sqrt{\frac{j}{\lambda}} \cdot \frac{f_i(\xi)}{\sqrt{r_i}} \cdot e^{-jkr_i} \cdot e^{j\phi_i} \cdot \cos\theta_i \cdot d\xi$$

with:-

$$\phi_i = -k \int_0^{r_i} \Delta n(x,z)\, dz$$

Therefore:-

$$E_x(x;d) \simeq \sqrt{\frac{j}{\lambda d}} \cdot e^{-jkd} \cdot e^{-j\frac{kx^2}{2d}} \int_{-\infty}^{+\infty} f(\xi) \cdot e^{j\frac{kx\xi}{d}} \cdot e^{-j\frac{k\xi^2}{2d}} \cdot e^{j\phi(\xi)}\, d\xi \qquad (3.9)$$

Taking the mean value of the electric field and noting that for a Gaussian phase process that[36]:-

$$\langle e^{j\phi(\xi)} \rangle = e^{-\sigma_{\phi_i}^2/2}$$

where:-

$$\sigma_{\phi_i}^2 = \sqrt{\pi} \cdot k^2 \cdot \zeta_0 \cdot \sigma_n^2 \cdot r_i \qquad (3.10)$$

Substituting for r_i by its approximate far field value, $r_i \simeq r - \frac{x}{r}\xi_i$, therefore:-

$$\sigma_{\phi_i}^2 \simeq mr - m\frac{x}{r} \cdot \xi_i$$

and:-

$$m = \frac{\sqrt{\pi} \cdot k^2 \cdot \zeta_0 \cdot \sigma_n^2}{2}$$

After integrating Equation (3.9), the average value of the electric field is then:-

$$\langle E_x(x;d) \rangle = E_x(x;d)\Big|_{\text{free space}} \cdot e^{-md} \cdot e^{-\alpha x^2} \cdot e^{-j\beta x^2} \qquad (3.11)$$

where: $E_x(x;d)\Big|_{\text{free space}}$ is that expressed in Equation (3.7).

and:-

$$\alpha = m/2d \quad , \quad \beta = \frac{k \cdot m \cdot w^2}{2d^2}$$

3.2.3 Phase Screen Representation of the Random Medium

It will be shown in the following discussion that, for all practical purposes, the random medium may be substituted by a phase screen situated at the transmitter aperture plane. The characteristics of the random phase screen are derived from those of the medium.

Equation (3.11) indicates that the free space field is attenuated or reduced uniformly due to the random medium, by the amount exp (- md), i.e. exp ($-\sigma_\phi^2/2$), which is a well-known result. However, in addition to this uniform reduction in magnitude, there is also an average x-dependent attenuation given by α, which is a function of m, i.e. of the randomness of the medium. Therefore, the Gaussian amplitude distribution is altered from its free space value.

The free space lateral phase distribution of the cylindrical wave is also altered due to the x-dependent phase shift β, which is also a function of the randomness of the medium.

To estimate the magnitude of the distortion caused by the medium, we shall consider a practical example. For a wavelength λ = 8 millimetres, in a medium with refractive index irregularities with a typical longitudinal scale size ζ_0 = 20 metres, and a variance σ_n^2 = $1 \cdot 10^{-12}$ n^2-units, which represents a relatively high degree of turbulence. The values of α and β for a Gaussian aperture "1/e" width w = 0.3 metres, and at a propagation distance d = 1,000 metres, are found to be:-

$$m = 1.1 \cdot 10^{-5}\ m^{-1} \quad , \quad \alpha = 5.7 \cdot 10^{-9}\ m^{-1} \quad \text{and} \quad \beta = 4.1 \cdot 10^{-10}\ m^{-2}$$

Substituting these values in Equation (3.10), it can be shown that the average field distribution is hardly affected, i.e. for all practical purposes, the x-dependent amplitude reduction and phase shift α and β respectively may be neglected.

Therefore, the average distribution of the complex electric field is given by:-

$$\langle E_x(x;d)\rangle = E_x(x;d)\Big|_{\text{free space}} \cdot e^{-\sigma_\phi^2/2} \tag{3.12}$$

This result is a standard result for the average value of the electric field in a random medium. The same result may have been obtained by setting $r_i = r$ in Equation (3.10) and collapsing the medium into a thin screen characterized by a random phase variation, i.e. a random phase screen.

The phase screen representation of the random medium is a commonly used technique. However, previous use has been limited to infinite plane waves incident on the screen. A useful discussion on the development of the random phase screen approach may be found in Fejer's[37] and Bramley's[38] works.

In the following analysis, the phase screen will be assumed to be random with a Gaussian phase ϕ, distribution with zero mean and variance σ_ϕ^2 given by:-

$$\sigma_\phi^2 = \sqrt{\pi} \cdot k^2 \cdot \zeta_0 \cdot \sigma_n^2 \cdot d \text{ radian}^2 \tag{3.13}$$

and a normalized lateral autocorrelation function $r_\phi(u) = \exp(-u^2/\xi_0^2)$, u being the lateral separation on the ξ-axis at the plane $z = 0$. ξ_0 is the lateral scale size of the refractive index irregularities and, hence,

of the phase variations across the screen.

Variance of the On-Axis Fluctuating Complex Electric Field at z = d

The on-axis electric field is obtained from Equation (3.9) with x = 0, and neglecting the constant phase components. Therefore:-

$$E_x(0;d) = \frac{b}{\sqrt{\lambda d}} \cdot \int_{-\infty}^{+\infty} e^{-\xi^2/w^2} \cdot e^{-jk\xi^2/2d} \cdot e^{j\phi(\xi)}\, d\xi \qquad (3.14)$$

The variance σ_E^2 is given by:-

$$\sigma_E^2 = \langle |E_x(0;d) - \langle E_x(0;d)\rangle|^2 \rangle = \langle |E_x(0;d)|^2 \rangle - |\langle E_x(0;d)\rangle|^2$$

where:-

$$\langle |E_x(0,d)|^2 \rangle = \langle E_x(0,d) \cdot E_x^*(0,d) \rangle$$

$E_x^*(0,d)$ is the conjugate of the random complex electric field.

$$\langle E_x(0,d) \cdot E_x^*(0,d) \rangle = \frac{b^2}{\lambda d} \int_{-\infty}^{+\infty} \int_{-\infty}^{+\infty} e^{-\xi^2/w^2} \cdot e^{-\xi_1^2/w^2} \cdot e^{+jk\xi_1^2/2d} \cdot e^{-jk\xi^2/2d} \cdot$$

$$\langle e^{j\phi} \cdot e^{-j\phi_1} \rangle \cdot d\xi \cdot d\xi_1 \qquad (3.15)$$

where $\xi_1 = \xi + u$, and u is a variable lateral separation along the ξ-axis. $\langle e^{j\phi} \cdot e^{-j\phi_1} \rangle$ is the characteristic function of the random phase process, with $\phi = \phi(\xi)$ and $\phi_1 = \phi(\xi + u)$. Since ϕ is a Gaussian random variable, it has been shown that[36]:-

$$\langle e^{j\{\phi(\xi) - \phi(\xi + u)\}} \rangle = e^{-\sigma_\phi^2\{1 - r_\phi(u)\}}$$

which for $\sigma_\phi^2 << 1$ reduces to $1 - \sigma_\phi^2\{1 - r_\phi(u)\}$.

The approximation that $\sigma_\phi^2 << 1$ is quite accurate at microwave wavelengths even at high degrees of turbulence. For example, for $\lambda = 8$ millimetres, $\zeta_0 = 20$ metres, $\sigma_n^2 = 1 \cdot 10^{-12}$ n^2-units and a propagation distance of 12 kilometres, $\sigma_\phi^2 = 0.28$ radian^2.

Solving the double integral Equation (3.14) by parts, and for $\sigma_\phi^2 << 1$, it may be shown that:-

$$\langle E_x(0,d) \cdot E_x^*(0,d) \rangle \simeq b^2 \cdot \frac{k}{2d} \cdot \left[(1 - \sigma_\phi^2) \cdot \frac{1}{\sqrt{\left(\frac{1}{w^2}\right)^2 + \left(\frac{k}{2d}\right)^2}} + \right.$$

$$\left. + \sigma_\phi^2 \cdot \frac{1}{\sqrt{\left(\frac{1}{w^2}\right)^2 + \frac{2}{w^2 \cdot \xi_0^2} + \left(\frac{k}{2d}\right)^2}} \right]$$

and from Equations (3.8) and (3.12), for $\sigma_\phi^2 << 1$:-

$$|\langle E_x(0,d) \rangle|^2 \simeq b^2 \cdot \frac{k}{2d} (1 - \sigma_\phi^2) \cdot \frac{1}{\sqrt{\left(\frac{1}{w^2}\right)^2 + \left(\frac{k}{2d}\right)^2}}$$

and, therefore, the variance of the on-axis complex electric field is given by:-

$$\sigma_E^2 = b^2 \cdot \frac{k}{2d} \cdot \sigma_\phi^2 \frac{1}{\sqrt{\left(\frac{1}{w^2}\right)^2 + \frac{2}{w^2 \cdot \xi_0^2} + \left(\frac{k}{2d}\right)^2}} \qquad (3.16)$$

The above expression for the variance of the on-axis complex electric field is accurate to the extent that $\sigma_\phi^2 << 1$. This expression for σ_E^2 holds at distances from the transmitting aperture extending from the Fresnel to the far field regions.

It is interesting to note the far field behaviour of σ_E^2, where the Rayleigh distance is defined as:-

$$d >> \frac{\pi A^2}{\lambda}$$

where A is the effective transmitting aperture size, which in this case is w, and, hence, in the far field:-

$$\frac{1}{w^2} >> \frac{k}{2d}$$

and the variance σ_E^2 reduces to:-

$$\sigma_E^2\Big|_{\text{far field}} = b^2 \cdot \frac{k}{2d} \cdot \sigma_\phi^2 \frac{1}{\sqrt{\left(\frac{1}{w^2}\right)^2 + \frac{2}{w^2 \cdot \xi_0^2}}}$$

3.3 Effect of System and Medium Parameters on the Field Fluctuations

A useful and practical quantity to deal with is the percentage relative fluctuations with respect to the mean value which, in this case, gives an indication of the fluctuations in the on-axis available power. This quantity is given by:-

$$\frac{\sigma_E^2}{|\langle E \rangle|^2} = \frac{\sigma_\phi^2}{1 - \sigma_\phi^2} \sqrt{\frac{\left(\frac{1}{w^2}\right)^2 + \left(\frac{k}{2d}\right)^2}{\left(\frac{1}{w^2}\right)^2 + \left(\frac{k}{2d}\right)^2 + \frac{2}{w^2 \cdot \xi_0^2}}} \qquad (3.17)$$

The percentage relative fluctuation with respect to the mean value of the electric field is the square root of the above ratio.

The relative field or power fluctuations are seen to be dependent on the aperture size w, the propagation distance d, and the wavelength λ, all of which may be considered to be system parameters. The effect of the medium is evident from the dependence on σ_ϕ^2, i.e. on σ_n^2 and ζ_0, and on ξ_0.

Fig. 3.3 shows the variation of the percentage field fluctuations versus the propagation distance. The Fresnel and far field cases are shown with the scale sizes ξ_0 and ζ_0 as variable parameters.

The variance of the refractive index fluctuations σ_n^2, is constant and is arbitrarily taken to be $1.0 \cdot 10^{-12}$ n-units, which represents a relatively high degree of turbulence.

The distance dependence of the variations of the relative field or power fluctuations has been previously studied by many authors for the case of plane wave propagation. For example, Uscinskii[33], who gives the name of scintillation index for the relative power fluctuations. In Uscinskii's prediction, the relative fluctuations saturate at a large distance from the random phase screen. This is due to the fact that the properties of the random phase screen used in his model are constant, whereas in this analysis, the variance of the phase of the random screen is varying as a function of the propagation distance as seen from Equation (3.13). This increase is limited by the condition that $\sigma_\phi^2 << 1$.

Effect of Transmitter Aperture Size on the Signal Fluctuations

The effect of increasing the transmitter aperture size on the magnitude of the fluctuations will now be studied. Looking at the expression (3.17) for the relative signal fluctuations, it may be seen

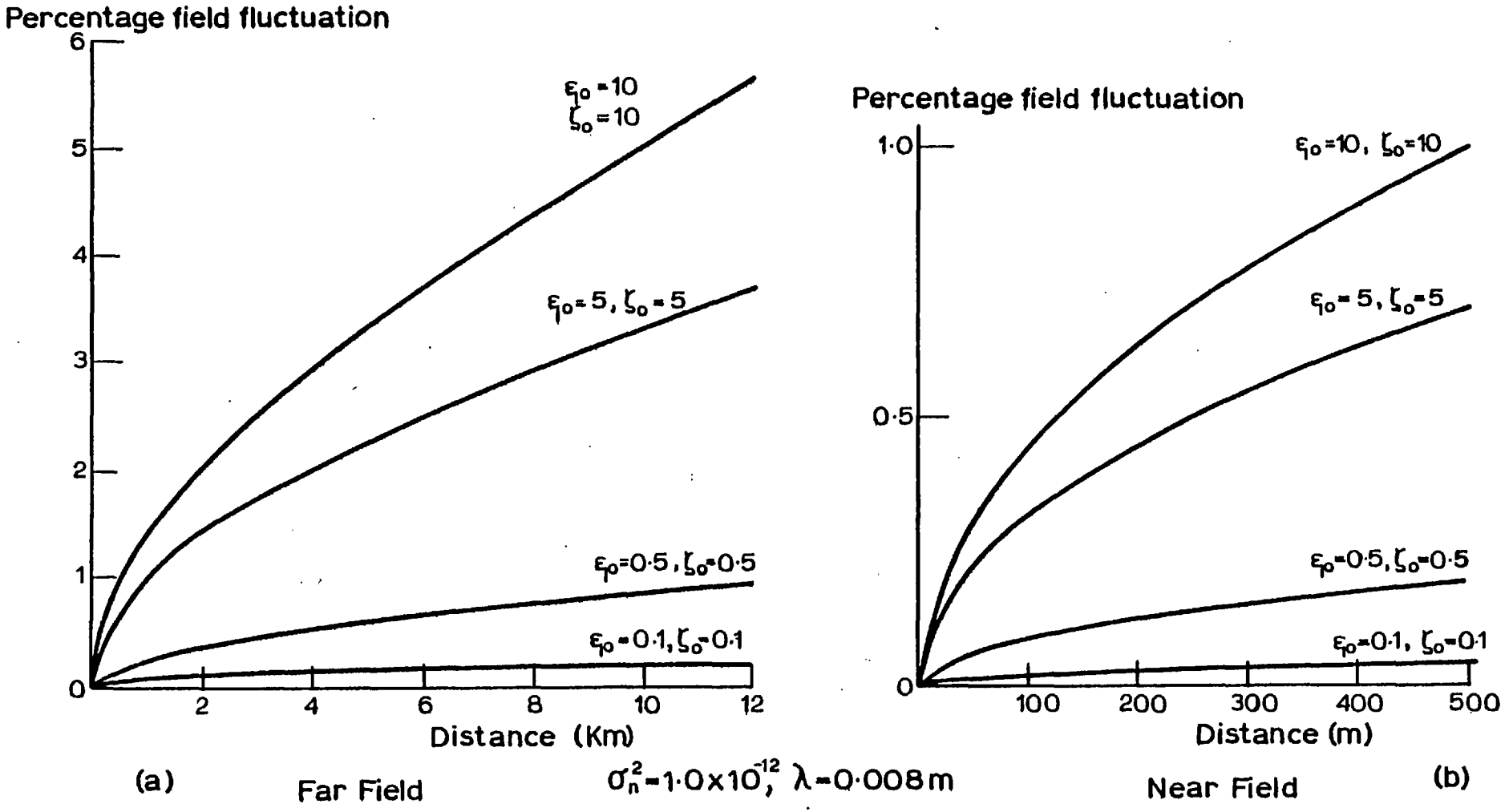

Fig. 3.3 Distance dependence of the percentage fluctuations of the electric field

that the relationship between the fluctuations and the aperture size w is not a straightforward one.

Differentiating Equation (3.17) with respect to w, it may be seen that the condition for minimum fluctuations is the solution of the following equation:-

$$\nu^3 \cdot \left[\frac{k}{2d}\right] - \nu^2 \cdot \left[\frac{k}{2d}\right]^2 + \nu \cdot \left[1 - \frac{2}{\xi_0^2}\right] - 1 = 0 \qquad (3.18)$$

where $\nu = w^2$.

The optimum aperture size for minimum fluctuations is seen to be a function of the wavelength, the propagation distance d and the lateral scale size ξ_0.

Figs. 3.4a and 3.4b show the variation of the percentage field fluctuations as a function of the aperture size w, for propagation distances of 12 and 1 kilometres respectively.

The percentage field fluctuations are seen to decrease dramatically when the lateral scale size ξ_0 is small, i.e. in the order of 1 metre. The reduction in the fluctuations becomes less apparent as ξ_0 increases.

An interesting result may be seen on comparing the fluctuations for the long and short path lengths. It may be seen that for the 1 kilometre path, the existence of an optimum aperture size for minimum fluctuations is quite obvious and is particularly evident for the smaller lateral scale sizes, whereas for the longer path, the optimum aperture size is not a very critical one.

The above phenomenon of an optimum transmitter aperture size, which is a function of the above-mentioned parameters, may possibly be qualitatively explained in terms of the mechanisms causing the signal fluctuations. Two mechanisms are considered, namely, random scattering

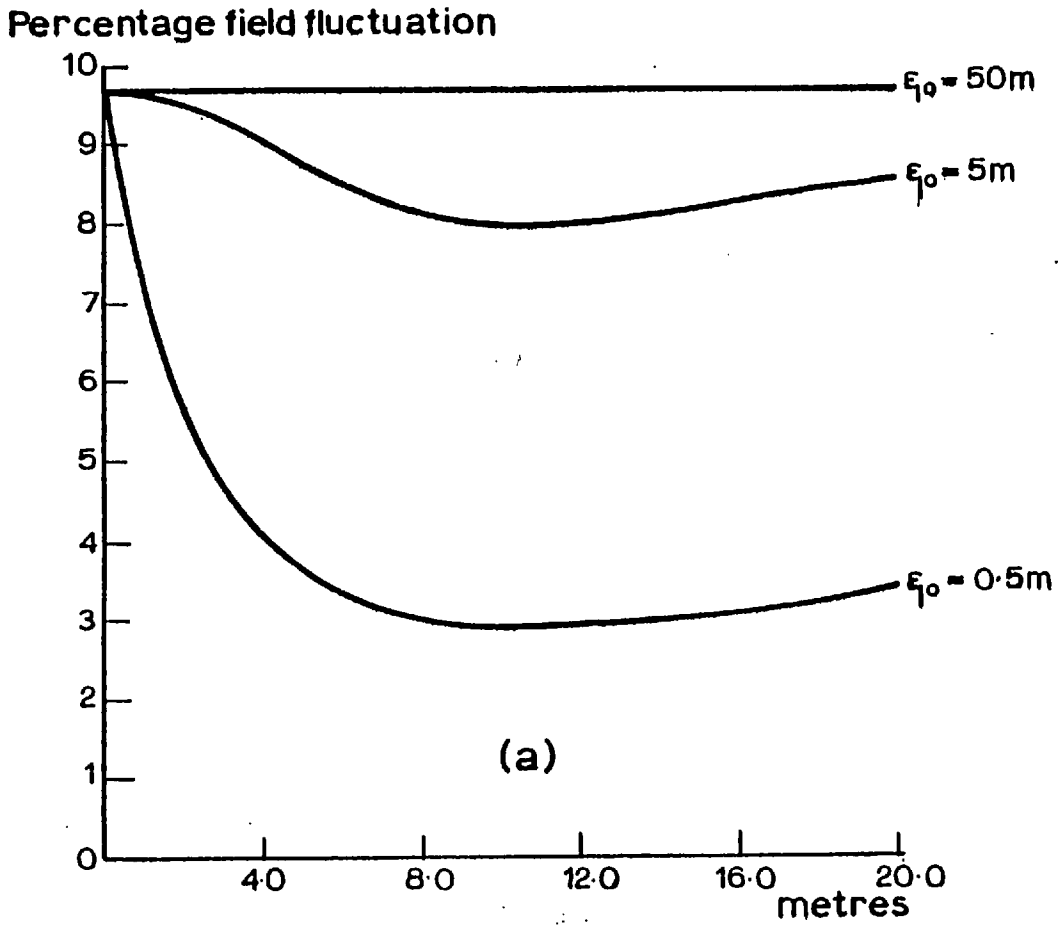

"1/e" Transmitter aperture width 2w,
path length 12Km, ζ_o = 20m, $\sigma_n^2 = 1{\cdot}0 * 10^{-12}$

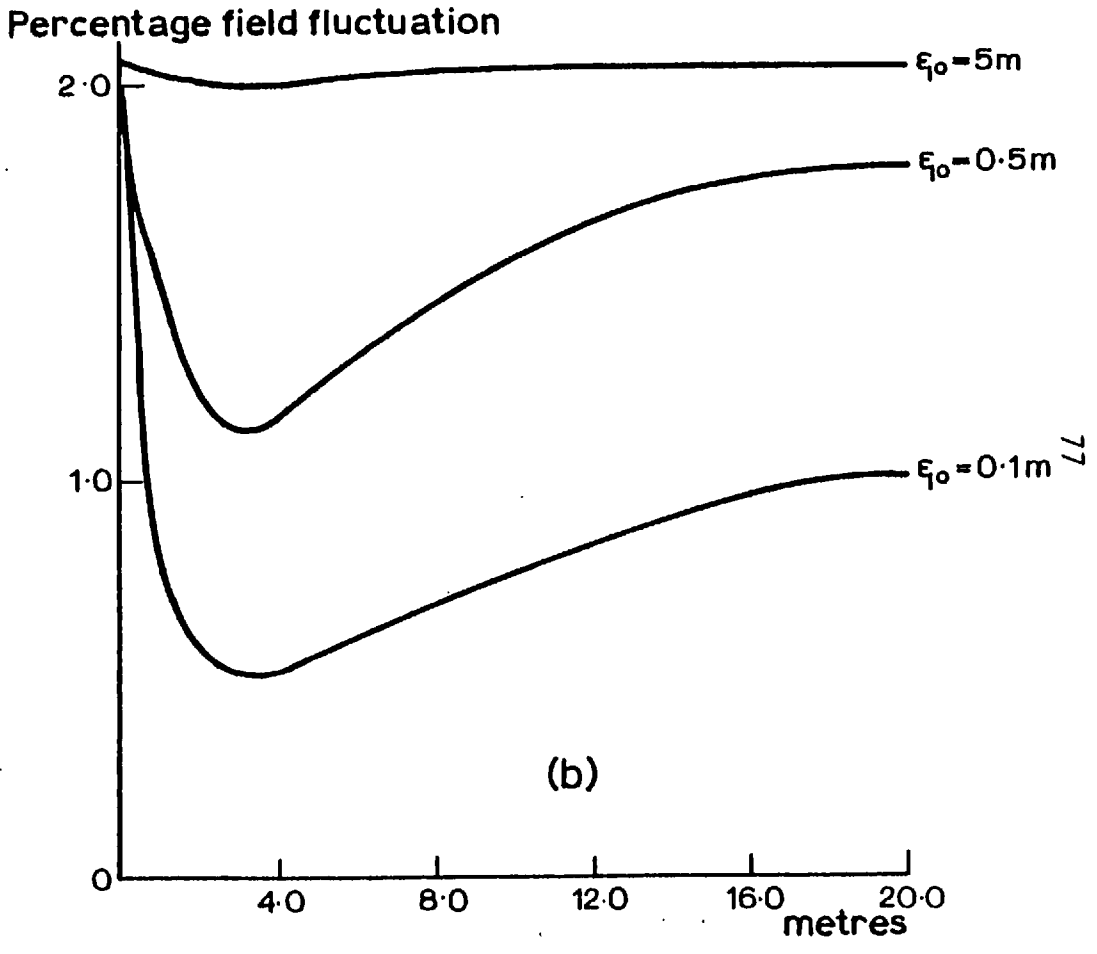

"1/e" Transmitter aperture width 2w,
path length 1Km, ζ_o = 20m, $\sigma_n^2 = 1{\cdot}0 * 10^{-12}$

Fig. 3·4 Transmitter aperture averaging effect

and random beam wandering.

Consider first the situation where the path length is relatively short, Fig. 3.4b. The fluctuations for a small aperture size may be mainly attributed to scattering; as the aperture size is increased, the beam width becomes narrower and hence less energy is scattered. The fluctuations due to scattering become more pronounced as the scale size ξ_0 increases.

As the beam width becomes narrower, beam wandering becomes the dominant mechanism causing fluctuations. Again, beam wandering becomes more pronounced as the scale size is increased. The effects of these two mechanisms can be combined qualitatively, as shown in the figure below.

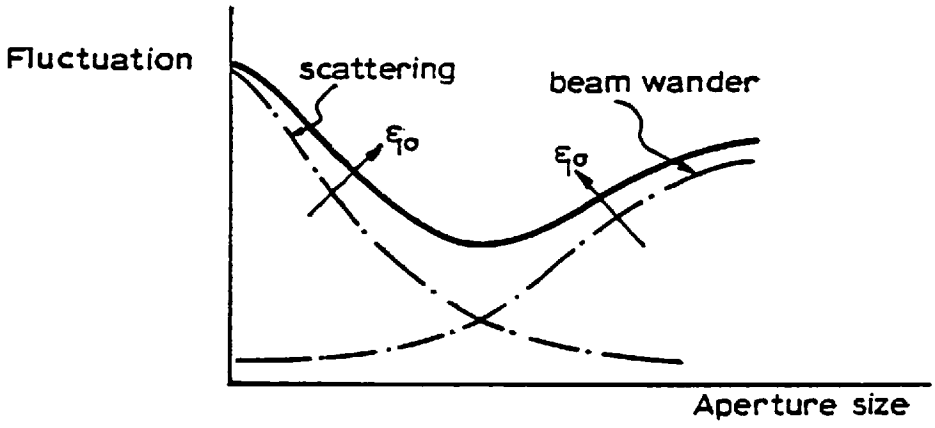

The hypothetical curves are seen to intersect at an optimum aperture size, which is relatively large, and from Fig. 3.4b, is of the order of 3 metres. In this case, the beam width is quite narrow and is 0.2 degrees, i.e. beam wandering is quite a possible mechanism to cause fluctuations.

On the other hand, for the larger propagation distance of 12 kilometres, Fig. 3.4a, both mechanisms probably still apply. However, due to the longer path length, the fluctuations due to the scattering

process tend to decrease less rapidly as the transmitter size increases due to the increased cross-sectional area of the beam at increased distances and, hence, more energy is scattered. The fluctuations due to beam wandering tend to increase at a smaller rate with increased aperture size. This may partially be due to the larger cross-sectional area of the beam and, hence, the wandering process is not very critical and may also be due to the random nature of the wandering process, which possibly tends to integrate over a longer path length, i.e. the beam wanders on and off the propagation axis. Therefore, the total effect is relatively low.

The behaviour discussed above is not easily explained quantitatively, since the expression for the relative signal fluctuation (3.17) does not yield separate information for the scattering and beam wandering mechanisms.

The dependence of the relative field fluctuations on the transmitter aperture size is not a surprising one. It will be shown later, in Chapter 5, that the efficiency of a receiving aperture is a function of the transmitting aperture size. The existence of an optimum receiver aperture size large enough to smooth out the fluctuations, yet not too large so as to suffer an appreciable loss in efficiency, is also discussed there. Reciprocally, one may expect a similar behaviour from a transmitting aperture.

3.4 Statistics of the Amplitude and Phase of the On-Axis Field

In this section, the magnitude and statistics of the amplitude and phase fluctuations of the electric field will be estimated. Such an investigation yields information for the probability distribution of the fluctuating electric field. Investigations of this sort have been previously carried out[39, 40] for the case of plane wave propagation.

In this study the field is investigated, in the Fresnel region and beyond, of a finite transmitting aperture. The approach followed is that of resolving the random complex electric field into its real and imaginary components and the statistics of each obtained individually.

As mentioned in the previous section, the weakly random medium may be replaced by a random phase screen at the radiating aperture plane. The effect of the phase screen is to alter randomly the phases of the elementary fields radiated by the assumed set of elementary Huygen sources. The magnitudes of the fields remain unchanged as they pass through the phase screen.

The resulting total electric field at any observation point is thus the combination or sum of the elementary waves in mutual phase interference. This situation may be represented on the Argand diagram shown in Fig. 3.5.

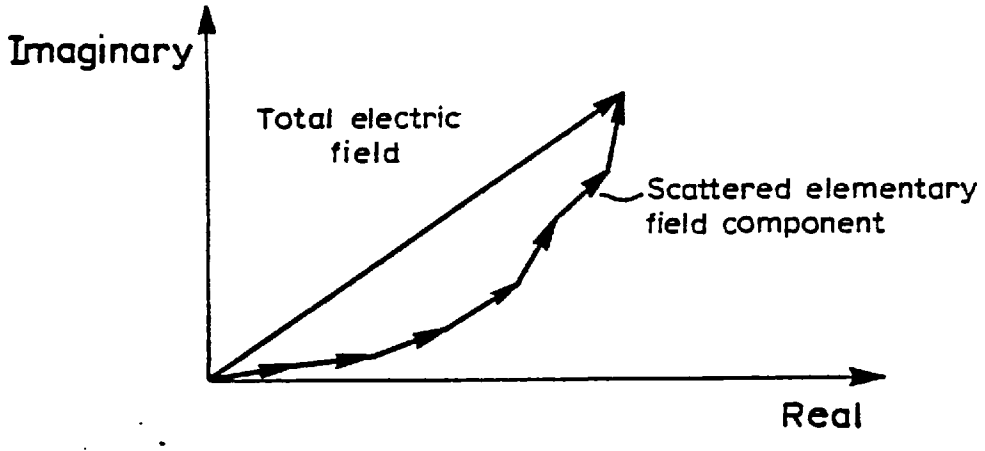

Fig. 3.5 Phasor representation of the scattered field components

The total electric field is the phasor sum of a large number of elementary field components, which, in the case of free-space propagation, make up the familiar Cornu Spiral.

Both the magnitude and phase of the total field change as the

observation plane progresses along the direction of propagation, up to the Rayleigh distance, beyond which the changes become negligible. However, in the presence of a random medium, there is a further addition of a random phase contributed by the medium to each elementary field component.

3.4.1 First and Second Order Statistics of the Real and Imaginary Field Components

The statistics of the real and imaginary components of the fluctuating field components will be obtained at an observation point p(0,d), i.e. the on-axis point at a propagation distance z = d, this being the point of most practical interest and may be considered to be the fluctuations observed by a point receiving aperture.

In the following analysis, the functional dependence of the random phase distribution $\phi(x)$ on the medium parameters will be suppressed for brevity.

First, the mean values will be evaluated; these may be obtained by considering Equation (3.14), with E_R and E_I the real and imaginary field components respectively:-

$$E_R = \frac{b}{\sqrt{\lambda d}} \int_{-\infty}^{+\infty} e^{-\xi^2/w^2} \cdot \cos\left[\frac{k\xi^2}{2d} - \phi\right] d\xi \qquad (3.19)$$

and:-

$$E_I = \frac{b}{\sqrt{\lambda d}} \int_{-\infty}^{+\infty} e^{-\xi^2/w^2} \cdot \sin\left[\frac{k\xi^2}{2d} - \phi\right] d\xi \qquad (3.20)$$

ϕ in both cases being the random phase contribution which has been assumed to be a Gaussian random variable. Hence:-

$$\langle e^{j\phi} \rangle = e^{-\sigma_\phi^2/2}$$

and:-

$$\langle \cos \phi \rangle = e^{-\sigma_\phi^2/2} \quad , \quad \langle \sin \phi \rangle = 0 \tag{3.21}$$

Taking the average values of Equations (3.19) and (3.20) and using the above values for $\langle \cos \phi \rangle$ and $\langle \sin \phi \rangle$, it may be shown using standard integrals[41] that:-

$$\langle E_R \rangle = \frac{b}{\sqrt{\lambda d}} \cdot e^{-\sigma_\phi^2/2} \cdot 2 \cdot \sqrt{\frac{\pi}{8}} \sqrt{\frac{\sqrt{p^2 + q^2} + p}{p^2 + q^2}}$$

$$= \frac{b}{\sqrt{\lambda d}} \cdot e^{-\sigma_\phi^2/2} \cdot \frac{\sqrt{\pi}}{4\sqrt{p^2 + q^2}} \cdot \cos \left[\frac{1}{2} \tan^{-1} \left(\frac{q}{p} \right) \right] \tag{3.22}$$

and:-

$$\langle E_I \rangle = - \frac{b}{\sqrt{\lambda d}} \cdot e^{-\sigma_\phi^2/2} \cdot 2 \cdot \sqrt{\frac{\pi}{8}} \sqrt{\frac{\sqrt{p^2 + q^2} - p}{p^2 + q^2}}$$

$$= - \frac{b}{\sqrt{\lambda d}} \cdot e^{-\sigma_\phi^2/2} \cdot \frac{\sqrt{\pi}}{4\sqrt{p^2 + q^2}} \cdot \sin \left[\frac{1}{2} \tan^{-1} \left(\frac{q}{p} \right) \right] \tag{3.23}$$

where in both Equations (3.22) and (3.23) $p = 1/w^2$ and $q = k/2d$.

It is apparent that the effect of the random medium is to cause a reduction in the mean value of both the real and imaginary field components from their free space values. The reduction is equal in both cases and is equal to $\exp \left[- \sigma_\phi^2/2 \right]$. A phasor representation is shown in the figure below.

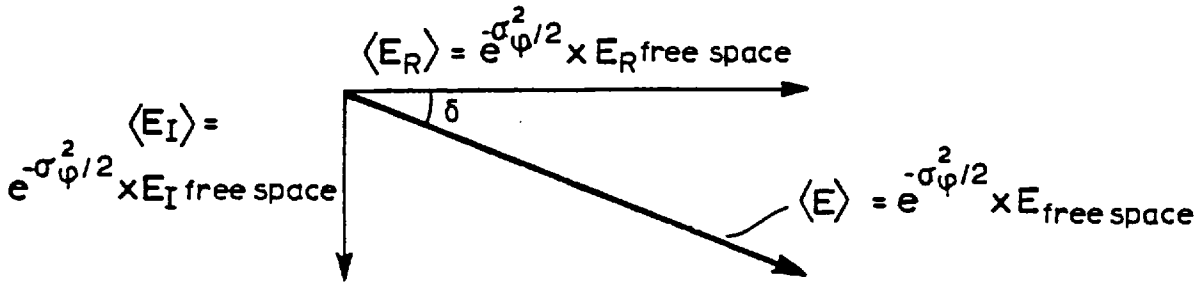

The resultant <E> is the sum of the average real and imaginary field components. The angle of inclination δ of the resultant with respect to the real axis is seen from Equations (3.22) and (3.23) to be given by:-

$$\delta = \frac{1}{2} \tan^{-1} \left[\frac{q}{p}\right] = \frac{1}{2} \tan^{-1} \left[\frac{kw^2}{2d}\right] \qquad (3.24)$$

The ratio of the mean values of the imaginary to the real component is given by tan δ. This ratio is unity at d = 0 and becomes smaller as d increases. For example, for λ = 8 millimetres, w = 0.3 metres and d = 500 metres, δ is equal to 2 degrees and hence:-

$$\langle E_R \rangle \simeq 30 \, . \, \langle E_I \rangle$$

Next, the variances of the real and imaginary components, σ_R^2 and σ_I^2 respectively will be evaluated. By definition:-

$$\sigma_R^2 = \langle E_R^2 \rangle - \langle E_R \rangle^2 \quad \text{and} \quad \sigma_I^2 = \langle E_I^2 \rangle - \langle E_I \rangle^2$$

with E_R and E_I given by Equations (3.19) and (3.20) respectively.

It can be shown (see Appendix I) that for $\sigma_\phi^2 << 1$:-

$$\sigma_R^2 = \frac{b^2}{\lambda d} \cdot \frac{\pi\sigma_\phi^2}{2} \cdot \frac{1}{4\sqrt{\beta}} \cdot$$

$$\cdot \left[\frac{1}{4\sqrt{\left(\frac{2}{w^2} - \frac{\gamma}{\beta}\right)^2 + \left(\frac{k}{2d}\right)^2 \left(1 - \frac{1}{\beta\xi_0^4}\right)^2}} \cdot \cos\left[\frac{1}{2}\tan^{-1}\frac{\frac{k}{2d}\left(1 - \frac{1}{\beta\xi_0^4}\right)}{\left(\frac{2}{w^2} - \frac{\gamma}{\beta}\right)} - \alpha\right] - \right.$$

$$\left. - \frac{1}{4\sqrt{\left(\frac{2}{w^2} - \frac{\gamma}{\beta}\right)^2 + \left(\frac{k}{2d}\right)^2 \left(1 + \frac{1}{\beta\xi_0^2}\right)^2}} \cdot \cos\left[\frac{1}{2}\tan^{-1}\frac{\frac{k}{2d}\left(1 + \frac{1}{\beta\xi_0^4}\right)}{\left(\frac{2}{w^2} - \frac{\gamma}{\beta}\right)} + \alpha\right]\right]$$

(3.25)

and:-

$$\sigma_I^2 = \frac{b^2}{\lambda d} \cdot \frac{\pi\sigma_\phi^2}{2} \cdot \frac{1}{4\sqrt{\beta}} \cdot$$

$$\cdot \left[\frac{1}{4\sqrt{\left(\frac{2}{w^2} - \frac{\gamma}{\beta}\right)^2 + \left(\frac{k}{2d}\right)^2 \left(1 - \frac{1}{\beta\xi_0^4}\right)^2}} \cdot \cos\left[\frac{1}{2}\tan^{-1}\frac{\frac{k}{2d}\left(1 - \frac{1}{\beta\xi_0^4}\right)}{\left(\frac{2}{w^2} - \frac{\gamma}{\beta}\right)} - \alpha\right] + \right.$$

$$\left. + \frac{1}{4\sqrt{\left(\frac{2}{w^2} - \frac{\gamma}{\beta}\right)^2 + \left(\frac{k}{2d}\right)^2 \left(1 + \frac{1}{\beta\xi_0^4}\right)^2}} \cdot \cos\left[\frac{1}{2}\tan^{-1}\frac{\frac{k}{2d}\left(1 + \frac{1}{\beta\xi_0^4}\right)}{\left(\frac{2}{w^2} - \frac{\gamma}{\beta}\right)} + \alpha\right]\right]$$

(3.26)

where:-

$$\alpha = \frac{1}{2}\tan^{-1}\frac{k/2d}{\left(\frac{1}{w^2}+\frac{1}{\xi_0^2}\right)}$$

$$\beta = \left(\frac{1}{w^2}+\frac{1}{\xi_0^2}\right)^2 + \left(\frac{k}{2d}\right)^2 \qquad (3.27)$$

and:-

$$\gamma = \left(\frac{1}{w^2}\right)^2 \cdot \left(\frac{1}{w^2}+\frac{1}{\xi_0^2}\right) + \left(\frac{k}{2d}\right)^2 \cdot \left(\frac{1}{w^2}-\frac{1}{\xi_0^2}\right)$$

The sum of the variances of the real and imaginary parts is:-

$$\sigma_R^2 + \sigma_I^2 = \frac{b^2}{\lambda d} \cdot \pi\sigma_\phi^2 \cdot \frac{1}{4\sqrt{\beta}} \cdot$$

$$\cdot \left[\frac{1}{4\sqrt{\left(\frac{2}{w^2}-\frac{\gamma}{\beta}\right)^2 + \left(\frac{k}{2d}\right)^2\left(1-\frac{1}{\beta\xi_0^4}\right)}} \cdot \cos\left[\frac{1}{2}\tan^{-1}\frac{\frac{k}{2d}\left(1-\frac{1}{\beta\xi_0^4}\right)}{\left(\frac{2}{w^2}-\frac{\gamma}{\beta}\right)} - \alpha\right]\right]$$

It is easy to show that in the far field, i.e. $d >> \frac{\pi w^2}{\lambda}$, the above expression is reduced to:-

$$\sigma_R^2 + \sigma_I^2 = \frac{b^2 \cdot \pi}{\lambda d} \cdot \sigma_\phi^2 \cdot \frac{1}{\sqrt{\left(\frac{1}{w^2}\right)^2 + \frac{2}{w^2 \cdot \xi_0^2}}}$$

which is identical to the expression for the variance of the far field complex electric field σ_E^2, i.e. in the far field:-

$$\sigma_R^2 + \sigma_I^2 = \sigma_E^2$$

This result is expected, and is expected to hold in the near field as well as the far field. However, due to the analytical complexity involved, this is difficult to show.

3.4.2 Estimates for the Magnitude of the Amplitude and Phase Fluctuations

To obtain the range of variations of the amplitude and phase of the random on-axis field, an approach will be used that is similar to that applied by Beckmann[40] in the investigation of the scattering of plane waves off rough surfaces. The field E will be represented as a sum of random real and imaginary phasors as shown in Fig. 3.6.

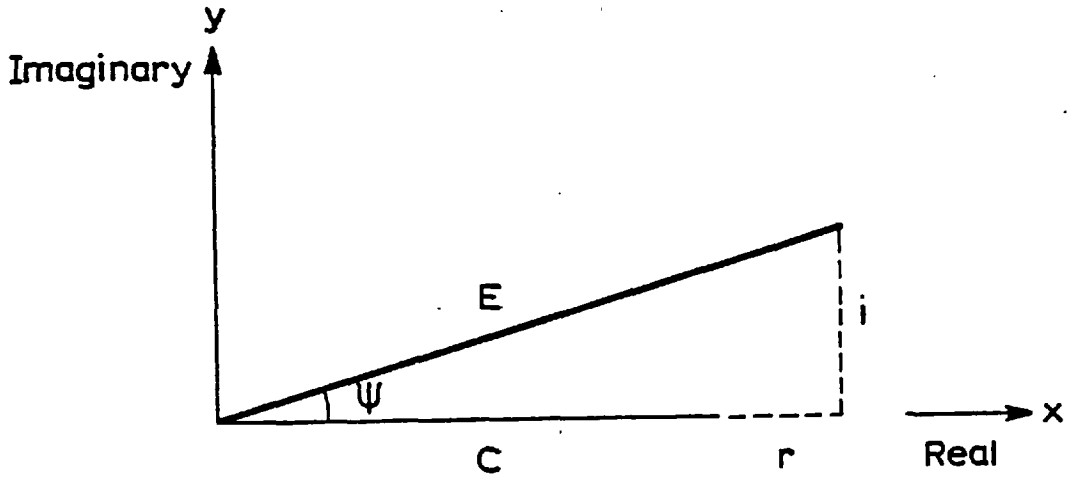

Fig. 3.6 Real and imaginary components of the electric field

The real part is considered to have a constant mean value C and a fluctuating part r, with variance v_1. The imaginary part is a zero mean quantity with a fluctuating part i, with variance v_2. Through knowledge of the relative magnitude of <E>, v_1 and v_2, the

magnitude of the amplitude and phase fluctuation and their probability distributions may be estimated.

The situation here is slightly more complex. This is due to the fact that the mean value <E> was found to be a rotated phasor, the angle of rotation δ being a function of the propagation distance and given by Equation (3.24).

To overcome this difficulty, the reference real and imaginary axes, x and y respectively, will be continuously rotated by the same angle δ and, hence, the mean value <E> will always lie on the real x-axis, i.e.:-

$$C = \langle E_R \rangle \cos\delta + \langle E_I \rangle \sin\delta = \frac{b}{\sqrt{\lambda d}} \cdot e^{-\sigma_\phi^2/2} \cdot \frac{\sqrt{\pi}}{4\sqrt{p^2 + q^2}} \qquad (3.28)$$

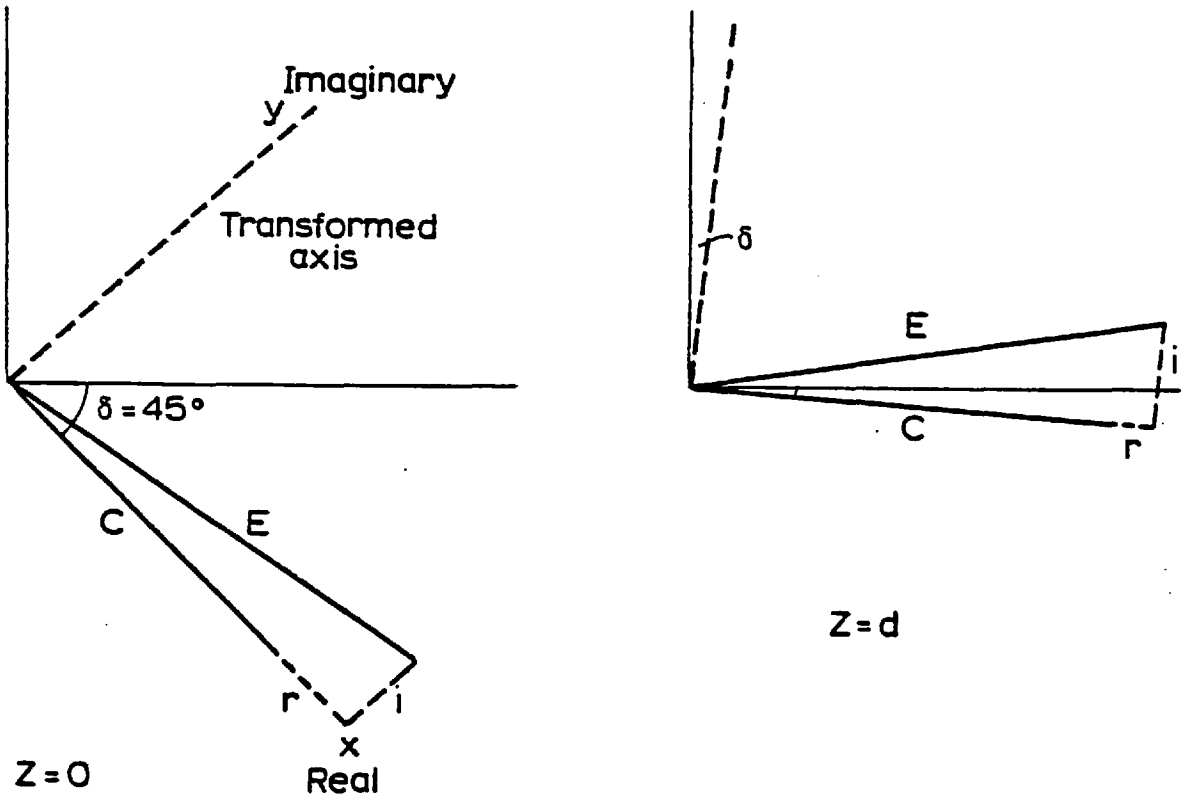

Fig. 3.7 Electric field representation on a rotating set of axis

Under the new set of axes, Fig. 3.7, it may be shown that the transformed real and imaginary variances v_1 and v_2 are given by:-

$$v_1 = \sigma_R^2 \cos^2 \delta + \sigma_I^2 \sin^2 \delta \tag{3.29}$$

$$v_2 = \sigma_R^2 \sin^2 \delta + \sigma_I^2 \cos^2 \delta \tag{3.30}$$

where σ_R^2 and σ_I^2 are given by Equations (3.25) and (3.26) and δ by Equation (3.24). As the propagation distance d increases from the near field to the far field, δ changes from 45^o at d = 0 and, hence, i = r and $v_1 = v_2$, to zero at $d >> \pi w^2/\lambda$, in this case the fluctuating real part tends to zero and the variance of the imaginary part v_2 tends to σ_I^2.

Fig. 3.8 shows the variation of the ratio $\sqrt{v_2/v_1}$ as the propagation distance increases from 0 to 1 kilometres.

The phase variation of the on-axis electric field ψ may be seen from Fig. 3.6 to be given by:-

$$\tan \psi = \frac{i}{C + r} \tag{3.31}$$

which, for a large mean value compared to the fluctuating real and imaginary component r and i, is approximately given by:-

$$\psi = \frac{i}{C}$$

Noting that <i> = 0, therefore, the variance of the phase fluctuations is given by:-

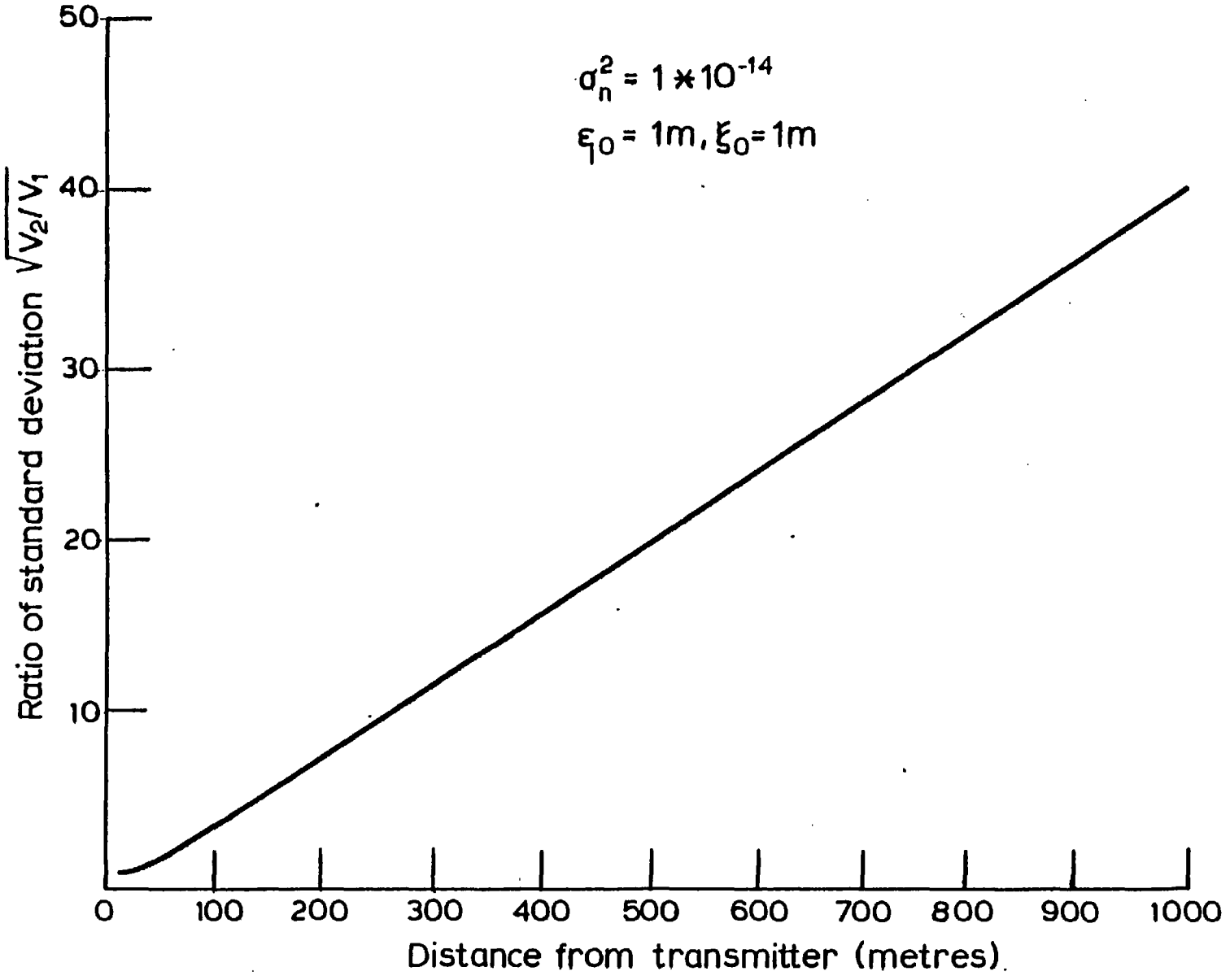
$\sigma_n^2 = 1 * 10^{-14}$
$\xi_{10} = 1m, \xi_{20} = 1m$
Ratio of standard deviation $\sqrt{V_2/V_1}$
50
40
30
20
10
0
100
200
300
400
500
600
700
800
900
1000
Distance from transmitter (metres)

Fig. 3.8

$$\sigma_\phi^2 = \frac{\sigma_i^2}{C^2} = \frac{v_2}{C^2}$$

Substituting from Equations (3.25), (3.26) and (3.28), therefore:-

$$\sigma_\psi^2 = \frac{\sigma_\phi^2}{2 \,.\, (1 - \sigma_\phi^2)} \cdot \frac{\sqrt{\left(\frac{1}{w^2}\right)^2 + \left(\frac{k}{2d}\right)^2}}{4\sqrt{\beta}} \cdot$$

$$\cdot \left[\frac{1}{4\sqrt{\left(\frac{2}{w^2} - \frac{\gamma}{\beta}\right)^2 + \left(\frac{k}{2d}\right)^2 \left(1 - \frac{1}{\beta\xi_0^4}\right)^2}} \,.\, \cos \left[\frac{1}{2} \tan^{-1} \frac{\frac{k}{2d}\left(1 - \frac{1}{\beta\xi_0^4}\right)}{\left(\frac{2}{w^2} - \frac{\gamma}{\beta}\right)} - \alpha \right] \right] +$$

$$+ (\cos^2 \delta - \sin^2 \delta) \,.\, \frac{1}{4\sqrt{\left(\frac{2}{w^2} - \frac{\gamma}{\beta}\right)^2 + \left(\frac{k}{2d}\right)^2 \left(1 + \frac{1}{\beta\xi_0^4}\right)^2}} \cdot$$

$$\cdot \cos \left[\frac{1}{2} \tan^{-1} \frac{\frac{k}{2d}\left(1 - \frac{1}{\beta\xi_0^4}\right)}{\left(\frac{2}{w^2} - \frac{\gamma}{\beta}\right)} + \alpha \right] \Bigg] \qquad (3.32)$$

with α, β and γ given by Equation (3.27).

It is seen from Equation (3.32) that the variance of the on-axis phase fluctuations is a function of the medium parameters ξ_0 and σ_ϕ^2 which is a function of σ_n^2 and ζ_0, and on the system parameters k, d and w.

Substituting in Equation (3.32) for $\xi_0 = \zeta_0 = 10$ metres, $\sigma_n^2 = 1.0 \,.\, 10^{-14}$ n^2-units, w = 0.3 metres, λ = 8 millimetres and d = 12

kilometres, the phase variance is 8.2 degrees, which is a reasonable figure as will be seen later from the experimental results.

The variance of the amplitude fluctuations is approximately given by the variance of the fluctuating real component σ_R^2. This approximate value is valid as long as the magnitudes of the real and imaginary components r and i are much less than the mean value C.

The probability distribution of the phase fluctuations ψ is a function of the probability distribution of the imaginary part i. Therefore, for i Gaussian, ψ is Gaussian distributed. A more detailed analysis of the distributions of the amplitude and phase distributions for various ratios of the variances of the real and imaginary components may be found in Beckmann[40].

In this chapter, the detailed statistics of the complex electric field have been studied after propagation through a random medium. The medium has been assumed to be a weakly random one and, hence, the phase integral results of the parabolic equation solution have been applied. The phase fluctuations caused by the phase screen representation of the medium have been shown to produce amplitude and phase fluctuations in the Fresnel region and beyond. The phase fluctuations for the on-axis field are seen to decrease progressively as the propagation distance increases and the amplitude fluctuations are the more dominant ones.

The elementary field approach gives insight into the effect of the different medium and system parameters, and indicates that there exists an optimum transmitter aperture size for minimum fluctuations.

To extend the analysis to a more turbulent medium, the path length should be broken into a number of regions or slabs, the medium within each slab could then be considered to be weakly random. The field at the end of each slab would then be considered as the aperture

field for the next slab, and so on. However, the complexity of the analysis involved makes this a formidable task.

Furthermore, the elementary field approach does not easily provide information for the lateral field statistics. This information is necessary to estimate the response of a finite receiving aperture to a randomly distorted wavefront.

The above drawback, namely, those of propagation through a strongly turbulent medium and of defining the lateral statistics of the distorted wavefront, are more easily dealt with using a lateral coherence angular spectrum approach. This approach is outlined and developed in Chapter 4.

CHAPTER 4

ANGULAR POWER SPECTRUM AND COHERENCE PROPERTIES OF A PROPAGATING BEAM IN A STRONGLY RANDOM MEDIUM

In this chapter, the lateral statistics of the random field will be investigated by means of a coherence function approach. The combined effect of the medium parameters and transmitter aperture size on the partial degradation of the lateral coherence will be investigated. The power distribution as a function of angle, i.e. the average angular power spectrum, is consequently affected and is also investigated.

The medium under consideration will be assumed to satisfy the conditions for which the parabolic equation is applicable. These conditions being that the scale sizes of the random irregularities are much larger than the wavelength, and that the relative fluctuations of the refractive index with respect to the mean value are small. Applying the parabolic equation to such a medium has been shown in the previous chapter to allow for collapsing the medium into a thin random phase screen at the transmitter plane.

For a strongly turbulent medium, the path length will be divided into several regions, each satisfying the condition that the magnitude of the refractive index fluctuations is small. Hence each region or slab of the medium may be adequately represented by its characteristic phase screen. This technique allows for the investigation of the continuous degradation of the lateral coherence and continuous scattering of the wave as it traverses the consecutive phase screens.

The analysis is limited to a forward scatter situation and it will be shown that a single scatter approximation is a reasonable one in view of the relatively very small magnitude of the multiple scatter components.

4.1 Angular Plane Wave Spectrum and Lateral Coherence Function

In this section the angular plane wave spectrum will be briefly reviewed and its properties for a propagating Gaussian beam will be determined. The lateral autocorrelation function and its propagation characteristics is also studied. As a start the propagation medium will be considered to be free space. The purpose is to outline the basic principles involved, which will then be applied to a random medium in the following section.

4.1.1 Angular Plane Wave Spectrum Representation of an Electromagnetic Field

The underlying concept is that if an electric field distribution is known in a planar domain, in terms of a lateral coordinate system, then alternatively it may be uniquely defined in an angular domain in terms of an angular coordinate system and vice versa. The conversion or transformation from one domain to the other is through a Fourier transform relationship.

In other words, a complicated field distribution may be thought of as a superposition of plane waves, the magnitude and orientation of each being determined in such a way as to reconstruct the existing field distribution.

The above relationship may be put in mathematical notation as follows:-

$$E_x(x,y,z) = \int_{-\infty}^{+\infty}\int_{-\infty}^{+\infty} F(S_1, S_2) \cdot e^{-jk(S_1 x + S_2 y + Cz)}\, dS_1 \cdot dS_2 \qquad (4.1)$$

where $E_x(x,y,z)$ is the x-component of the electric field at the observation point $p(x,y,z)$. S_1, S_2 and C are the direction cosines for

the observation point p.

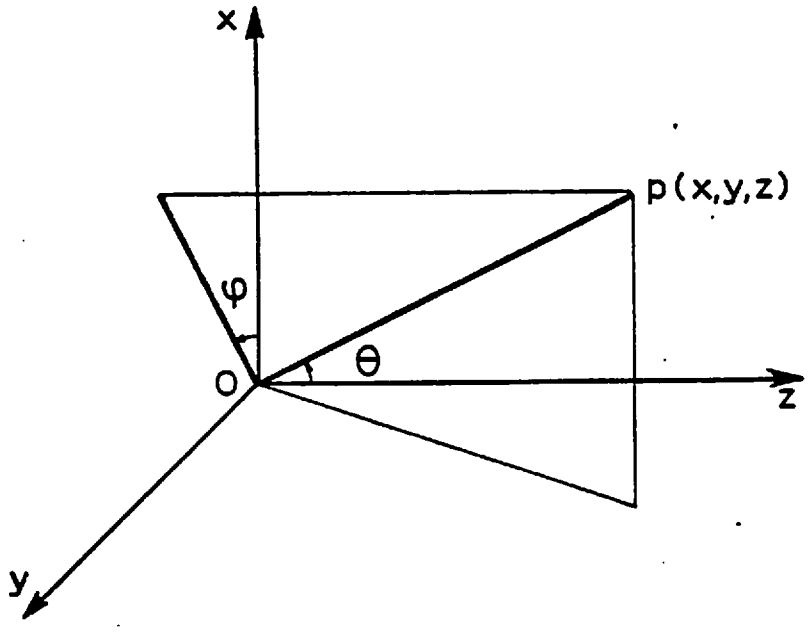

$S_1 = \sin\theta \cdot \cos\phi$, $S_2 = \sin\theta \sin\phi$, $C = \cos\theta$

i.e.:-

$$S_1^2 + S_2^2 + C^2 = 1$$

The angular power spectrum $F(S_1, S_2)$ may be obtained through the inverse transform of the electric field distribution in the plane $z = d$:-

$$F(S_1, S_2)\Big|_{z=d} = \frac{1}{\lambda^2} \int_{-\infty}^{+\infty} \int_{-\infty}^{+\infty} E(x,y;d) \cdot e^{jk(xS_1 + yS_2 + Cd)}\, dx\, dy \qquad (4.2)$$

The representation of a propagating field by an angular plane wave equation has been shown in principle to be exact[42, 43]. This is due to the linearity of the wave equation after neglecting the depolarization term. Therefore, the superposition of plane waves, each

of which is a solution of the wave equation constitutes a valid solution. Lalor[44] has discussed in some detail the conditions under which the transformation from a planar to an angular domain, and vice versa, to be valid, these being similar to analogous situations found in circuit theory.

The fields obtained from the angular spectrum representation (4.1) include plane wave components travelling in directions such that $S_1^2 + S_2^2 > 1$, i.e. the third direction cosine is imaginary. Such fields can be shown to be evanescent fields[34], which are rapidly decaying and hence are of no practical consequence.

Angular Spectrum for a Gaussian Aperture Field

The aperture field to be considered is a uniform phase Gaussian amplitude distribution, with a "1/e" width w, which is similar to that considered in the previous chapters, i.e.:-

$$E(x,y;0) = b \exp - (x^2 + y^2)/w^2 \qquad (4.3)$$

Since the above field is a separable quantity, therefore, for analytical simplicity, the two-dimensional form, E(x,z) will only be considered. In this case, $\phi = 0$ and $S_1 = S = \sin\theta$.

The angular spectrum corresponding to the Gaussian aperture field is then determined from Equation (4.1) and may be shown to be:-

$$F(S)\Big|_{z=0} = \sqrt{\pi} \cdot \frac{w}{\lambda} b \cdot \exp - S^2 / \left(\frac{\lambda}{\pi w}\right)^2 \qquad (4.4)$$

It is seen that the angular spectrum is also Gaussian with a "1/e" width $\lambda/\pi w$, which is inversely proportional to the Gaussian width of the radiating aperture, i.e. a wide aperture radiates a narrow spectrum

of plane waves, and vice versa, which is to be expected.

The electric field distribution at a normal plane z = d may be obtained through the transform of the angular spectrum at this plane. Therefore:-

$$E(x;d) = \int_{-\infty}^{+\infty} F(S)\Big|_{z=0} \cdot e^{-jk(Sx + Cd)}\, dS \qquad (4.5)$$

As an approximation, it will be assumed that the propagating field is confined within a narrow range of angles, i.e. θ will be considered to be small. This small angle approximation is valid at microwave frequencies where $w >> \lambda$. For $\theta \lesssim 12^{o}$ the direction cosine C may be approximated to:-

$$C = \sqrt{1 - S^2} \simeq 1 - \frac{S^2}{2} \qquad (4.6)$$

Substituting for C in Equation (4.5), it may be shown that:-

$$E(x;d) = \frac{b}{\sqrt{1 - j\,\frac{\lambda d}{\pi w^2}}} \cdot e^{-x^2/w_d^2} \cdot e^{-j\,\frac{kx^2}{2R_d}} \qquad (4.7)$$

where:-

$$w_d = w^2 \cdot \left[1 + \left(\frac{\lambda d}{\pi w^2}\right)^2\right]$$

$$R_d = d \cdot \left[1 + \left(\frac{\pi w^2}{\lambda d}\right)^2\right]$$

The above expression for the waist and radius of curvature w_d and R_d respectively for the Gaussian beam at the plane z = d is similar to that obtained by solving the parabolic equation in a free space medium, Equation (2.13) with p = 0, and also similar to that obtained using Huygens' principle, Equation (3.7).

4.1.2 Lateral Autocorrelation Function and the Angular Power Spectrum for a Gaussian Aperture Field

The lateral autocorrelation function for a deterministic field distribution at the plane z = d is defined in terms of the lateral separation ξ as follows:-

$$\Gamma(\xi;d) = \int_{-\infty}^{+\infty} E(x;d) \cdot E^*(x + \xi;d)\, dx \qquad (4.8)$$

The term coherence function will be used only for a random field distribution, instead of the autocorrelation function.

Substituting for the aperture field distribution, $E(x;0) = b \exp - x^2/w^2$, therefore:-

$$\Gamma(\xi;0) = b^2 \cdot w \sqrt{\frac{\pi}{2}} \exp - \frac{\xi^2}{2w^2} \qquad (4.9)$$

which is a Gaussian function with a "1/e" width of $\sqrt{2}$ w. For a normalized aperture field, i.e.:-

$$\int_{-\infty}^{+\infty} |E(x;0)|^2\, dx = 1 \quad \text{and hence} \quad b = \frac{1}{w}\sqrt{\frac{2}{\pi}}$$

Therefore $\Gamma(\xi;0) = \exp(-\xi^2/2w^2)$.

To observe the behaviour of the autocorrelction function as it propagates in the forward z-direction to the plane z = d, it may be shown from Equations (4.7) and (4.8) that:-

$$\Gamma(\xi;d) = \frac{1 + ja}{\sqrt{1 + a^2}} \exp - \xi^2/2w^2 \qquad (4.10)$$

$$a = \lambda d/\pi w^2$$

It may be seen from Equations (4.9) and (4.10) that the magnitude and shape of the autocorrelation function remain unchanged as it propagates along the z-direction. However, there is a phase shift equal to $\tan^{-1} \lambda d/\pi w^2$, which is insignificant since it is a uniform phase shift.

The above result is a realization of the Van-Cittert Zernicke theorem[45] which says that the normalized autocorrelation function of the complex wave amplitude over each plane is the same.

The distribution of power in the angular domain may be obtained by Fourier transforming the autocorrelation function[46]. Therefore:-

$$|F(S)|^2 \longleftrightarrow \Gamma(\xi)$$

where $|F(S)|^2$ is the angular power spectrum. The physical significance of $|F(S)|^2$, S = sin θ, is its relationship with the gain function $G(\theta)$, of an antenna. This relationship has been shown[47] for a narrow beam pattern with the maximum in the θ = 0 direction to be:-

$$G(\theta) = \frac{2\pi\lambda^2}{ZP_o} |F(S)|^2 \qquad (4.11)$$

where Z is the plane wave impedance of the medium and P_o is the power delivered to the antenna.

Therefore, for an antenna with a Gaussian aperture field distribution, the free space angular power spectrum is given by:-

$$|F(S)|^2 = \frac{\pi \cdot w^2 \cdot b^2}{\lambda^2} \cdot \exp \frac{-S^2}{\frac{1}{2}\left(\frac{\lambda}{\pi w}\right)^2} \qquad (4.12)$$

which, as an example, corresponds to a radiation pattern with a three decibel beam width of 0.47 degrees for an aperture width 2 w equal to 0.6 metres at a wavelength of 8 millimetres.

4.2 Partial Destruction of the Lateral Coherence Function and the Angular Power Spectrum in a Random Medium

It has been suggested in Chapter 3, and shown to be quite accurate, that a weakly random medium may be collapsed into a thin random phase screen situated at the transmitter aperture plane. The statistics of the random phase variations are obtained from those of the refractive index fluctuations as outlined in Section 3.2.

In this section, the random phase screen approach will be applied to observe the effects of the medium on the coherence function and, hence, on the corresponding angular power spectrum. The analysis will proceed on similar lines as that of Clarke's[34]. However, the situation here is not limited to the plane wave case and the transmitter aperture size is taken into consideration.

4.2.1 Propagation of the Coherence Function in a Weakly Random Medium

Due to the presence of the phase screen, the aperture field will

be modified by the random phase contribution $\phi(x)$, calculated according to Equation (3.3). For a random field distribution, the coherence function is accordingly defined as follows:-

$$\Gamma(x_1, x_2) = \int_{-\infty}^{+\infty} \langle E(x_1) \cdot E^*(x_2) \rangle \, dx \tag{4.13}$$

where x_1 and x_2 are two points on the phase screen separated by the distance ξ. Assuming a homogeneous phase screen, i.e. the first and second order statistics of the random phase are independent of the position of the arbitrary observation point x_1. Under this assumption $\Gamma(x_1, x_2)$ is thus only a function of the lateral separation ξ and, hence, the coherence function just after the phase screen at $z = 0$ is given by:-

$$\Gamma(\xi;0) = \int_{-\infty}^{+\infty} \langle E_0(x) \cdot e^{j\phi(x)} \cdot E_0(x + \xi) \cdot e^{-j\phi(x + \xi)} \rangle \, dx$$

The suffix "o" denotes free space values. This notation applies to the rest of the analysis.

Since the aperture field distribution $E_0(x)$ is independent of the random phase $\phi(x)$, therefore, the above expression is shown (Appendix II) to be:-

$$\Gamma(\xi;0) = \Gamma_0(\xi) \cdot \langle e^{j\left[\phi(x) - \phi(x + \xi)\right]} \rangle \tag{4.14}$$

The quantity in the square brackets is the characteristic function of the random phase fluctuations evaluated for the parameters ± 1, viz. $C_\phi(-1, 1, \xi)$, and which for a Gaussian phase process has been shown to be[36]:-

$$\langle e^{j\left[\phi(x) - \phi(x+\xi)\right]} \rangle = C_\phi(-1, 1, \xi) = e^{-\sigma_\phi^2\left[1 - r_\phi(\xi)\right]} \qquad (4.15)$$

σ_ϕ^2 and $r_\phi(\xi)$ are the phase variance and normalized auto-correlation function respectively and are defined in terms of the refractive index fluctuations as shown in Equation (3.4).

Substituting for the characteristic function in Equation (4.14), therefore:-

$$\Gamma(\xi;0) = \Gamma_o(\xi) \cdot e^{-\sigma_\phi^2\left[1 - r_\phi(\xi)\right]} =$$

$$= \Gamma_o(\xi) \cdot e^{-\sigma_\phi^2} + \Gamma_o(\xi) \cdot e^{-\sigma_\phi^2}\left[e^{\sigma_\phi^2 \cdot r_\phi(\xi)} - 1\right] \qquad (4.16)$$

It is seen from Equation (4.16) that the coherence function is split into two parts. The first part is independent of the lateral scale size and is simply the reduced free space value, whereas the second part is a function of the lateral statistics of the phase screen $r_\phi(\xi)$.

It has been established in Appendix II that the lateral coherence function propagates without change in magnitude or distribution. Therefore, in the free space medium following the phase screen, the two parts of the coherence function will remain unchanged.

Since the angular power spectrum is the Fourier transform of the coherence function, therefore, any disruption of the coherence function indicates a disruption of the angular distribution of the radiated power and, hence, the gain function of the antenna is altered.

The problem of studying the effect of random phase errors, which is equivalent to the presence of a random phase screen, on the radiation characteristics of an antenna, has been analysed by a number

of authors. For example, Ruze[48] and Jairam[49] have treated the problem and estimated the resulting distortion of the radiation pattern. However, no emphasis has been placed on distinguishing between the scattered and unscattered power.

4.2.2 Angular Power Spectra in a Random Medium

Since the Fourier transform is a linear one, therefore, the splitting of the coherence function, as shown in Equation (4.16), gives rise to two angular power spectra, a coherent and an incoherent spectrum. The reasons for using the terms coherent and incoherent will be shown below.

The Coherent Angular Power

This is the Fourier transform of the first part of the lateral coherence function and is thus given by:-

$$|F(S)|^2_{\text{coherent}} = \frac{1}{\lambda^2}\int_{-\infty}^{+\infty} \Gamma_0(\xi) \cdot e^{-\sigma_\phi^2} \cdot e^{jk\xi S}\, d\xi = e^{-\sigma_\phi^2} \cdot |F_0(S)|^2 =$$

$$= |\langle F(S)\rangle|^2 \qquad (4.17)$$

where $|F_0(S)|^2$ is the free space angular power spectrum and noting that:-

$$\langle E_0(x) \cdot e^{j\phi(x)}\rangle = E_0(x) \cdot e^{-\sigma_\phi^2/2}$$

It is seen that the coherent angular power spectrum is the expected or average value of the available power. This is similar in its directional properties to the free space value. However, the overall

magnitude of the different spectral components is reduced by the factor (exp $-\sigma_\phi^2$). The preservation of the free space directional properties leads to the presumption that this portion of the angular power does not contain any scattered components and, hence, the term coherent angular power.

From Equations (4.12) and (4.17) and for the particular case of a Gaussian transmitted beam, the coherent angular power is given by:-

$$|\langle F(S)\rangle|^2 = \frac{\pi \cdot w^2 \cdot b^2 \cdot e^{-\sigma_\phi^2}}{\lambda^2} \cdot \exp \frac{-S^2}{\frac{1}{2}\left(\frac{\lambda}{\pi w}\right)^2} \qquad (4.18)$$

The Incoherent Angular Power

This is the power contributed by the randomly scattered field components. These components are randomly phase modulated by the medium and, hence, the power contribution is incoherent. Since the total available angular power is the sum of the mean square angular spectrum and the variance of the angular spectrum, therefore, the incoherent power is the variance or the fluctuating portion of the angular spectrum. This incoherent portion is given by the Fourier transform of the second part of the lateral coherence function in Equation (4.16) and, hence:-

$$|F(S)|^2_{\text{incoherent}} = \text{VAR}\left[F(S)\right] = \frac{1}{\lambda^2}\int_{-\infty}^{+\infty} \Gamma_o(\xi) \cdot e^{-\sigma_\phi^2} \cdot$$

$$\cdot \left[e^{\sigma_\phi^2 \cdot r_\phi(\xi)} - 1\right] e^{jk\xi S}\, d\xi \qquad (4.19)$$

To evaluate the above integral, again making the assumption that $\sigma_\phi^2 << 1$:-

$$\text{VAR}\left[F(S)\right] = \frac{\sigma_\phi^2 \cdot e^{-\sigma_\phi^2} \cdot b^2 \cdot w^2 \cdot \pi}{\lambda^2} \cdot \frac{1}{\sqrt{1 + \frac{2w^2}{\xi_0^2}}} \cdot$$

$$\cdot \exp\left[\frac{-S^2}{\frac{1}{2}\left(\frac{\lambda}{\pi w}\right)^2 \left(1 + \frac{2w^2}{\xi_0^2}\right)}\right] \qquad (4.20)$$

which also has a Gaussian width dependence with a modified waist and magnitude. The figure below shows a diagrammatic sketch of the distribution of both coherent and incoherent power as a function of the angular displacement S.

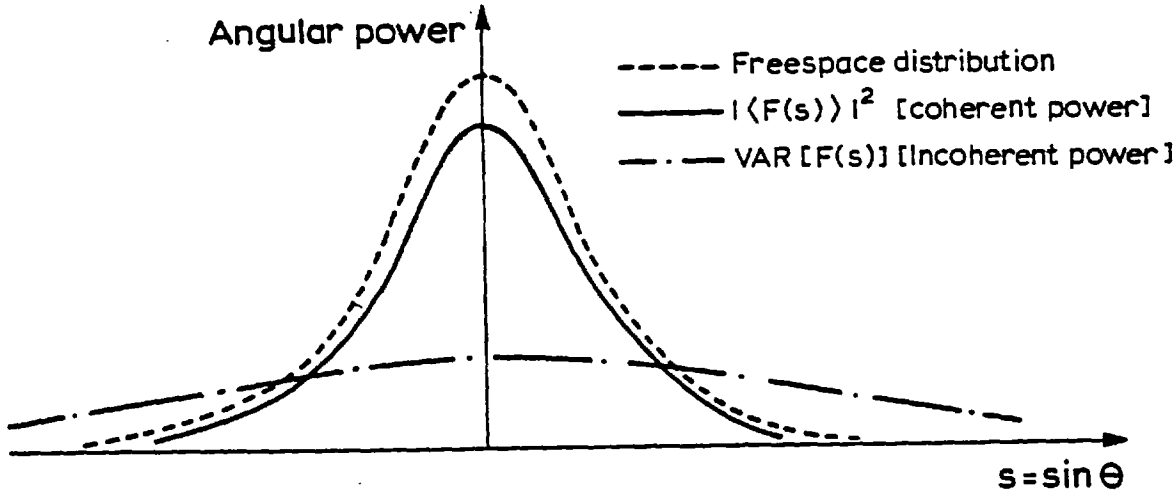

It may be seen from Equations (4.12), (4.17) and (4.20) that the incoherent angular power has a much smaller magnitude than the coherent power, the on-axis (S = 0) ratio being:-

$$\frac{\text{Magnitude of Incoherent Power}}{\text{Magnitude of Coherent Power}} = \frac{\sigma_\phi^2}{\sqrt{1 + \frac{2w^2}{\xi_0^2}}} \qquad (4.21)$$

which is a function of the degree of turbulence implied in σ_ϕ^2, and on the aperture dimension w relative to the lateral scale-size ξ_0.

The spread of the incoherent or scattered power relative to the free space "1/e" beam width, which is the same as the spread of the coherent power is:-

$$\frac{\text{Spread of Incoherent Power}}{\text{Spread of Coherent Power}} = \sqrt{1 + \frac{2w^2}{\xi_0^2}} \qquad (4.22)$$

which is seen to be independent of the strength of turbulence of the medium and is simply a function of w/ξ_0.

Therefore, it may be seen that as the aperture size is increased, i.e. the beam width becomes narrower, the magnitude of the incoherent power relative to the coherent power becomes smaller, and the relative spread of the incoherent power spectrum is wider. The opposite is also true, i.e. the wider the beam width, the relatively narrower is the scattering angle, and relatively more power is scattered due to the increased number of irregularities present in the path of the wider beam.

Fig. 4.1a shows the ratio of the spread of the incoherent to coherent powers given by Equation (4.22), as a function of the transmitter aperture size w, with the medium scale size ξ_0 as a parameter. Fig. 4.1b shows the ratio of the on-axis magnitude of the incoherent to coherent power given by Equation (4.21) given as a percentage, as a function of w, with ξ_0 as a parameter. The significance of the shown variation of relative spectral width and magnitude will be discussed in detail in Chapter 5.

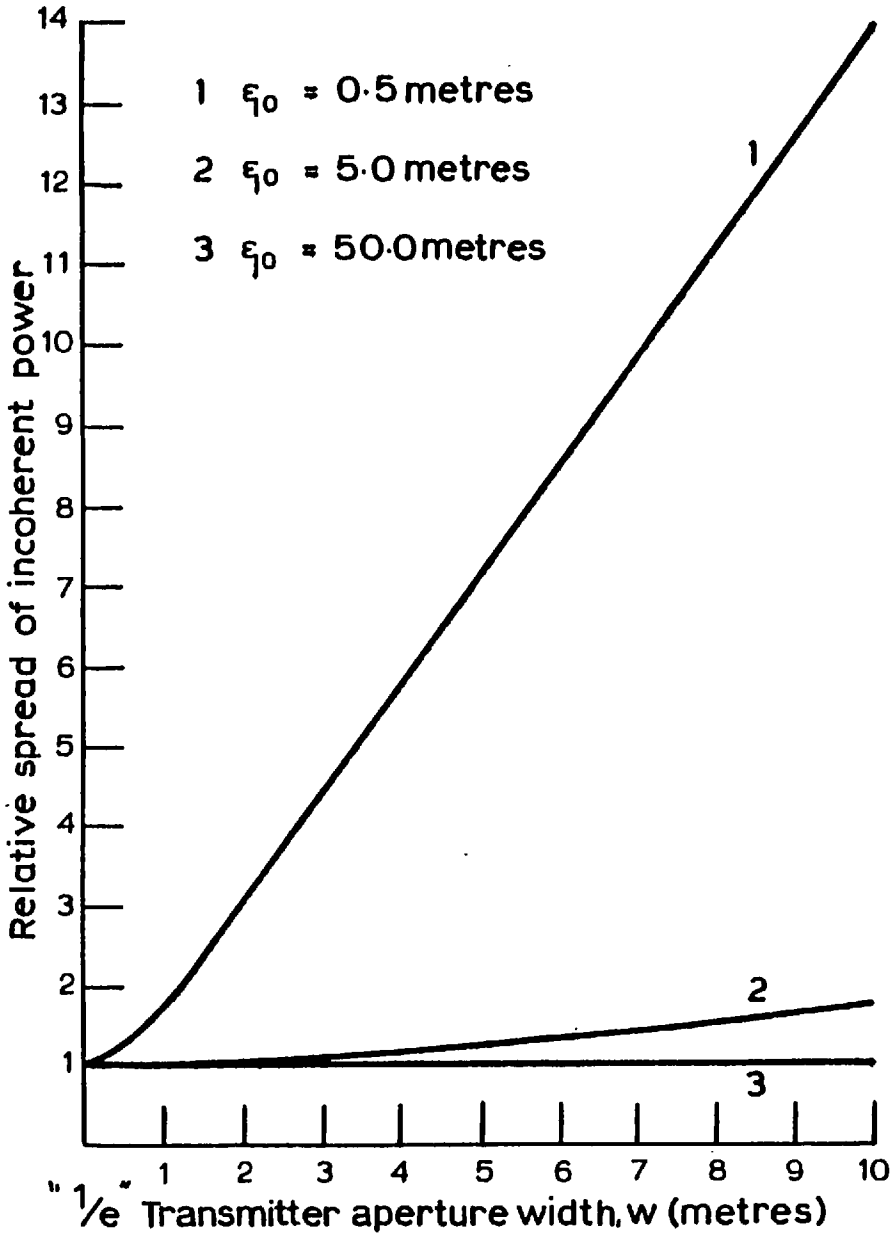

Fig. 4·1 (a)

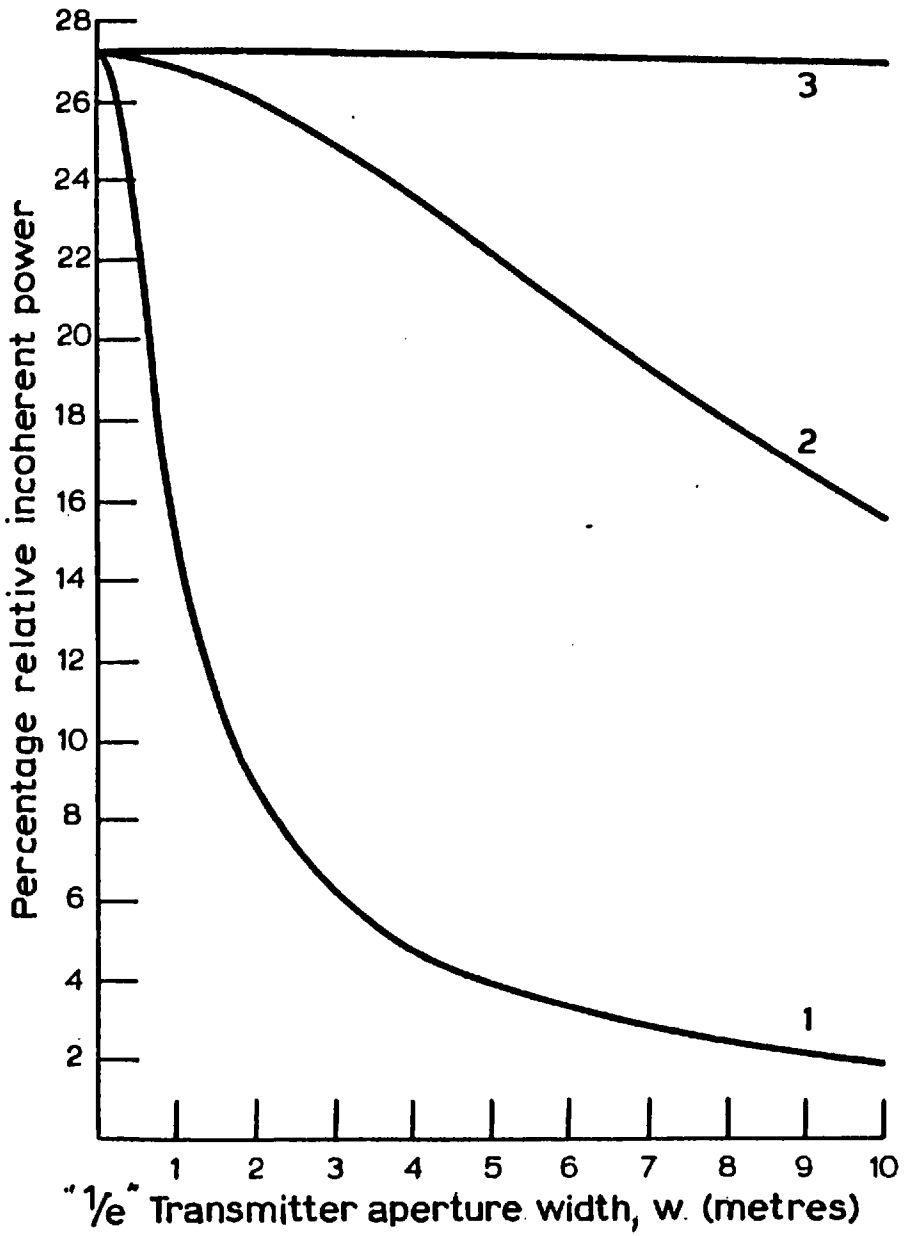

Fig. 4·1 (b)

4.3 Propagation of the Coherence Function Through a Strongly Turbulent Medium

In the previous section, it was assumed that the coherent and incoherent portions of the lateral coherence function propagate without change to the observation plane z = d. The incoherent portion was calculated under the condition that $\sigma_\phi^2 << 1$. This condition is easily met for relatively short path lengths or alternatively for weak turbulence situations. However, under strong turbulence conditions or for non-homogeneous media, for example, the strength of turbulence σ_n^2 is not constant throughout the path length, or for varying scale sizes of the refractive index irregularities, the previous analysis does not accurately represent the effect of the medium on the propagating wave.

4.3.1 Multiple Phase Screen Representation of the Medium

A suitable procedure to overcome the above inadequacies is to divide the total path length L into a series of m consecutive homogeneous regions or slabs as shown in Fig. 4.2. The magnitude of the turbulence within each slab is then considered to be weak and, hence, each slab may be collapsed into its characteristic random phase screen, each satisfying the condition that $\sigma_\phi^2 << 1$.

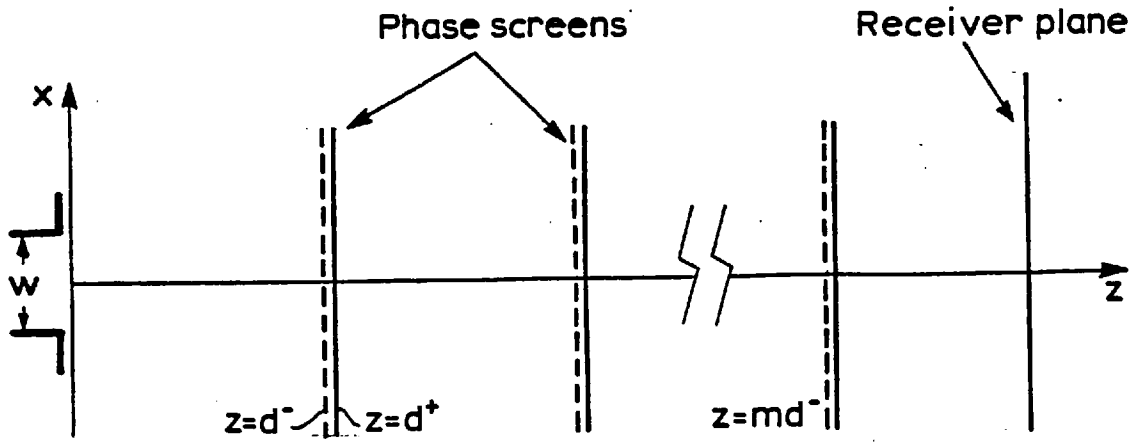

Fig. 4.2 Multiple phase screen representation of the random medium

The lateral coherence function calculated at z = 0, propagates without change to the plane z = d^-. The medium from z = d to z = 2d is collapsed into a phase screen at z = d^+.

In the following analysis the notations to be used are:-

$\Gamma_0(\xi)$ is the lateral autocorrelation function of the aperture field distribution, which for a normalized field distribution is:-

$$\Gamma_0(\xi) = \exp - (\xi^2/2w^2)$$

$T_1(\xi)$ is the lateral autocorrelation function of the phase screen at z = 0, and is split into two parts - a coherent part $T_{1C}(\xi)$ and an incoherent part $T_{1i}(\xi)$ as shown in Equation (4.15), which are given by:-

$$T_{1C}(\xi) = \exp (- \sigma_1^2)$$

and for $\sigma_1^2 \ll 1$, $T_{1i} \simeq \sigma_1^2 \cdot r_1(\xi) \cdot e^{-\sigma_1^2}$ and:-

$$T_1(\xi) = T_{1C}(\xi) + T_{1i}(\xi)$$

where σ_1^2 is the variance of the random phase distribution across the phase screen at z = 0 and $r_1(\xi)$ is the Gaussian phase autocovariance function.

Similar notations will be used for the second phase screen at z = 2d with the appropriate suffixes, and so on for the rest of the phase screens.

Returning to Fig. 4.2, the coherence function at the plane

$z = d^-$ has been shown to be:-

$$\Gamma(\xi;d^-) = \Gamma_0(\xi) \cdot \left[\overline{T}_{1c}(\xi) + T_{1i}(\xi)\right] \tag{4.23}$$

The precise knowledge of the random complex field distribution at $z = d^-$ is not particularly relevant and for argument's sake, will be assumed to be $E_1(x) = a_1(x) \cdot e^{j\beta_1(x)}$.

The phase screen at $z = d^+$ representing the region from $z = d$ to $z = 2d$ introduces a random phase $\phi_2(x)$, the characteristics of which are determined by the characteristics of the refractive index fluctuations in the second region. Therefore, the field distribution is:-

$$E_1(x;d^+) = E_1(x,d^-) \cdot e^{j\phi_2(x)} = a_1(x) \cdot e^{j\beta_1(x)} \cdot e^{j\phi_2(x)}$$

and hence the coherence function at $z = d^+$ is given by:-

$$\begin{aligned}\Gamma_2(\xi;d^+) &= \int_{-\infty}^{+\infty} \langle E_1(x;d^+) \cdot E_1^*(x+\xi;d^+) \rangle \cdot dx \\ &= \int_{-\infty}^{+\infty} \langle a_1(x) \cdot a_1(x+\xi) \cdot e^{j\left[\beta_1(x) - \beta_1(x+\xi)\right]} \cdot e^{j\left[\phi_2(x) - \phi_2(x+\xi)\right]} \rangle \cdot dx\end{aligned} \tag{4.24}$$

If the second phase screen at $z = d^+$ is situated at a relatively large distance away from the first one at $z = 0$, i.e. many longitudinal correlation lengths ζ_0 away, therefore, the phase contributions of the first and second phase screens $\phi_1(x)$ and $\phi_2(x)$, may be considered to be uncorrelated. Since $\phi_1(x)$ and $\phi_2(x)$ are both assumed to be Gaussian random variables, therefore, lack of correlation indicates independence[36]. Hence, the random field distribution $E_1(x,d^-)$ and $\phi_2(x)$ are independent.

Therefore, Equation (4.24) may be split as follows:-

$$\Gamma_2(\xi,d^+) = \Gamma_1(\xi,d^-) \cdot T_2(\xi) = \Gamma_0(\xi) \cdot T_1(\xi) \cdot T_2(\xi) =$$

$$= \Gamma_0(\xi) \left[T_{1c}(\xi) \cdot T_{2c}(\xi) + T_{1c}(\xi) \cdot T_{2i}(\xi) + T_{2c}(\xi) \cdot T_{1i}(\xi) + T_{1i}(\xi) \cdot T_{2i}(\xi) \right] \tag{4.25}$$

Corresponding to the four separate coherence functions of Equation (4.25), there are four angular power spectra after the second phase screen. They are:-

(I)

$$|F_I(\xi)|^2 \longleftrightarrow \Gamma_0(\xi) \cdot T_{1c}(\xi) \cdot T_{2c}(\xi) = \frac{\pi \cdot w^2 \cdot b^2}{\lambda^2} \cdot$$

$$\cdot e^{-(\sigma_1^2 + \sigma_2^2)} \cdot \exp \frac{-S^2}{\frac{1}{2}\left(\frac{\lambda}{\pi w}\right)^2} \tag{4.26}$$

This angular power is the twice attenuated free space power, first from the first phase screen and then from the second phase screen, the attenuation factor being exp - $(\sigma_1^2 + \sigma_2^2)$. The width of the angular power spread is obviously similar to the free space value.

(II)

$$|F_{II}(S)|^2 \longleftrightarrow \Gamma_0(\xi) \cdot T_{1c}(\xi) \cdot T_{2i}(\xi) =$$

$$= \frac{\pi \cdot w^2 \cdot b^2 \cdot \sigma_2^2 \cdot e^{-(\sigma_1^2 + \sigma_2^2)}}{\lambda^2 \cdot \sqrt{1 + \frac{2w^2}{\xi_2^2}}} \cdot \exp\left[\frac{-S^2}{\frac{1}{2}\left(\frac{\lambda}{\pi w}\right)^2 \cdot \left(1 + \frac{2w^2}{\xi_2^2}\right)}\right] \qquad (4.27)$$

This angular power corresponds to that reduced by the first phase screen and then scattered and reduced by the second phase screen. The reduction in magnitude is a function of the phase variance σ_1^2 and σ_2^2, and on the ratio of the transmitting aperture size to the lateral scale size of the phase variations across the second phase screen, ξ_2.

(III)

$$|F_{III}(S)|^2 \longleftrightarrow \Gamma_o(\xi) \cdot T_{2c}(\xi) \cdot T_{1i}(\xi) =$$

$$= \frac{\pi \cdot w^2 \cdot b^2 \cdot \sigma_1^2 \cdot e^{-(\sigma_1^2 + \sigma_2^2)}}{\lambda^2 \cdot \sqrt{1 + \frac{2w^2}{\xi_1^2}}} \cdot \exp\left[\frac{-S^2}{\frac{1}{2}\left(\frac{\lambda}{\pi w}\right)^2 \cdot \left(1 + \frac{2w^2}{\xi_1^2}\right)}\right] \qquad (4.28)$$

This angular power is that reduced and scattered by the first phase screen and then reduced only without further scattering by the second phase screen. The spread of the scattered power is a function of the scale size ξ_1, of the first phase screen.

(IV)

$$|F_{IV}(S)|^2 \longleftrightarrow \Gamma_o(\xi) \cdot T_{1i}(\xi) \cdot T_{2i}(\xi) =$$

$$= \frac{\pi \cdot w^2 \cdot b^2 \cdot \sigma_1^2 \cdot \sigma_2^2 \cdot e^{-(\sigma_1^2 + \sigma_2^2)}}{\lambda^2 \cdot \sqrt{\frac{2w^2}{\xi_{12}^2} + 1}} \cdot \exp\left[\frac{-S^2}{\frac{1}{2}\left(\frac{\lambda}{2\pi}\right)^2 \cdot \left(1 + \frac{2w^2}{\xi_{12}^2}\right)}\right] \quad (4.29)$$

where:-

$$\xi_{12} = \frac{\xi_1 \cdot \xi_2}{\sqrt{\xi_1^2 + \xi_2^2}}$$

This part of the angular power spectrum represents that portion of the energy which is scattered and reduced by the first screen and further scattered and reduced by the second phase screen. The magnitude and spread of this angular power are both a function of both scale sizes ξ_1 and ξ_2. Since ξ_{12} is always less than ξ_1 or ξ_2, then the spread is always wider than the single scatter terms $|F_{II}(S)|^2$ and $|F_{III}(S)|^2$.

This part of the angular power may be considered to be the first multiple scatter term and its magnitude relative to the reduced unscattered component is:-

$$\frac{\text{Magnitude of Multiple Scatter Term}}{\text{Magnitude of Unscattered Component}} = \frac{\sigma_1^2 \cdot \sigma_2^2}{\sqrt{1 + \frac{2w^2}{\xi_{12}^2}}} \quad (4.30)$$

For σ_1^2 and σ_2^2 both $<< 1$, it is seen that the multiple scatter component is relatively a very small quantity. The multiple scatter term is further reduced by the quantity σ_3^2 and so on as it is further scattered along the path length.

It is easy to see that proceeding along the path, each phase screen contributes a coherent and an incoherent part. Finally at the output of the m'th phase screen, the lateral coherence function may be written as follows:-

$$\Gamma(\xi;md^+) = \Gamma_o(\xi) \cdot \left[T_{1c}(\xi) + T_{1i}(\xi)\right] \cdot \left[T_{2c}(\xi) + T_{2i}(\xi)\right] \cdots \left[T_{mc}(\xi) + T_{mi}(\xi)\right] \tag{4.31}$$

A full expansion of the above expression would give all the multiple scattering terms, the single scatter terms of each phase screen, and the continuously reduced free space component. The resulting expression would be very cumbersome.

As an approximation, terms which are scattered more than once will be neglected, in this case the lateral coherence function at the end of the final slab at $z = md^+$ is:-

$$\Gamma(\xi;md^+) = \Gamma_o(\xi) \cdot \left[\prod_{j=1}^{m} T_{jc}(\xi) + \sum_{\ell=1}^{m} \cdot \prod_{j=1}^{m} T_{cj}(\xi) \cdot T_{\ell i}(\xi)\right] \tag{4.32}$$

where Π indicates a product.

Since $T_{jc}(\xi) = \exp(-\sigma_j^2)$, therefore, the above product is merely an addition of the variances of the phases of the individual screens.

The corresponding angular power spectra for the single scatter result of Equation (4.32) are the Fourier transforms of the individual terms resulting from the expansion of Equation (4.32).

Normally the medium need not be divided into a large number of regions, since it has been previously shown that even for relatively strong turbulence σ_ϕ^2 is much less than unity. However, if the medium is

inhomogeneous, then the above approach is useful.

To appreciate the physical reasoning of the multiple slab approach, consider a strongly turbulent medium or alternatively a long propagation path such that σ_ϕ^2 is large. Furthermore, assume the medium to be homogeneous, i.e. the scale sizes ξ_0 and ζ_0 and the variance σ_n^2 of the refractive index fluctuations are constant throughout the medium. Dividing the medium into m slabs, such that $\sigma_\phi^2 << 1$ within each slab, the lateral coherence function including multiple scatter terms is given by:-

$$\Gamma(\xi;md^+) = \Gamma_0(\xi) \cdot \left(e^{-m\sigma_\phi^2} + e^{-m\sigma_\phi^2} \left[e^{m\sigma_\phi^2} - 1 \right] \right) \tag{4.33}$$

Applying Equation (4.32) for a homogeneous medium, i.e. neglecting multiple scatter terms, the lateral coherence function is then simply given by:-

$$\Gamma(\xi;md^+) = \Gamma_0(\xi) \cdot \left[e^{-m\sigma_\phi^2} + m \cdot \sigma_\phi^2 \cdot r_\phi(\xi) \cdot e^{-m\sigma_\phi^2} \right] \tag{4.34}$$

which obviously is a result that may have similarly been obtained for a single slab, but replacing σ_ϕ^2 by $m\sigma_\phi^2$, where $m\sigma_\phi^2$ is not restricted to be much less than unity. Hence, this indicates that a strongly turbulent medium may be collapsed into a single phase screen with the phase variance being that acquired along the total path length.

This result has been predicted by Bramley[50] and has been seen from the above analysis to be valid under conditions of single scatter.

4.3.2 Angular Power Spectrum of an Incident Wave with Random Amplitude and Phase Distributions

A wave propagating through a random medium has been seen to suffer destruction of its lateral coherence, corresponding to the splitting of the angular power incident on a receiver plane into a coherent and one or more incoherent components. The lateral statistics of the complex wave amplitude are determined through knowledge of the lateral coherence function.

Although the destruction of lateral coherence originates due to the random phase only modulation by the phase screen, the amplitude distribution is progressively altered from its free space value. This may be appreciated by the results of the previous chapter for the on-axis field fluctuations. Hewish[51] has calculated the amplitude and phase distributions due to a phase screen with sinusoidal variations and he has shown that the amplitude distribution is progressively altered as the wave is observed at consecutive planes.

The calculation of the individual amplitude and phase lateral fluctuations in the receiver plane in this situation is impossible due to the random nature of the modulating phase screen. However, if it were possible to estimate the magnitude of the amplitude and phase fluctuations and their scale sizes across a lateral observation plane, it would be possible to determine the relative magnitude and spread of the scattered energy.

Consider an incident wavefront with the following complex field distribution:-

$$E(x) = A(x) \cdot e^{j\phi(x)}$$

where $A(x)$ and $\phi(x)$ are the random amplitude and phase distributions

respectively.

Assuming a homogeneous distribution for the amplitude and phase variations, the coherence function is thus given by:-

$$\Gamma_E(\xi) = \int_{-\infty}^{+\infty} \langle A(x) \cdot A(x+\xi) \cdot e^{j\phi(x)} \cdot e^{-j\phi(x+\xi)} \rangle \cdot dx$$

Assuming that the amplitude and phase fluctuations are independent, which is a reasonable assumption based on the analysis of Chapter 3, therefore:-

$$\Gamma_E(\xi) = \Gamma_A(\xi) \cdot \Gamma_\phi(\xi) \tag{4.35}$$

where $\Gamma_A(\xi)$ and $\Gamma_\phi(\xi)$ are the amplitude and phase lateral coherence functions respectively and:-

$$\Gamma_A(\xi) = \int_{-\infty}^{+\infty} \langle A(x) \cdot A(x+\xi) \rangle \cdot dx \tag{4.36}$$

Noting that the amplitude autocorrelation coefficient $r_A(\xi)$ is defined as:-

$$r_A(\xi) = \frac{\langle A(x) \cdot A(x+\xi) \rangle - \langle A(x) \rangle \cdot \langle A(x+\xi) \rangle}{\sigma_{A(x)} \cdot \sigma_{A(x+\xi)}} \tag{4.37}$$

Assuming spatial stationarity of the first and second degree, which again is a reasonable assumption over small separations of the order of metres, after a propagation distance of the order of a few kilometres, therefore:-

$$\langle A(x) \rangle = \langle A(x+\xi) \rangle = m$$

which is the mean value of the amplitude variations and is a function of the power radiated and the gain of the transmitting antenna and:-

$$\sigma_{A(x)} = \sigma_{A(x+\xi)} = \sigma_A$$

Furthermore, for analytical simplicity, assuming a Gaussian autocorrelation function, with a lateral scale size ξ_A, i.e.:-

$$r_A(\xi) = \exp - \xi^2/\xi_A^2$$

Therefore, from Equations (4.36) and (4.37), the amplitude coherence function is given by:-

$$\Gamma_A(\xi) = m^2 + \sigma_A^2 \cdot e^{-\xi^2/\xi_A^2} \qquad (4.38)$$

Assuming a zero mean phase process, and a Gaussian phase autocorrelation function, with a scale size ξ_ϕ, the phase lateral coherence function is then given by:-

$$\Gamma_\phi(\xi) = e^{-\sigma_\phi^2} + e^{-\sigma_\phi^2}\left[e^{\sigma_\phi^2 \cdot e^{-\xi^2/\xi_0^2}} - 1\right]$$

It will be shown later in the experimental investigations that the phase variance σ_ϕ^2 is much less than unity, therefore, for $\sigma_\phi^2 \ll 1$:-

$$\Gamma_\phi(\xi) \simeq e^{-\sigma_\phi^2} + \sigma_\phi^2 \cdot e^{-\xi^2/\xi_0^2}$$

Substituting for $\Gamma_A(\xi)$ and $\Gamma_\phi(\xi)$ in Equation (4.35), the

complex field coherence function is given by:-

$$\Gamma_E(\xi) \simeq m^2 \cdot e^{-\sigma_\phi^2} + m^2 \cdot \sigma_\phi^2 \cdot e^{-\xi^2/\xi_\phi^2} + \sigma_A^2 \cdot e^{-\sigma_\phi^2} \cdot e^{-\xi^2/\xi_A^2} +$$

$$+ \sigma_A^2 \cdot \sigma_\phi^2 \cdot \exp\left[\frac{-\xi^2(\xi_A^2 + \xi_\phi^2)}{\xi_A^2 \cdot \xi_\phi^2}\right] \qquad (4.39)$$

It is seen that the coherence function is split into four parts and, hence, the corresponding angular power spectrum is also split into four parts. These will be obtained individually below:-

(I)

$$|F_I(S)|^2 \longleftrightarrow m^2 \cdot e^{-\sigma_\phi^2} = \frac{m^2}{\lambda^2} e^{-\sigma_\phi^2} \cdot \delta(S) \qquad (4.40)$$

where $\delta(S)$ is the Dirac-Delta function and the angular power is simply the free space power reduced in magnitude by $e^{-\sigma_\phi^2}$.

(II)

$$|F_{II}(S)|^2 \longleftrightarrow m^2 \cdot \sigma_\phi^2 \cdot e^{-\xi^2/\xi_\phi^2} = \frac{m^2 \cdot \sigma_\phi^2 \cdot \sqrt{\pi}}{\lambda^2} \cdot \xi_\phi \cdot \exp\frac{-S^2}{\left\{\frac{\lambda}{\pi\xi_\phi}\right\}^2} \qquad (4.41)$$

which is the scattered power contributed by the random phase variations.

(III)

$$|F_{III}(S)|^2 \longleftrightarrow \sigma_A^2 \cdot e^{-\sigma_\phi^2} \cdot e^{-\xi^2/\xi_A^2} =$$

$$= \frac{\sqrt{\pi} \cdot e^{-\sigma_\phi^2} \cdot \sigma_A^2 \cdot \xi_A}{\lambda^2} \cdot \exp \frac{-S^2}{\left(\frac{\lambda}{\pi \xi_A}\right)^2} \qquad (4.42)$$

This is the scattered power contributed by the random amplitude fluctuations and is seen to be independent of the amplitude level. This part of the scattered power is much smaller in magnitude than that due to the phase fluctuations.

(IV)

$$|F_{IV}(S)|^2 \longleftrightarrow \sigma_A^2 \cdot \sigma_\phi^2 \cdot \exp - \left[\frac{\xi^2(\xi_A^2 + \xi_\phi^2)}{\xi_A^2 \cdot \xi_\phi^2}\right] =$$

$$= \frac{\sqrt{\pi} \cdot \sigma_A^2 \cdot \sigma_\phi^2 \cdot \xi_A \cdot \xi_\phi}{\lambda^2 \cdot \sqrt{\xi_A^2 + \xi_\phi^2}} \cdot \exp \frac{-S^2}{\left(\frac{\lambda}{\pi \xi_A \cdot \xi_\phi}\right)^2 (\xi_A^2 + \xi_\phi^2)} \qquad (4.43)$$

This portion of the angular power spectrum represents the incoherent or scattered power due to both amplitude and phase fluctuations. The spread of this portion is larger than either the amplitude or phase scattering components. The magnitude is also much smaller than either one.

The conclusions drawn from the above angular power representations is that if amplitude and phase fluctuations are detected in a plane normal to the direction of propagation, one can predict the angular power

distribution.

The angular power is seen to consist of four components. The magnitude of the phase fluctuations σ_ϕ^2 seems to be the most effective parameter in determining the magnitude of the scattered components relative to the reduced free space component.

To summarize the conclusions reached in this chapter, it may be said that the random medium degrades the coherence of the propagating wave. This has been seen to correspond to the splitting of the angular power spectrum into a coherent and incoherent portions. The relative magnitude and spread of the two portions have been seen to be a function of the transmitter aperture size, the strength of turbulence and the scale sizes of the refractive index irregularities.

The strongly random medium has been represented by a series of parallel phase screens; the maximum separation between the screens is limited such that the magnitude of the characteristic phase variance is much less than unity. On the other hand, the minimum separation is limited by the requirement that the phase contribution of one region is statistically independent of that of the next region. It has been shown that for a homogeneous medium and for single scatter considerations, the entire medium may be collapsed into one phase screen, with the phase variance being that acquired along the total path length.

It has also been seen that a wavefront distorted in amplitude and phase corresponds to an angular power distribution with a reduced free space component and a broader scattered portion. The magnitude of the scattered portion relative to the reduced specular component being mainly determined by the variance and scale size of the phase fluctuations, with the variance of the amplitude fluctuations playing a minor role.

The incoherent portion of the angular power spectrum has been seen to be equivalent to the variance of the available fluctuating signal.

This variance is that which would be sensed by a point receiver which has the property of receiving energy from all directions without discrimination. However, practical receiving antennas having a finite size and consequently a finite beam width and, hence, the amount of received power, coherent and incoherent, is a function of the receiver aperture size.

Having studied the behaviour of a finite beam propagating in a random medium, the problem then is to investigate the effects of the medium induced wavefront distortions and their corresponding angular power spectra, on the mechanism of coupling to a finite receiving aperture. The next chapter is concerned with the treatment of this problem.

CHAPTER 5

TRANSMITTER TO RECEIVER COUPLING IN A RANDOM MEDIUM

In this chapter, the coupling of a randomly distorted wave front to a finite receiving aperture is studied. In Chapter 3, the fluctuations in the complex field were estimated for an on-axis observation point. This corresponds to reception by a point receiver, i.e. an isotropic receiver with no angular discrimination. In Chapter 4, the power fluctuations were estimated using angular power spectrum and coherence function considerations. The variance of the power incident on the receiver plane has been shown to be the incoherent power available. This has been determined relative to the mean or incoherent portion. The on-axis ratio, i.e. at S = 0 corresponds to the amount of incoherent or noise power relative to the mean power received by an aperture sensitive only to the field incident from the on-axis direction.

The practical case of a finite dimension receiving aperture with a finite angular response, receiving a partially coherent incident beam with a finite angular spread for both the coherent and incoherent portions will be developed in the following analysis.

The analysis is an extension of Brown's free space field coupling formula[52]. The random medium is represented by a random phase screen situated at the transmitter aperture plane. To approach a practical representation of the medium, the phase screen and the aperture responses will be considered in their three-dimensional form. Furthermore, the phase variations across the phase screen will be taken to be time varying, with the time variations corresponding to those of the medium irregularities.

As a consequence of the random medium, the power coupled between the transmitting and receiving antennas is reduced from the free space value and, hence, the efficiency of the propagation system is reduced. At the same time, the random medium introduces a noise component into the system and, hence, the signal-to-noise level is deteriorated.

The system efficiency and signal-to-noise ratio will be defined and obtained as a function of the system and medium parameters. Their variations with the above parameters will be investigated.

5.1 Free Space Transmitter-Receiver Power Coupling

In the previous chapter, the angular power spectrum of the field radiated by a transmitting aperture has been shown to be the Fourier transform of the lateral autocorrelation function of the electric field distribution across the transmitter aperture plane or across any plane normal to the direction of propagation. The angular power spectrum has also been seen to be directly related to the antenna gain function.

In this section, the power coupled from the angular spectrum of incident plane waves onto a receiving aperture will be obtained under free space propagation conditions. The dependence of the power coupled on the aperture sizes and the propagation distance will be investigated.

The three-dimensional case will be considered and for analytical simplicity, the aperture field will be assumed to be separable in the x and y lateral direction and, hence, the aperture field is given by:-

$$E(x, y) = b \cdot E(x) \cdot E(y)$$

For further analytical simplicity, the example to be studied will be concerned with Gaussian aperture field distributions. The effective aperture dimensions are taken to be the "1/e" widths of the Gaussian distributions in the x and y directions, w_{Tx} and w_{Ty} respectively.

Therefore, the transmitter aperture field is given by:-

$$E_T(x, y) = b_T \cdot \exp \frac{-x^2}{w_{Tx}^2} \cdot \exp \frac{-y^2}{w_{Ty}^2} \tag{5.1}$$

The normalization will again be taken as:-

$$\int_{-\infty}^{+\infty} |E_T(x, y)|^2 \, dx \, dy = 1$$

Therefore:-

$$b_T = \sqrt{\frac{2}{\pi}} \cdot \frac{1}{\sqrt{w_{Tx} \cdot w_{Ty}}}$$

Similarly, the receiving aperture will be assumed to have an equivalent Gaussian aperture field distribution when transmitting given by:-

$$E_R(x', y') = b_R \cdot \exp \frac{-x'^2}{w_{Rx}^2} \cdot \exp \frac{-y'^2}{w_{Ry}^2} \tag{5.2}$$

where, for a normalized aperture field:-

$$b_R = \sqrt{\frac{2}{\pi}} \cdot \frac{1}{\sqrt{w_{Rx} \cdot w_{Ry}}}$$

In Equation (5.2) the receiver aperture field is defined in terms of the lateral coordinate system in the receiver aperture plane.

The following analysis will be concerned only with the situation of both transmitting and receiving antennas facing each other, as shown in Fig. 5.1. Under this condition, it is seen that $x' = x$, $y' = -y$ and $z' = L - z$.

5.1.1 Angular Spectrum Coupling

To calculate the power coupled from the transmitter to the receiver aperture, the analysis will be based on the coupling formula produced by Brown[52], where the complex signal coupled from a radiating aperture with an angular plane wave spectrum $F_T(S_1, S_2)$ to a receiving aperture with an equivalent angular plane wave spectrum $F_R(S_{1r}, S_{2r})$ is U, where U is given by:-

$$U = \frac{\lambda^2}{2Z} \cdot \int_{-\infty}^{+\infty} \int_{-\infty}^{+\infty} F_T(S_1, S_2) \cdot F_R(S_{1r}, S_{2r}) \frac{1 - S_{2r}^2}{C} e^{-jkLC_r} \cdot dS_1 \cdot dS_2 \tag{5.3}$$

where Z is the plane wave impedance in free space.

The above formula is given as an exact result for the complex field coupled to a receiving aperture in the near field of the transmitting aperture.

In the coordinate system shown in Fig. 5.1, the direction cosines of the receiver aperture are given by:-

$$S_{1r} = -S_1 \quad , \quad S_{2r} = S_2 \quad , \quad C_r = C$$

Considering narrow plane wave angular spectra, i.e. the

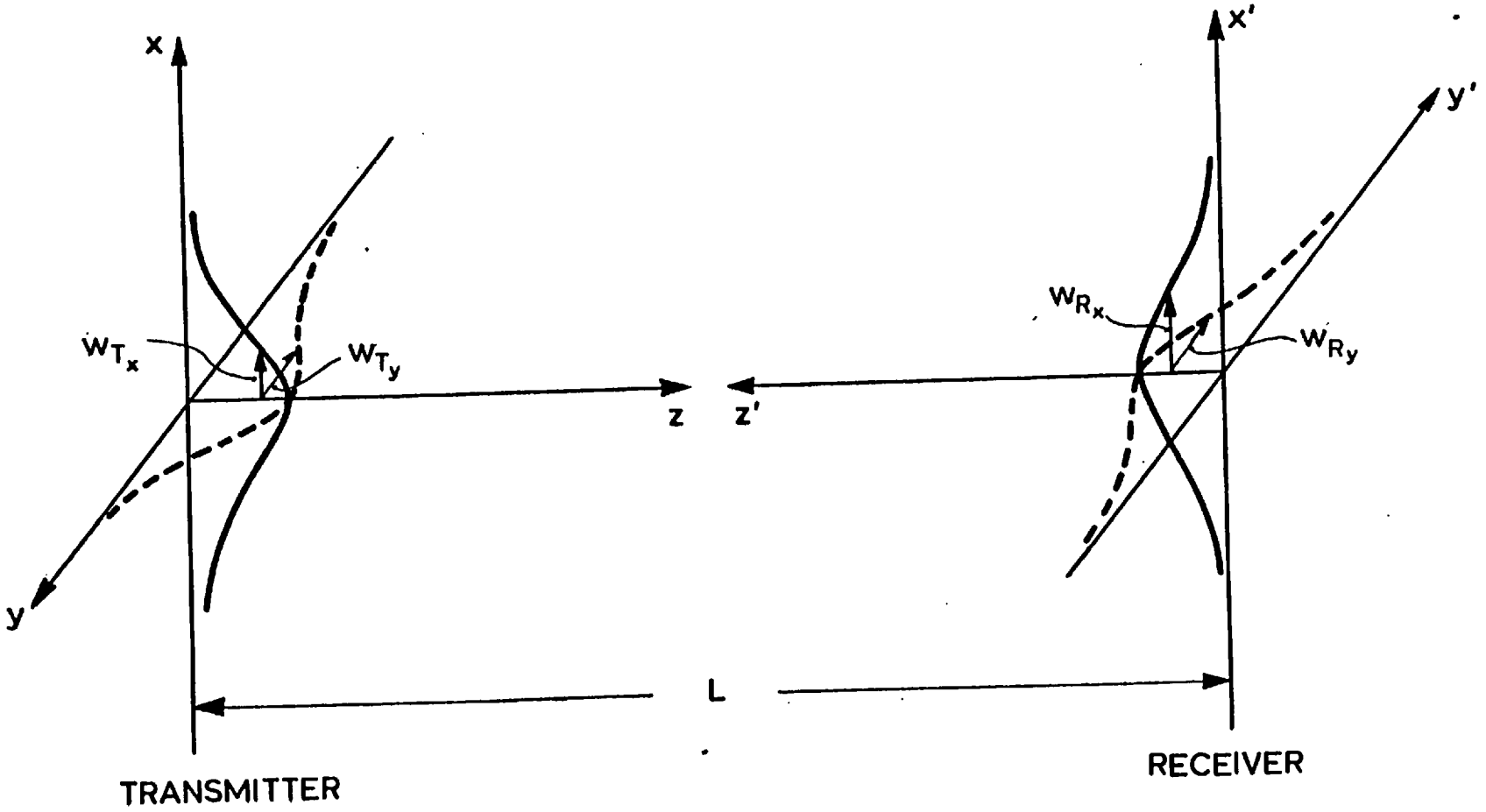

Fig. 5·1

dimensions of both transmitting and receiving aperture are many wavelengths, which is a very reasonable assumption at microwave frequencies, the following approximation may be made for θ and ϕ within ± 15 degrees:-

$$\frac{1 - S_2^2}{C} = \frac{1 - \sin^2\theta \,.\, \sin^2\phi}{\cos\theta} \simeq 1 \qquad (5.4)$$

and also:-

$$C \simeq 1 - \frac{(S_1^2 + S_2^2)}{2}$$

The power coupled to the receiving aperture is obviously given by U^2. To obtain the complex field and, hence, the power coupled using formula (5.3), is relatively simple under free space conditions. However, if the field is a random one due to the presence of a random medium, the situation is much more difficult due to the lack of knowledge of the random field distribution. It has been shown in Chapter 4 that, although the random medium varies the complex field distribution in a random manner which is impossible to describe in detail, the coherence function remains constant for the random wave after it passes through the random phase screen at the transmitter plane.

To make use of this feature of the propagation of the coherence function, the calculation of the power coupled to a receiving aperture, will proceed from a lateral autocorrelation function point of view for the free space case. This will be extended to the random case by considering the coherence function.

Substituting the approximations of Equation (5.4) into the coupling formula of Equation (5.3), the complex electric field coupled is thus given by:-

$$U = \frac{\lambda^2}{2Z} \cdot \int_{-\infty}^{+\infty}\int_{-\infty}^{+\infty} F_T(S_1, S_2) \cdot F_R(-S_1, S_2) \cdot e^{-jkL\left[1 - \frac{(S_1^2 + S_2^2)}{2}\right]} \cdot dS_1 \cdot dS_2$$

The conjugate of the complex coupled field is:-

$$U^* = \frac{\lambda^2}{2Z} \cdot \int_{-\infty}^{+\infty}\int_{-\infty}^{+\infty} F_T^*(S_1, S_2) \cdot F_R^*(-S_1, S_2) \cdot e^{+jkL\left[1 - \frac{(S_1^2 + S_2^2)}{2}\right]} \cdot dS_1 \cdot dS_2$$

Therefore, the power received is given by:-

$$|U|^2 = U \cdot U^* = \frac{\lambda^4}{4z^2} \cdot \int_{-\infty}^{+\infty}\int_{-\infty}^{+\infty}\int_{-\infty}^{+\infty}\int_{-\infty}^{+\infty} F_T(S_1', S_2') \cdot F_T^*(S_1, S_2) \cdot F_R(-S_1', S_2') \cdot$$

$$\cdot F_R^*(-S_1, S_2) \cdot e^{-j\frac{kL}{2}(S_1^2 - S_1'^2)} \cdot e^{-j\frac{kL}{2}(S_2^2 - S_2'^2)} \cdot dS_1 \cdot dS_2 \cdot dS_1' \cdot dS_2' \qquad (5.5)$$

where $S_1' = S_1 + \sigma_1$ and $S_2' = S_2 + \sigma_2$. σ_1 and σ_2 are angular displacements.

To calculate the quantity $F_T(S_1', S_2') \cdot F_T^*(S_1, S_2)$, since:-

$$F_T(S_1, S_2) = \frac{1}{\lambda^2} \cdot \int_{-\infty}^{+\infty}\int_{-\infty}^{+\infty} E_T(x, y) \cdot e^{+jk(S_1 x + S_2 y)} \cdot dx \cdot dy$$

Therefore:-

$$F_T(S_1', S_2') \cdot F_T^*(S_1, S_2) = \frac{1}{\lambda^4} \cdot \int_{-\infty}^{+\infty}\int_{-\infty}^{+\infty}\int_{-\infty}^{+\infty}\int_{-\infty}^{+\infty} E_T(x', y') \cdot E_T^*(x, y) \cdot$$

$$e^{jk(x'S_1' + y'S_2' - xS_1 - yS_2)} \cdot dx \cdot dx' \cdot dy \cdot dy'$$

where $x' = x + \xi$ and $y' = y + \eta$. ξ and η are lateral displacements.

For separable field distributions, the above equation may be written as:-

$$F_T(S_1', S_2') \cdot F_T^*(S_1, S_2) = \frac{1}{\lambda^4} \cdot \int_{-\infty}^{+\infty}\int_{-\infty}^{+\infty}\int_{-\infty}^{+\infty}\int_{-\infty}^{+\infty} E_T(x + \xi) \cdot E_T^*(x) \cdot E_T(y + \eta) \cdot E_T^*(y)$$

$$\cdot e^{+ jk\sigma_1 x} \cdot e^{+ jk\sigma_2 y} \cdot e^{+ jk\xi (S_1 + \sigma_1)} \cdot e^{+ jk\eta (S_2 + \sigma_2)} \cdot dx \cdot dy \cdot d\xi \cdot d\eta$$

The above equation may be written in terms of the lateral auto-correlation functions as follows:-

$$F_T(S_1', S_2') \cdot F_T^*(S_1, S_2) = \frac{1}{\lambda^4} \cdot \int_{-\infty}^{+\infty}\int_{-\infty}^{+\infty} \Gamma_{Tx}(\xi, \sigma_1) \cdot \Gamma_{Ty}(\eta, \sigma_2) \cdot$$

$$\cdot e^{+ jk\xi (S_1 + \sigma_1)} \cdot e^{+ jk\eta (S_2 + \sigma_2)} \cdot d\xi \cdot d\eta \qquad (5.6)$$

where:-

$$\Gamma_{Tx}(\xi, \sigma_1) = \int_{-\infty}^{+\infty} E_T^*(x) \cdot E_T(x + \xi) \cdot e^{jk\sigma_1 x} \cdot dx \qquad (5.7)$$

and:-

$$\Gamma_{Ty}(\eta, \sigma_2) = \int_{-\infty}^{+\infty} E_T^*(y) \cdot E_T(y + \eta) \cdot e^{jk\sigma_2 y} \cdot dy \qquad (5.8)$$

are the general forms of the lateral autocorrelation of Equation (4.8) and are reduced to it when σ_1 and $\sigma_2 = 0$.

Similar expressions for the receiver autocorrelation functions are obtained on the same lines, with the appropriate suffixes. Furthermore, assuming symmetry about the z-axis in the x-z receiver plane, therefore:-

$$F_R(-S_1', S_2') \cdot F_R^*(-S_1, S_2) = F_R(S_1', S_2') \cdot F_R^*(S_1, S_2) = \frac{1}{\lambda^4} \cdot \int_{-\infty}^{+\infty}\int_{-\infty}^{+\infty} \Gamma_{Rx}(\xi, \sigma_1) \cdot$$

$$\cdot \Gamma_{Ry}(\eta, \sigma_2) \cdot e^{+ jk\xi (S_1 + \sigma_1)} \cdot e^{+ jk\eta (S_2 + \sigma_2)} \cdot d\xi \cdot d\eta \qquad (5.9)$$

Therefore, from Equations (5.6) and (5.9), Equation (5.5) may be written as follows:-

$$|U|^2 = \frac{\lambda^4}{4Z^2} \cdot \int_{-\infty}^{+\infty}\int_{-\infty}^{+\infty}\int_{-\infty}^{+\infty}\int_{-\infty}^{+\infty} \Gamma_{Tx}(\xi, \sigma_1) \circledast \Gamma_{Rx}(\xi, \sigma_1) \cdot \Gamma_{Ty}(\eta, \sigma_2) \circledast \Gamma_{Ry}(\eta, \sigma_2) \cdot\cdot$$

$$\cdot e^{jkLS_1\sigma_1} \cdot e^{jkLS_2\sigma_2} \cdot e^{j\frac{kL}{2}\sigma_1^2} \cdot e^{j\frac{kL}{2}\sigma_2^2} \cdot dS_1 \cdot dS_2 \cdot d\sigma_1 \cdot d\sigma_2 \qquad (5.10)$$

where $\circledast$ denotes a convolution over ξ and η.

Therefore, the coupled power may be obtained through knowledge of the lateral autocorrelation functions of the complex field distributions across the transmitter and receiver planes.

Example

As an example, the power coupled between two antennas will be calculated for the case of Gaussian amplitude illuminated antennas, the aperture field is of the form described in Equations (5.1) and (5.2) for

the transmitter and receiver apertures respectively. Therefore:-

$$\Gamma_{Tx}(\xi, \sigma_1) = b_T \cdot \int_{-\infty}^{+\infty} e^{-(x+\xi)^2/w_{Tx}^2} \cdot e^{-x^2/w_{Tx}^2} \cdot e^{jk\sigma_1 x} \cdot dx =$$

$$= b_T \sqrt{\frac{\pi}{2}} \cdot e^{-\xi^2/2w_{Tx}^2} \cdot e^{-j\frac{k\sigma_1 \xi}{2}} \cdot e^{-\frac{k^2\sigma_1^2 w_{Tx}^2}{8}}$$

Similarly:-

$$\Gamma_{Ty}(\eta, \sigma_2) = b_T \sqrt{\frac{\pi}{2}} e^{-\eta^2/2w_{Ty}^2} \cdot e^{-j\frac{k\sigma_2 \eta}{2}} \cdot e^{-\frac{k^2\sigma_2^2 w_{Ty}^2}{8}}$$

$$\Gamma_{Rx}(\xi, \sigma_1) = b_R \sqrt{\frac{\pi}{2}} e^{-\xi^2/2w_{Rx}^2} \cdot e^{-j\frac{k\sigma_1 \xi}{2}} \cdot e^{-\frac{k^2\sigma_1^2 w_{Rx}^2}{8}}$$

and:-

$$\Gamma_{Ry}(\eta, \sigma_2) = b_R \sqrt{\frac{\pi}{2}} e^{-\eta^2/2w_{Ry}^2} \cdot e^{-j\frac{k\sigma_2 \eta}{2}} \cdot e^{-\frac{k^2\sigma_2^2 w_{Ry}^2}{8}} \qquad (5.11)$$

Carrying out the transformation to the angular domain as shown in Equation (5.6), therefore, it can be shown that:-

$$F_T(S_1', S_2') \cdot F_T^*(S_1, S_2) = \frac{b_T^2}{4} \cdot \pi^2 \cdot w_{Tx}^2 \cdot w_{Ty}^2 \cdot \exp\frac{-k^2 w_{Tx}^2 \sigma_1^2}{4} \cdot \exp\frac{-k^2 w_{Ty}^2 \sigma_2^2}{4} \cdot$$

$$\cdot \exp\frac{-k^2 w_{Tx}^2 \sigma_1 S_1}{2} \cdot \exp\frac{-k^2 w_{Ty}^2 \sigma_2 S_2}{2} \cdot \exp\frac{-k^2 w_{Tx}^2 S_1^2}{2} \cdot \exp\frac{-k^2 w_{Ty}^2 S_2^2}{2} \qquad (5.12)$$

A similar expression for the receiver equivalent angular spectrum may be obtained by replacing w_{Tx} and w_{Ty} with w_{Rx} and w_{Ry} respectively and b_T by b_R.

Substituting Equation (5.9) for both transmitter and receiver angular spectra into Equation (5.5) and carrying out the integration with respect to S_1 and S_2 first, then σ_1 and σ_2, it may be shown that for normalized aperture fields that:-

$$|U|^2 = \left(\frac{\pi}{Z}\right)^2 \cdot \frac{w_{Tx} \cdot w_{Rx}}{\sqrt{\pi^2(w_{Tx}^2 + w_{Rx}^2)^2 + \lambda^2 L^2}} \cdot \frac{w_{Ty} \cdot w_{Ry}}{\sqrt{\pi^2(w_{Ty}^2 + w_{Rx}^2)^2 + \lambda^2 L^2}} \qquad (5.13)$$

For circularly symmetrical antennas, i.e. $w_{Tx} = w_{Ty} = w_T$, and $w_{Rx} = w_{Ry} = w_R$, therefore:-

$$|U|^2 = \left(\frac{\pi}{Z}\right)^2 \cdot \frac{w_T^2 \cdot w_R^2}{\pi^2(w_T^2 + w_R^2)^2 + \lambda^2 L^2} \qquad (5.14)$$

The above expression for $|U|^2$ may similarly be obtained by calculating the coupled complex field and squaring the magnitude. A similar result for the coupled power in free space has also been obtained by Chu[53].

5.1.2 Effect of Aperture Dimensions and Path Length on the Free Space Near and Far Field Coupled Power

Since the complex field coupling formula of Equation (5.3) is correct for near and far field calculations, therefore, the expression for the power coupled between two Gaussian field apertures, Equation (5.14), is also accurate for near and far field calculations for narrow beam antennas, i.e. the beam width is limited to approximately ± 15 degrees.

Fig. 5.2a shows the power coupled between a transmitting and a receiving aperture with Gaussian amplitude distributions with "1/e" half widths w_T and w_R respectively. The power coupled in all cases is calculated relative to the power coupled between two open wave guides,

situated at the same distance, and hence at a wave length of 8 millimetres we have $w_T = w_R = 4$ millimetres, i.e.:-

$$\text{Relative Gain} = 10 \cdot \log \left[\frac{\text{Power Coupled Between } w_T \text{ and } w_R}{\text{Power Coupled Between Two Open Waveguides}} \right]$$

The distance between transmitter and receiver in Fig. 5.2a is 12 kilometres.

Obviously as the aperture dimension increases in size the situation tends to that of calculating the power coupled between apertures in the near field of one or both apertures. It may be seen that the power coupled seems to saturate, and even slightly decrease for small transmitting apertures as the receiving aperture increases in size. As the distance between both apertures is increased, as shown in Fig. 5.2b, the power coupled is seen to increase for the larger aperture sizes and begins to saturate as the distance is increased such that each antenna lies in the far field of the other.

Knowledge of the near field coupled power and its variation with distance may provide useful information for measurements carried out in the near field of large apertures. This may be done by providing a correction factor which is aperture size and distance dependent.

Having obtained a free space power coupling formula based on the knowledge of the lateral autocorrelation function, the next step is to examine the effect of a random medium on the coupled power. It has been seen in Chapter 4 that the random medium causes a degradation of the lateral coherence function and, hence, the angular power spectrum is distorted.

The next section deals with the coupling of the distorted angular power spectrum to a finite receiving aperture.

FREE SPACE

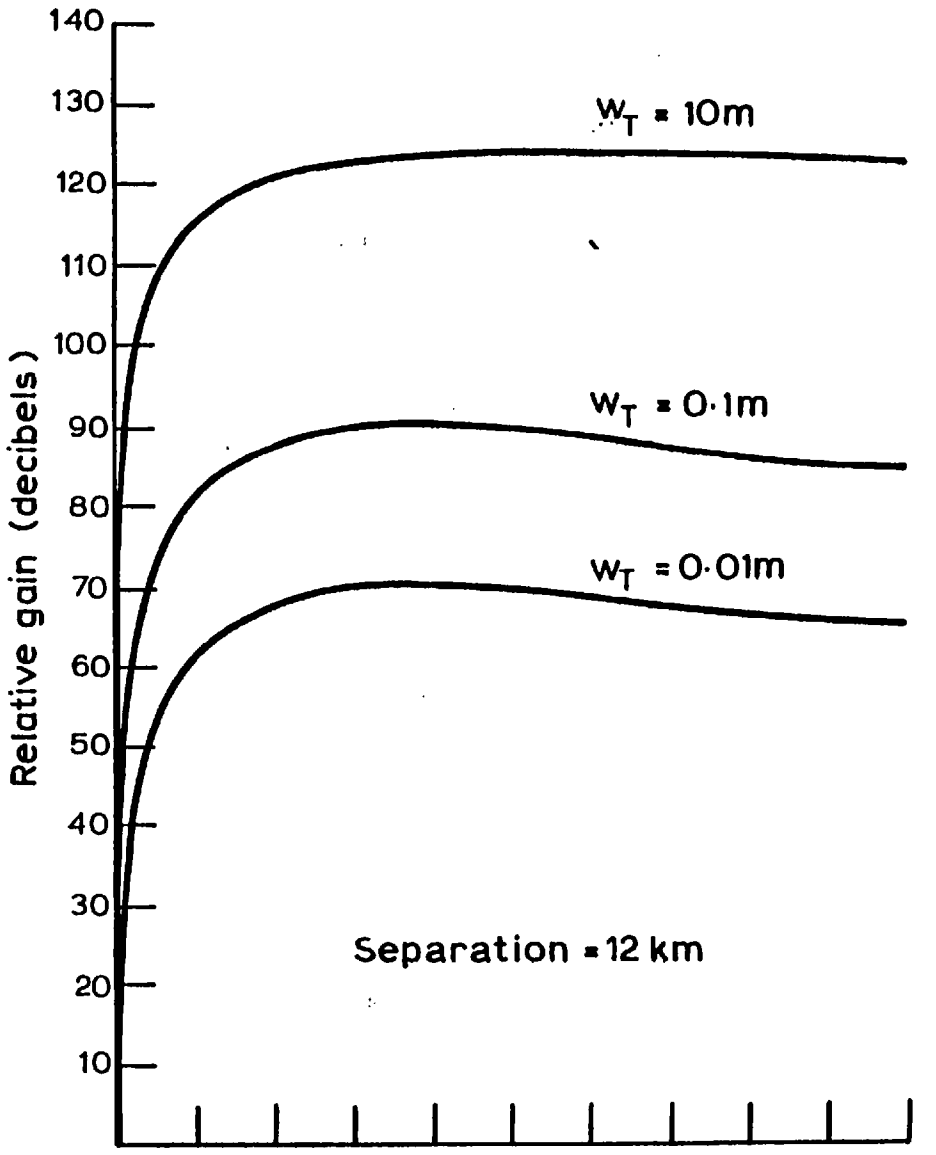

Fig. 5·2 (a)

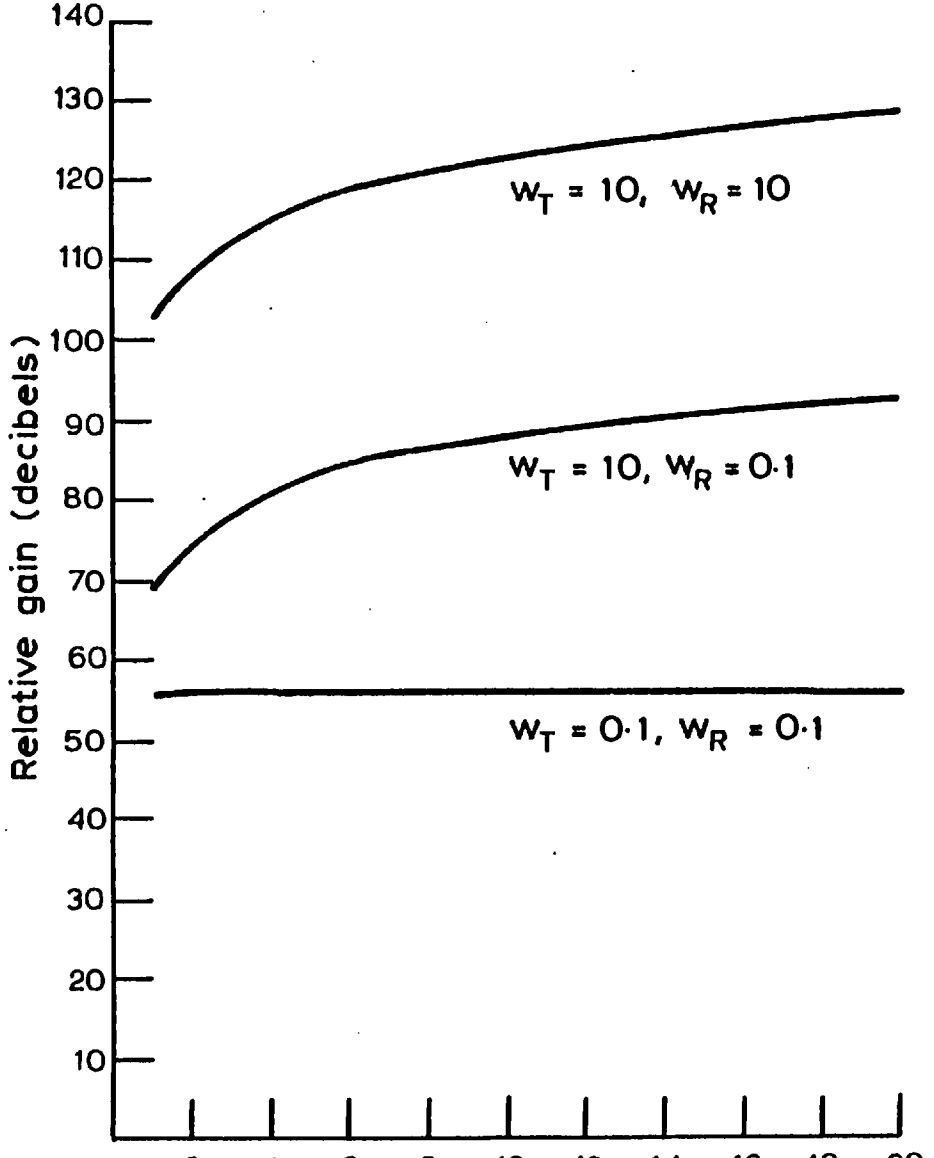

Fig. 5·2 (b)

5.2 Transmitter-Receiver Power Coupling Through a Random Medium

The random medium under consideration is basically that outlined in Chapter 3. However, in this analysis the three-dimensional case will be considered and in addition to the spatial randomness, temporal variations will be incorporated.

It has been previously shown that the phase autocorrelation function is directly related to the refractive index autocorrelation function, i.e. in normalized form:-

$$r_\phi(\xi, \eta, \tau) = r_n(\xi, \eta, \tau)$$

where τ is time shift. Assuming that the functional dependence of the autocorrelation function is a separable one, therefore:-

$$r_\phi(\xi, \eta, \tau) = r_\phi(\xi) \cdot r_\phi(\eta) \cdot r_\phi(\tau) \tag{5.15}$$

Furthermore, it will be assumed that the medium is stationary and, hence, the phase variance σ_ϕ^2 is time independent.

It has been shown for $\sigma_\phi^2 << 1$ that the random medium may be collapsed into a thin phase screen situated at the transmitter aperture plane. The effect of the screen has been seen to split the coherence function in the transmitter plane into a coherent and an incoherent part and, consequently, the radiated angular power is composed of a coherent and an incoherent portion, both of which propagate through what is now a free space medium and are coupled to the receiving aperture.

Due to the randomness of the medium, the power coupled is now a random quantity and hence expected values will be dealt with. Therefore, from Equation (5.5):-

$$\langle U \cdot U^* \rangle = \langle |U|^2 \rangle = \frac{\lambda^4}{4Z^2} \cdot \int_{-\infty}^{+\infty} \int_{-\infty}^{+\infty} \int_{-\infty}^{+\infty} \int_{-\infty}^{+\infty} \langle F_T(S_1', S_2') \cdot F_T^*(S_1, S_2) \rangle \cdot$$

$$\cdot F_R(-S_1', S_2') \cdot F_R^*(-S_1, S_2) \cdot e^{+jkLS_1\sigma_1} \cdot e^{+j\frac{kL}{2}\sigma_1^2} \cdot e^{+jkLS_2\sigma_2} \cdot$$

$$e^{+j\frac{kL}{2}\sigma_2^2} \cdot dS_1 \cdot dS_2 \cdot d\sigma_1 \cdot d\sigma_2 \qquad (5.16)$$

The quantity in the square brackets is the expected value for the angular power spectrum after the phase screen and is obtained from knowledge of the lateral coherence function. Hence, for the random medium under consideration and adding the temporal dependence, this quantity has been shown, Equation (4.16), with $\sigma_\phi << 1$ to be:-

$$\Gamma(\xi, \eta, \tau) = \Gamma_{\text{free space}} \cdot \left[e^{-\sigma_\phi^2} + \sigma_\phi^2 \cdot e^{-\sigma_\phi^2} \cdot r_\phi(\xi, \eta, \tau) \right] \qquad (5.17)$$

Therefore, substituting in Equation (5.6) and noting that the phase autocorrelation function has been assumed to be separable, we get:-

$$\langle F_T(S_1', S_2') \cdot F_T^*(S_1, S_2) \rangle = \frac{1}{\lambda^4} \cdot e^{-\sigma_\phi^2} \left[\int_{-\infty}^{+\infty} \Gamma_{Tx}(\xi, \sigma_1) \cdot e^{jk\xi(S_1 + \sigma_1)} \cdot d\xi \cdot \right.$$

$$\cdot \int_{-\infty}^{+\infty} \Gamma_{Ty}(\eta, \sigma_2) \cdot e^{jk\eta(S_2 + \sigma_2)} \cdot d\eta + \sigma_\phi^2 \cdot r_\phi(\tau) \cdot \int_{-\infty}^{+\infty} \Gamma_{Tx}(\xi, \sigma_1) \cdot r_\phi(\xi) \cdot$$

$$\left. \cdot e^{jk\xi(S_1 + \sigma_1)} \cdot d\xi \cdot \int_{-\infty}^{+\infty} \Gamma_{Ty}(\eta, \sigma_2) \cdot r_\phi(\eta) \cdot e^{jk\eta(S_2 + \sigma_2)} \cdot d\eta \right] \qquad (5.18)$$

The angular power spectrum radiated from the transmitter aperture

plane is composed of two parts and, as previously shown, they are the coherent portion and the incoherent portion; the first is equivalent to a reduced free space component, the second portion is incoherent power with a much smaller magnitude and wider spectrum than the reduced free space component and has been shown to correspond to the variance of the received signal.

Substituting the two portions of the radiated angular power given by Equation (5.18) into the power coupling Equation (5.10), we get both the mean power coupled and the temporal co-variance function of the coupled signal, which are given by:-

Mean Power Coupled : $|\langle U \rangle|^2 =$

$$\frac{e^{-\sigma_\phi^2} \cdot \lambda^4}{4Z^2} \left[\int_{-\infty}^{+\infty} \int_{-\infty}^{+\infty} \Gamma_{Tx}(\xi, \sigma_1) \circledast \Gamma_{Rx}(\xi, \sigma_1) \cdot dS_1 \cdot d\sigma_1 \cdot \right.$$

$$\left. \cdot \int_{-\infty}^{+\infty} \int_{-\infty}^{+\infty} \Gamma_{Ty}(\eta, \sigma_2) \circledast \Gamma_{Ry}(\eta, \sigma_2) \cdot dS_2 \cdot d\sigma_2 \right] \qquad (5.19)$$

Co-Variance of the Coupled Signal : $COV_U[\tau] = \langle U^*(t) \cdot U(t+\tau) \rangle - |\langle U(t) \rangle|^2 =$

$$\frac{\sigma_\phi^2 \cdot e^{-\sigma_\phi^2} \cdot r_\phi(\tau) \cdot \lambda^4}{4Z^2} \left[\int_{-\infty}^{+\infty} \int_{-\infty}^{+\infty} \Gamma_{Tx}(\xi, \sigma_1) \cdot r_\phi(\xi) \circledast \Gamma_{Rx}(\xi, \sigma_1) \cdot dS_1 \cdot d\sigma_1 \cdot \right.$$

$$\left. \cdot \int_{-\infty}^{+\infty} \int_{-\infty}^{+\infty} \Gamma_{Ty}(\eta, \sigma_2) \cdot r_\phi(\eta) \circledast \Gamma_{Ry}(\eta, \sigma_2) \cdot dS_2 \cdot d\sigma_2 \right] \qquad (5.20)$$

Example

The example considered here is similar to that taken for the free space medium, namely, that of Gaussian amplitude aperture distributions as given by Equations (5.1) and (5.2). Furthermore, the phase autocorrelation function will be taken as Gaussian with spatial scale sizes ξ_0 and η_0 and a temporal scale size τ_0, i.e.:-

$$r_\phi(\xi, \eta, \tau) = r_\phi(\xi) \cdot r_\phi(\eta) \cdot r_\phi(\tau) = e^{-\xi^2/\xi_0^2} \cdot e^{-\eta^2/\eta_0^2} \cdot e^{-\tau^2/\tau_0^2} \tag{5.21}$$

Substituting for the aperture fields in Equation (5.19), it may be seen that the mean power coupled is simply the free space power coupled reduced by exp - σ_ϕ^2 and, hence, the mean power coupled is given by:-

$$|\langle U \rangle|^2 = e^{-\sigma_\phi^2} \cdot \left(\frac{\pi}{Z}\right)^2 \cdot \frac{w_{Tx} \cdot w_{Rx}}{\sqrt{\pi^2(w_{Tx}^2 + w_{Rx}^2)^2 + \lambda^2 L^2}} \cdot \frac{w_{Ty} \cdot w_{Ry}}{\sqrt{\pi^2(w_{Ty}^2 + w_{Ry}^2)^2 + \lambda^2 L^2}} \tag{5.22}$$

and for circularly symmetrical antennas, we get:-

$$|\langle U \rangle|^2 = e^{-\sigma_\phi^2} \cdot \left(\frac{\pi}{Z}\right)^2 \cdot \frac{w_T^2 \cdot w_R^2}{\pi^2(w_T^2 + w_R^2)^2 + \lambda^2 L^2} \tag{5.23}$$

It is worthwhile noting here that the mean coupled power is time independent. This is due to the assumption that the medium under consideration is a stationary one.

To obtain the co-variance function of the coupled signal, the phase autocorrelation function given by Equation (5.21) is substituted in Equation (5.20). Solving this equation it may be shown that:-

$$COV_U(\tau) = \langle U^*(t) \cdot U(t+\tau)\rangle - |\langle U\rangle|^2 = e^{-\sigma_\phi^2} \cdot \sigma_\phi^2 \cdot r_\phi(\tau) \cdot \left[\frac{\pi}{Z}\right]^2 \cdot$$

$$\cdot \frac{m_x \cdot w_{Rx}}{\sqrt{\pi^2(w_{Tx}^2 + w_{Rx}^2) \cdot (m_x^2 + w_{Rx}^2) + \lambda^2 L^2}} \cdot \frac{m_y \cdot w_{Ry}}{\sqrt{\pi^2(w_{Ty}^2 + w_{Ry}^2) \cdot (m_y^2 + w_{Ry}^2) + \lambda^2 L^2}} \qquad (5.24)$$

where: $m_x = \dfrac{w_{Tx}}{\sqrt{1 + \dfrac{2w_{Rx}^2}{\xi_0^2}}}$ and $m_y = \dfrac{w_{Ty}}{\sqrt{1 + \dfrac{2w_{Ty}^2}{\eta_0^2}}}$

It is worthwhile noting here that the frequency power spectrum of the coupled signal fluctuations is given by $F_U(\omega)$, where $F_U(\omega) \longleftrightarrow R_U(\tau)$ and $R_U(\tau)$ is the temporal autocorrelation function, and is given by:-

$$R_U(\tau) = \langle U^*(t) \cdot U(t+\tau)\rangle = COV_U(\tau) - |\langle U\rangle|^2$$

The variance of the coupled signal is thus given by $VAR\left[U\right]$, where:-

$$VAR\left[U\right] = COV_U(0) = \langle U^*(t) \cdot U(t)\rangle - |\langle U\rangle|^2$$

and hence for circularly symmetrical antennas, and from Equation (5.24) we have:-

$$VAR\left[U\right] = e^{-\sigma_\phi^2} \cdot \sigma_\phi^2 \cdot \left[\frac{\pi}{Z}\right]^2 \cdot \frac{m^2 \cdot w_R^2}{\pi^2(w_T^2 + w_R^2) \cdot (m^2 + w_R^2) + \lambda^2 L^2} \qquad (5.25)$$

where:- $m^2 = \dfrac{w_T^2}{\sqrt{\left(1 + \dfrac{2w_T^2}{\xi_0^2}\right)\left(1 + \dfrac{2w_T^2}{\eta_0^2}\right)}}$

It may be seen from Equation (5.24) that for a separable refractive index autocorrelation function and for $\sigma_\phi << 1$, the temporal characteristics of the coupled signal are identical to those of the medium. Hence, the time variations of this portion of the coupled signal are relatively very slow.

It may be seen that the effect of the random medium is to split the coupled power into two portions. The first portion is the coherent component of the power coupled and for a stationary medium, is a time independent quantity. The coherent power coupled is reduced from the free space value by exp - σ_ϕ^2, where σ_ϕ^2 is a function, among other things, of the strength of the medium turbulence. The other portion is the variance of the coupled signal and is a time dependent quantity. The temporal variation of the coupled power has been seen to be identical to the refractive index fluctuations. This is true for the situation when the refractive index autocorrelation function is a separable one as assumed in Equation (5.15). The variance of the coupled signal given in Equation (5.25) is a function of the system parameters, i.e. path length and both transmitter and receiver aperture dimensions. It is also a function of the medium parameters inherent in σ_ϕ^2 and the lateral scale sizes ξ_0 and η_0.

The total power coupled, which is the sum of the squared mean and the variance, is less than the free space value and, hence, the free space system gain is reduced, i.e. the efficiency drops. Furthermore, atmospheric induced noise is introduced in the power coupled. This is implied in the variance of the coupled signal and, hence, the system signal-to-noise ratio is degraded.

The next section discusses in physical terms the two consequences of coupling a distorted wavefront to a receiving aperture. The dependence of the efficiency or gain degradation and the noise power coupled on the

receiving aperture size and the relationship with the scale size of the distortions will be outlined.

5.3 Efficiency and Aperture Averaging Effects of Large Receiving Aperture Antennas

In this section, the gain degradation of large aperture receiving antennas will be related in physical terms to the scale sizes of the wave front distortions from an angular spectrum point of view. The aperture averaging property of large aperture antennas will also be discussed from the same point of view.

Both phenomena, aperture averaging and gain degradation, have been discussed individually by several authors. However, no attempt has been previously made to study both phenomena simultaneously and to incorporate the medium scale sizes and the transmitting aperture dimensions. It will be seen further on that, under certain turbulence conditions, adjusting the system parameters for higher efficiencies causes the aperture averaging effect to decrease and, hence, an increase in the noise level and vice versa. It will also be seen that turbulence conditions which cause a loss in efficiency, simultaneously enhance the signal-to-noise level of the system and vice versa.

5.3.1 Efficiency of Large Aperture Antennas

It has been seen in the previous section that if the propagation medium is turbulent, the coherence function is distorted which indicates that the amplitude and phase of the wave incident at the receiver plane vary with respect to time, together with a spatial variation along a plane normal to the direction of propagation. When these fluctuations increase in magnitude and their correlation distance decreases and is comparable in size to the receiving aperture dimensions, the power coupled from such a wave front to the aperture is no longer proportional

to the area of the receiving aperture, but rather to its square root. Hence the apparent loss in power or decrease in efficiency. The scale sizes of the wave front distortions are a function of the transmitting aperture size and the scale sizes of the medium irregularities. A receiving aperture will be considered to be large if the scale sizes of the wave front distortions are smaller than the dimensions of the aperture.

Destruction of lateral coherence is equivalent to a broadening of the angular spectrum of plane waves incident on the receiver plane. The width of the incoherent portion of the angular power spectrum is inversely proportional to the scale sizes of the wave front distortions.

Therefore, from an angular spectrum point of view, the gain degradation may be explained by considering the receiving antenna as a filter which responds to incident waves from a specified direction and the "band" of the filter decreases as the aperture size increases and, hence, the wider the angular power spectrum, the less the amount of power passing through the narrow band filter.

Experiments[18, 54] carried out using different size receiving apertures have shown that the difference in power levels is much smaller under turbulent conditions than under calm reception conditions. Experiments investigating the variation of the relative efficiencies of two different size apertures (an 0.3 metre dish and a 35.20 millimetre horn) will be described in Chapter 7.

It has been seen that the efficiency is a function of the lateral coherence function. D'Auria and Solimini[55] have shown that the efficiency decreases sharply as the coherence length decreases. Barzilai[56] predicts that introducing an amplitude taper results in a lower degradation of gain. This is expected since the effective

receiving area decreases with such a taper. D'Auria and Colavito[57] have shown that the shape of the lateral coherence function has an effect on the efficiency deterioration curves.

Although much work has been done to predict the loss of efficiency of a receiving aperture under turbulent conditions, the bulk of the work assumes an incident plane wave whose coherence has been deteriorated by the medium, and a coherence function is assumed for the incident wave at the receiver plane. Hence, the effect of the transmitter aperture size and its interaction with the medium is neglected. Furthermore, the relationship between the assumed coherence function and the properties of the random medium is often neglected. In this analysis, both the transmitter aperture size and the medium are taken into consideration when producing an expression for the efficiency.

The efficiency of a receiving aperture has been described by some authors. For example, D'Auria and Colavito[57] define an efficiency which takes into account the fact that the average power received from a partially coherent incident wave is not the same as the power received from an incident plane wave. An alternative, and practically realizable, method for defining and determining the loss in plane wave gain, is described by Hall and Misme[54] who use two antennas simultaneously and the gain degradation is defined as the difference between the outputs from the two receiving antennas subtracted from the difference of their plane wave gains.

System Efficiency

In this analysis, the efficiency "ε" will be defined as the total power coupled between transmitter and receiver with an intervening random medium relative to that coupled under free space conditions, i.e.:-

$$\varepsilon = \frac{\langle |U|^2 \rangle}{|U|^2_{\text{free space}}} \cdot 100 = \frac{|\langle U \rangle|^2 + \text{VAR}[U]}{|U|^2_{\text{free space}}} \cdot 100$$

For circularly symmetrical apertures and for the example given in the previous section and substituting Equations (5.14), (5.23) and (5.25), we get:-

$$\varepsilon = e^{-\sigma_\phi^2} \left[1 + \frac{\sigma_\phi^2}{\sqrt{1 + \frac{2w_T^2}{\xi_0^2}} \sqrt{1 + \frac{2w_T^2}{\eta_0^2}}} \cdot \frac{\pi^2 (w_T^2 + w_R^2)^2 + \lambda^2 L^2}{\pi^2 (w_T^2 + w_R^2)(m^2 + w_R^2) + \lambda^2 L^2} \right] \cdot 100 \qquad (5.26)$$

with m^2 defined as in Equation (5.25).

It may be seen that the efficiency as described above is a function of both system and medium parameters. The efficiency as defined is that of the complete propagation circuit, i.e. transmitting antenna, medium and receiving antenna. A system efficiency not limited to that of the receiving aperture only is possibly more realistic and more useful to system designers.

5.3.2 Aperture Averaging Effect of Large Receiving Apertures

A wave propagating through a random medium is no longer a uniform plane wave and the wave front incident on the receiver aperture plane is a distorted one. When the crinkled wave front impinges on the receiving aperture, the aperture contains field components of various phases and possibly various amplitudes. The field components may add either constructively or destructively. This random addition causes a fluctuation in the signal at the feed or focus of the antenna. However, as the number of the out-of-phase components collimated in the aperture

increases by increasing the aperture size, and due to their random nature, the constructive and destructive additions tend to cancel out. Hence the signal level fluctuations are effectively smoothed or averaged out. As the medium scale sizes become smaller, the scale size of the wave front distortions becomes smaller and a larger number of out-of-phase field components are present within the aperture. Hence the larger aperture averages out the distortions more effectively.

The same conclusions may be drawn by treating the problem from an angular spectrum point of view. Since the angular spread of the incoherent or noise portion of the incident power is broader than the coherent or the free space component, therefore, a large aperture or narrow beam antenna "filters" out the "noisy" part of the signal. As the medium scale sizes become smaller, the angular spread of the incoherent portion becomes wider and hence less noise energy passes through the narrow-band receiver.

An aperture averaging factor has been defined by Tatarskii[58], which compares the fluctuations in the signal received by an aperture of a certain dimension, under turbulent conditions, to those received by a point aperture over which the incident field is entirely correlated. The expression derived under the terms of the above definition is shown by Tatarskii to be a function of the radius of the receiving aperture and the coherence function in the receiver plane. The aperture averaging defined by Tatarskii is not a function of the transmitter aperture size and is not an explicit function of the medium parameters, scale size and strength of turbulence.

In this analysis, the averaging effect of the receiving aperture will be combined with that of the transmitting aperture size to determine a total system averaging factor. This will be defined in terms of a signal-to-noise ratio given as a function of the aperture

sizes and the medium parameters.

System Signal-to-Noise Ratio

In this analysis, the system signal-to-noise ratio "S/N" will be defined as the ratio of the coherent or non-fluctuating portion of the power coupled to the incoherent or noise power coupled, i.e. in decibels this ratio is given by:-

$$S/N = \text{Log} \frac{|\langle U \rangle|^2}{\text{VAR}\left[U\right]}$$

For circularly symmetrical apertures and for the example given in the previous section, and substituting Equations (5.23) and (5.25), we get:-

$$S/N = \text{Log} \left[\frac{\sqrt{\left(1 + \frac{2w_T^2}{\xi_0^2}\right)\left(1 + \frac{2w_T^2}{\eta_0^2}\right)}}{\sigma_\phi^2} \cdot \frac{\pi^2(w_T^2 + w_R^2) \cdot (m^2 + w_R^2) + \lambda^2 L^2}{\pi^2 (w_T^2 + w_R^2)^2 + \lambda^2 L^2} \right] \quad (5.27)$$

with m^2 defined as in Equation (5.25).

As for the definition of efficiency, the signal-to-noise ratio is that of the complete propagation circuit, i.e. transmitting antenna, medium and receiving antenna. This definition of the signal-to-noise ratio and its compatibility with the definition of the efficiency possibly makes it a useful quantity for system designers.

In the following section, the effects of the system and medium parameters on the efficiency and signal-to-noise ratio as defined in

Equations (5.26) and (5.27) respectively, will be investigated.

5.4 Effect of System and Medium Parameters on the Efficiency and Signal-to-Noise Ratio

Due to the dependence of the efficiency and the signal-to-noise ratio on a large number of system and medium parameters as indicated by Equations (5.26) and (5.27) respectively, the investigation will be limited to certain fixed conditions, namely, the degree of turbulence will be constant throughout, with a value of the variance of the refractive index fluctuations taken to be 1×10^{-12} n^2-units. The longitudinal scale size ζ_0 will also be constant at 10 metres. The propagation distance will be taken as 12 kilometres throughout the investigations. The above values imply that the variance of the phase fluctuations across the phase screen is 0.136 radians^2 at a wave length of 8 millimetres. Furthermore, the lateral scale sizes ξ_0 and η_0 will be taken to be equal in all cases. Normalization will not be attempted due to the varying parameters involved in defining the efficiency and the signal-to-noise ratio. Hence their physical significance may be lost in the process.

The investigation then will be conducted for varying scale size ξ_0, and transmitter and receiver aperture dimensions w_T and w_R, bearing in mind that w_T and w_R are the "1/e" widths of the transmitting and receiving antennas.

5.4.1 Efficiency and Signal-to-Noise Ratio as a Function of w_R

Figs. 5.3a and 5.3b show the efficiency and signal-to-noise ratio versus receiving aperture size w_R for a transmitter aperture size w_T = 0.3 metres for varying scale size ξ_0. It may be seen that the efficiency and signal-to-noise ratio are independent of w_T. However, the

efficiency increases as ξ_0 increases and the signal-to-noise ratio is inversely proportional to ξ_0. This behaviour may be understood by considering Fig. 4.1a where it is seen that the spread of the incoherent power relative to the coherent power is insignificant for small transmitting apertures for all scale sizes. Therefore, increasing the receiving aperture size and hence narrowing the receiving beam width would hardly make any difference.

Figs. 5.4a and 5.4b show the same situation with w_T = 10 metres. Here it is seen that the efficiency remains constant for the small scale sizes ($\xi_0 \simeq 0.1$ metres), whereas it begins to decrease quite rapidly as w_R is increased for scale sizes of the order of w_T. As the scale sizes increase, the efficiency begins to taper off less rapidly. The above situation may be explained again by considering Figs. 4.1a and 4.1b. It is seen that although the relative spread of the incoherent power is greater for smaller scale sizes, the magnitude of the incoherent portion becomes much smaller as the scale size decreases for large w_T. As the scale size becomes much larger than w_T, the relative spread is insignificant. However, the magnitude of the scattered power remains quite large.

Therefore, increasing w_T and narrowing the beam width does not make any difference for the small scale sizes since the magnitude of the incoherent component is very small anyway, whereas for the large scale sizes, the relative spread of the incoherent component is insignificant and, hence, increasing w_T does not make much difference. In between the two extremes the efficiency drops as w_T is increased.

The behaviour of the signal-to-noise ratio in Fig. 5.4b may be understood by following the same reasoning as above.

An interesting feature is the saturation of the signal-to-noise ratio as the receiver aperture size is increased for small scale sizes.

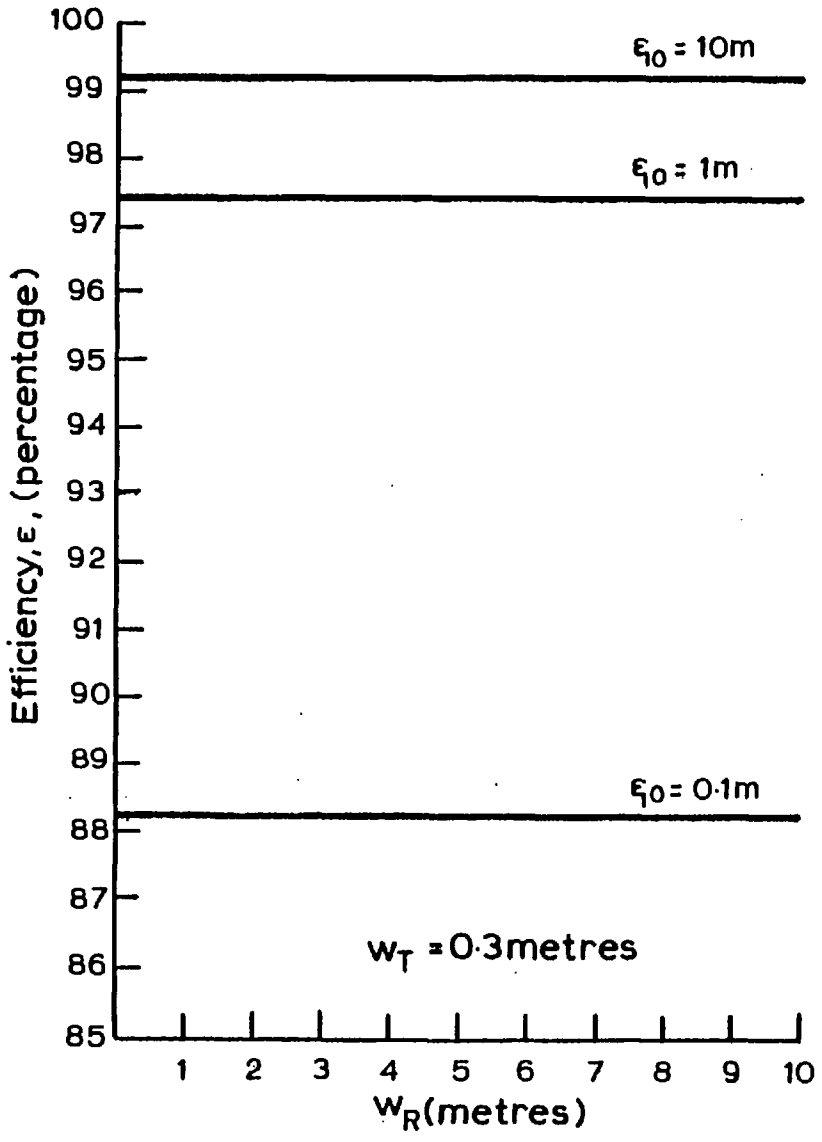

Fig. 5·3 (a)

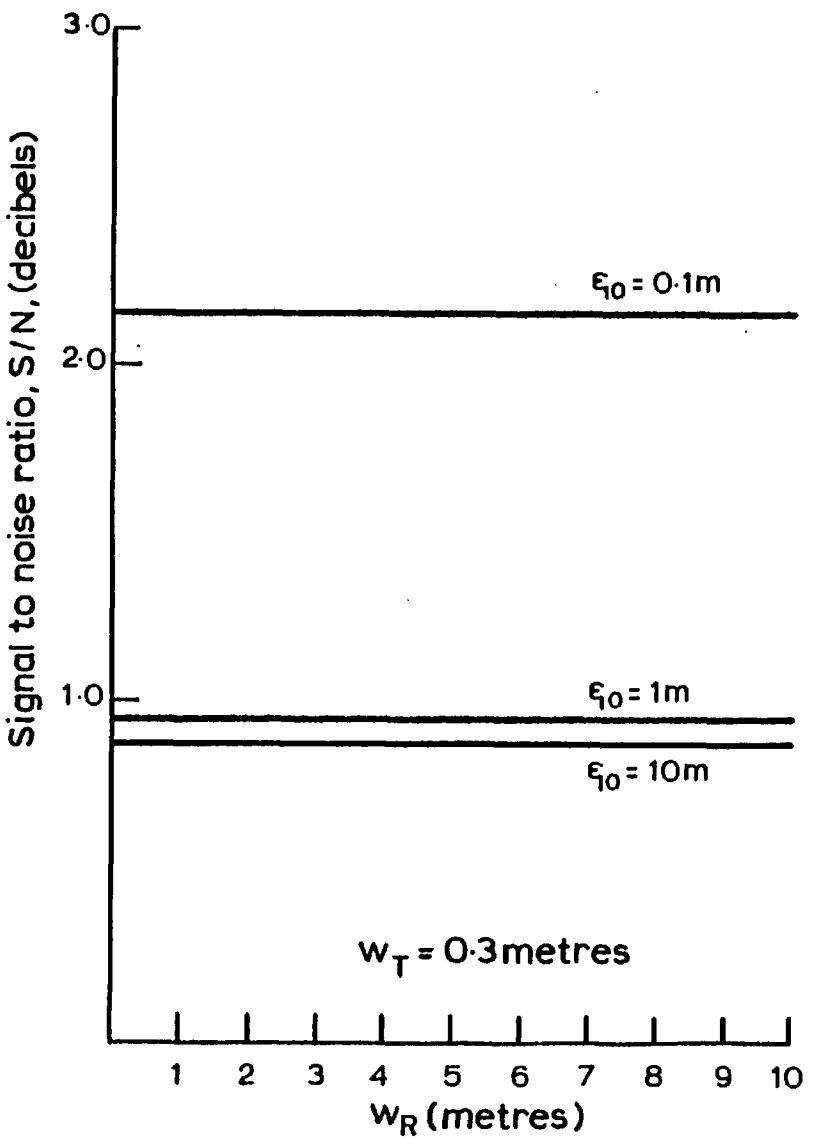

Fig. 5·3 (b)

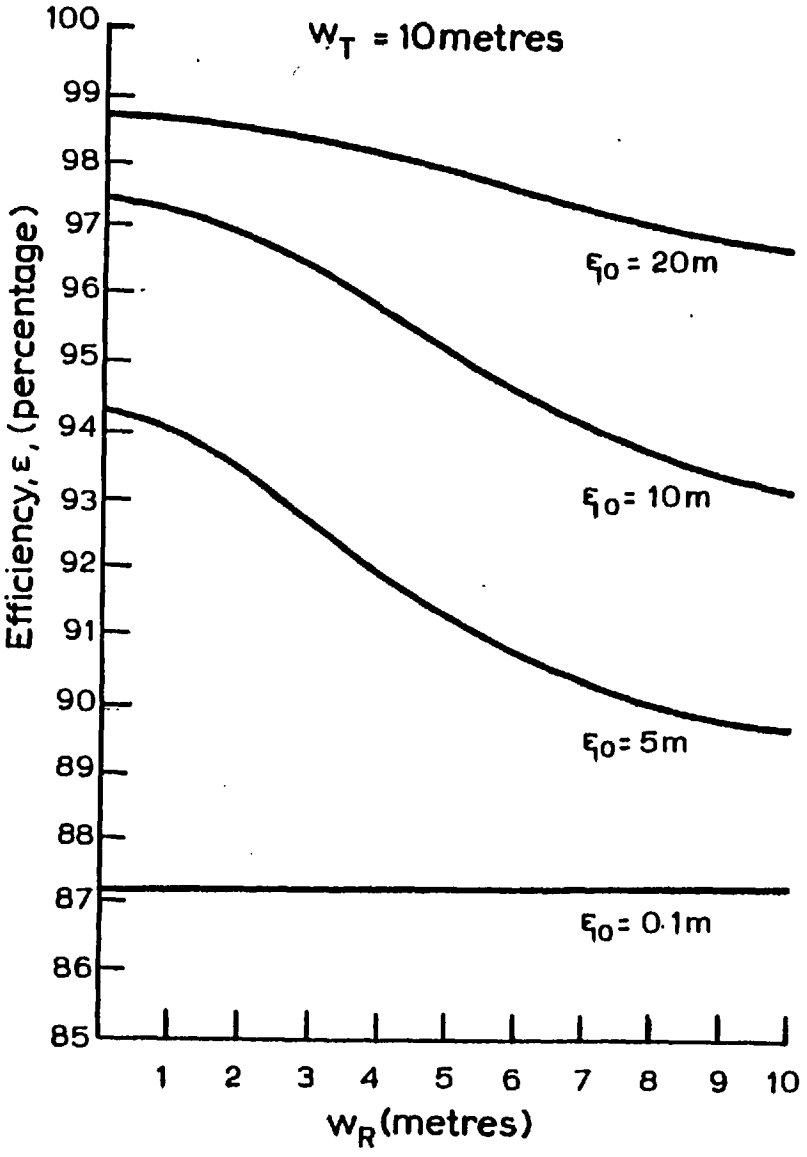

Fig 5·4 (a)

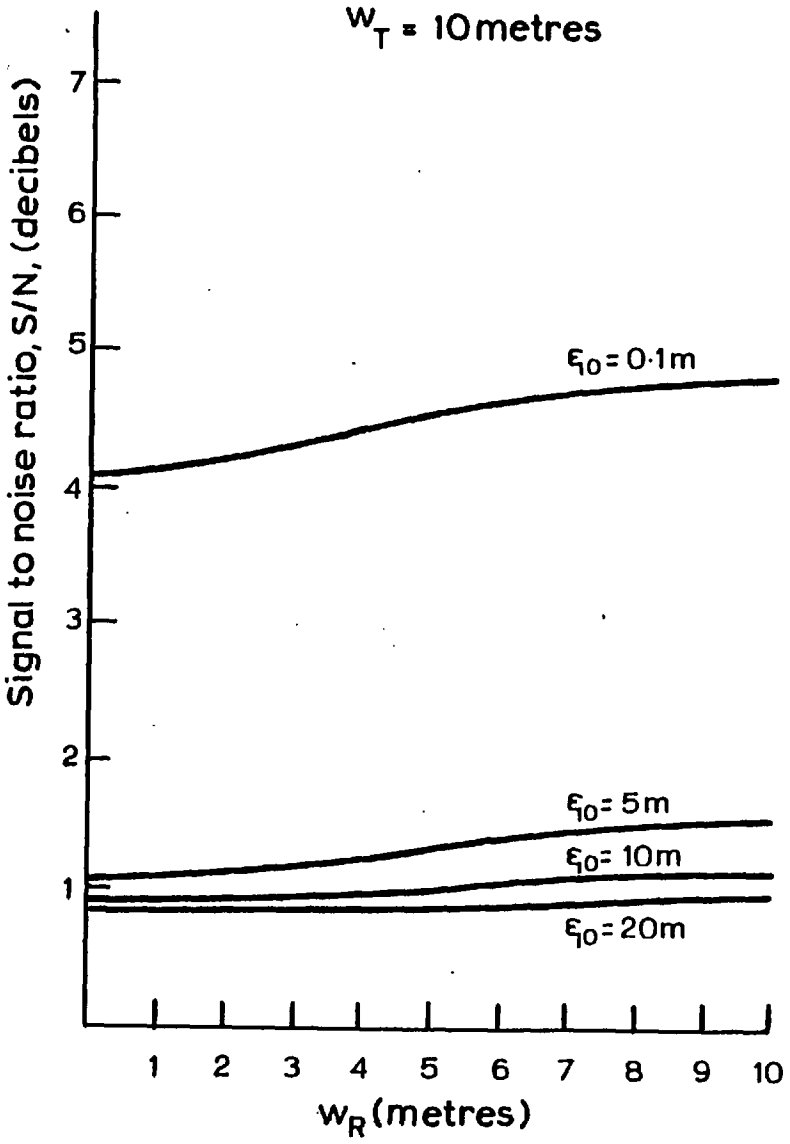

Fig. 5·4 (b)

This saturation dimension has also been discovered by Fried[59] and is obtained in terms of the phase and log amplitude structure functions. Increasing w_R beyond the saturation dimension does not significantly increase the signal-to-noise ratio. No attempt will be made here to obtain an analytical expression for the saturation dimension. However, it may be seen from Fig. 5.4b that for a certain w_T, it is a function of the lateral scale size ξ_0.

5.4.2 Efficiency and Signal-to-Noise Ratio as a Function of w_T

Figs. 5.5a and 5.5b show the efficiency and signal-to-noise ratio versus transmitting aperture size w_T for a receiver aperture size w_R = 0.01 metres for varying scale size ξ_0. It is interesting to note that the efficiency drops down to a minimum value and then rises again. The scale size ξ_0 is seen to be a critical factor in determining the rate of variation of the efficiency. The signal-to-noise ratio follows a similar behaviour. However, it is inversely proportional to the scale size ξ_0.

The above-mentioned behaviour is rather difficult and tedious to explain. However, returning to Figs. 4.1a and 4.1b and noting the dependence of the spread and magnitude of the incoherent component on w_T and ξ_0, the behaviour of the efficiency and signal-to-noise ratio of a small receiving aperture may be understood. The example given for w_R = 0.01 metres is chosen because of the broadness of the beam width at such a dimension. Hence the receiver's sensitivity to the incoherent component and thus the above results are obtained.

Reception by a larger aperture, makes the receiver insensitive to variations in the incoherent component of the incident power. This may be seen in Figs. 5.6a and 5.6b where the response observed by a

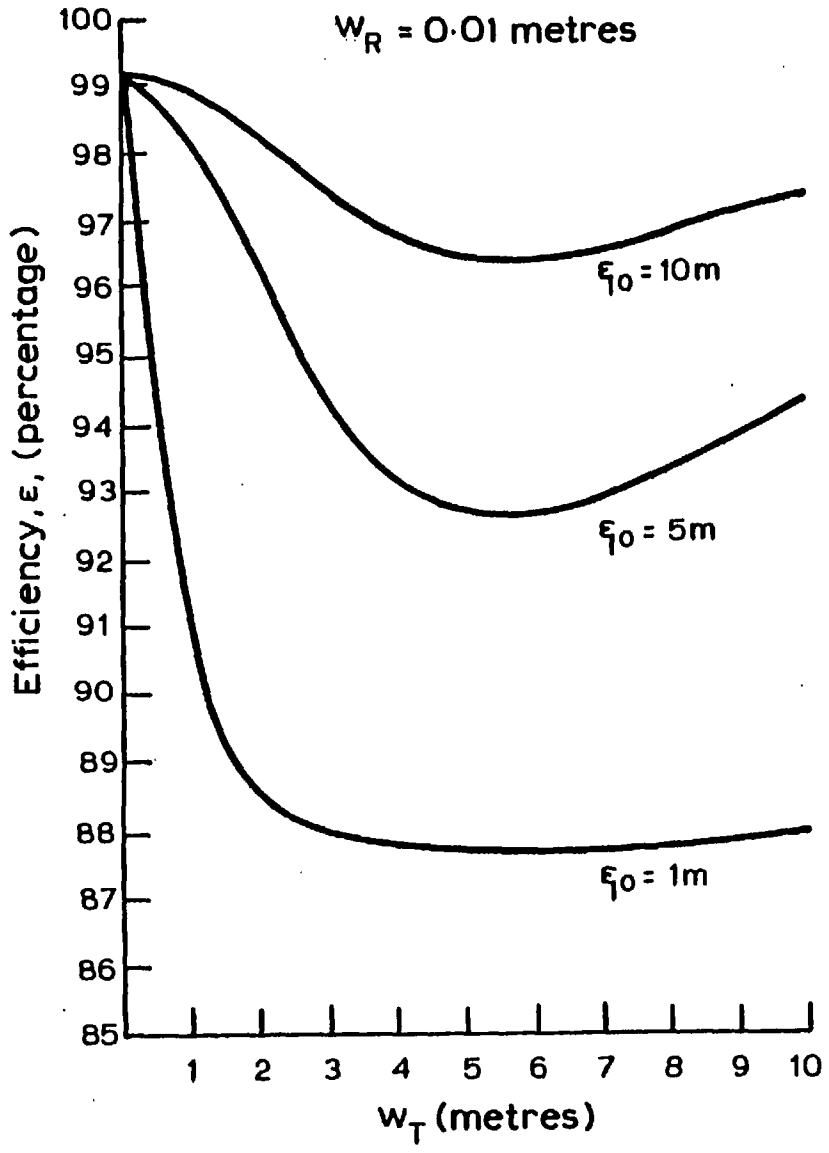

Fig. 5·5 (a)

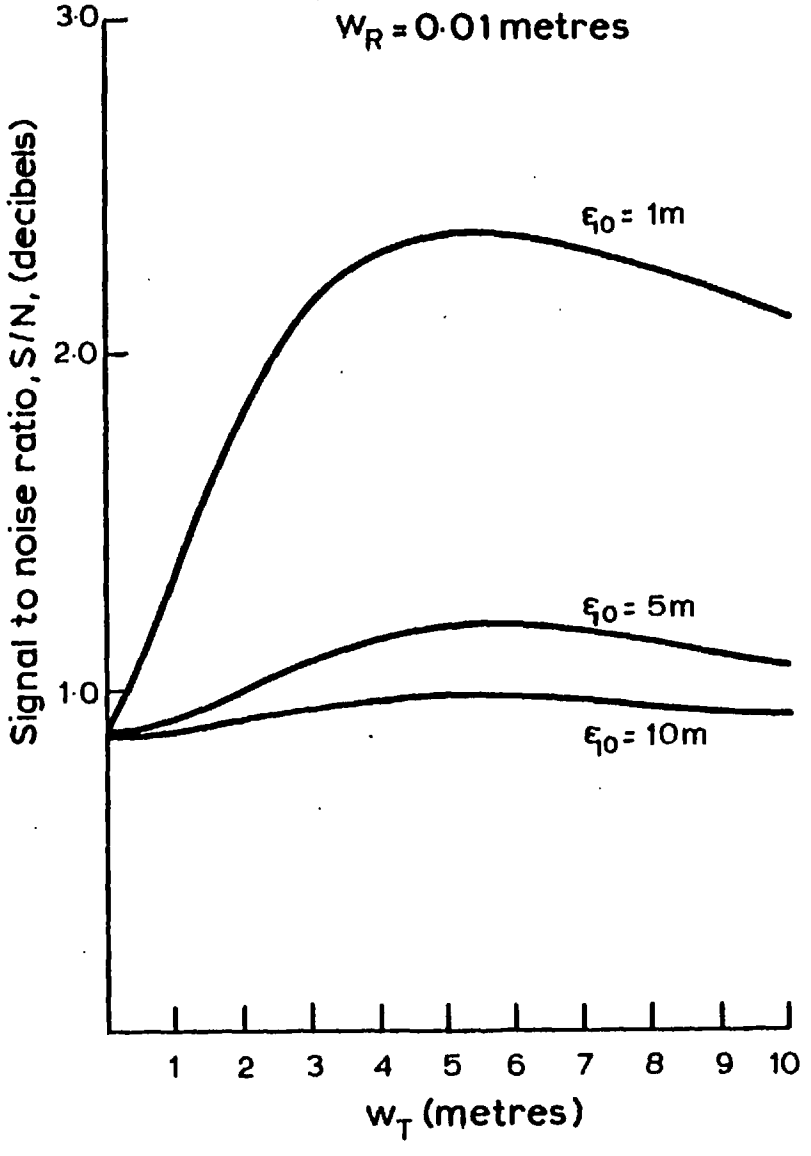

Fig. 5·5 (b)

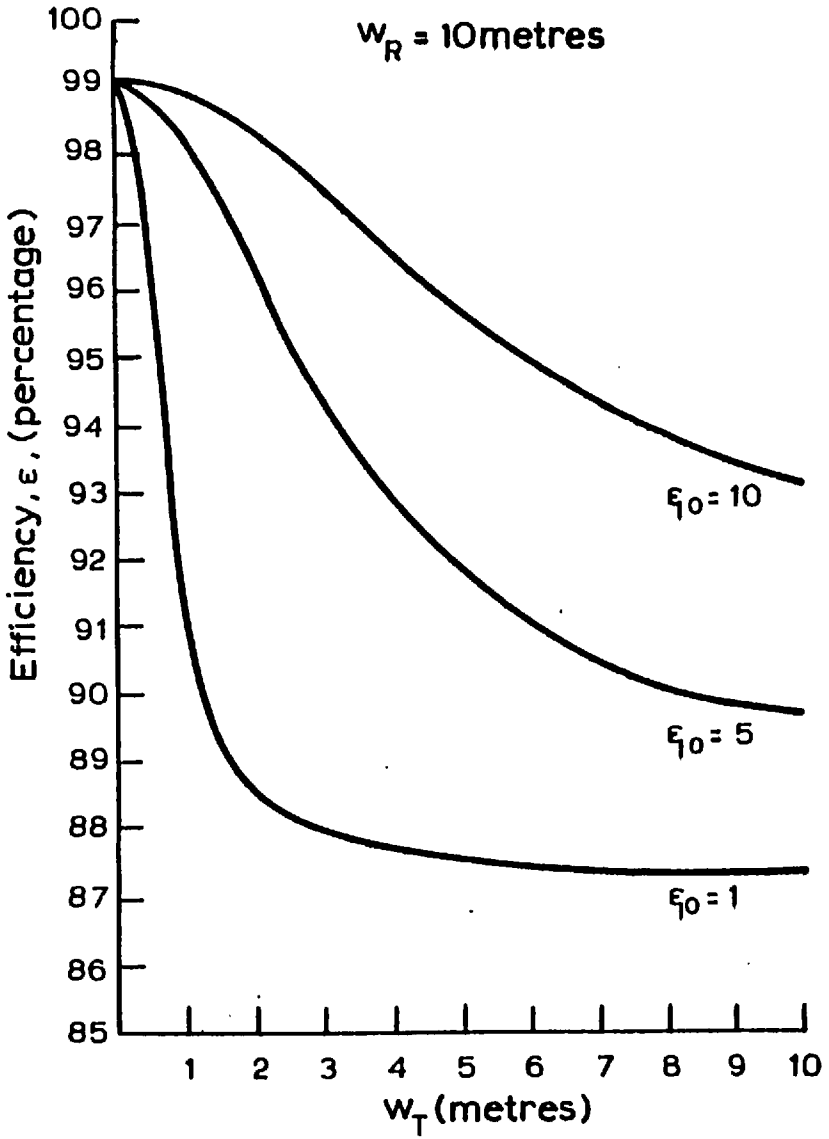

Fig. 5·6 (a)

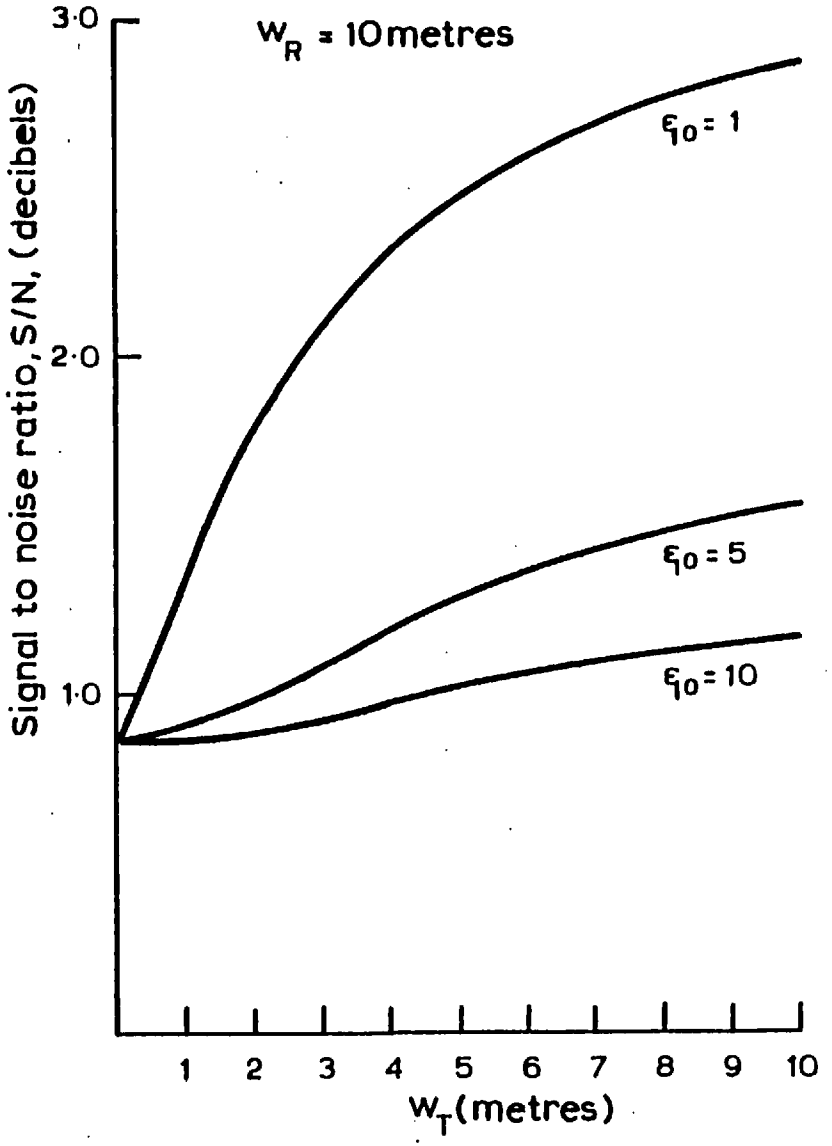

Fig. 5·6 (b)

smaller receiving aperture is now "filtered out".

5.4.3 Efficiency and Signal-to-Noise Ratio as a Function of ξ_0

It has been shown that the efficiency and signal-to-noise ratio are a function of the scale size ξ_0, the efficiency being directly proportional to the scale size ξ_0, whereas the signal-to-noise ratio is inversely proportional to it.

Figs. 5.7a and 5.7b show this dependence for various pairs of apertures. Fig. 5.7a shows the variation for two pairs of apertures. In both cases, w_T is large and is taken to be 5 metres. w_R is taken for two extreme cases - a small aperture size w_R = 0.1 metres and a large aperture size w_R = 5 metres. It may be seen that the variation of both the efficiency and the signal-to-noise ratio is basically independent of w_R.

Fig. 5.7b shows the variation for a small transmitting aperture size w_T = 0.1 metres with w_R taken in both extremes. Again, it is seen that the efficiency and the signal-to-noise ratio are independent of w_R.

Therefore, from Figs. 5.7a and 5.7b it may be seen that the system efficiency and signal-to-noise ratio are much more sensitive to variations in the size of the transmitting aperture relative to the medium scale size ξ_0 than similar variations in the size of the receiving aperture.

5.5 Conclusions

In this chapter, Brown's[52] coupling formula, which allows for the calculation of the electric field coupled between finite transmitting and receiving apertures, based on the knowledge of their angular plane wave spectra, has been extended. The extension provides a power coupling

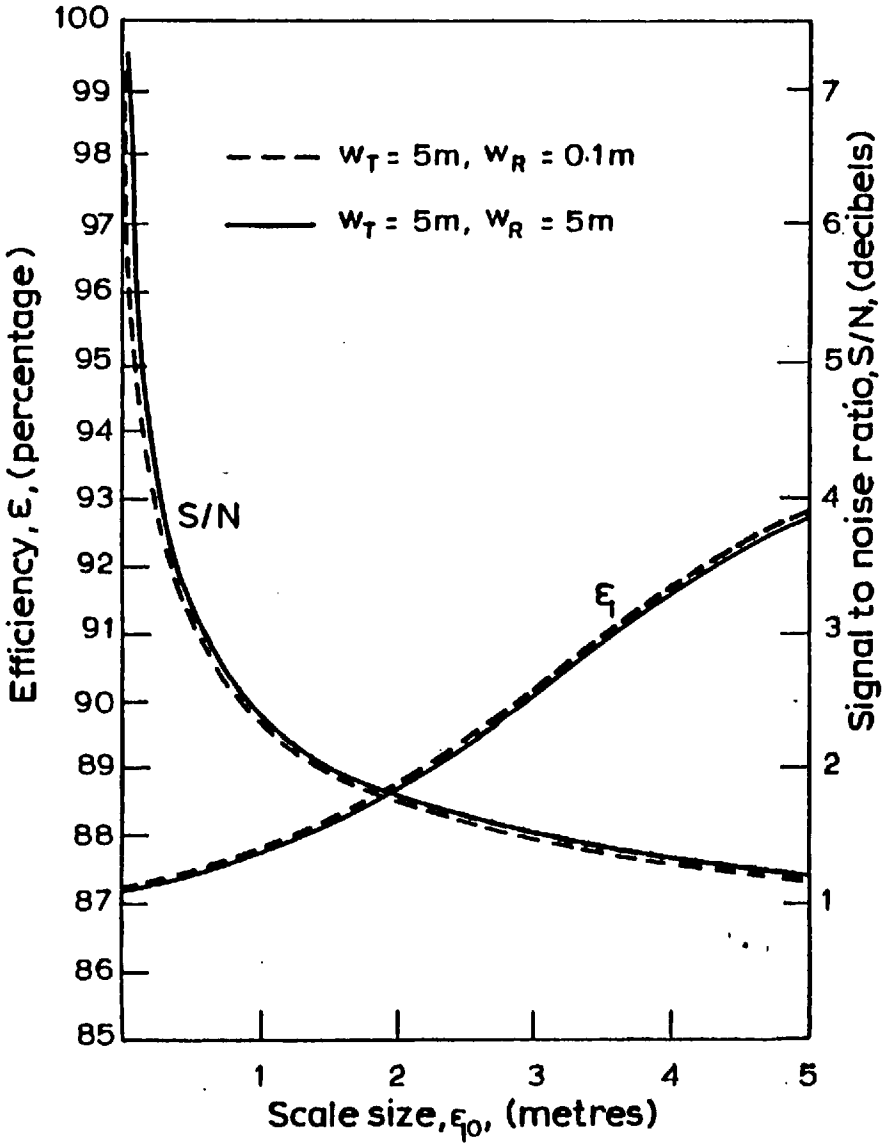

Fig. 5·7 (a)

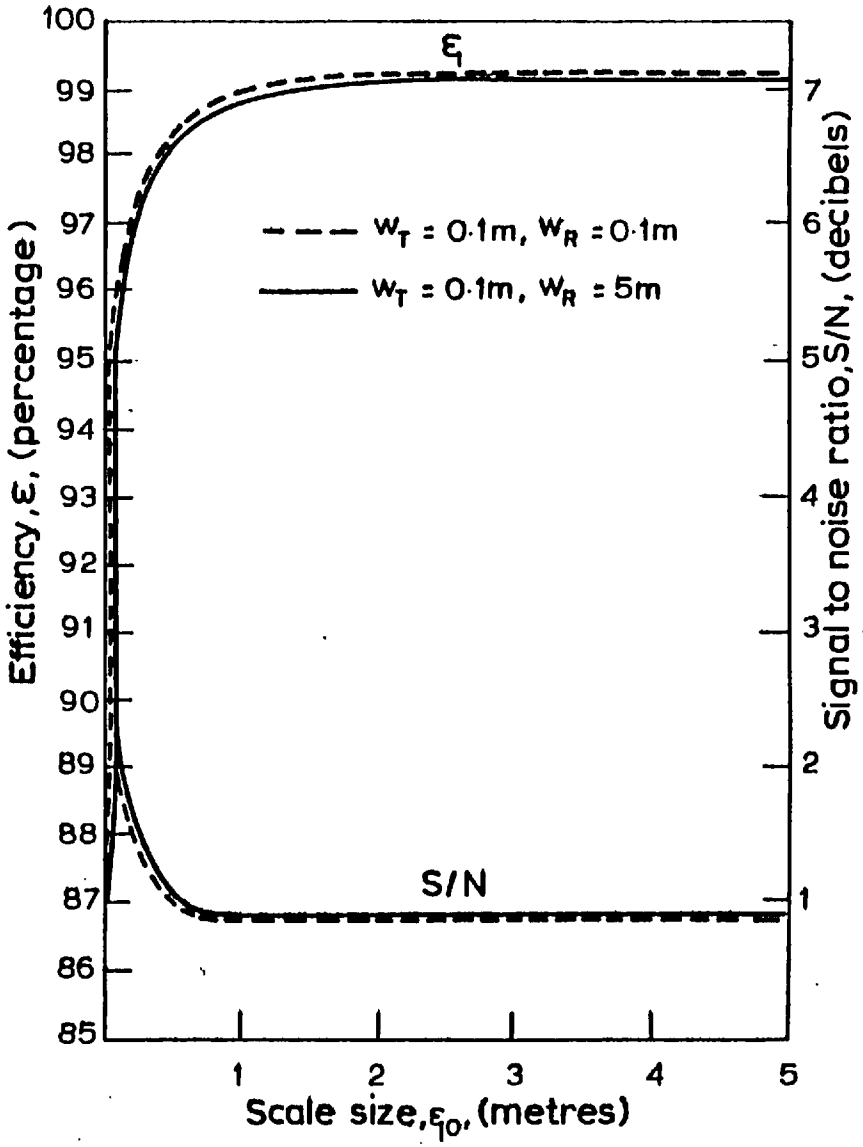

Fig. 5·7 (b)

formula in a time varying random medium. The result obtained is based on the coherence function and is applicable in the near and far fields of the apertures.

The restrictions imposed in the analysis are that the variance of the phase fluctuations contributed by the random medium is small, i.e. $\sigma_\phi^2 << 1$. This has previously been shown to be a very reasonable assumption for microwaves propagating in a turbulent atmosphere. Furthermore, the angular spread of the field radiated by the apertures is assumed to be narrow, i.e. confined to approximately ± 15 degrees. Again, this is a very reasonable assumption for microwave antennas.

As a result of the randomness of the medium, the power coupled has been found to be split into two portions. A mean value, which for a stationary random medium, is time independent. The second portion is the co-variance of the coupled signal which is time dependent. The time dependence has been found, for $\sigma_\phi^2 << 1$ and for a separable phase autocorrelation function, to be identical to the temporal dependence of the medium fluctuations. Hence it is a relatively slowly varying function of time.

A system efficiency and signal-to-noise ratio have been defined. These take into account the transmitting and receiving aperture dimensions in both lateral directions and the path length. The medium parameters are also included in the definition. Hence the efficiency of power coupling and the signal-to-noise ratio may be calculated for a variety of transmitting and receiving antenna beam shapes, either symmetrical or fan shaped beams, in a random medium with varying lateral and longitudinal scale sizes. The example considered was for circularly symmetrical Gaussian illuminated apertures and a random medium with a Gaussian autocorrelation function for the refractive index fluctuations. The lateral scale sizes were assumed to be identical.

The efficiency and signal-to-noise ratio have been found to be two conflicting phenomena, in the sense that a variation of some medium parameters which cause a drop in the efficiency tends to enhance the signal-to-noise ratio and vice versa. Similarly, the system parameters, w_T and w_R, which may be adjusted to enhance the signal-to-noise ratio under certain medium conditions are likely to cause a drop in the efficiency and vice versa.

Therefore, there is a certain trade-off for system designers in attempting to optimize a propagation circuit for maximum reception and minimum noise, the design being adjusted to cater for the most critical of the phenomena or adjusted for an optimum value of transmitting and receiving aperture sizes under certain medium conditions.

CHAPTER 6

DESCRIPTION OF AN EXPERIMENTAL 38 GHz RADIO LINK

In this chapter, an experimental 38 GHz continuous wave, vertically polarized radio link will be described. The link under consideration was installed to obtain practical estimates of the effects of an urban environment on a propagating wave at this frequency. The effects to be investigated were the spatial and temporal fluctuations of both the amplitude and phase of the wavefront incident at the receiver plane. This investigation necessitated the installation of an interferometer type receiver.

The contents of this chapter are divided into four main sections. The first is concerned with the propagation path. The second is a description of the C.W. transmitter. The third section deals with the description of the interferometer receiver system; the design and installation are discussed. The fourth section is a description of the meteorological sensors used to monitor the relevant weather parameters.

It must be noted here that the radio link was planned and the main parts of it were designed prior to the author's joining the project. Therefore, although a description of the system is undertaken, the author's contribution was mainly in the joint installation and calibration of the transmitter and receiver. However, the partial design and manufacture of a second receiver channel and the design and the implementation of a phase difference detector was undertaken by the author.

6.1 Description of the Propagation Path

The experimental link was 11.6 kilometres long over South London. The transmitter was placed on the BBC transmitter tower at

Crystal Palace at the 90 metre level. The receiver was situated in a hut on the roof of the Department of Electrical Engineering, Imperial College in South Kensington, London.

Fig. 6.1 shows a plan of the propagation path. It may be noted that the path crosses over the River Thames and over two parks. The rest of the path is over urban areas. Tall buildings did not exist in the vicinity of the line-of-sight axis. Fig. 6.2 shows a profile of the propagation path. A photograph of the transmitting tower as seen from the receiver site is shown in Fig. 6.3.

Interference from ground reflections, which give rise to multipath effects, may be considered to be very small. This is due to the confinement of the radiated energy within a narrow beam. The main source of interference comes from rays reflected from the first Fresnel ellipse as shown in the figure below. This ellipse results from the intersection of the first Fresnel ellipsoid with the ground.

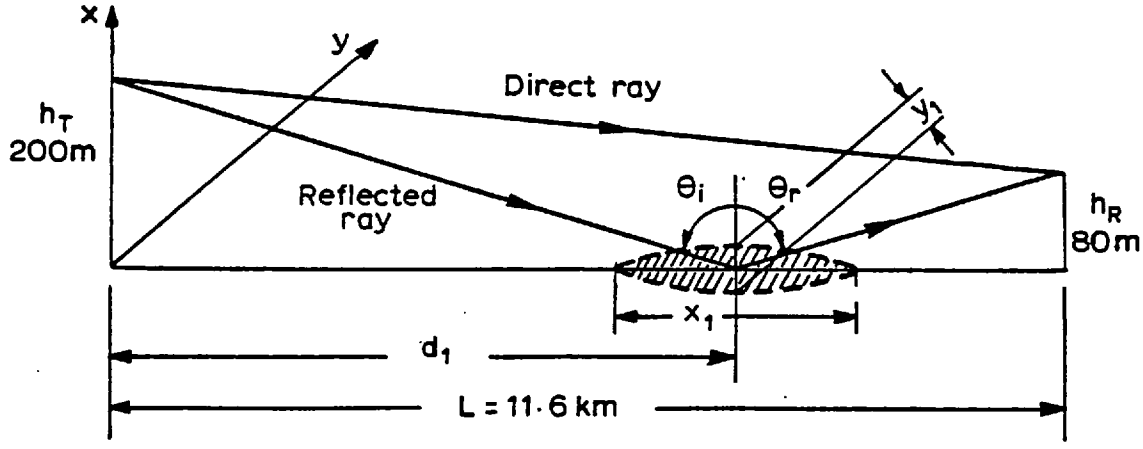

From the link geometry, and assuming that h_T and h_R are << L, therefore, it may be shown[23] that the centre of the ellipse lies at a distance d_1 from the transmitter where:-

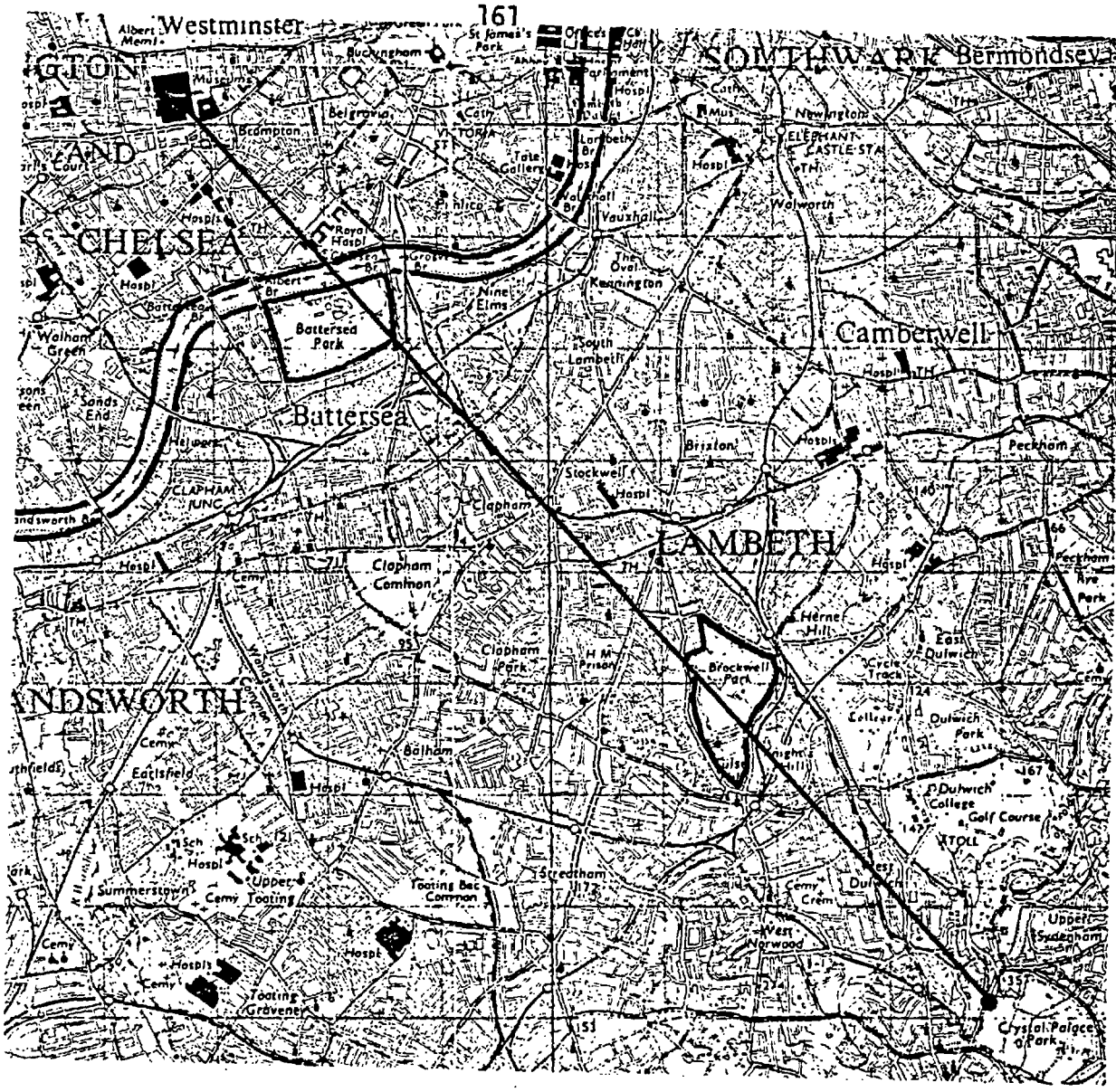

Fig. 6.1

Map of propagation path

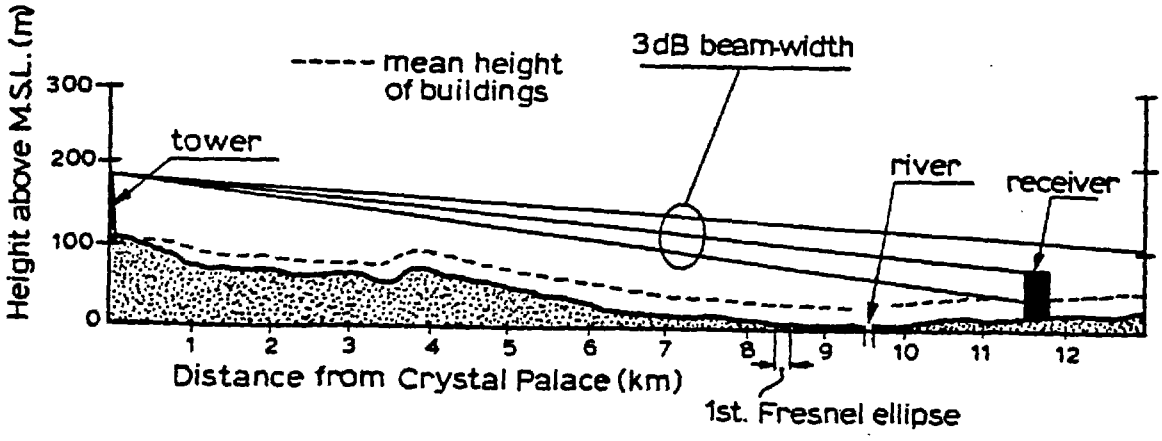

Fig. 6·2

Vertical profile of propagation path

Fig.6.3: Transmitter tower as observed from receiver site

$$d_1 \simeq \frac{L}{2} \frac{1 + \frac{2h_T\,(h_T + h_R)}{\lambda \cdot L}}{1 + \frac{(h_T + h_R)^2}{\lambda \cdot L}} \qquad (6.1)$$

For λ = 8 millimetres, d_1 = 8.28 kilometres. Hence from the path geometry, $\theta_i = \theta_r$ = 88.6 degrees.

The length of the major axis x_1 is given by:-

$$x_1 \simeq \frac{L \cdot \sqrt{1 + \frac{2 \cdot h_T \cdot h_R}{\lambda \cdot L}}}{1 + \frac{(h_T + h_R)^2}{\lambda \cdot L}} \simeq 356 \text{ metres} \qquad (6.2)$$

The length of the minor axis y_1 is given by:-

$$y_1 \simeq \sqrt{\lambda L} \sqrt{\frac{1 + \frac{2h_T \cdot h_R}{\lambda \cdot L}}{1 + \frac{(h_T + h_R)^2}{\lambda \cdot L}}} \simeq 6 \text{ metres} \qquad (6.3)$$

Therefore the area of the first Fresnel ellipse may be shown to be approximately equal to 2403 m^2.

It may be seen from the map of the propagation path that the ellipse lies over an urban area and the reflected rays are thus randomly scattered and, hence, would not cause multipath problems.

6.2 The Transmitter

The transmitter circuitry was housed in an insulated weather-proof box, which was connected to a 1 metre cassagrain antenna. The antenna was mounted on a panning frame mounted on the 90 metre level of

Fig. 6.4a: T t

Fig. 6.4b: Transmitter fixed at 90 meter level

the tower as shown in Figs. 6.4a and 6.4b.

The oscillator used was a Plessey GD044 Gunn diode, which provided an output power of 10 milliwatts. The frequency and power output of the cavity oscillator are a function of the supply voltage and the cavity size, which is varied by means of a micrometre type plunger. Therefore, to stabilize the frequency and hence the power output, the negative d.c. supply voltage was regulated. To overcome variations due to temperature changes, the temperature within the box was kept constant by means of a variable speed cooling fan, controlled by a temperature sensing circuit. The temperature was thus kept constant to within $1^{o}C$ r.m.s. at $40^{o}C$. To ensure further stability, the oscillator cavity was manufactured from Invar which is an alloy with a very low temperature coefficient of linear expansion.

A block diagram of the transmitter is given in Fig. 6.5. A detailed description of the circuitry used may be found in a co-worker's report[60].

Figs. 6.6 and 6.7 show the E and H plane radiation patterns of the transmitter as supplied by the manufacturer (C and S Antennas Ltd.). The quoted gain of the antenna was between 50 and 51 decibels at 38 GHz. This was reduced by 1.5 ± 0.5 decibels due to the radome.

The antenna was provided with a telescopic sighting attachment. This was used together with the aid of portable radios to align the antenna for maximum signal at the receiver site.

6.3 The Interferometer Receiver System

The simplest method to obtain the objectives of the experimental investigation was to have a dual channel receiver system, with variable spacing. It was found later on that such a set-up was also well suited for the investigation of aperture size effects on the coupled signal.

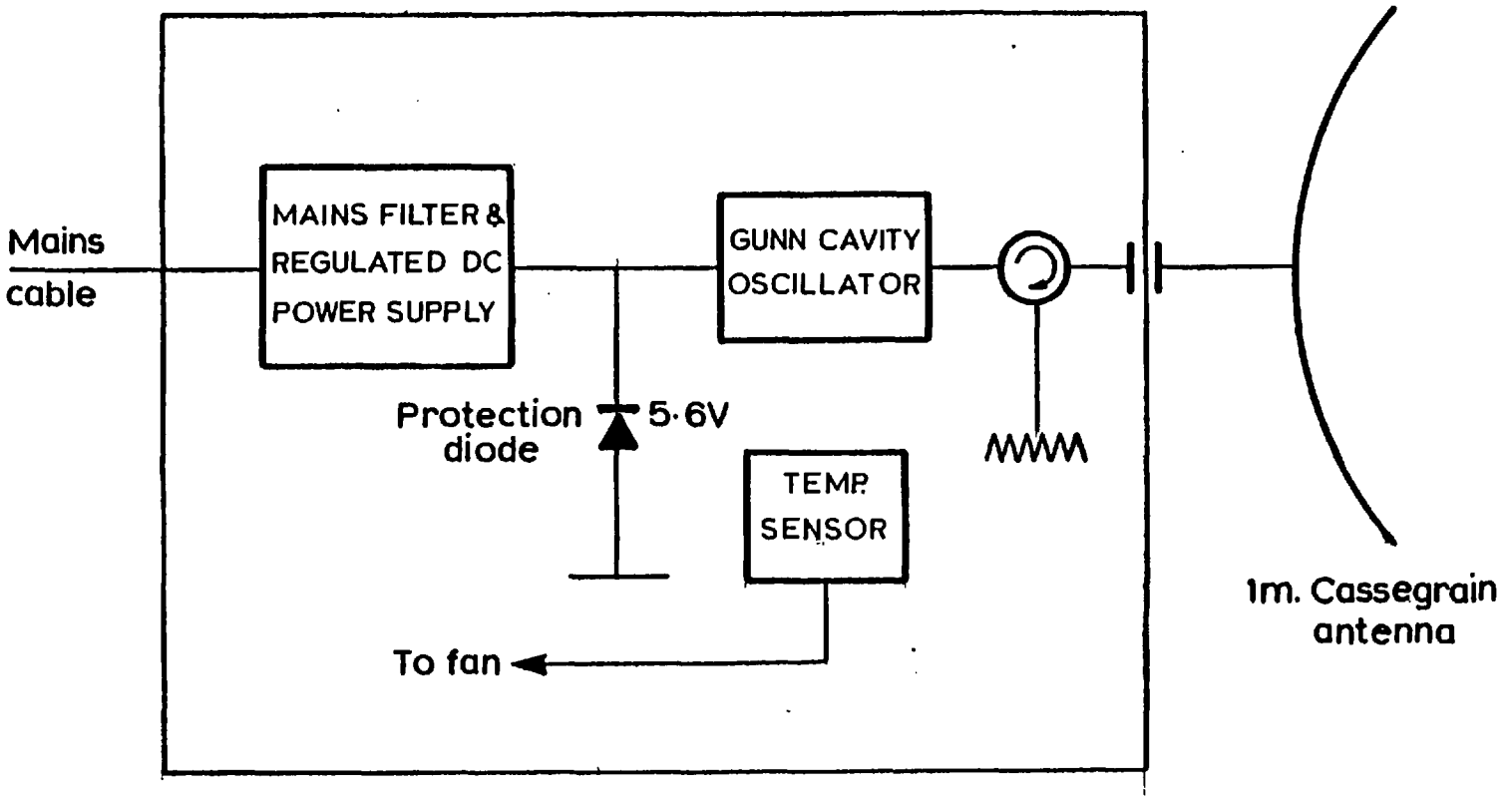

Fig. 6·5 Transmitter block diagram

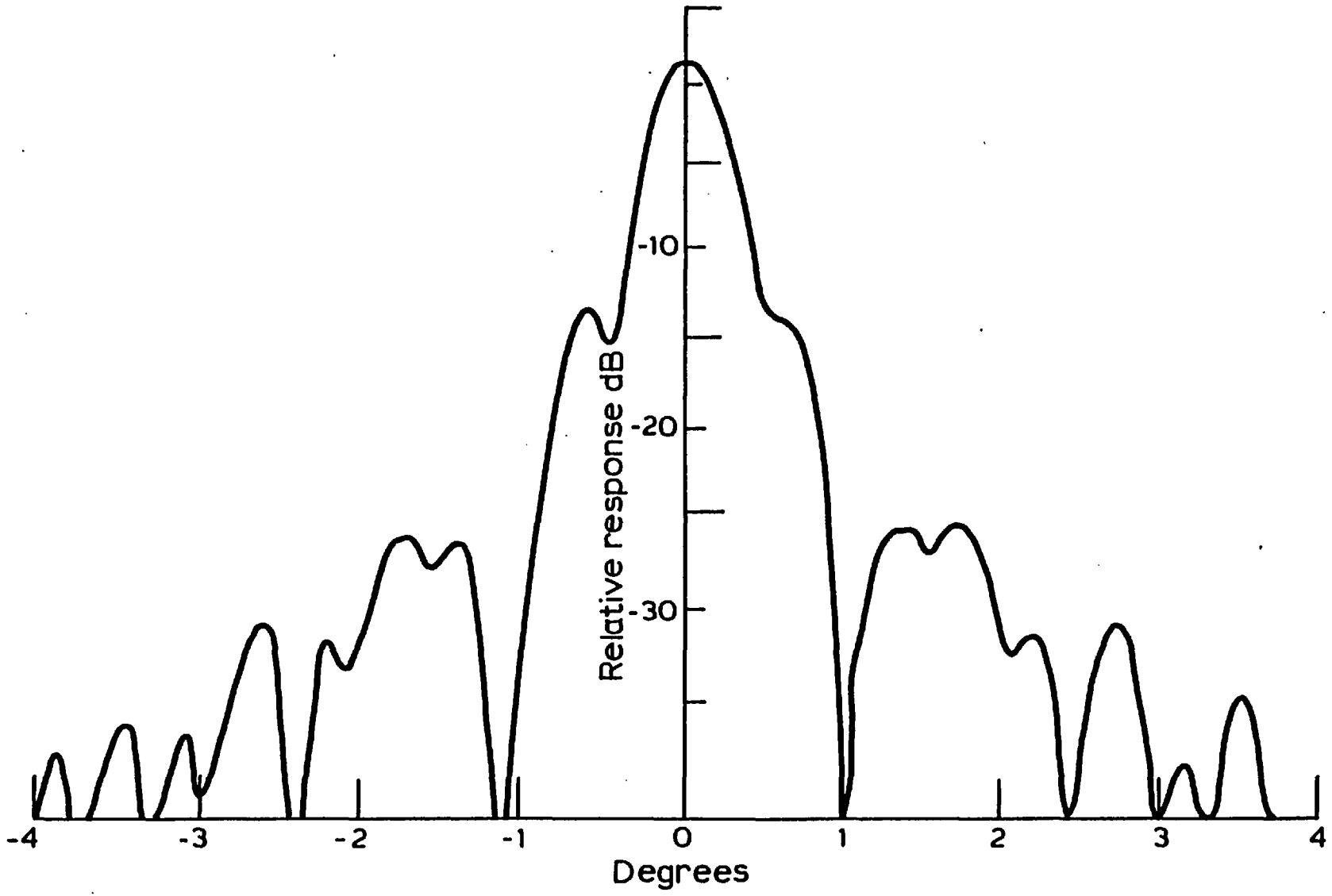

Fig. 6·6 4' Cassegrain reflector at 38 GHz. Radiation pattern in E plane

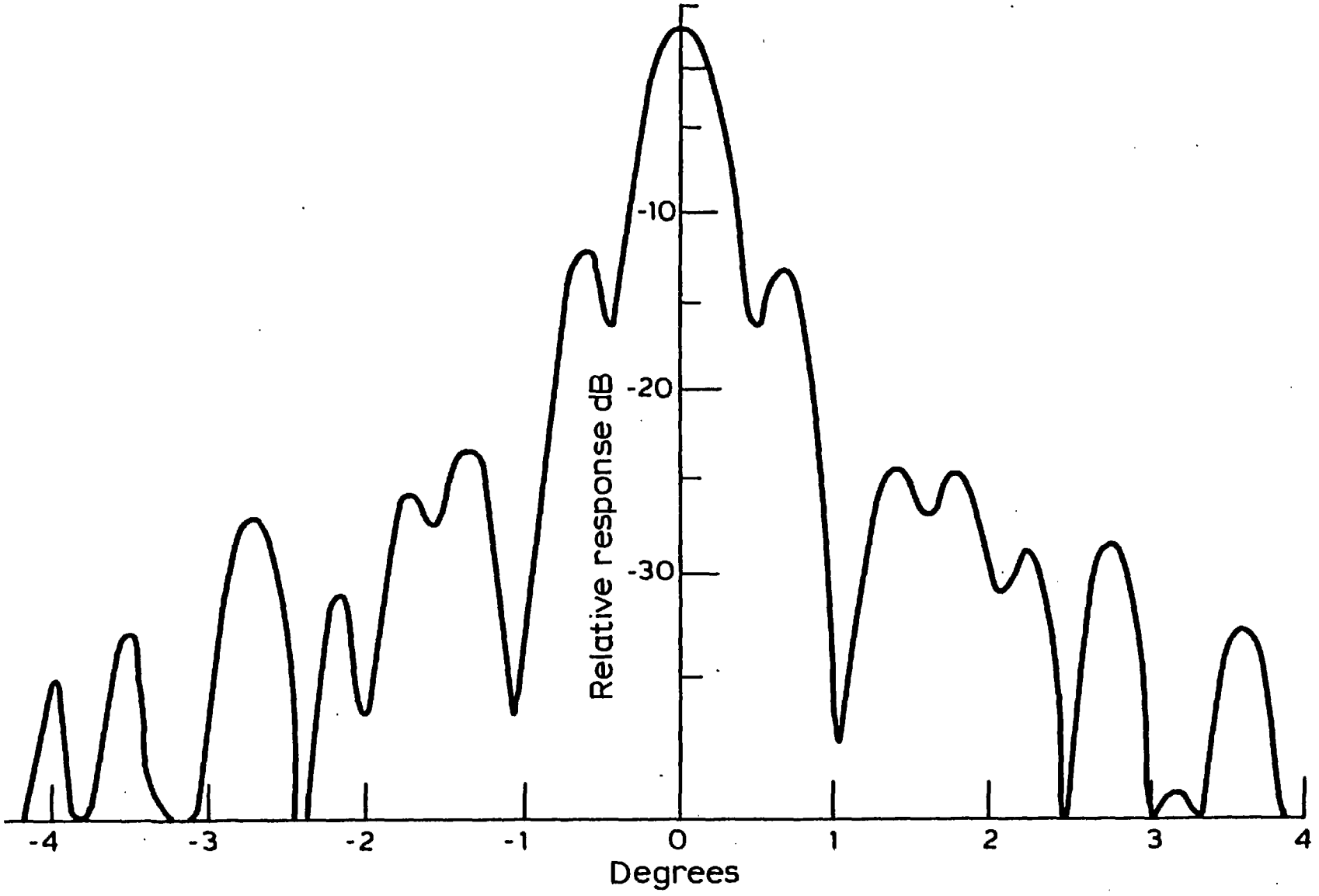

Fig. 6·7 4' Cassegrain reflector at 38 GHz. Radiation pattern in H plane

The single channel receiver operating at a local oscillator frequency of 37.93 GHz was previously designed to provide stable reception. This was achieved by means of phase locking techniques, the design considerations of which were carried out and are reported in detail[60].

A second receiver detector and a phase difference meter were designed by the author. These were incorporated to complete the dual channel interferometer system. These will be discussed in detail in the next section.

6.3.1 Description of the Dual Channel Receiver

Figs. 6.8 and 6.9 show the receiver set-up housed in a hut on the roof of the Electrical Engineering building.

Fig. 6.10 shows the block diagram of the receiver. The A.F.C. system proved to be very stable over the measurement periods, which lasted for 3 - 5 minutes. Perfect "locking" of the receiver was carried out before each measurement was made, thus ensuring the accuracy of the readings. The signals of interest which were recorded simultaneously were the detected field strengths of channels 1 and 2 and the phase difference $\Delta\phi$.

In order to compare the signals received from each channel, the response of the second channel detector had to be very close to that of the first one.

A block diagram of the second channel detector is shown in Fig. 6.11. A detailed circuit diagram is given in Appendix III.

The calibration curves for both receiving channels are shown in Fig. 6.12. These were obtained by varying an identical 120 MHz I.F. input supplied by an R.F. signal generator, to both channels. The output in decibels is normalized to the maximum value.

Fig. 6.8: Interferometer receiver site

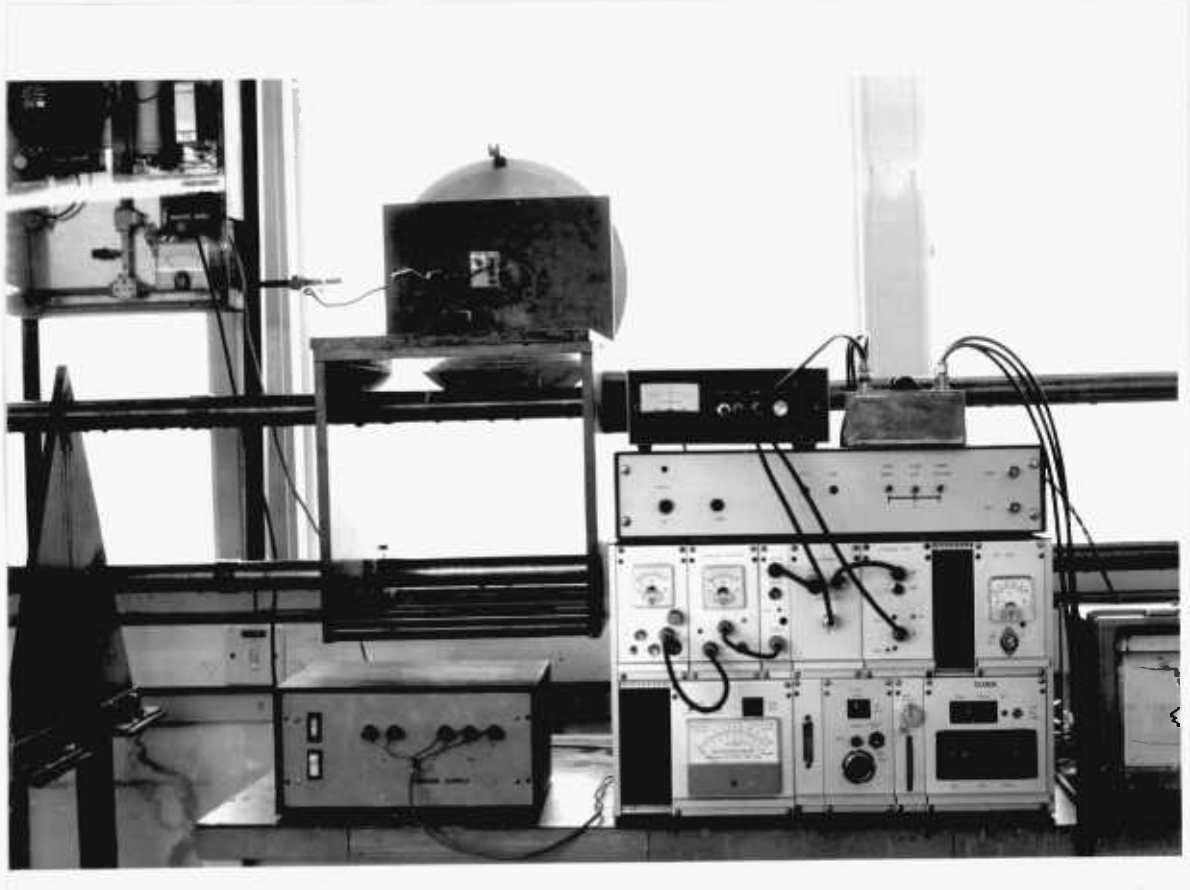

Fig.6.9: Receiver equipment

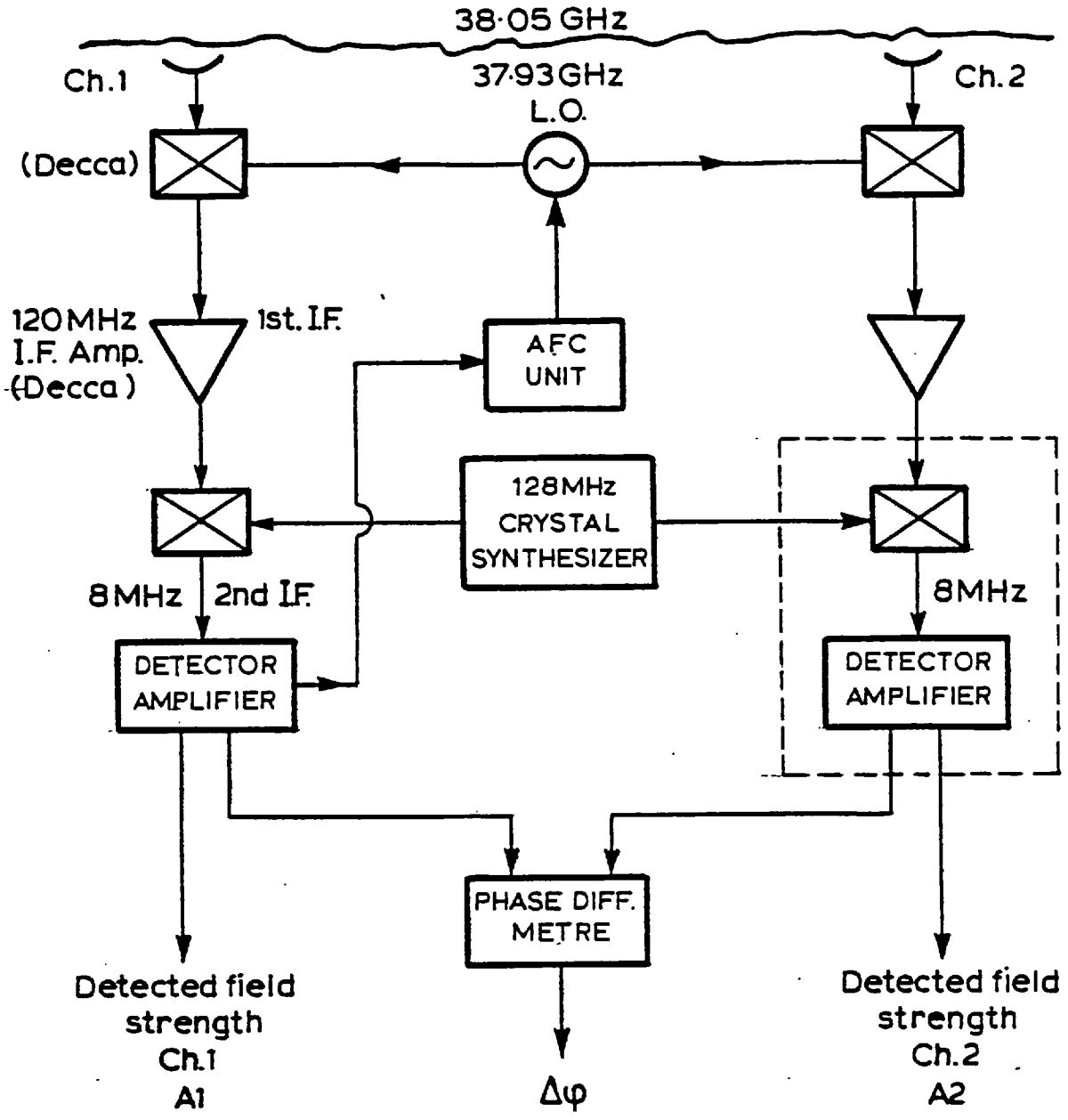

Fig. 6·10 Block diagram of the dual channel receiver

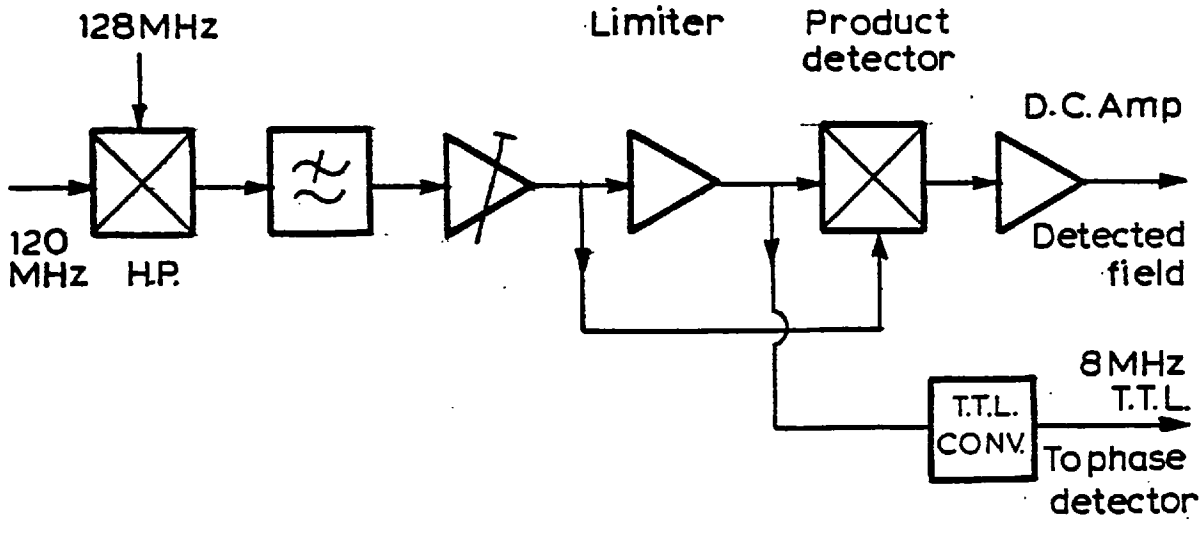

Fig. 6·11 Detector amplifier module

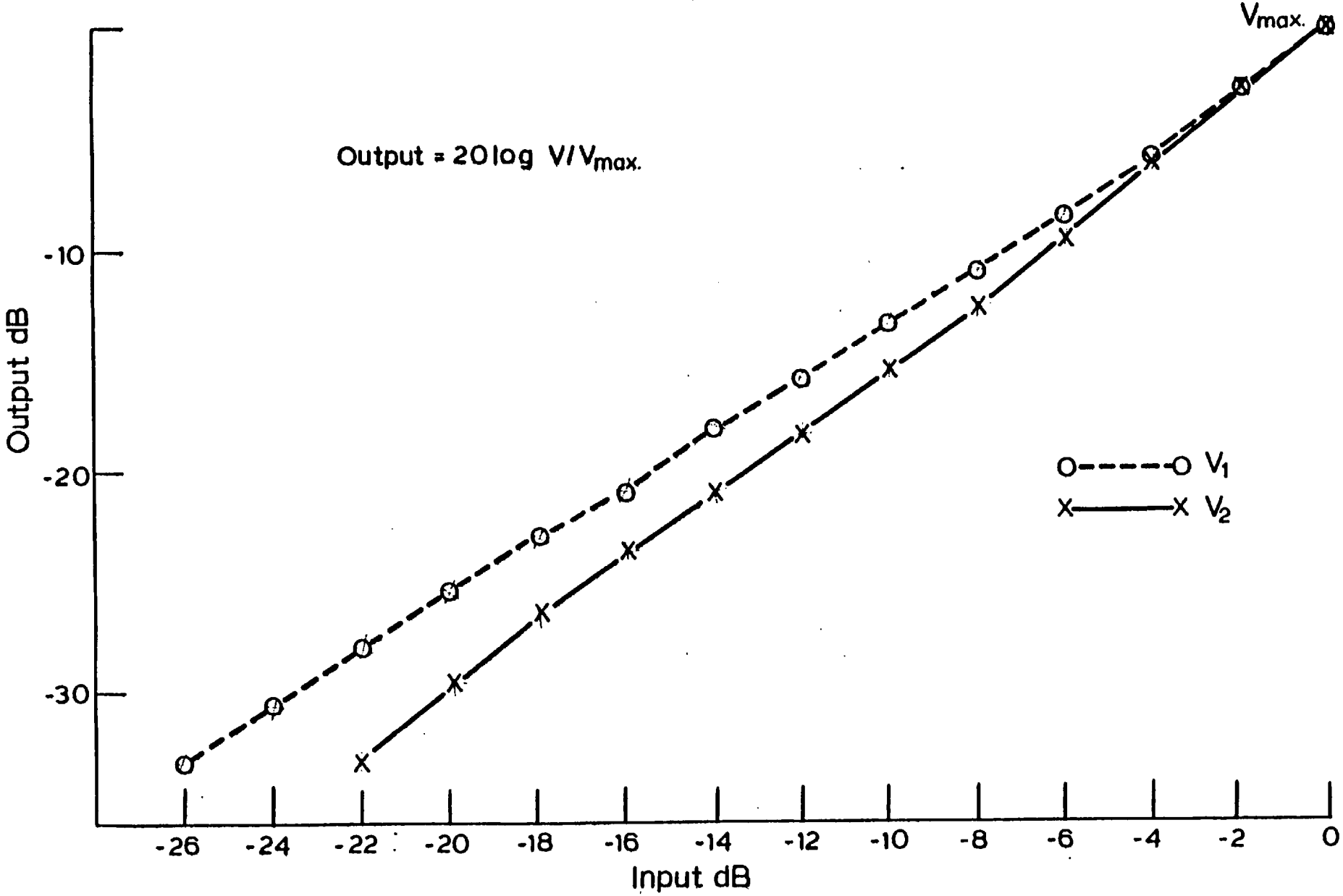

Fig. 6·12 Input - output characteristics of Ch.1 and Ch.2

It may be seen from the calibration curves that neither channel is quite linear. However, this does not affect the accuracy of the investigation of temporal fluctuations or cross-correlation coefficients. For experiments which required exact similarity and linearity of both channels, an R.F. Hewlett-Packard linear detector was used alternatively for both channels. These experiments are discussed in detail in Chapter 8.

6.3.2. Characteristics of the Different Size Receiving Apertures

Three different size apertures were used to investigate the effect of the aperture size on the coupled signal. The largest aperture used was an 0.25 metre diameter dish, supplied by C and S Antennas Ltd. The smallest one was a 35 x 25 millimetre horn supplied by Flann Ltd. The gain of the horn was calculated from its dimensions to be 21.5 decibels. On this basis, the gain of the dish was measured to be 37.5 ± 0.5 decibels, the uncertainty being mainly due to the different matching properties of the dish and the horn to the wave guide structure connected to a Marconi microwave power metre.

A rectangular horn with a gain of 30 decibels was built to provide an intermediate aperture size. The design of the horn was made on the basis of the formulae proposed by Braun[61] for the design of an optimum pyramidal horn. The aperture dimensions were calculated to be 122 x 92 millimetres. The overall dimensions which were calculated to give a true gain of 30 decibels, with minimum sidelobes at an operating frequency of 38 GHz, are shown in Fig. 6.13.

Fig. 6.14 shows a pictorial view of the three different apertures used in the investigation of the effect of the aperture size on the coupled signal.

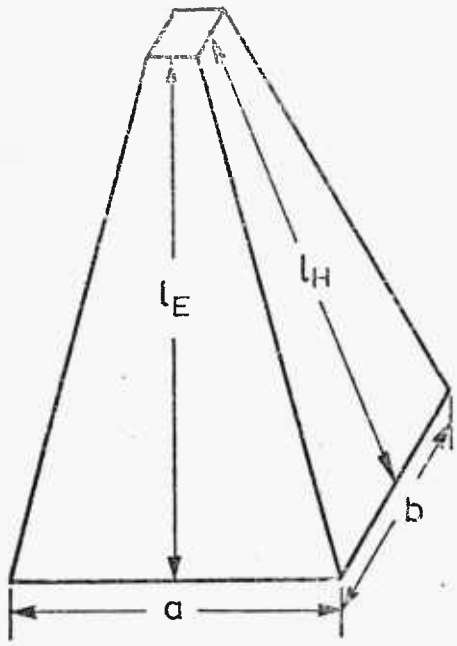

l_E = 498 mm

l_H = 509 mm

a = 122 mm

b = 90 mm

Fig.6.13: Dimensions of a 30 dB, 8mm. optimum horn

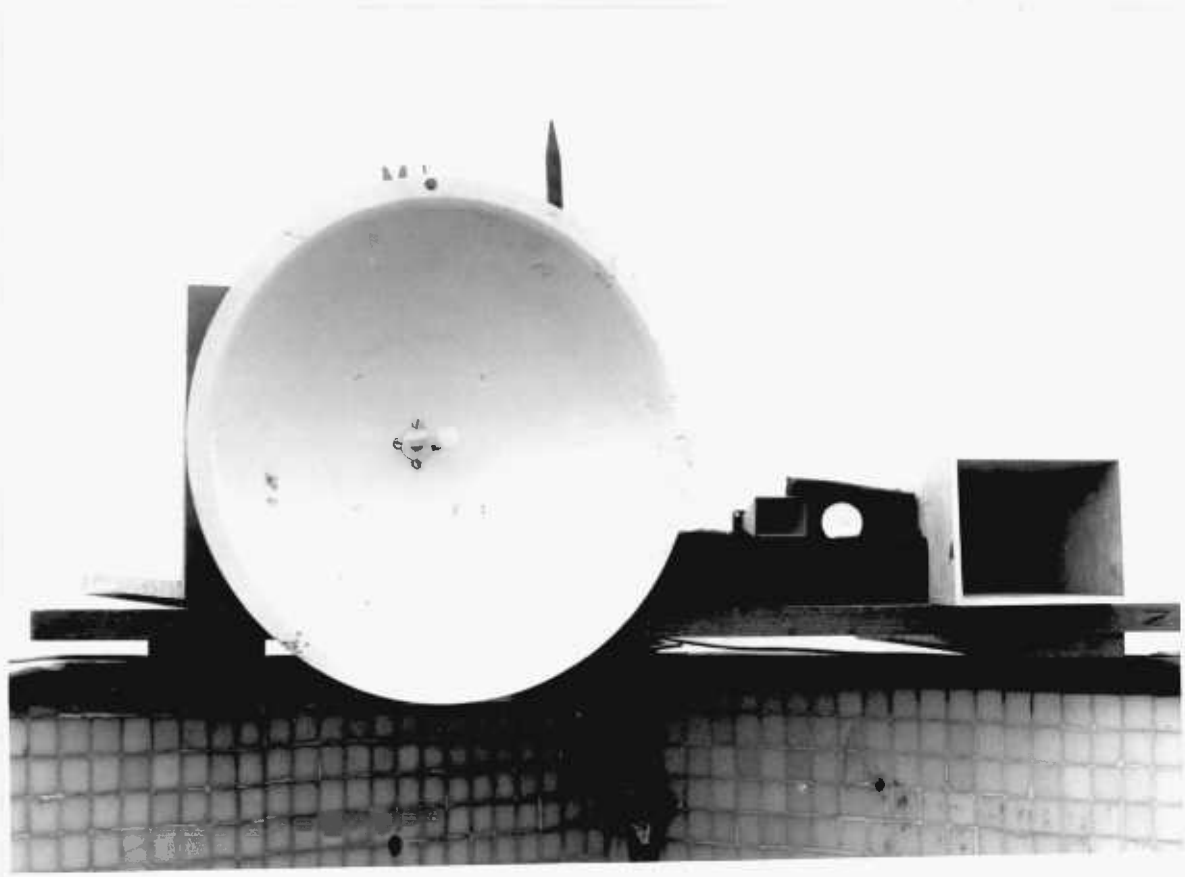

Fig.6.14: Three different size receiving apertures

Figs. 6.15, 6.16 and 6.17 show the H-plane radiation patterns of 0.25 metre diameter dish, the 122 x 92 millimetres and 35 x 25 millimetres horns respectively. The radiation patterns were obtained by rotating the aperture under investigation on a calibrated turntable. The radiating source in all cases was an open wave guide. The measurements for the two horns were carried out in an anechoic chamber. The measurements for the 0.25 metre dish were carried out on the roof to provide adequate separation between transmitter and receiver, greater than the Rayleigh distance ($2a^2/\lambda$).

It may be seen from the radiation patterns, that the cross-polar patterns are relatively quite high. This prohibited any experimental investigation of the medium cross-polarization effects.

Under clear air conditions, where the reception was exceptionally high, an open wave guide was also used as a receiving aperture.

6.3.3 Phase Difference Measurements

One of the main objectives of the experimental investigation was to examine the lateral distortions of the phase at the receiver plane. The scale size of the distortions was expected to vary from a few centimetres to a few metres. The magnitude of the slowly varying phase fluctuations, which are angle-of-arrival fluctuations, was not expected to exceed a few tens of degrees. However, provisions had to be made to detect any possible large magnitude fluctuations in the range of hundreds of degrees.

The method chosen to measure the phase difference was that based on the multiplication of the two signals. One of the advantages of this method is that the phase difference between the two 38 GHz signals is preserved throughout the I.F. stages. Obviously this is only true if the I.F. oscillator source is the same for the mixers of either

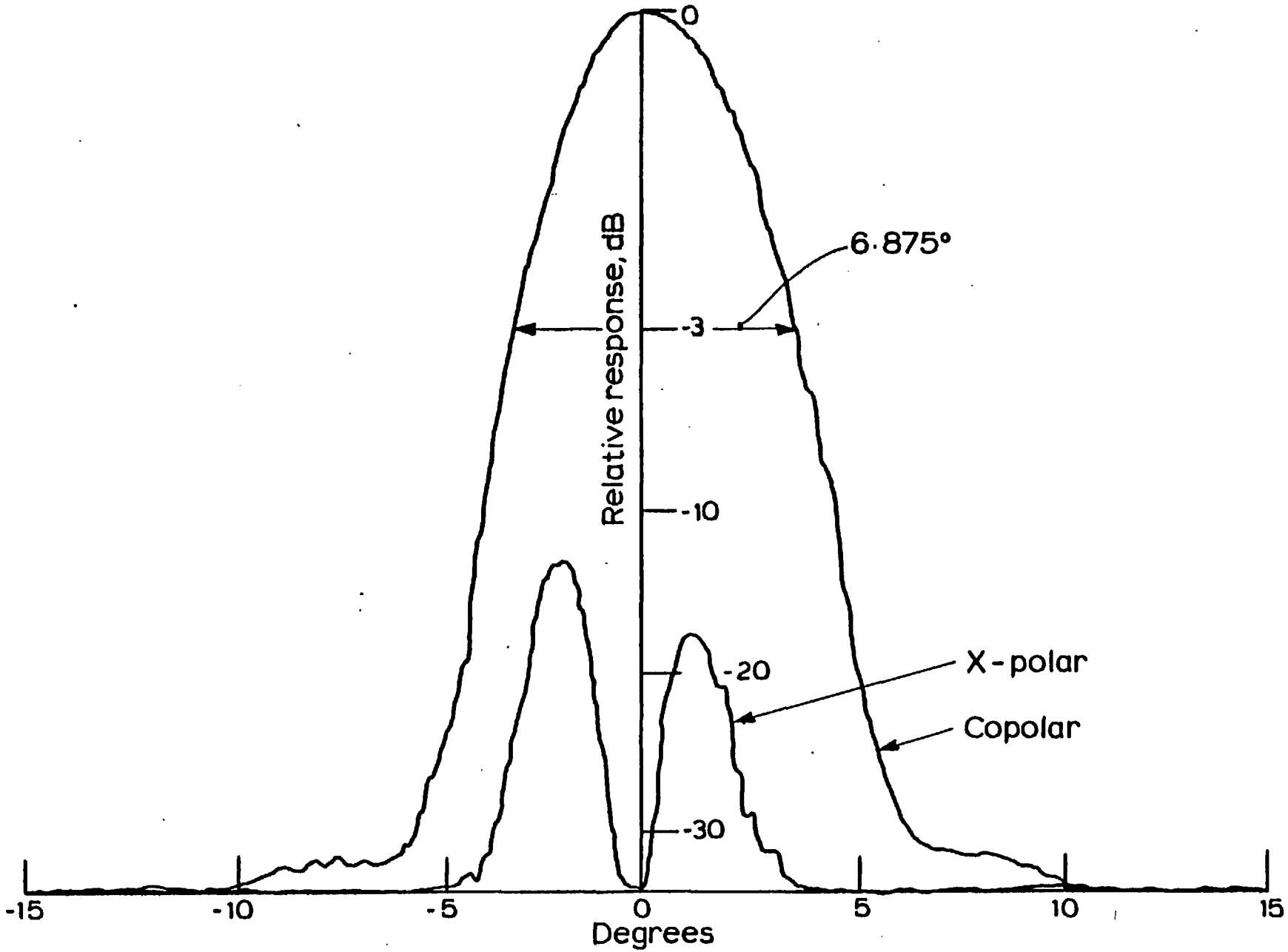

Fig. 6·15 H-plane radiation pattern for the 0·25 metre diameter dish

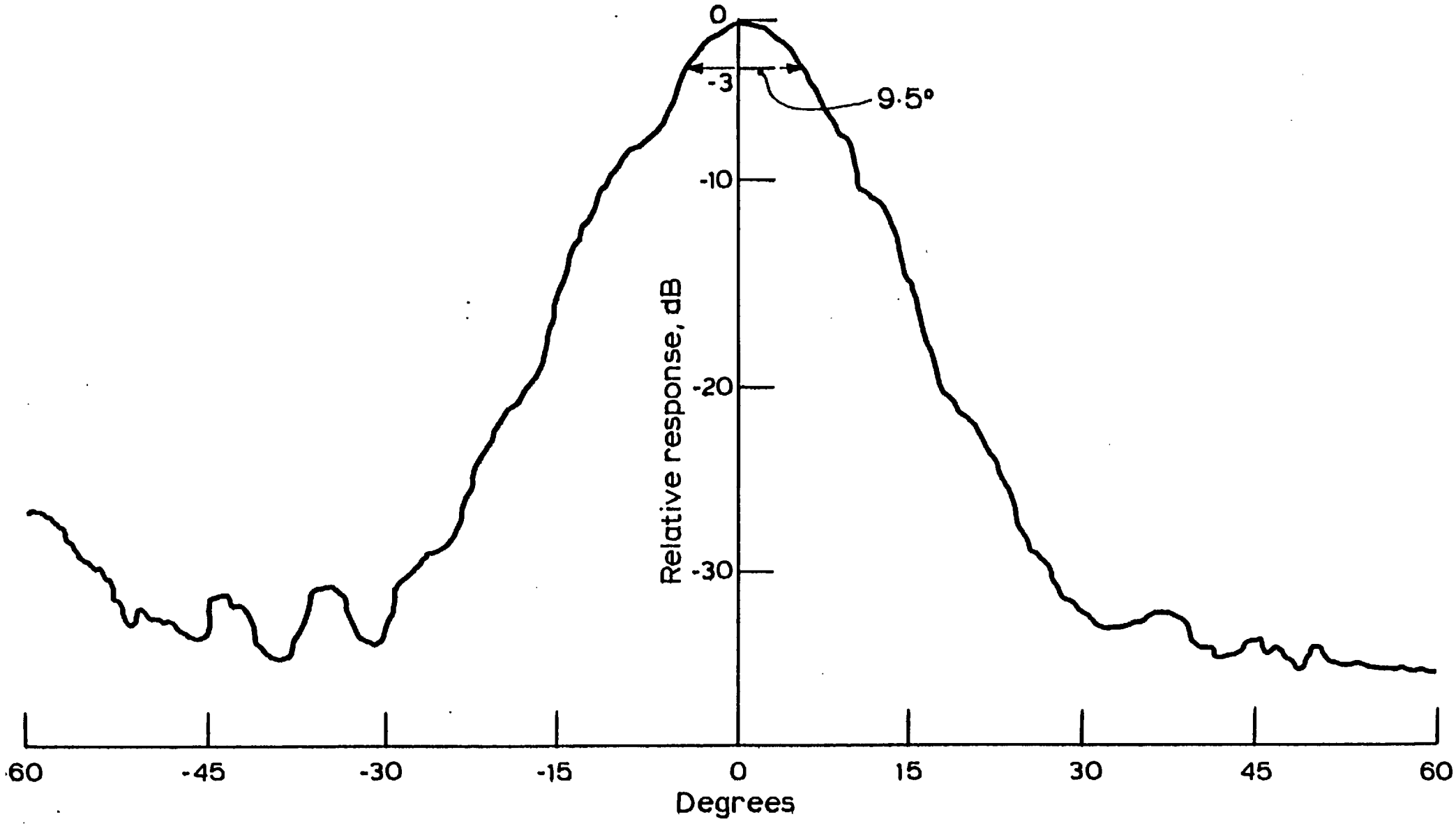

Fig. 6·16 H-plane radiation pattern for the 122 x 92mm horn

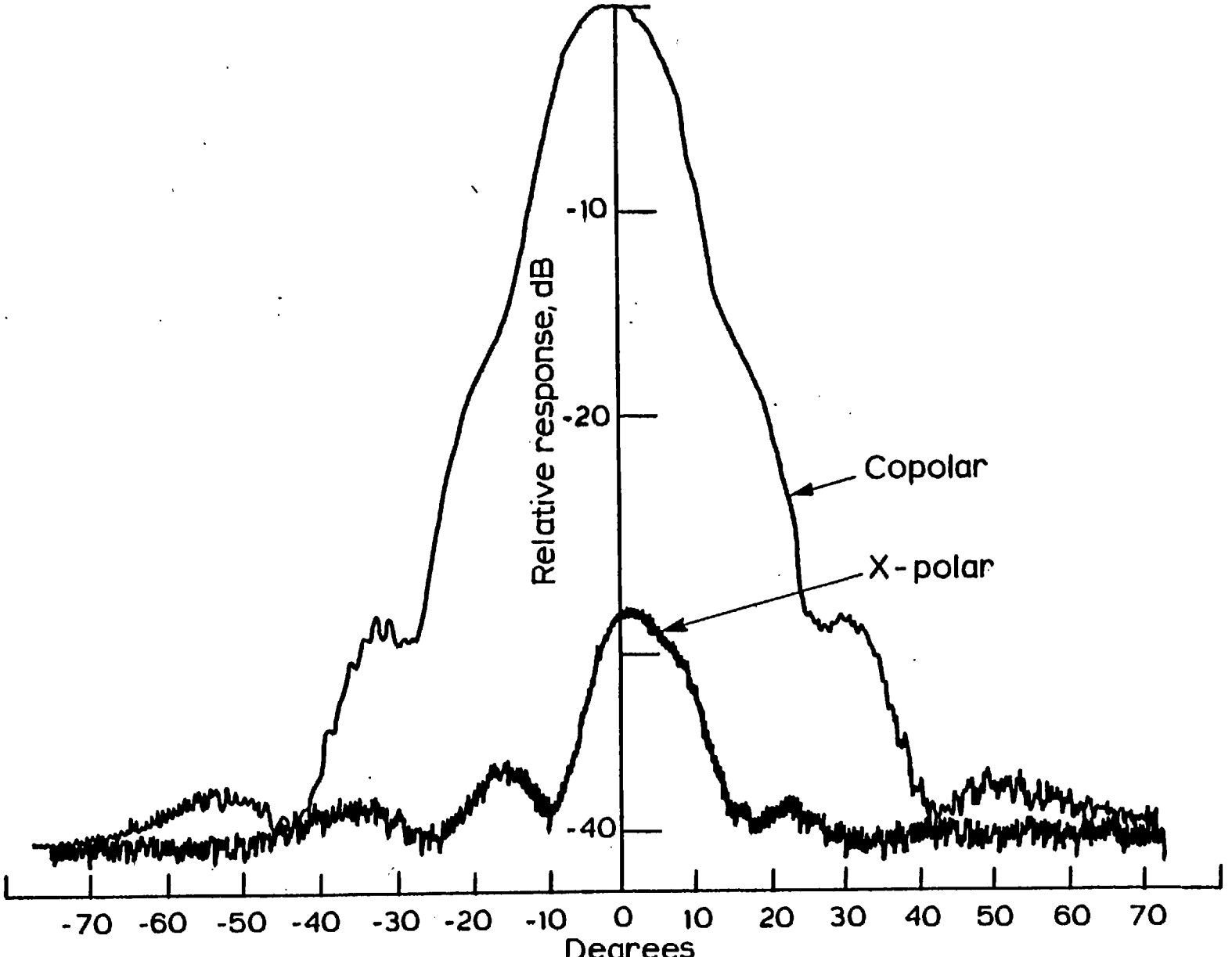

Fig. 6·17 H-plane radiation pattern for the 35x25mm horn

channel, which is the case for the dual channel receiver previously discussed.

The appropriate I.F. stage for the phase difference measurements was the second I.F. stage, i.e. at a frequency of 8 MHz. This was chosen for the availability and cheapness of the required components at this frequency.

As mentioned above, the phase detector should be able to measure phase differences of a few hundred degrees, linearly at 8 MHz. For this to be possible, the I.F. of 8 MHz is divided by a factor of 10 and the phase difference is measured at 800 KHz. The phase difference measured at 800 KHz is thus multiplied by a factor of 10 for 8 MHz. This may be seen as follows.

Consider the two input signals to be of equal and constant amplitudes and with a phase shift ϕ, i.e.:-

$$V_1 = V \cdot \sin wt \qquad \text{and} \qquad V_2 = V \cdot \sin (wt + \phi) \tag{6.4}$$

Dividing the frequency by 10, therefore:-

$$V_1 = V \cdot \sin \frac{wt}{10} \qquad \text{and} \qquad V_2 = V \cdot \sin \frac{(wt + \phi)}{10} \tag{6.5}$$

Multiplying both signals, the output signal V_o is then:-

$$V_o = V^2 \cdot \sin \left(\frac{wt}{10}\right) \cdot \sin \left(\frac{wt + \phi}{10}\right) \tag{6.6}$$

$$= V^2 \cdot \cos \left(\frac{\phi}{10}\right) + \text{filtered out higher frequency components} \tag{6.7}$$

Therefore, a phase detector measuring phase difference values

of $\phi/10$, at a frequency of f/10, is in effect measuring phase difference values of ϕ at a frequency f.

The principle of operation is basically that of multiplying two square waves together. The optional frequency division is obtained by a decade counter. The resultant filtered signal is then linearly proportional to the phase difference between them.

A block diagram of the phase difference detector is given in Fig. 6.18. A detailed circuit description is given in Appendix IV.

The detector can measure phase difference fluctuations up to a rate of 10 c/s. This has been determined by switching, on and off, a phase screen connected to a motor. The detector was found to give its full response up to rotational speeds of 10 r.p.s.

A Hewlett-Packard network analyzer was used to calibrate the phase difference detector. This was done by rotating a source signal on a turn-table and receiving with two apertures. The fact that the network analyzer could only measure phase differences of ± 180 degrees was accounted for.

Fig. 6.19 shows the calibration curve for the phase difference detector.

6.3.4 Installation and Performance of the Interferometer Receiver

At the time of the receiver installation, the transmitter output level was 14.7 dbm. The received power level was measured to be - 58.8 dbm ± 0.2.

Theoretically the received power is given by P_R where:-

$$P_R = 14.7 + G_T + G_R - \text{Path Loss} - \text{Excess Losses} \qquad \text{(dbm)}$$

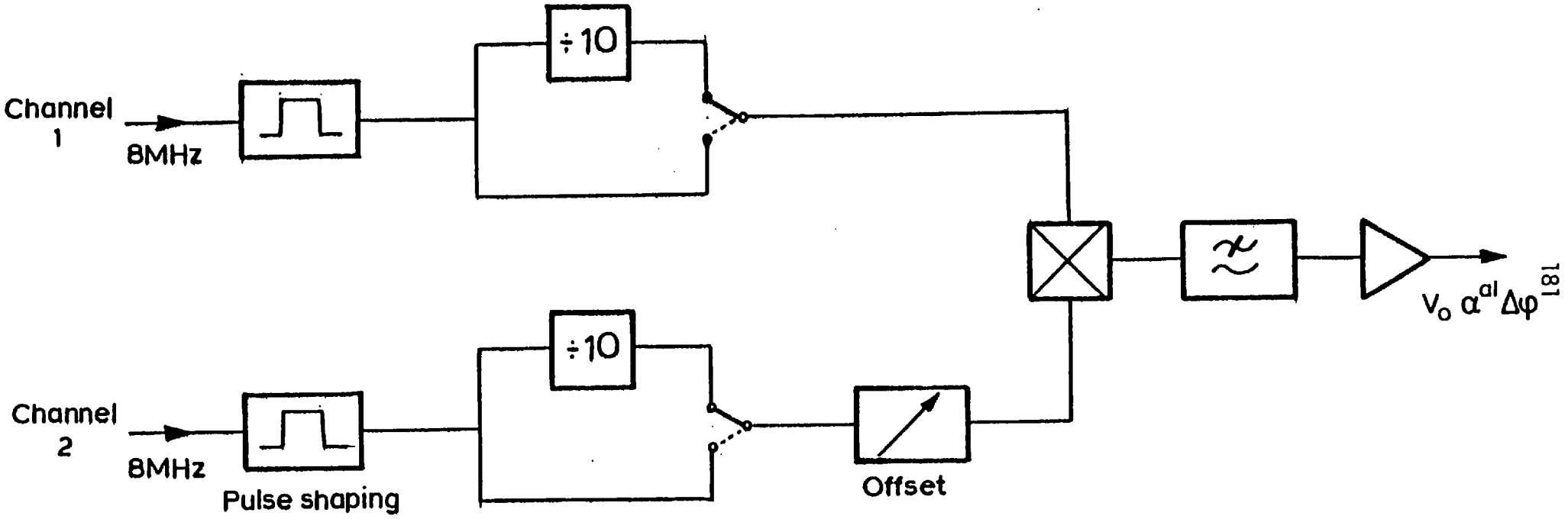

Fig. 6.18 Phase difference detector

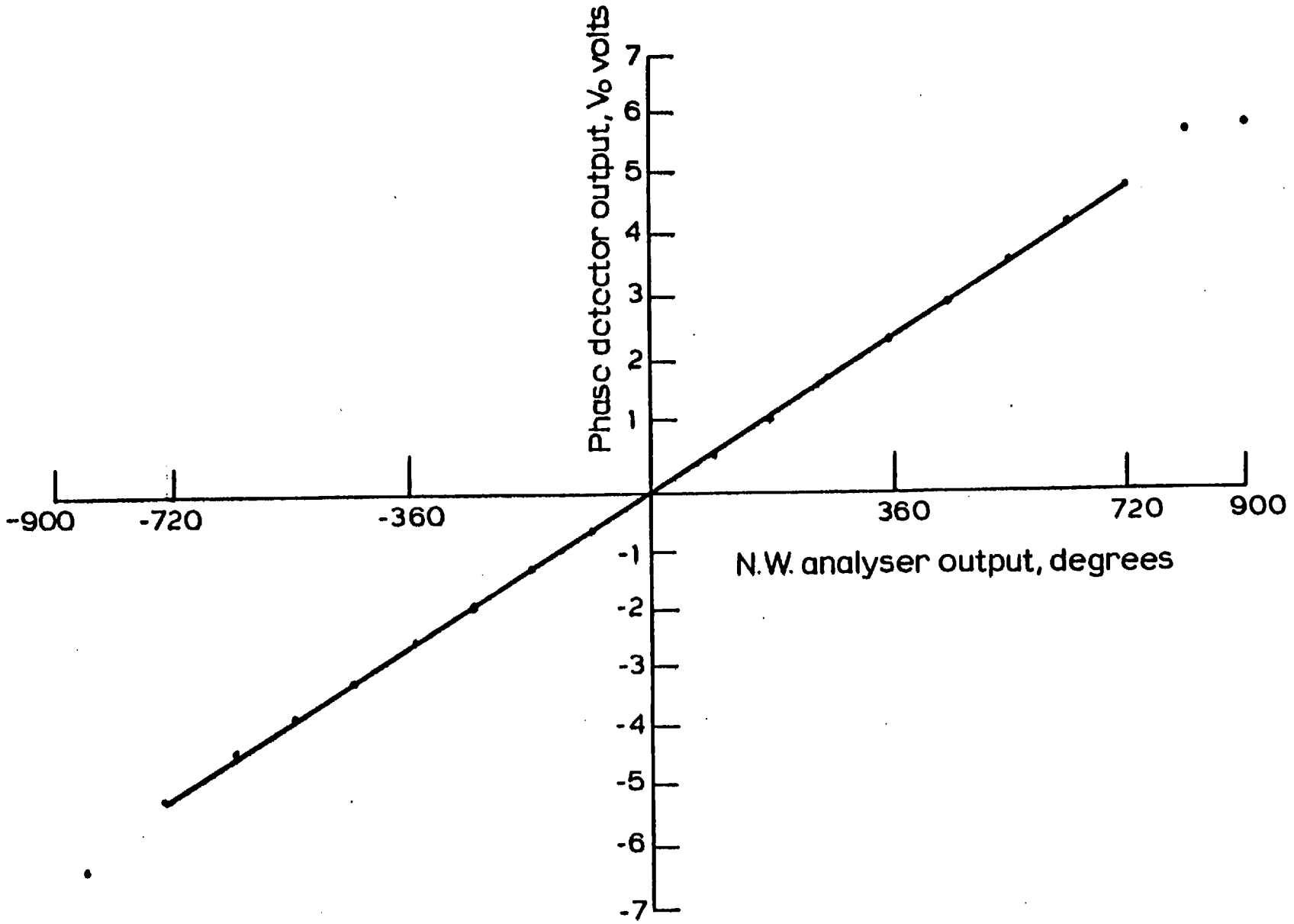

Fig. 6·19 Phase difference detector calibration curve

where G_T and G_R are the gains of the transmitting and receiving antennas respectively. The path loss is calculated to be 145.5 decibels. Excess losses are due to water vapour absorption and loss due to the glass window of the hut, which was measured to be 3.4 decibels. Therefore:-

$$P_R = 14.7 + 49 + 37.5 - 145.5 - 3.4 - \text{Water Vapour Loss}$$

$$= - 47.7 - \text{Water Vapour Loss} \quad \text{(dbm)}$$

Therefore, the difference between the measured and the theoretical received powers, is very small. This difference may be attributed to the varying water vapour loss, which is in the range of 1 - 2 decibels and also to the error bounds of the experiment.

The signal-to-noise ratio was 40 decibels under clear air conditions. This figure presents a limit to reception under medium rain conditions. Since for a rain rate of 20 mm/hr, the loss in signal has been predicted to be[62] approximately 3.5 dbs/Km for a wave length of 8 millimetres.

Physical and Structural Considerations

The separation between both receiving antennas was varied by manually pushing either or both of the receiver mounts shown in Figs. 6.8 and 6.9. The mixers were then connected to the local oscillator box by wave guide sections. Part of the connection was made by semi-rigid coaxial cables to provide the desired flexibility.

The receiver mounts were designed to slide on a heavy mounting frame. This frame was supported by means of building jacks onto the roof of the building through holes in the floor of the hut. Since the oscillator box connected to the wave guide sections was also mounted on

the frame, therefore, the only connection to the hut was through cables connected to the various detectors. Hence any vibration of the hut would not affect the physical stability of the system.

The reason for these extra precautions was that the fluctuations observed due to the medium were very small, such that they were comparable to those produced by the hut vibrations. However, under strong wind conditions, e.g. greater than 20 metres/second, the fluctuations due to the vibration of the glass windows were comparatively large. Therefore, under such conditions the measurements were unreliable.

6.4 Meteorological Sensors

In order to understand the relationship between the medium and signal fluctuations, various sensors were used to gather meteorological data. Ideally weather conditions should be monitored along the propagation path. However, due to practical conditions, the sensors were placed at the receiver site. The atmospheric conditions that were thought to be of interest and were monitored are:-

1. Wind velocity.
2. Wind direction.
3. Temperature.
4. Rainfall rate.

On a few occasions, the refractive index was also measured.

Following is a brief description of the various sensors which the author made use of.

1. Wind Velocity

The wind velocity was manufactured by Prosser Scientific

Instruments. It worked on the principle of heat convection. A hot ($100^{o}C$) thermistor placed in a bridge circuit was used to give an indication of the amount of cooling and hence the wind velocity.

2. Wind Direction

A wind direction indicator was designed by a co-worker[60]. Binary coded information of the wind direction was obtained by means of a coded disc. The disc was fixed to a freely moving vane. The angular resolution was 18 degrees with 0 degrees coinciding with the propagation axis.

3. Temperature

The design of a simple electronic thermometer was developed from a graduation project[63]. The sending device was a transistor, based on the variation of the emitter-base voltage with temperature. The change in voltage, 2 $mv/^{o}C$, was then amplified and converted into binary code. The electronic thermometer was calibrated over a range of - 10 to 40 degrees centigrade.

4. Rainfall Rate

The rain gauge used was developed and supplied by the Appleton Laboratory. The rainfall rate was established by counting the number of standard size drops within a certain period of time. The drops formed through a capillary tube would interrupt a light beam as they dropped, thus producing a pulse which was then registered.

The data from the above-mentioned sensors was gathered sequentially through analogue-to-digital convertors producing a Binary Coded Decimal (BCD) output, the implementation of which was carried out

by a co-worker. The digitized variables were then fed in parallel to a data formatter. The formatter, which was developed as a graduation project[64], scanned and converted the parallel input BCD data to a serial ASC II RS232 standard output. The serial data was then fed to a a programmable TEK31 calculator. The programs developed by a co-worker produced the mean value and standard deviation of the atmospheric variables.

A refractometer was available from the Appleton Laboratories for some periods during the experimental investigation.

The refractometer had two X-band wave guide cavities, one of which was closed and the other open to the surrounding air. The variation of the impedance of the open cavity relative to that of the closed one then gives an indication of the refractive index of the flowing air.

During measurements, the refractometer was suspended freely on a platform 3 metres above the ground. The analogue output of the refractometer was then recorded on magnetic tape, which was subsequently processed as will be shown in Chapter 7.

CHAPTER 7

DATA PROCESSING : PROCEDURE AND TECHNIQUES

Introduction

In this chapter, the handling and analysis of the data available from the interferometer will be described. Normally three signals were available for analysis, these being the output of the two amplitude detectors and the phase difference signal. All three signals were available simultaneously in analogue form.

Since various investigations were to be carried out on the signals, therefore, an off-line data processing procedure was preferred to an on-line one. Off-line data analysis has the added advantage of allowing the application of newly devised analytical techniques at a later stage.

Experience has shown that an efficient and practical data acquisition and handling procedure is one which allows for accurate storage and simple retrieval of data. Easily accessible data encourages to a great extent the analysis of the same set of data in many different ways. This enables the analyst to extract as much information as possible from the available data.

The procedure followed by the author may briefly be described as follows. The three-channel interferometer data was recorded onto a multichannel F.M. tape recorder in analogue form. After accumulating a reasonable amount of data, the tapes were played back into a PDP-15 digital computer, through an analogue-to-digital converter (ADC). The digitized data was then stored on computer magnetic tape. The tapes were then used as the data base for subsequent analysis and processing.

Modern computers are geared to handling and storing data in a straightforward manner. This was not the case for the PDP-15, which

required extensive programming in a low level assembler language to produce the desired handling facilities. In spite of the relative primitiveness of the PDP-15, it proved to be attractive in other ways. This was evident in the presence of a high-resolution ADC with the associated multiplexer. Direct plotting facilities on standard paper were an added attraction. Also useful were the small-size, high-density magnetic Dectapes which were simple to mount. Being a departmental computer proved to be particularly useful from the cost and utilization point of view.

Basically, an off-line data analysis procedure may be split into three separate and consecutive stages:-

1. Data acquisition.
2. Data handling and storage.
3. Analytical processing.

The procedure followed in handling and analysing the experimental data is described in detail below, according to the above stages.

7.1 Data Acquisition

For practical reasons, the data to be analysed was transmitted from the hut on the roof of the Electrical Engineering building to the laboratory on the floor below. The 3 analogue channels were transmitted via a shielded multipair cable to the F.M. tape recorder in the laboratory. As a precaution against noise pick-up en route to the tape recorder, each signal was amplified, after removing the mean value, to assure a high signal-to-noise ratio. The linear amplifiers used had a variable gain of 1, 3, 10 and 20 decibels. As a further precaution, the signals

were passed through a low-pass filter before being recorded. The filters had a variable 3-decibel cutoff frequency of 1.75 and 3.0 Hz with a slope of 4 decibels/octave.

The tape recorder used was a Racal Store 4 F.M./Digital tape recorder. The tape speed used was 3¾ inches/second, with a band width of D.C. to 1,250 Hz. The peak-to-peak percentage flutter was 0.35%. The signal-to-noise ratio was 48 decibels.

The duration of each set of measurements was approximately 5 minutes. The tape counter and a voice recording were used to determine the start and end of each data run. The relevant information was logged for reference on playback.

Fig. 7.1 shows the configuration of the data transmission and recording procedure. Fig. 7.2 shows the circuitry of the active low-pass filters used.

7.2 Data Handling and Storage

After recording a reasonable amount of data, the tape recorder was taken down to the PDP-15 computer for subsequent digitization and storage. The analogue data was played back via a 3-channel active low-pass filter with a cutoff frequency of 4 Hz into a multichannel ADC. The 3 filtered data channels were multiplexed and subsequently digitized. The conversion rate was set by an external clock. The procedure is shown in the figure below.

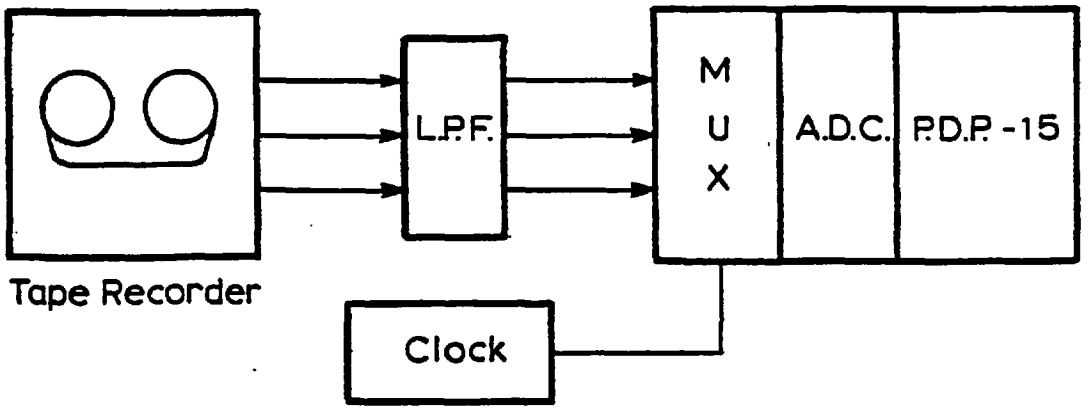

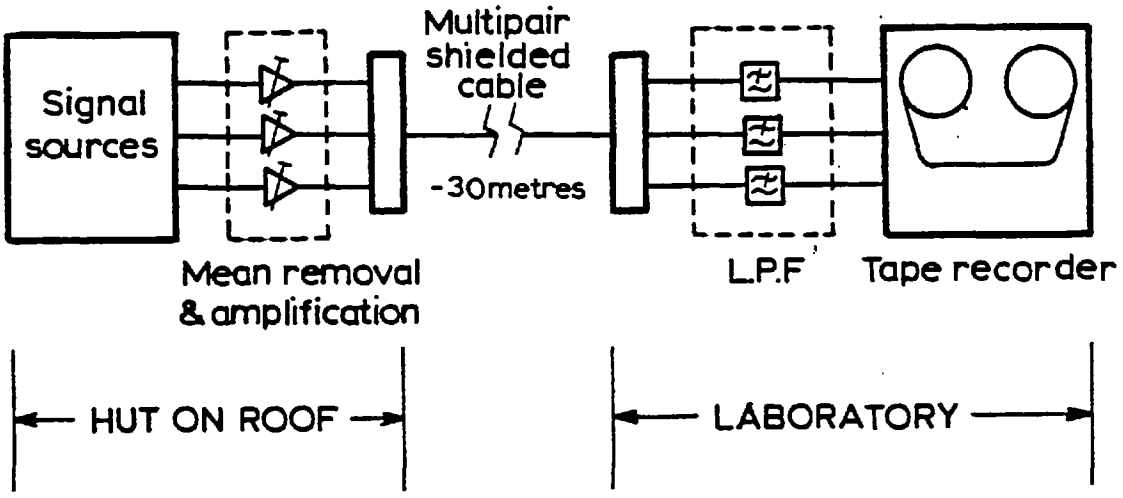

Fig. 7.1

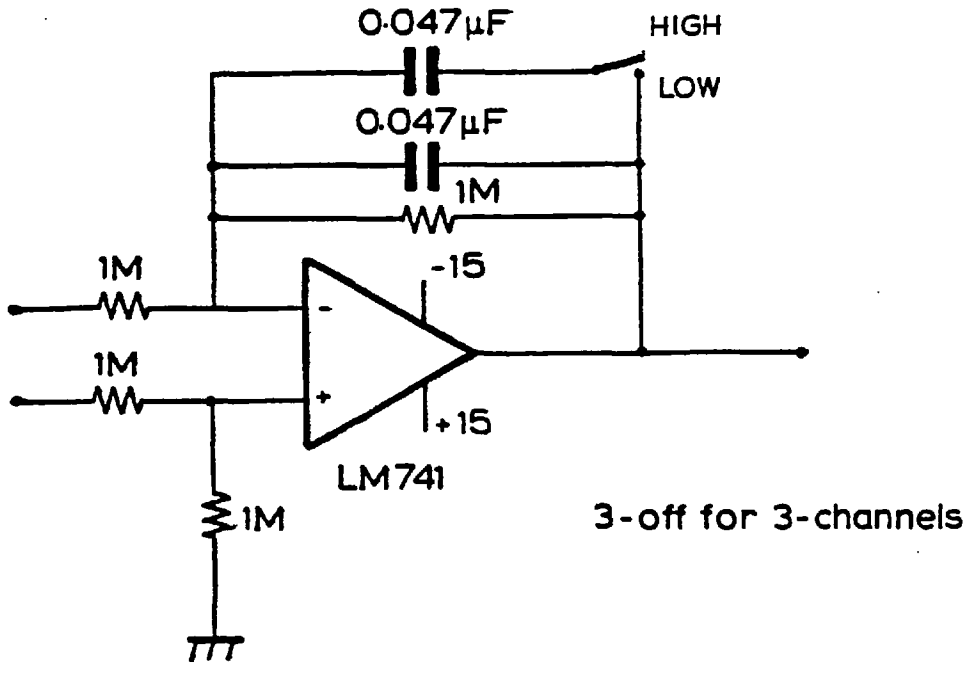

Fig. 7.2: Low pass active filter

The ADC used had an 11-bit word plus a sign bit, operating between ± 10 volts; this corresponds to a resolution of 5×10^{-4} volts.

The main disadvantage of the PDP-15 computer is its limited core memory. This in effect limits the number of sampled points it can store and, consequently, the duration of the signal to be analysed. To overcome this difficulty, the analogue data from each channel after digitization is made to fill up a block of 256 data words. The three blocks corresponding to the three channels are then transferred to the disk. The process is then repeated, without loss of incoming data, for any required number of 256-word blocks. For a 3-channel sampling rate of 30 Hz, a 256-word block corresponds to 25.6 seconds. After the required length of data record has been sampled, the 3-channel data available on disk may be copied, if requested, onto user specified locations on Dectape for further analysis later on.

The data transfers from the ADC to core to disk and finally to Dectape proved to be rather awkward due to the varying bit lengths and justification of the words used at each stage. The multiplexing, sampling, data transfers, writing and reading off and on disk and Dectape had to be written in low level Macro-assembler language[65], due to the relatively unsophisticated operating system of the PDP-15.

The main interactive program was written in FORTRAN, program IAM. The main program utilized three macro-assembler subroutines - ADC, READ and DKDT. The program sequence and functions are as follows:-

Program IAM

Interactive. Requires sampling frequency, length of data record and location of data storage on Dectape for each channel. Calculates the mean value and standard deviation for each data channel.

Subroutine ADC

Multiplexes and samples three analogue channels and stores the data on disk in block form.

Subroutine READ

Reads the stored data blocks off specified disk or Dectape locations into core.

Subroutine DKDT

Transfers a specified number of data blocks from disk to user specified locations on Dectape.

A flow chart of the programs is shown in Figs. 7.3a and 7.3b.

The data after storage on Dectapes was available for subsequent analysis. Each Dectape has a storage capacity of 512 data blocks each consisting of 256 data words. The data analysis was carried out in FORTRAN with the data read off Dectape by means of the assembler program READ.

At a later stage of the project, a data link was installed by the department between the PDP-15 and the College CDC computer. Thus data could be read off Dectape and transmitted to the CDC for analysis. However, this data link came after the bulk of the analysis had been carried out.

Fig. 7.4 shows the logging procedures used for cross-referencing the data from tape recorder to Dectape locations. A record of the basic statistics of the data, together with the relevant atmospheric and system information, was kept for each data run. This classification method proved to be a fast and simple way to pick out the interesting data records under different conditions.

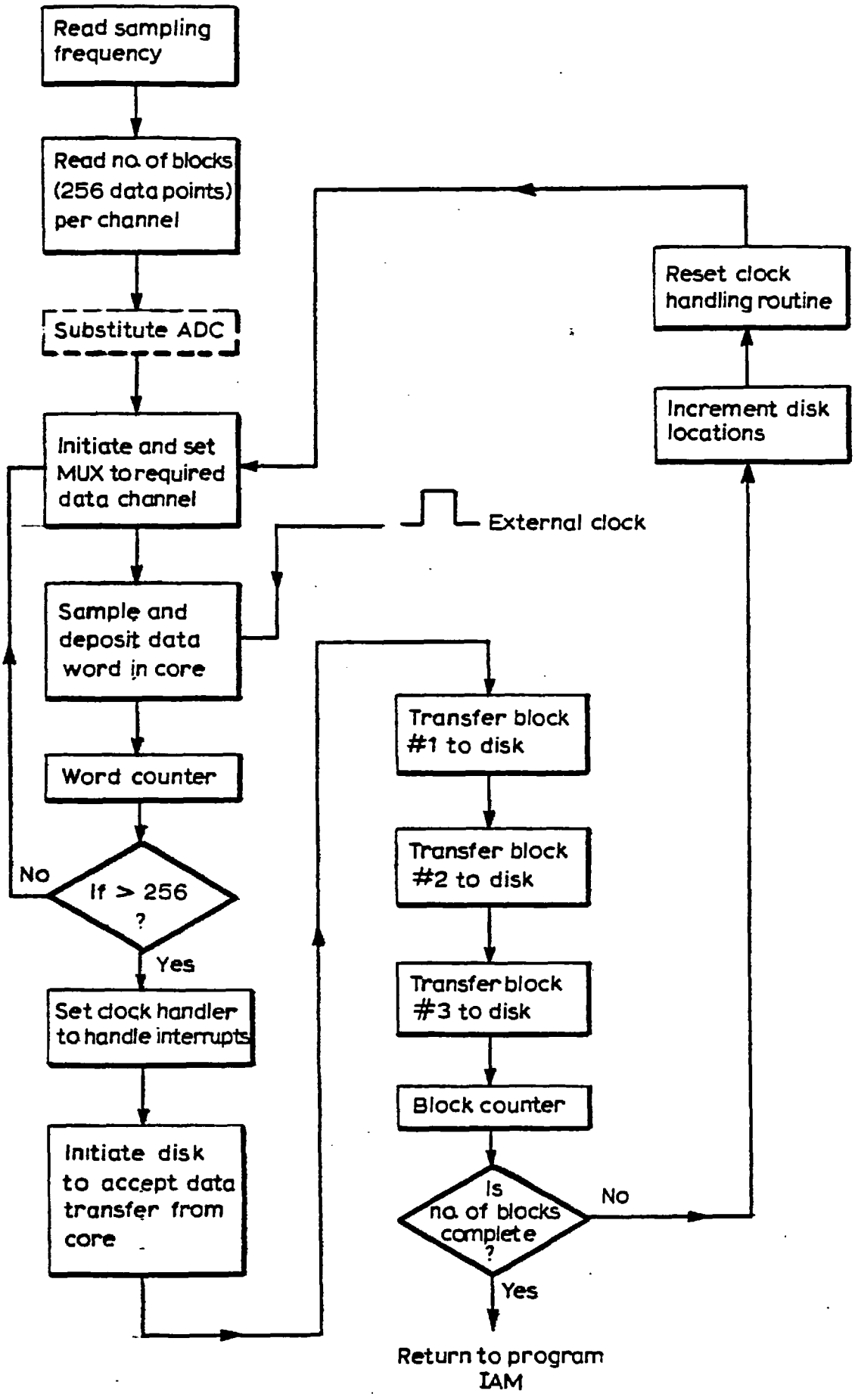

Fig. 7·3a: Program IAM

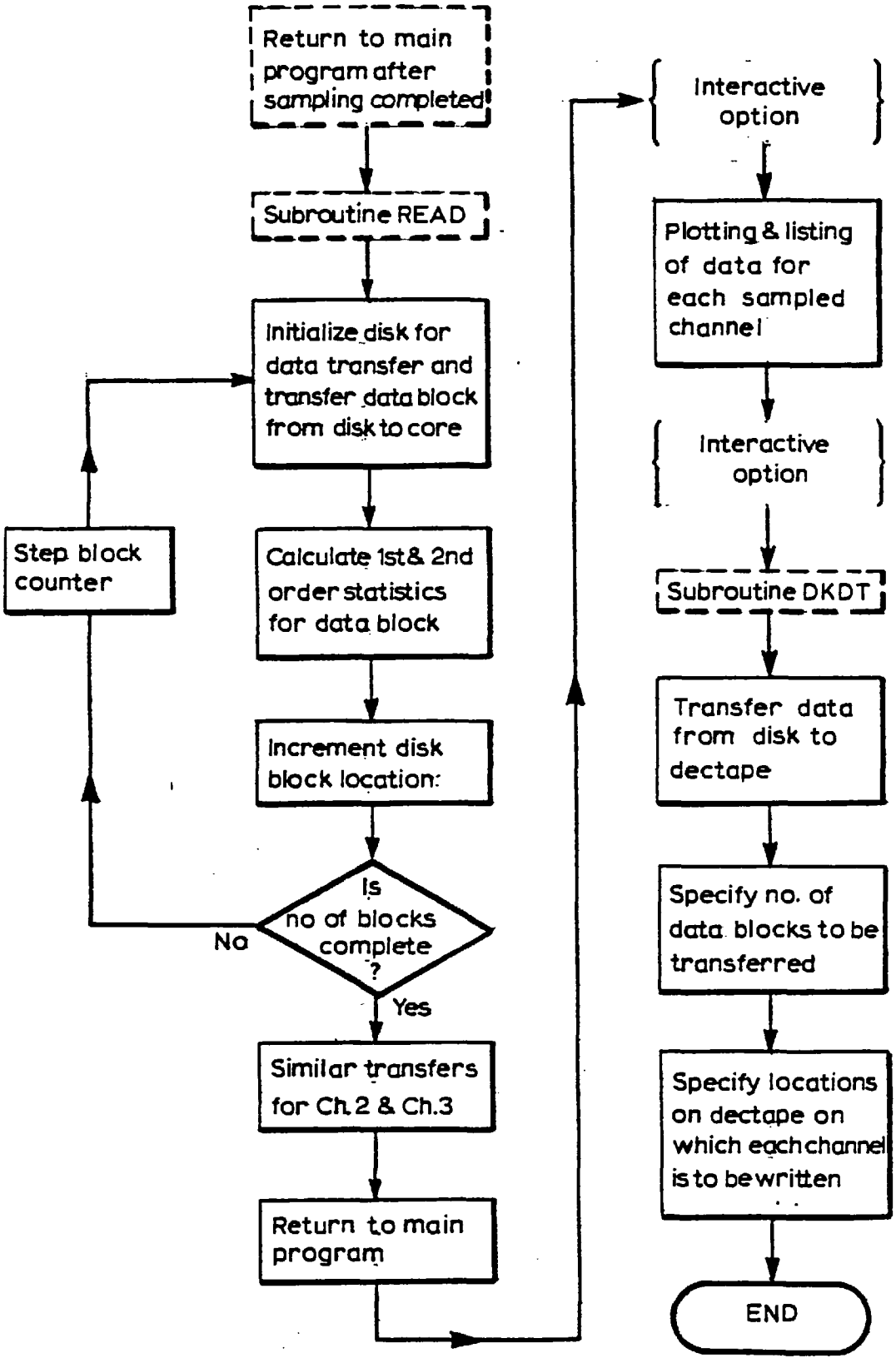
Return to main program after sampling completed
Subroutine READ
Initialize disk for data transfer and transfer data block from disk to core
Calculate 1st & 2nd order statistics for data block
Increment disk block location
Is no of blocks complete ?
No
Yes
Step block counter
Similar transfers for Ch.2 & Ch.3
Return to main program
Interactive option
Plotting & listing of data for each sampled channel
Interactive option
Subroutine DKDT
Transfer data from disk to dectape
Specify no. of data blocks to be transferred
Specify locations on dectape on which each channel is to be written
END

Fig. 7.3b

TAPE NO. _____

RUN	TIME	COUNTER		CHANNEL 1		CHANNEL 2		CHANNEL 3		REMARKS
		START	END	CONTENTS	S F	CONTENTS	S F	CONTENTS	S F	

	Mnth	Day	Hr-Min
DATE			

DURATION OF RECORD : _____ Secs.

DATA RECORDS:

DEC-TAPE: ____

Block Nos. (inclusive)	
Start	End

Tape recorder

Tape no. _____ Run no. _____

Counter	Start	End

SIGNAL

RECEIVER SPACING: _____

	Contents	Std. Dev.	Aperture
Ch. 1			
Ch. 2			
Ch. 3			

CORRELATION COEFFTS.	1 & 2	1 & 3	2 & 3

METEOROLOGICAL DATA

	MEAN	%age fletn.
Wind speed		
//'l comp.		
⊥ comp.		
Temperature		

RAIN: _____ Sky condition

DEC-TAPE REEL NO. _____

BLOCK NUMBER. (Inclusive)	CONTENTS	SAMPLING FREQ.	DATE			TAPE RECORDER		REMARKS
			Mnth	Day	Hr Min	Tape No.	Run No.	

Fig. 7.4

7.3 Analytical Processing

The available data was analysed to provide the following information:-

1. Standard deviation, time shifted cross-correlation coefficients and temporal plots.

2. Probability density functions.

3. Frequency spectra.

FORTRAN programs were written on the PDP-15 to carry out the required analysis. A brief review of the methods used and the structure of the programs will be given below.

1. Standard Deviation, Time Shifted Cross-Correlation Coefficients and Temporal Plots

The standard deviation for all three channels, together with the three cross-correlation coefficients, between the two amplitudes and the phase difference, were calculated as the data was sampled. This was done in program IAM and printed out. The cross-correlation coefficient r_{xy} between N pairs of the random variables x and y was calculated according to the following formula[66]:-

$$r_{xy} = \frac{\sum_{i=1}^{N} x_i\, y_i - N\langle x\rangle \,.\, \langle y\rangle}{\left[\left(\sum_{i=1}^{N} x_i^2 - N\langle x\rangle^2\right) \,.\, \left(\sum_{i=1}^{N} y_i^2 - N\langle y\rangle^2\right)\right]^{1/2}} \qquad (7.1)$$

Normally the cross-correlation coefficient is a function of

the time shift between the two random variables under investigation. Under some conditions, the maximum value of the coefficient occurred at a non-zero time shift. These conditions are discussed in detail in Chapter 8.

Program SHCOR was written to calculate and plot the cross-correlation coefficient versus the time shift. The program used two main subroutines - READ, which is described above and PLOTTR, which is a library plotting routine.

Temporal plots were obtained for any length of data record, up to 128 seconds at a sampling rate of 10 Hz. Therefore, the time-scale resolution was variable.

2. Probability Density Functions

The probability density function was calculated as a high resolution histogram. The lower and upper limits for the data values, over which the function was to be calculated, are specified by the user. Also specified was the number of slots in which the data points were counted. An increased number of slots provides a higher resolution.

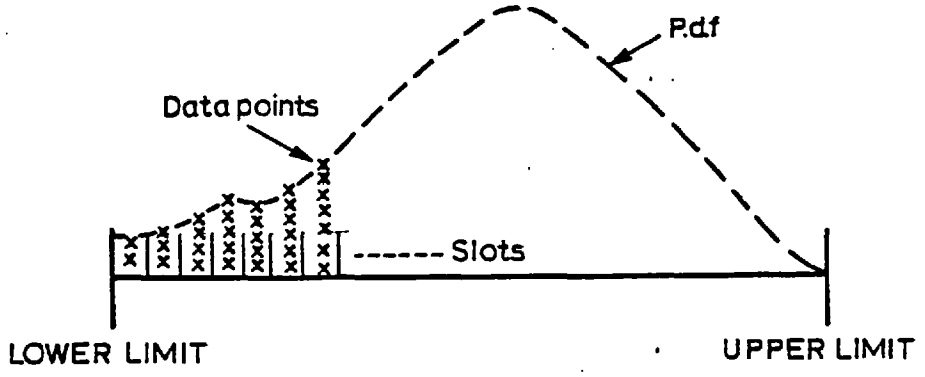

A program DISLOG was written to calculate and plot probability density functions. The data was read off Dectape via the assembler subroutine READ. The mean value was then removed, with an option for taking the logarithmic value of the data. A cumulative probability

distribution was also calculated and plotted.

3. Frequency Spectral Analysis

The spectral analysis was carried out using a College computer-library, Fast Fourier Transform (FFT) subroutine. The subroutine chosen was based on the Cooley-Tukey method of transformation. This method provides a relatively fast means of computing the frequency power spectra, since it does not require the intermediate computation of the autocorrelation function. The library subroutine was trimmed to "fit in" the PDP-15 computer without loss of accuracy.

Because of the digital nature of the time series under investigation, and its limited record length, some problems arise in the computation of the spectra. These have been discussed in detail in several monographs[66, 67] and papers[68, 69]. The possibly serious problems which may arise in the present data analysis were considered to be aliasing, leakage, d.c. swamping and variation of the spectral estimates.

These problems will be briefly discussed below, together with the approaches used to overcome them.

(a) Aliasing

The aliasing problem arises when the sampling rate is less than the maximum frequency present in the signal under consideration. Consider a sampling frequency f_s; therefore, the folding frequency is $f_s/2$. Beyond this folding frequency, the spectrum will repeat itself as a mirror image. Hence if a frequency higher than $f_s/2$ is present in the data, it will appear in both sides of the mirror spectrum, thus giving false spectral estimates[66]. The Nyquist criterion to avoid aliasing is to have the sampling frequency twice that of the highest

frequency component.

In the data analysis carried out, a sampling frequency of 10 Hz was used. A 3-channel active low-pass filter cutting off at 4 Hz was used before the ADC.

To further ensure the suppression of higher frequencies, which might possibly arise from the digitization or tape-storage process, a digital band-stop filter was made available before the Fourier transformation. The stop band of the filter was user defined and was usually set at 5 Hz. The development of the digital filter is given in Appendix V.

The decision to limit the sampling frequency to 5 Hz was made after observing the real-time spectrum of the signals on a scope. The spectrum was calculated by a saicor spectrum analyzer and was rarely observed to exceed 2 Hz.

(b) Leakage

The problem of leakage is well studied in the literature[66, 69]. It is due to the fact that the data under investigation is limited in duration. This is equivalent to the multiplication of an ideally finite data record by a rectangular window in the time domain. Therefore, the resultant frequency spectrum is the convolution of the Fourier transforms of these functions. Since the Fourier transform of the rectangular window is a sinc function, therefore, the calculated spectral components are not pure, but contain "sidelobes". The adjacent sidelobes interfere with each other, thus creating frequency components which are not present in the original time series.

A reduction of the leakage problem may be achieved by varying the data window from the simple rectangular one. The desirable effect of the various windows is to reduce the magnitudes of the sidelobes. However, other effects are also present, these mainly being a reduction

in the main lobe height and a decrease in the frequency resolution[70].

The window chosen to partially reduce the leakage was a Hamming window. The analogue form is:-

$$A(t) = 0.08 + 0.46 \left[1 - \cos \frac{2\pi t}{T}\right] \qquad (7.2)$$

where: T = the length of the data record.

t = 1, 2, ... N , N is the number of sampled points.

The Hamming window causes a reduction in the level of the sidelobes of 41.9 decibels. At the same time, the frequency resolution of each spectral component is only reduced by 80%[70].

(c) d.c. Swamping

The presence of a high d.c. component or linear trend in the data causes the resulting power spectrum to have a large peak at zero or very near zero frequencies. Such a peak would over-ride and swamp the other spectral components, thus reducing their significance.

As previously mentioned in Chapter 6, the mean value was eliminated by a mean-removal amplifier prior to recording. Any linear trends were also removed by this amplifier. In addition to the practical removal of the mean value, any residual d.c. component was calculated and analytically removed before the Fourier transformation.

(d) Smoothing of the Spectral Estimates

The estimate of the power spectral density function produced as a straight-forward transform of a single data record is inconsistent[66]. The normalized standard error which defines the random portion of the estimation error, ε_r, has been shown to be[66]:-

$$\varepsilon_r = \sqrt{\frac{2}{n}} \tag{7.3}$$

where n is the number of degrees of freedom of the sampling distribution of each frequency component of the power spectrum. If the transform is calculated from a single data record, n is equal to 2. This is due to the fact that the transform is the summation of a real and an imaginary part. Substituting in Equation (7.3), ε_r is equal to unity. This means that the standard deviation of the estimate is as great as the quantity being estimated which is unacceptable. Increasing the length of the data record does not produce any reduction in ε_r.

The smoothing of the estimates and hence a reduction of ε_r may be achieved in two ways[66]. The first is to smooth over an ensemble of estimates. This is achieved by splitting the data record into q segments; the estimates are then calculated for each individual record. The magnitude of the final spectral component is taken as the average over the q estimates. The second way is to smooth over frequency. This is done by averaging the spectral estimates over ℓ overlapping segments obtained from a single sample record. The two methods produce the same reduction in ε_r for $q = \ell$.

It may be shown[66] that the resulting averaged estimates will have n degrees of freedom, with $n = 2q$. Therefore, the resulting ε_r is $1/\sqrt{q}$, which is the value of the error reduction.

The first method, namely, the smoothing over an ensemble of estimates was used in the calculation of the power spectra. In calculating the spectra, the data was read off Dectape in 256 word blocks. For a sampling rate of 10 Hz, each block corresponds to a 25.6 seconds data record. The data was Fourier transformed and the spectral estimates were stored in array form; a second data block was then read off Dectape and similarly transformed. The process was carried on for

q blocks and the resulting spectral estimates were continuously averaged over q. Usually q was taken to be 5 blocks and, hence, the error reduction was $1/\sqrt{5}$, i.e. 45%.

The number of segments q may have been taken to be greater than 5 for the same overall number of data points, hence each segment would have contained a number of data points less than 256. Increasing q would result in a higher error reduction. However, decreasing the number of data points to be transformed also results in a lower number of spectral estimates and, hence, a deterioration in the frequency resolution.

Taking into account the above considerations, the procedure followed in calculating the frequency power spectrum is shown in a flow chart, Fig. 7.5.

The averaged spectral estimates were transmitted to the CDC-6600 College computer for further analysis. Curve fitting routines were utilized to calculate the slopes and for band width calculations. However, the fitted curves were sometimes observed to be biased towards the higher end of the log-frequency spectrum. Therefore, in some cases, fake estimates for the slopes were obtained. Therefore, the spectral slopes were calculated by observation from log-frequency plots obtained from the PDP-15 computer.

In some cases, the analysis required was quite simple, e.g. calculation of the percentage fluctuations of the signals under investigation. In such situations, a TEK31 programmable calculator was used to sample on-line and calculate the required quantities.

The following chapter shows the results obtained from the experimental link. The results were obtained by means of the above-described procedures and data processing techniques.

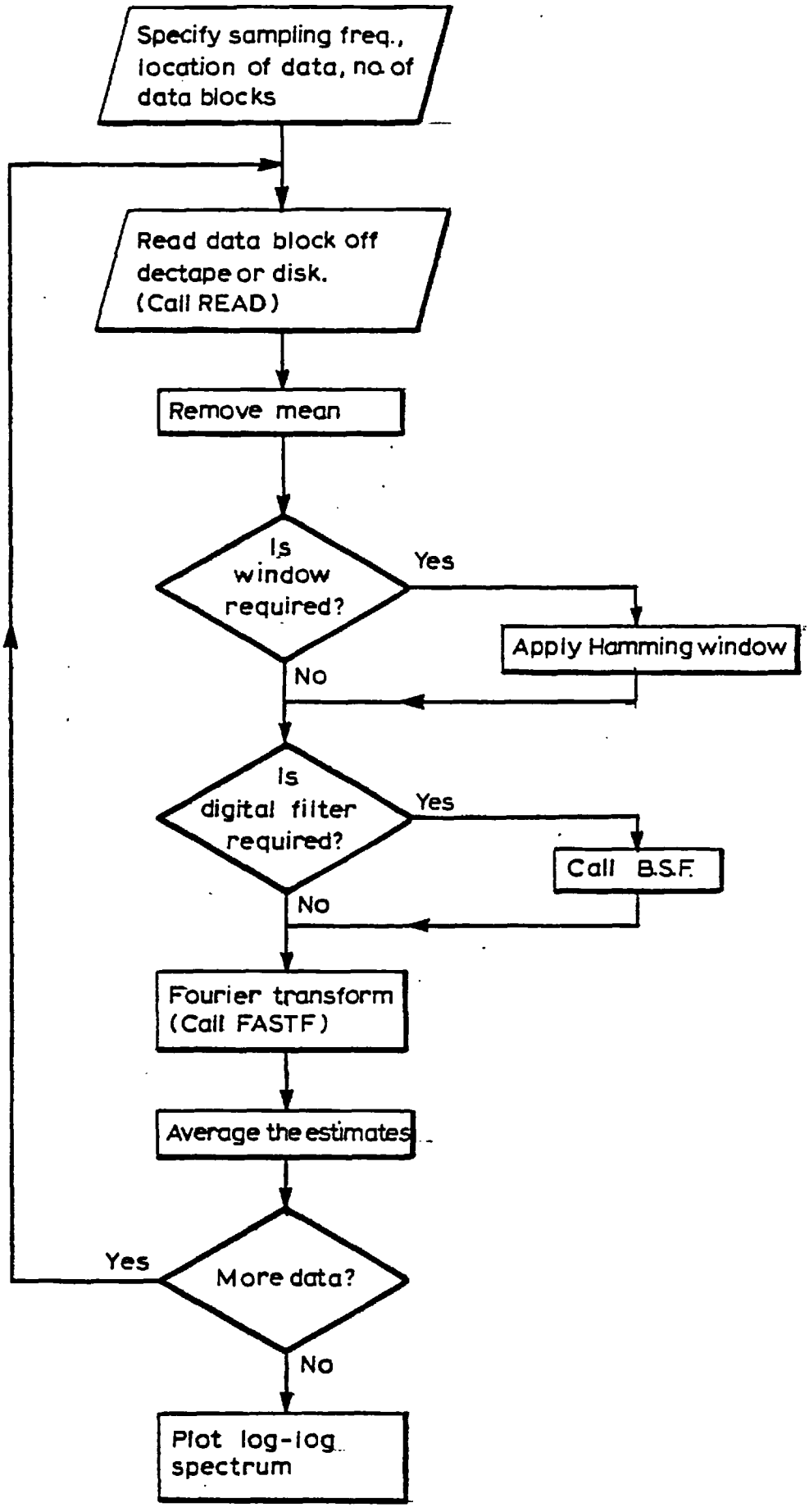

Fig.7.5: Program FTLOG for the calculation and plotting of the frequency power spectrum

CHAPTER 8

EXPERIMENTAL INVESTIGATION OF THE EFFECTS OF AN URBAN ENVIRONMENT ON AN 8-MILLIMETRE PROPAGATING WAVE

The results obtained from the 38 GHz interferometer receiver will be presented and discussed. The availability of an interferometer provided an opportunity to carry out a variety of experiments. These were made to examine different aspects and consequences of an incident randomized wave-front. The primary objective was to estimate the extent of the partial destruction of the lateral coherence across the wave front. This may be determined by the magnitude and lateral scale-size of the amplitude and phase distortions.

The results are divided into three sections. The first one deals with some aspects of the amplitude fluctuations. The magnitude and the frequency spectra are calculated, together with examples of the refractive index fluctuations. The lateral correlation is examined as a function of the receiver separation. The lateral scale-size of the amplitude fluctuations is also estimated from the experimental observations.

The second section is an investigation of the phase difference fluctuations. Examples of the magnitude and probability density functions of the phase difference fluctuations are given. The presence of large scale angle-of-arrival fluctuations is investigated by measuring the phase difference at different receiver separations. Spectra of the phase difference fluctuations are calculated and compared with those of the corresponding amplitude fluctuations.

Following the investigation of the amplitude and phase distortions, the effect of the receiver aperture size is looked into. Experiments determining the variation of the aperture averaging effect

and the simultaneous gain variations of a comparatively large receiving aperture relative to a smaller one are outlined together with the relevant results obtained.

It has been found experimentally that the effect of the medium on the propagating wave is almost insignificant from a practical point of view. The amplitude and phase difference fluctuations were very small under various atmospheric conditions. Therefore, long term measurements which would correlate the fluctuations with the different atmospheric parameters would be difficult to interpret and are unnecessary from a practical point of view.

Hence the experimental results displayed are for examples of short term measurements. These show the range of fluctuations observed under various atmospheric conditions.

8.1 Investigation of the Amplitude Fluctuations

8.1.1 Magnitude of the Amplitude Fluctuations Observed by an 0.25 Metre Dish

In the following analysis the magnitude of the signal fluctuations will be determined and measured as a percentage value. This is a convenient and practically useful measure of the short term fluctuations given as a ratio of the standard deviation to the mean value of the signal variations.

The percentage fluctuations for a particular propagation path may be theoretically predicted from the coupling formula obtained in Chapter 5. For circularly symmetrical antennas, and assuming an isotropic random medium, where the scale-sizes of the refractive index irregularities may be considered to be similar in all directions, and equal to r_o. The percentage power fluctuations may be shown from Equations (5.23) and (5.25) to be:-

$$\frac{VAR[U]}{|<U>|^2} \cdot 100 = \frac{\sigma_\phi^2}{1 + \frac{2w_T^2}{r_0^2}} \frac{\pi^2(w_T^2 + w_R^2)^2 + \lambda^2 L^2}{\pi^2(w_T^2 + w_R^2)(m^2 + w_R^2) + \lambda^2 L^2} \cdot 100 \qquad (8.1)$$

The percentage amplitude fluctuations may be considered to be the square root of the above quantity.

Substituting for w_R, w_T, λ and L by the experimental link figures, i.e. w_T = 0.3 metres, w_R = 0.12 metres, λ = 8 millimetres and L = 11.6 kilometres. Therefore, the percentage amplitude fluctuations as a function of the medium scale-size r_0, and the variance of the refractive index fluctuations σ_n^2, is shown in Fig. 8.1. It is seen that increasing r_0 and/or increasing σ_n^2 causes an increase in the percentage fluctuations. The rate of increase is observed to be larger for the smaller scale-sizes.

To determine experimentally the percentage amplitude fluctuations, the following setup, shown in Fig. 8.2, was used:-

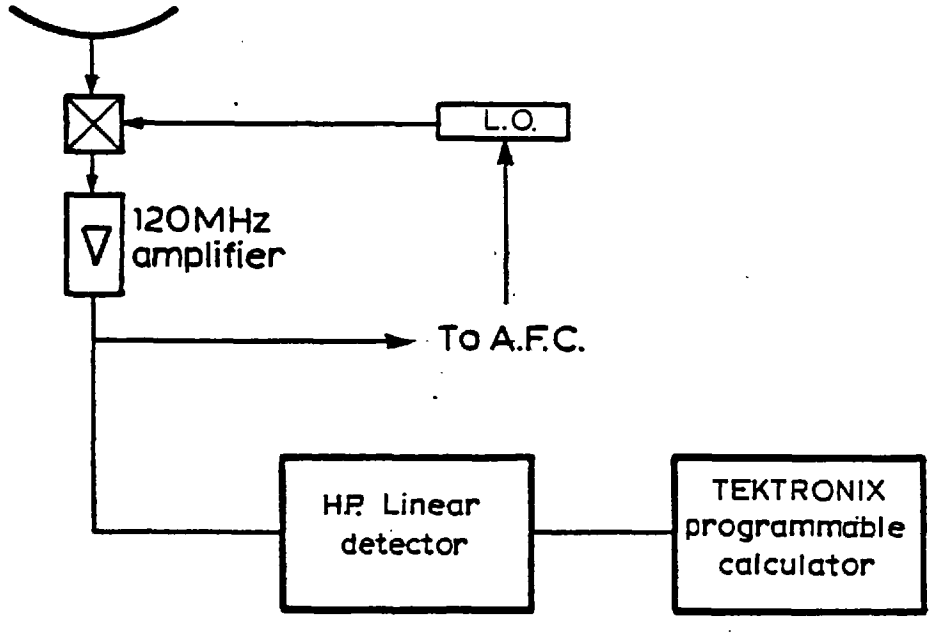

Fig. 8.2 Receiver setup for measurement of single-channel amplitude fluctuations

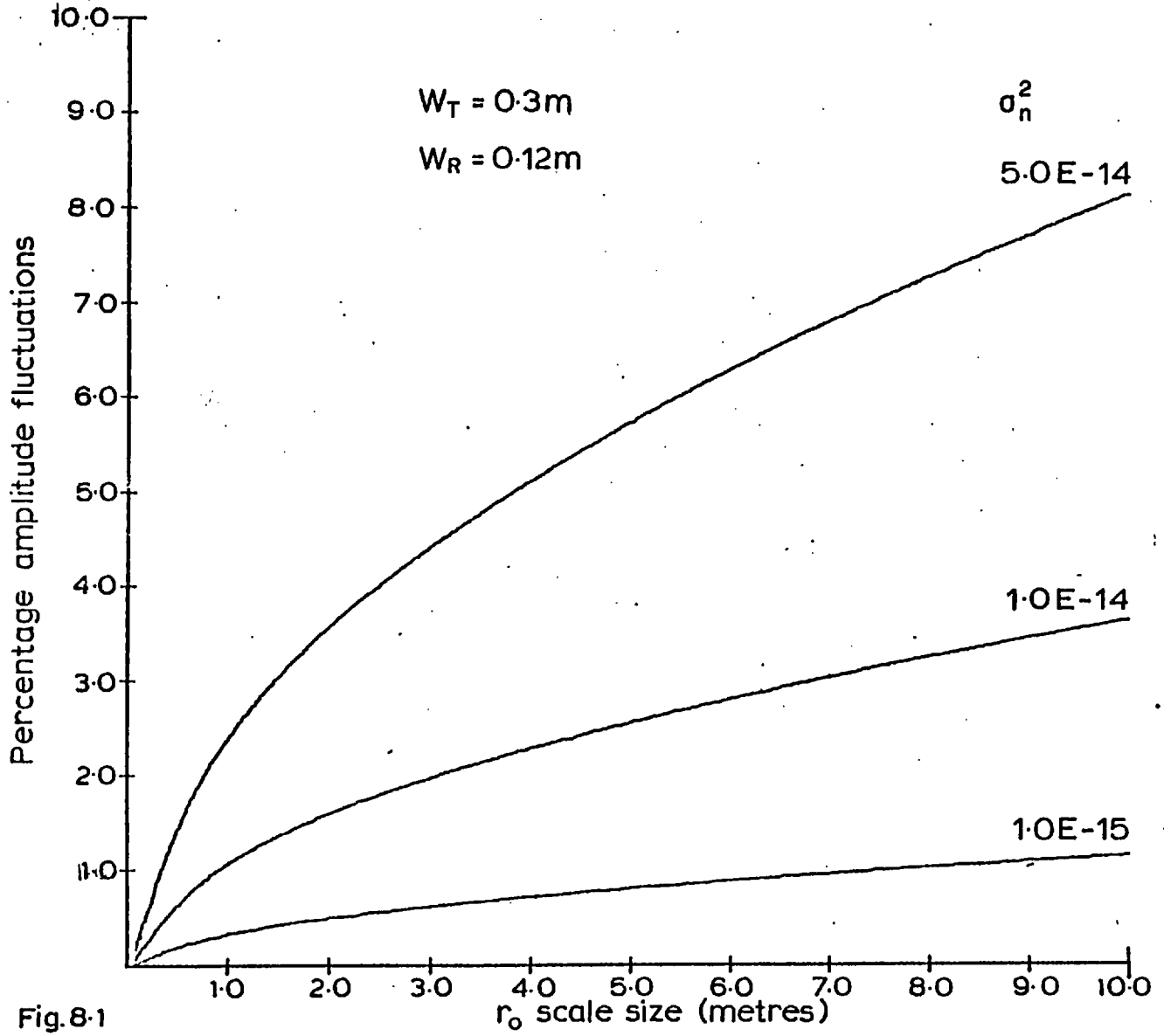
10·0
9·0
8·0
7·0
6·0
5·0
4·0
3·0
2·0
1·0
Percentage amplitude fluctuations
W_T = 0·3m
W_R = 0·12m
σ_n^2
5·0E-14
1·0E-14
1·0E-15
1·0
2·0
3·0
4·0
5·0
6·0
7·0
8·0
9·0
10·0
r_o scale size (metres)

Fig. 8·1

The receiving antenna which was an 0.25 metre diameter dish was clamped in position throughout the experiment to avoid pointing errors. The output of the Hewlett-Packard linear detector, which is proportional to the amplitude of the 120 megahertz input signal, was sampled by a Tektronix programmable calculator. The sampling rate was 2.0 samples/second and the data record was two minutes long. The calculator then calculated the mean value and standard deviation of the signal and hence the percentage fluctuations.

The above setup was used instead of the interferometer system detectors, because of the linearity of the Hewlett-Packard detector over a much wider range and hence the ratio of the fluctuations to the mean value would be more accurate.

Table 8.1 shows the results of the above experiment which was carried out throughout August, 1978. Shown in the table are the measured percentage fluctuations and the prevailing weather conditions.

The table, which includes some examples of the percentage fluctuations observed, indicates that the percentage fluctuations are very low, bearing in mind that a 1% fluctuation is equivalent to a variation of approximately 0.09 decibels. It is worthwhile noting here that the percentage fluctuations give an indication as to the amount of noise contributed by the random medium.

It may be seen from Table 8.1 that the percentage fluctuations increase as the temperature increases; the exact long-term relationship is difficult to determine due to the relatively limited period of time over which this particular experiment was carried out. However, an increase in temperature possibly indicates an increase in the energy of the refractive index irregularities, i.e. an increase in σ_n^2 and/or an increase in their scale-size. An increase in either factor would cause an increase in the percentage fluctuations as shown in Fig. 8.1. Under

TABLE 8.1

Date and Time	Percentage Fluctuations	Sky Condition	Temp. Degrees Cent.	Wind Velocity metres/sec
9/8				
1220	0.72	Cloudy		
1435	1.38	Rain at transmitter only		
1450	2.66	Light rain across total path		
11/8				
1015	0.81	Sun, haze	13	
1225	1.48	Sun, haze	17	
1425	0.98	Sun, haze	22	
14/8				
1020	0.59	Sunny and some cloud	13	
1400	0.92	Sunny and some cloud	18	
1545	1.42	Sunny and some cloud	19	8.0
1715	1.82	Sunny and clear	19	8.0
15/8				
0715	0.51	Cloudy	10	8.0
0815	0.44	Cloudy	11	8.0
0915	0.25	Cloudy	11	4.0
0930	0.30	Cloudy	11	4.0
1505	1.15	Sunny and some cloud	17	10.0
18/8				
0955	2.25	Sun	17	2.5
1010	1.78	Sun	17	3.0
1425	1.09	Sun	20	2.5
22/8				
1120	1.07	Sun, haze	17	
1430	1.80	Cloudy	19	
1730	0.93	Overcast	17	
29/8				
1010	0.93	Cloudy, haze	12	
1300	1.17	Cloudy	12	
1635	0.62	Overcast	14	
1750	0.46	Overcast	14	
1835	0.32	Overcast	14	
30/8				
1530	0.93	Sunny, clear	13	
1630	0.94	Sunny, clear	14	
1730	0.54	Sunny, clear	13	

light rain conditions, the percentage fluctuations are relatively quite high. This is probably due to a large σ_n^2 amd small scale-size of the irregularities. However, the coupling formula is intended mainly for predictions under clear-air turbulence conditions.

The percentage fluctuations seem to be at their highest level towards early afternoon and to be at their lowest level in the early morning and evening.

It is difficult to determine from this experiment the degree of turbulence indicated by σ_n^2 and the scale-size of the irregularities. However, previous measurements of σ_n^2 give values in the range of 1.0 . 10^{-14} n^2-units. Hence, from Fig. 8.1, this indicates that the effective scale sizes are predicted to be of the order of 10 metres.

8.1.2 Examples of the Frequency Power Spectra of the Amplitude and Refractive Index Fluctuations

In this section, some examples of the frequency power spectra of the amplitude fluctuations observed by the 0.25 metre diameter dish will be given. The examples shown are chosen such that they span the range of the fluctuations observed under various atmospheric conditions. First, an example of the relationship between the amplitude and refractive index power spectra will be given.

Relationship Between Amplitude and Refractive Index Power Spectra

Simultaneous measurements of the refractive index and the amplitude fluctuations were carried out for a brief period of time. Figs. 8.3a and 8.3b show the power spectra of the refractive index and the corresponding amplitude fluctuations respectively. The measurements were carried out at 1500 hours on August 1, 1978 under partly cloudy and mainly sunny conditions. The measured wind speed was 8.3 metres/second,

with a normal component of 2.0 metres/second. The air temperature was 20 degrees Centigrade. The spectra were calculated over a period of 3 minutes 25 seconds. The variance of the refractive index fluctuations was measured to be 1.8×10^{-14} n^2-units. The slope of the refractive index spectrum may be shown to be approximately - 1.9 (i.e - 5.7/3) decibels/Hz. The slope of the amplitude spectrum is approximately - 3.0 (i.e. - 9/3) decibels/Hz.

Figs. 8.3c and 8.3d show the power spectra of the refractive index and the corresponding amplitude fluctuations respectively. The measurements were also carried out on August 1 at 1740 hours under a mainly cloudy sky. The spectra were calculated over a period of 2 minutes 13 seconds. The mean wind speed was 6.4 metres/second, with a normal component of 3.5 metres/second. The air temperature was 13.0 degrees Centigrade. The variance of the refractive index fluctuations had dropped to 7.7×10^{-16} n^2-units. The slope of the refractive index power spectrum may be seen to be approximately - 1.6 (- 4.8/3) decibels/Hz and the slope of the amplitude power spectrum is approximately - 2.7 (- 8.1/3) decibels/Hz.

The above observations appear to agree to a certain extent to the predictions made by Tatarskii[58], namely, that the slope of the frequency power spectrum of the amplitude fluctuations is equal to m + 1, where m is the slope of the refractive index fluctuations.

In the above and following examples, the slopes of the frequency power spectra are determined through personal judgement. This is due to the fact that the computer programs which have been used to fit a third or fourth degree polynomial to the calculated spectra, and from which the slope is determined, do not accurately represent the calculated spectrum at the higher end of the spectrum.

Table 8.2 shows some examples of the variation of the frequency

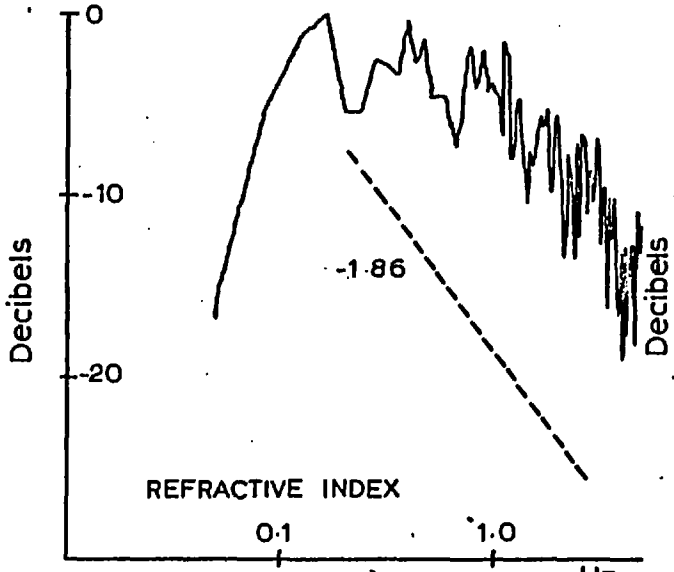

Fig. 8·3a

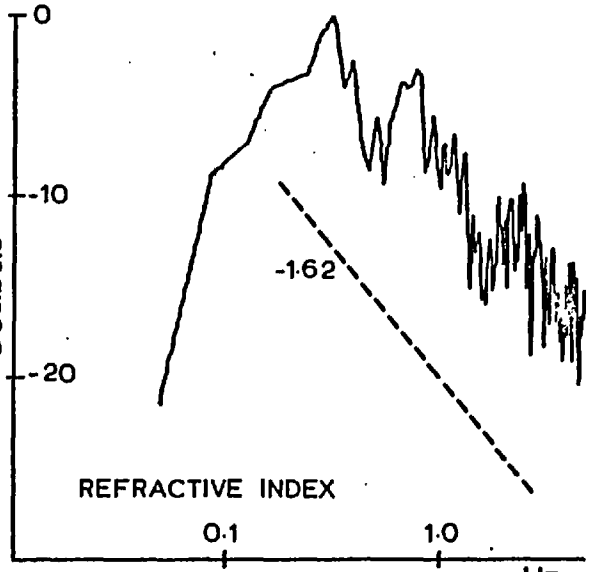

Fig. 8·3c

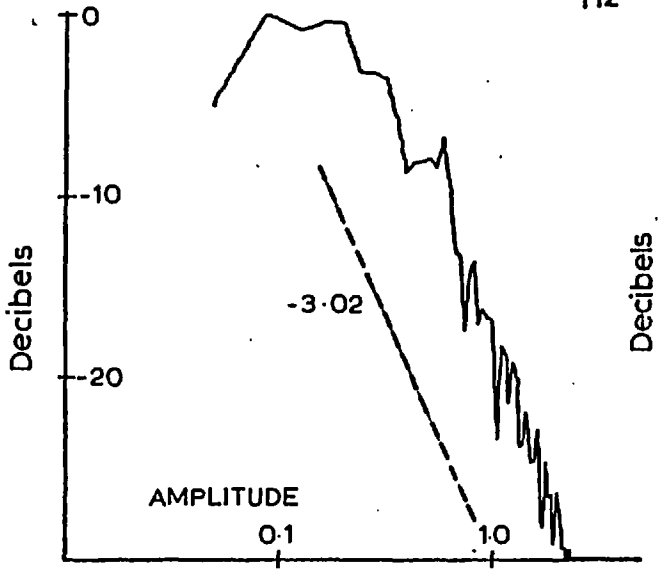

Fig. 8·3b

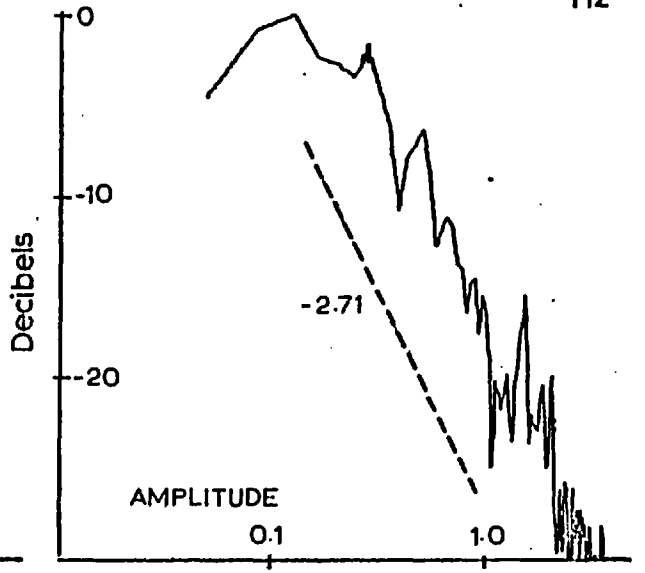

Fig. 8·3d

TABLE 8.2

Time	Fig.	Slope Decibels/Hz	Sky Cond.	Mean Wind Vel.		Temp. Deg. Cent.
				Total m/sec	Normal m/sec	
0850	8.4a	- 3.3 (- 9.9/3)	Sunny	2.5	0.7	20
1720	8.4b	- 3.7 (- 11.1/3)	Calm, hot	5.2	4.3	27
1115	8.4c	- 2.7 (- 8.1/3)	Calm, sunny	6.0	2.0	19
1020	8.4d	- 3.4 (- 10.2/3)	Drizzle, cool			

power spectra of the amplitude fluctuations observed under different atmospheric conditions. The slopes indicated in the table are obtained from the figures of the spectra shown in Figs. 8.4a, b, c and d. The spectra were all calculated over a period of 2 minutes 13 seconds.

It may be seen from the above examples that a variety of slopes may be observed under different atmospheric conditions. This is probably attributed to the various slopes of the spectra of the refractive index fluctuations under the prevailing atmospheric conditions. However, the slopes observed are close to approximately - 8/3 which agrees with similar measurements carried out in the summer of 1976 over London at a frequency of 36 GHz[22, 71].

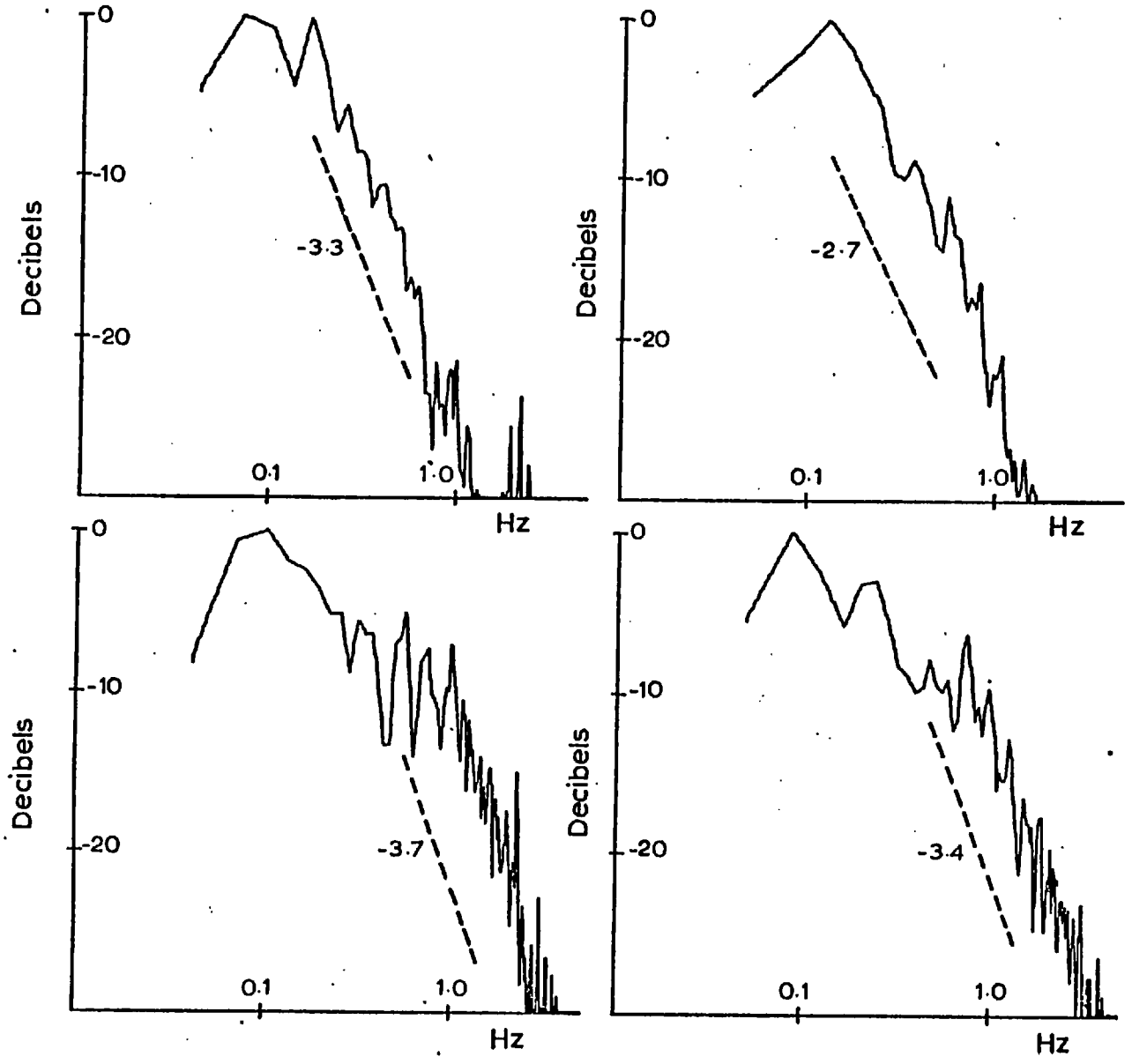

Fig. 8.4a

Fig. 8.4c

Fig. 8.4b

Fig. 8.4d

8.1.3 Measurement of the Cross-Correlation of the Amplitude Fluctuations

It has been previously shown (Chapter 4) that the lateral coherence function of a wave propagating through a random medium is partially destroyed. This indicates that the spatial amplitude and phase distribution of the electric field incident on the receiver plane normal to the direction of propagation are distorted from their free space value. In this section, the emphasis will be on the experimental investigation of the distortion of the amplitude distribution across the receiver plane by means of the interferometer system.

Due to the random nature of the medium irregularities, the scale-sizes of the amplitude distortions will vary randomly. It is expected that there is a distribution of lateral scale-sizes involved, with a certain amount of distortion associated with each scale-size. However, there probably exists a dominant scale-size which is determined by the distribution and strength of the medium scale-sizes. The figure below shows a hypothetical visualization of the distorted amplitude distribution across the receiver plane.

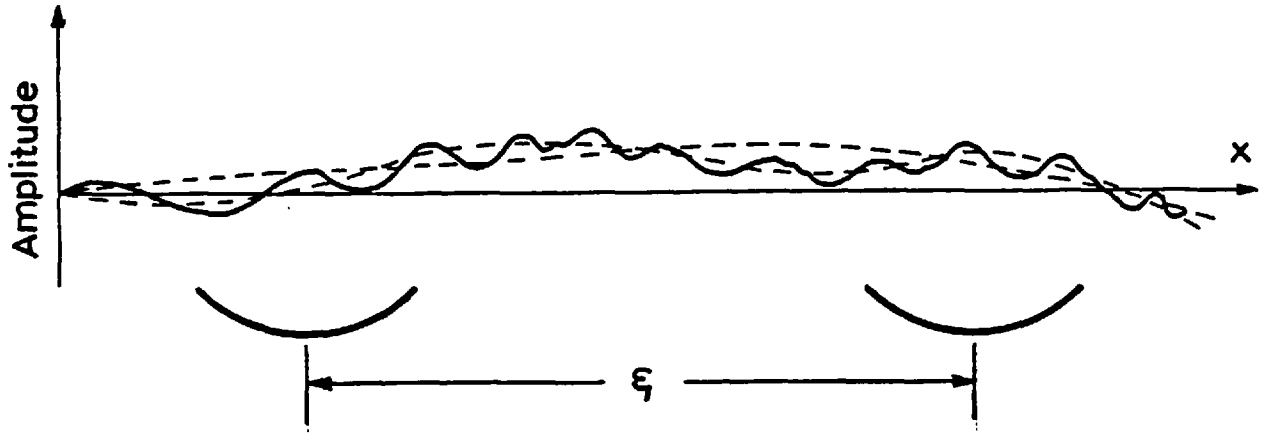

The results shown and discussed in this section are for the variation of the cross-correlation coefficient for the amplitude received

by two laterally spaced receivers. The variation of the correlation coefficient is investigated for different receiver separations ξ and for different weather conditions and, hence, different medium and amplitude distortion scale-sizes.

The cross-correlation coefficient is calculated for the two received signals as a function of a time shift between the signals as shown below.

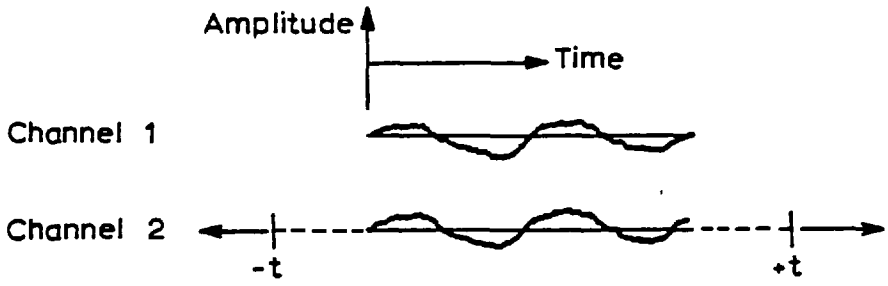

It must be noted here that the variation of the cross-correlation coefficient as a function of the time shift yields first-hand information for the temporal scale-sizes involved and not the spatial scale-sizes. The spatial scale-sizes may be deduced through knowledge of the wind velocity as will be shown later. Thus for relatively rapid temporal variations, the cross-correlation coefficient is expected to rapidly decrease as the time shift increases, whereas for slow variations, the decrease is expected to be relatively small as the time shift is increased.

Calculating the cross-correlation coefficient as a function of the time shift makes it possible to detect the maximum coefficient. This maximum is not necessarily obtained at a zero time shift. This may

be explained by considering Taylor's hypothesis of "frozen turbulence"[15], i.e. the refractive index inhomogeneities are "frozen in" and are carried along by the wind. The only motion of interest in this case is the transverse one.

Hence assuming Taylor's hypothesis, the field observed at a point x and at a time t, on the interferometer axis, is the same as the field observed at a point $(x + v_n \tau)$ at a time $(t + \tau)$ where v_n is the average wind velocity component normal to the propagation path.

Therefore, for two receivers separated by a distance ξ and assuming Taylor's hypothesis to be valid, the maximum cross-correlation coefficient occurs after a time shift τ_m where $\tau_m = \xi/v_n$.

Variation of the Cross-Correlation Coefficient with Receiver Separation

The results shown below are some examples of a number of experiments carried out in which the correlation coefficient was calculated at two different receiver separations, namely, at 0.8 and 3.0 metres. The antennas used were 0.25 metre dishes. The examples chosen are for some of the cases where the coefficient decreases appreciably with increased separation.

Figs. 8.5a and 8.5b show the cross-correlation coefficient versus time shift for receiver separations of 0.8 and 3.0 metres respectively. The time of the data records was 1045 hours and 1130 hours for the 0.8 and 3.0 metre separations respectively.

The relevant atmospheric conditions may be seen in Table 8.3.

The cross-correlation coefficients observed were 0.91 at τ_m = 0.2 seconds and 0.48 at τ_m = 0.5 seconds at receiver separations of 0.8 and 3.0 metres respectively. Hence the lateral amplitude correlation length for this particular measurement is less than 3.0 metres. It is

TABLE 8.3

Figure	Duration of Record seconds	Sky Condition	Air $^{o}_{C}$ Temp.	Mean Wind Velocity m/sec	Normal Wind Comp. m/sec
8.5a and 8.5b	25.6	Calm and sunny	19.0	6.2	3.9
8.6a and 8.6b	25.6	Sunny with cloud	20.0	5.0	0.4
8.7a and 8.7b	25.6	Sunny and haze	19.0	3.2	1.4

interesting to note that if Taylor's hypothesis is assumed to be valid, the normal wind velocity v_n would have to be 4.0 metres/second to produce a value of τ_m = 0.2 seconds for a receiver separation of 0.8 metres and 6.0 metres/second to produce a value of τ_m = 0.5 seconds for a receiver separation of 3.0 metres. The mean value of the cross-wind component was measured at the time of the experiment and had a value of 3.9 metres/second. Therefore, Taylor's hypothesis may be considered to be valid bearing in mind that the fluctuations in the wind velocity had a measured standard deviation of 0.4 metres/second.

Similarly it may be seen from Figs. 8.6a and 8.6b and 8.7a and 8.7b that the cross-correlation coefficient is relatively quite high, 0.85 and 0.84 respectively at a receiver separation of 0.8 metres. The coefficient is again seen in both cases to be almost insignificant at a separation of 3.0 metres. It may also be seen that Taylor's hypothesis is not obviously valid due to the relatively high wind velocities theoretically required to produce the observed τ_m. However, the possibility of short term variations in the wind velocity and direction occurring over the duration of the measurements must be taken into account.

It must be emphasized here that the examples shown do not represent the general trend observed for the variation of the cross-correlation coefficient with receiver separation, since in many cases the cross-correlation coefficient was quite low, i.e. less than 0.5, at a separation of 0.8 metres.

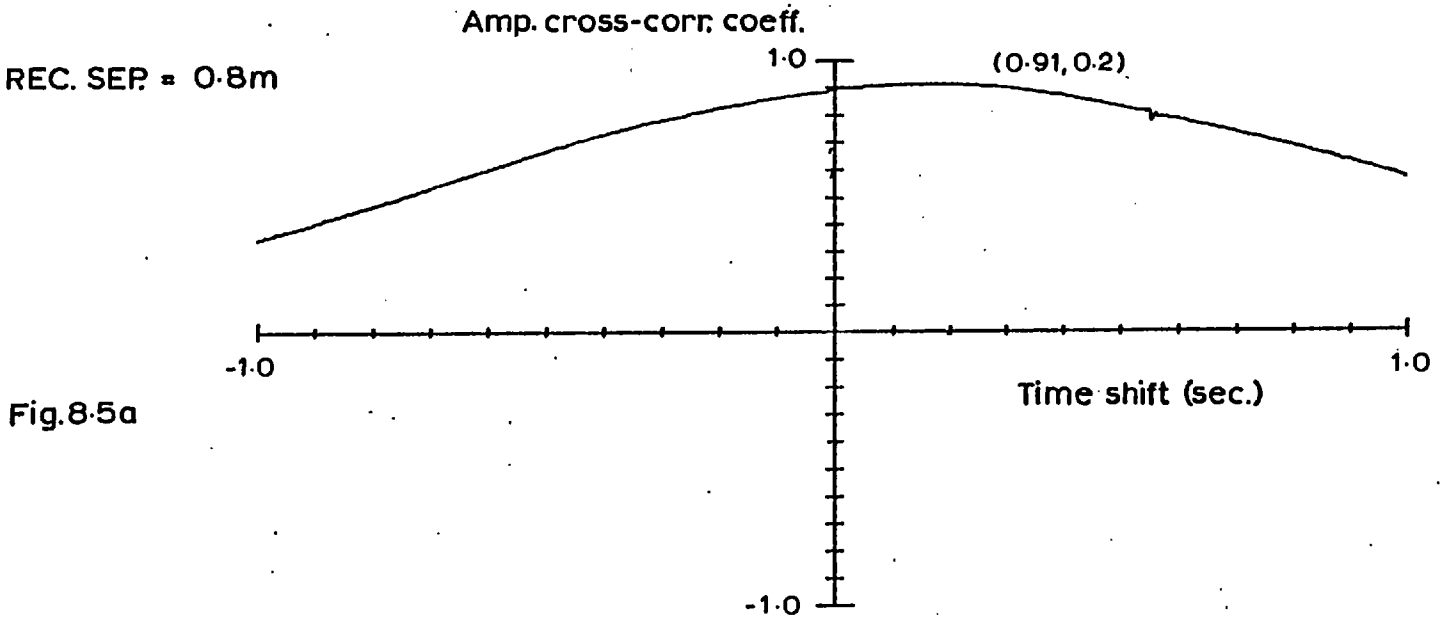

Fig. 8·5a

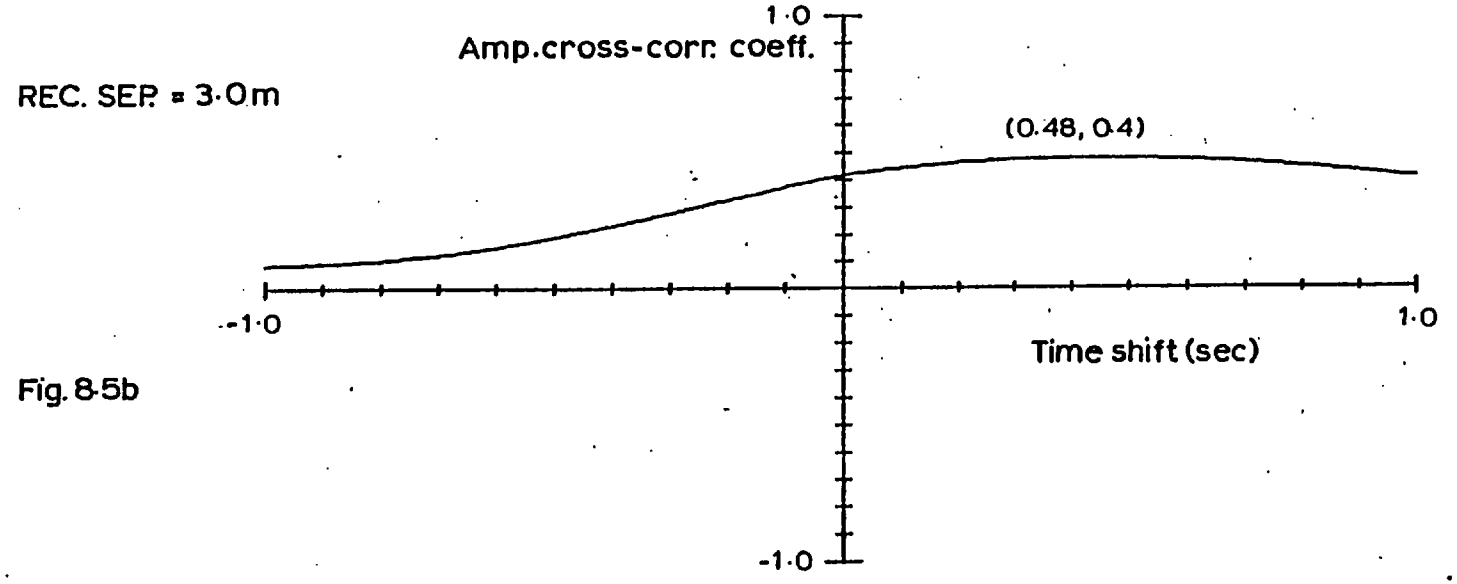

Fig. 8·5b

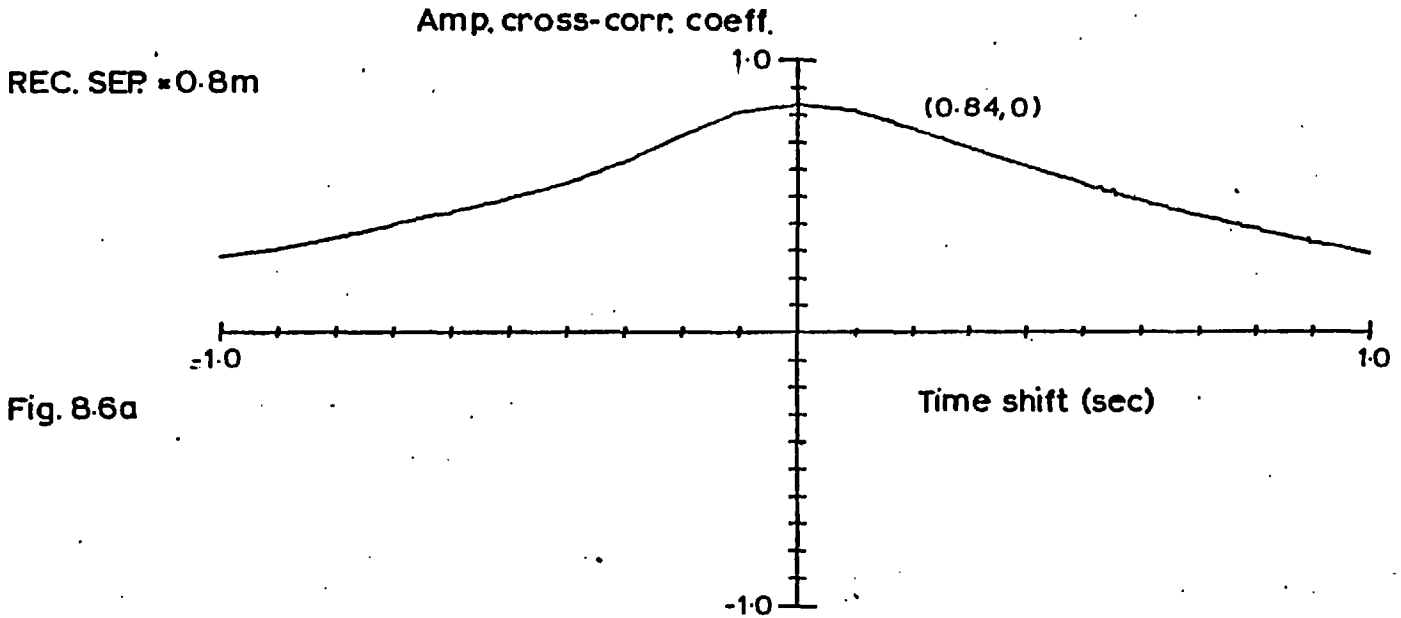

Fig. 8·6a

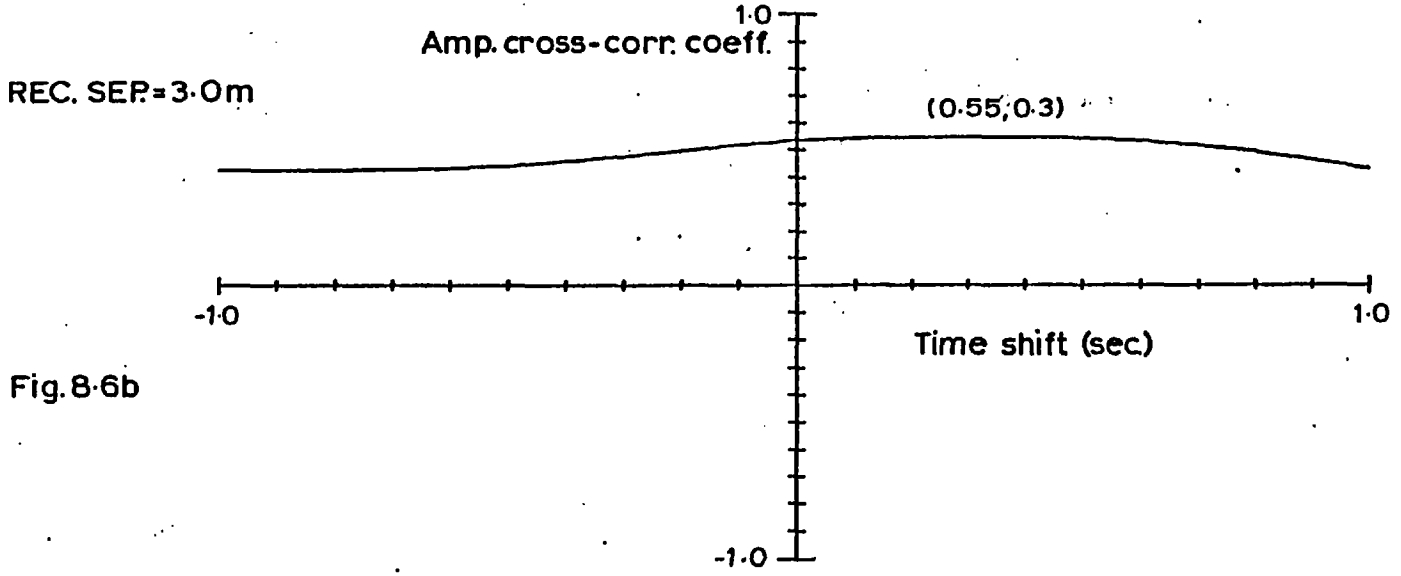

Fig. 8·6b

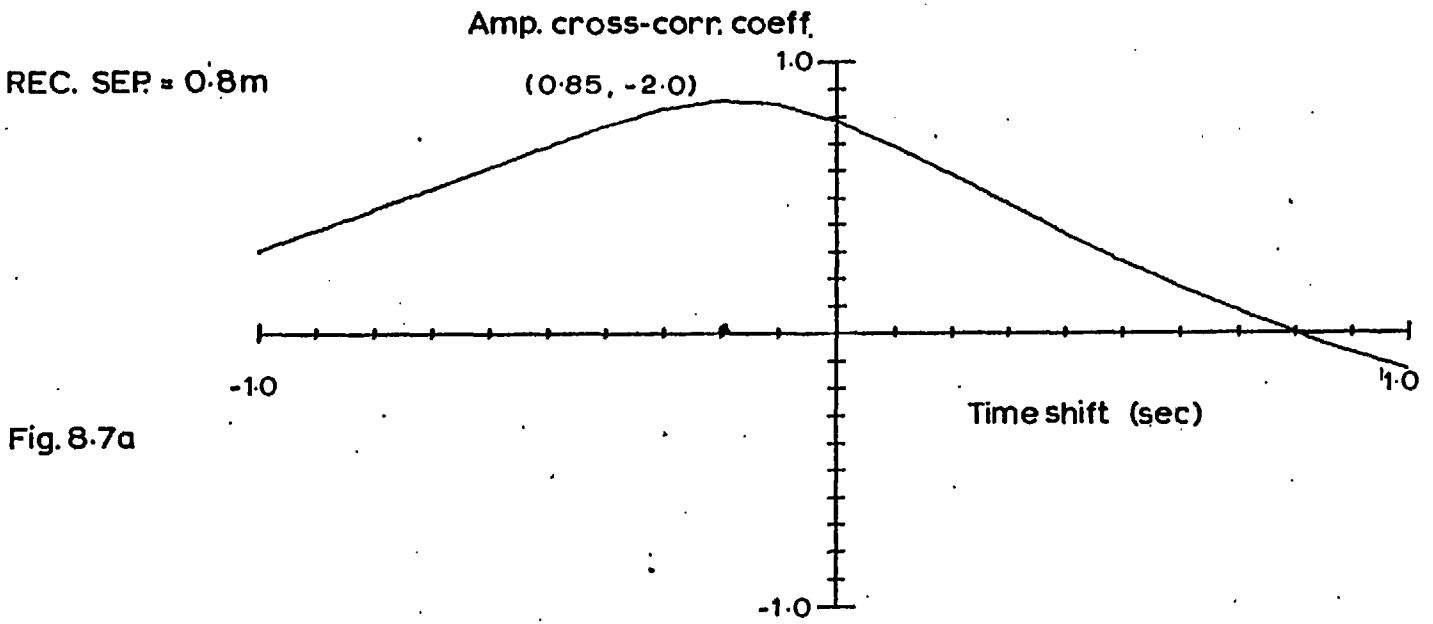

Fig. 8·7a

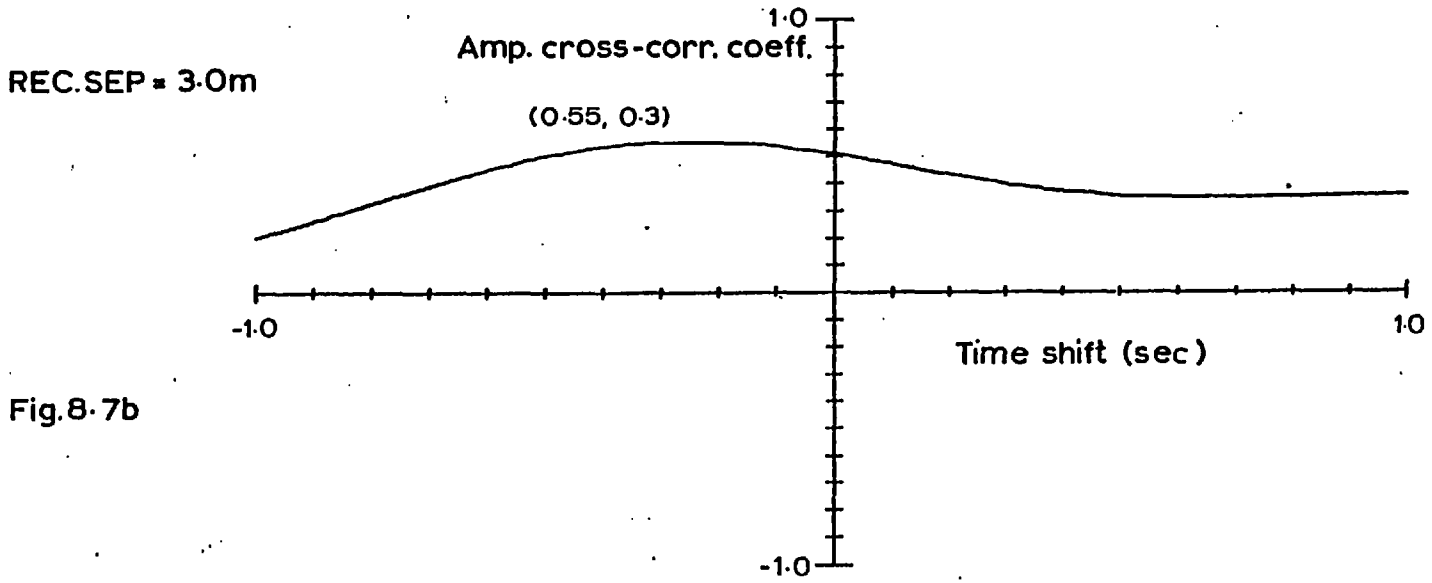

Fig. 8·7b

8.1.4 Estimation of the Effective Lateral Scale-Size of the Amplitude Fluctuations

The lateral scale-size of the amplitude fluctuations may be determined by investigating the variation of the cross-correlation coefficient as a function of a time shift between the two received signals. The effective lateral scale-size may be determined by considering the dominant periodicity in the cross-correlation coefficient versus time shift plot δt as shown in the figure below. Assuming Taylor's hypothesis to be valid as it has been shown to be occasionally true, and for a cross-wind velocity v_n, the dominant lateral scale-size ξ_0 is then given by:-

$$\xi_0 = v_n \cdot \delta t \qquad (8.2)$$

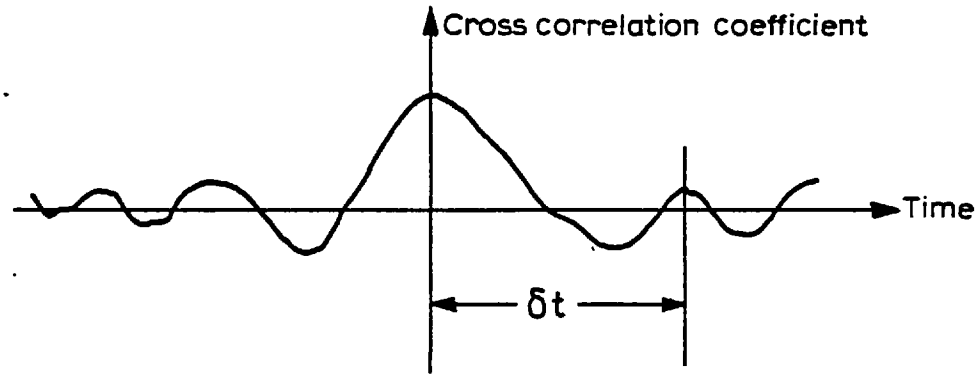

Figs. 8.8a, b, c and d show the cross-correlation coefficient plotted versus the time shift for various atmospheric conditions. The receiver spacing was 3.0 metres for all the cases shown.

Fig. 8.8a shows the situation for a cloudy and hot day ($24^{o}C$) with a wind velocity of 3.5 m/sec and a normal component of 3.0 m/sec. It may be seen from Fig. 8.8a that δt is approximately equal to 8.0

seconds. Hence from Equation (8.2) the dominant scale-size ξ_0 is approximately equal to 24.0 metres.

Fig. 8.8b shows the situation for a hot ($23^{o}C$) calm period, with a wind velocity of 0.6 m/sec and a normal component of 0.5 m/sec. δt is seen to be approximately 6.0 seconds. Hence ξ_0 is approximately equal to 12.0 metres.

Fig. 8.8c shows the situation for a relatively cool period ($16^{o}C$) with some cloud and a wind velocity of 8.0 m/sec with a cross-wind velocity component of 3.0 m/sec. δt is approximately equal to 2.5 seconds. Hence ξ_0 is approximately equal to 7.5 metres.

The dominant scale-size ξ_0 under light rain conditions may be seen to be quite small as is evident from Fig. 8.8d, where δt is seen to be approximately 1.0 second with a cross-wind velocity component of approximately 1.0 m/sec. ξ_0 is then approximately equal to 1.0 metres.

Comparison of the Vertical and Horizontal Lateral Scale-Sizes of the Amplitude Fluctuations

An estimate of the vertical scale-sizes may be obtained using the same method as detailed above, with the interferometer placed in a vertical position. The antennas used in this case were the two 35.25 mm horns. The separation between both antennas was 0.7 metres.

Figs. 8.9a and 8.9b show the cross-correlation coefficient plotted versus the time shift for a vertical and a horizontal interferometer respectively. The horizontal measurements were carried out using the 50 millimetre horns at a separation of 0.8 metres. There was a two-hour difference between both data records. However, the atmospheric conditions were quite similar with sun and some cloud with a moderate breeze.

It may be seen from Figs. 8.9a and 8.9b that the periodicity

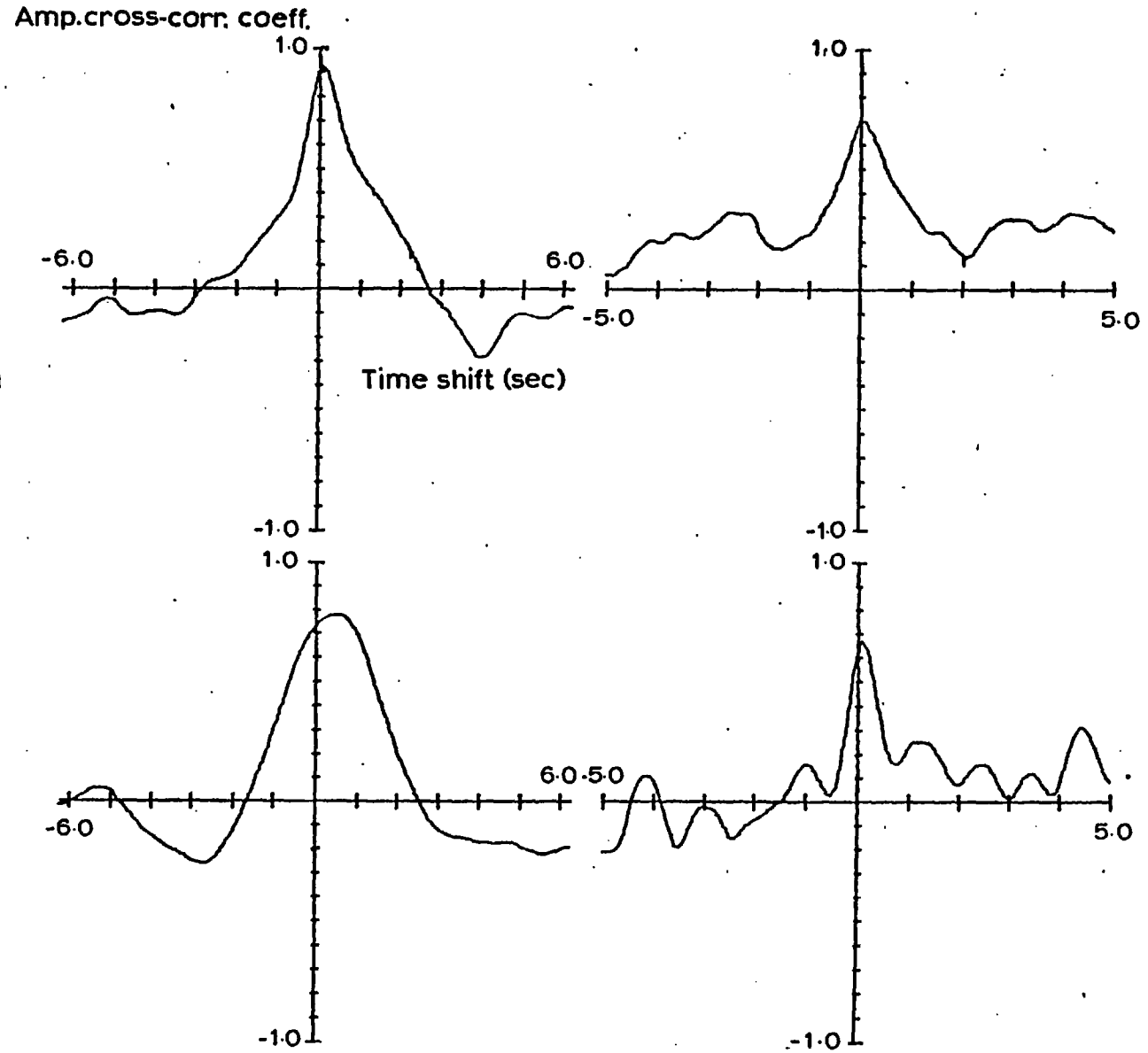

Fig. 8·8a

Fig. 8·8c

Fig. 8·8b

Fig. 8·8d

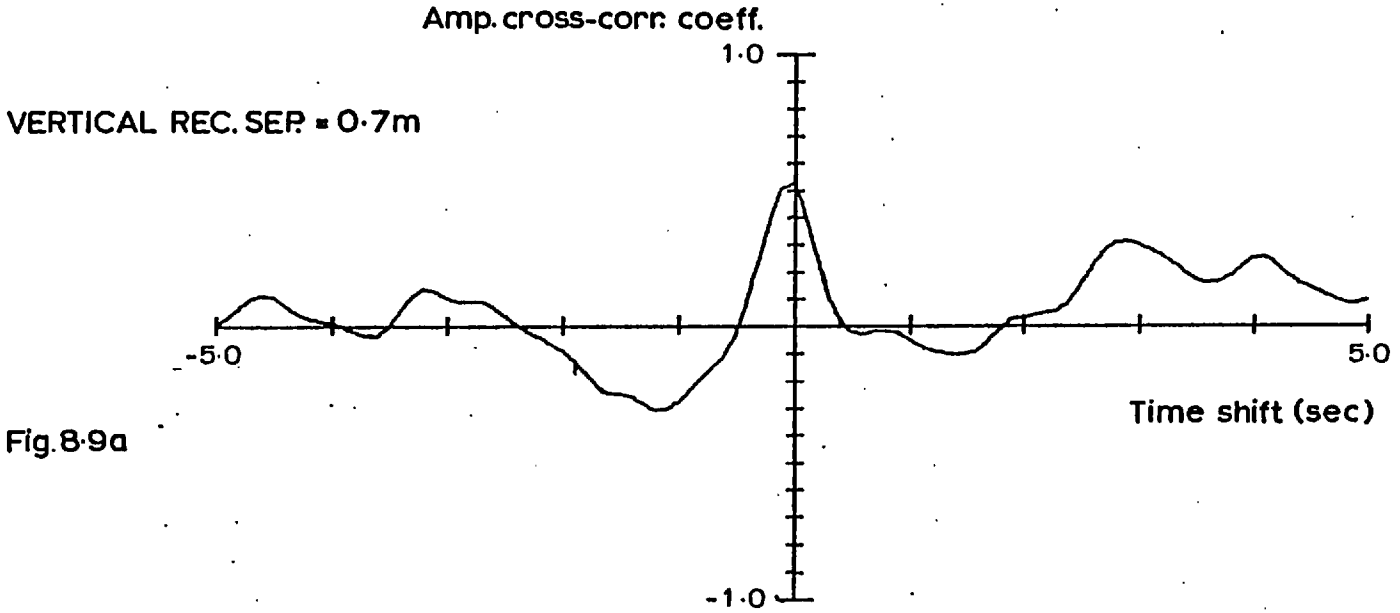

Fig. 8·9a

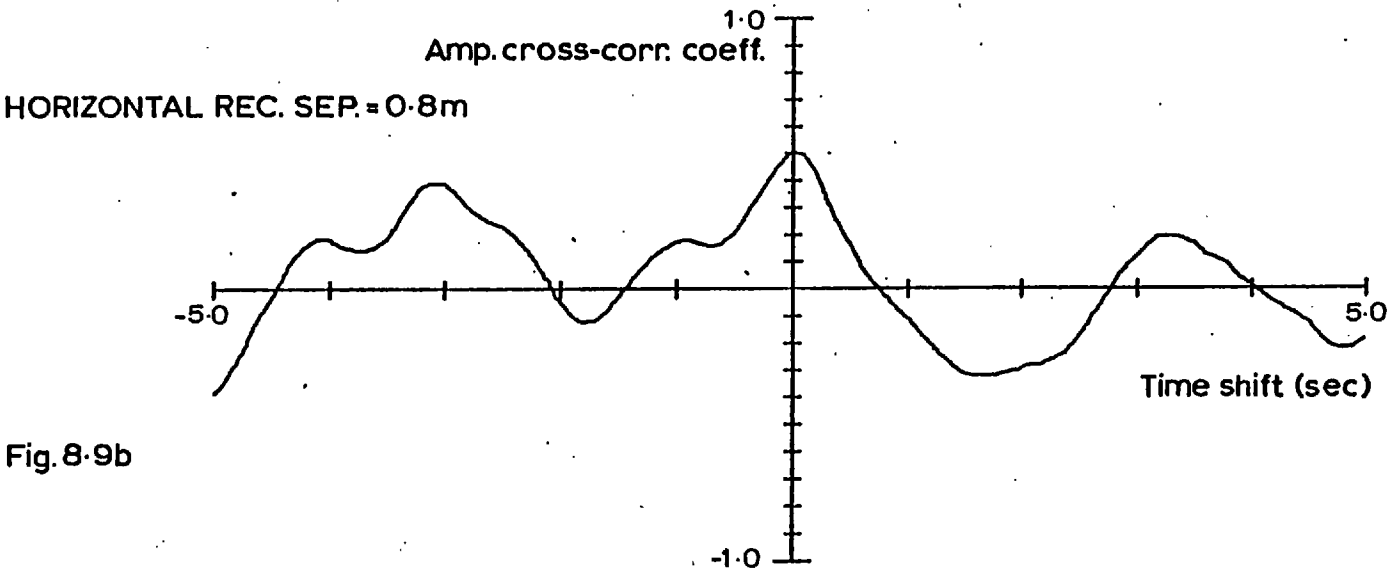

Fig. 8·9b

in both cases is quite similar with a value of δt approximately equal to 3.0 seconds. Hence for this particular period of time, it may be seen that the horizontal and vertical scale-sizes are of the same order of magnitude.

8.2 Investigation of the Phase Difference Fluctuations

One of the main purposes of the interferometer receiver system was to estimate the extent of the distortion of the free-space phase distribution across the receiver plane and induced by the random medium. The phase difference measured between both receivers situated along the x-axis and separated by a distance ξ is a direct means of obtaining the phase structure function $D_\phi(\xi)$, which is defined as:-

$$D_\phi(\xi) = \left\langle \left[\phi(x) - \phi(x + \xi) \right]^2 \right\rangle \tag{8.3}$$

To predict the behaviour of $D_\phi(\xi)$ and its variation as a function of the medium parameters, the phase screen approach discussed in Chapter 3 will be considered. It was previously shown that the medium may be collapsed into a thin phase screen situated at the transmitter site which gives rise to amplitude and phase fluctuations in the receiver plane. Since we are only concerned with the phase fluctuations at the moment, therefore, to facilitate the estimation of the phase structure function, the phase screen will be assumed to be situated at the receiver plane. The parameters of the phase screen will be considered to be equivalent to those determined in Chapter 3. Therefore, $D_\phi(\xi)$ is given by:-

$$D_\phi(\xi) = \left\langle \left[\phi(x) \right]^2 \right\rangle + \left\langle \left[\phi(x + \xi) \right]^2 \right\rangle - 2\langle \phi(x) \, . \, \phi(x + \xi) \rangle$$

Since the phase process is a zero mean one and for a homogeneous medium, therefore:-

$$D_\phi(\xi) = 2\sigma_\phi^2 \left[1 - r_\phi(\xi)\right] \tag{8.4}$$

Hence for a Gaussian refractive index autocorrelation function with a scale-size ξ_0 and for σ_ϕ^2 defined as in Equation (3.4), the phase structure function which is equivalent to the variance of the phase difference fluctuations is given by:-

$$D_\phi(\xi) = \sigma_{\Delta\phi}^2 = 2\sqrt{\pi} \cdot \sigma_n^2 \cdot k^2 \cdot L \cdot \zeta_0 \left[1 - e^{-\xi^2/\xi_0^2}\right] \tag{8.5}$$

Fig. 8.10 shows the variation of $\sigma_{\Delta\phi}$ as a function of the receiver separation ξ, with the medium scale-size ξ_0 as a variable parameter. The value of the variance of the refractive index fluctuations σ_n^2 is taken as 5.0×10^{-14} n^2-units. The longitudinal scale-size ζ_0 is taken to be equal to the lateral one ξ_0. The curves shown are calculated for an 11.6 kilometre path and a wavelength of 8 millimetres.

For small scale-sizes, less than the receiver separation, and hence the autocorrelation function $r_\phi(\xi)$ becomes negligibly small, $\sigma_{\Delta\phi}$ increases to a steady value of $\sqrt{2}\,\sigma_\phi$. As the scale-size is increased beyond the receiver separation, the phase difference fluctuations may be considered to be angle-of-arrival fluctuations, where the angle-of-arrival γ is shown in the figure below.

$$\gamma = \sin^{-1}\left[\frac{\{\phi(x) - \phi(x + \xi)\}}{k \cdot \xi}\right] = \sin^{-1}\left[\frac{\Delta\phi}{k \cdot \xi}\right] \tag{8.6}$$

For small values of $\Delta\phi$, γ is approximately given by:-

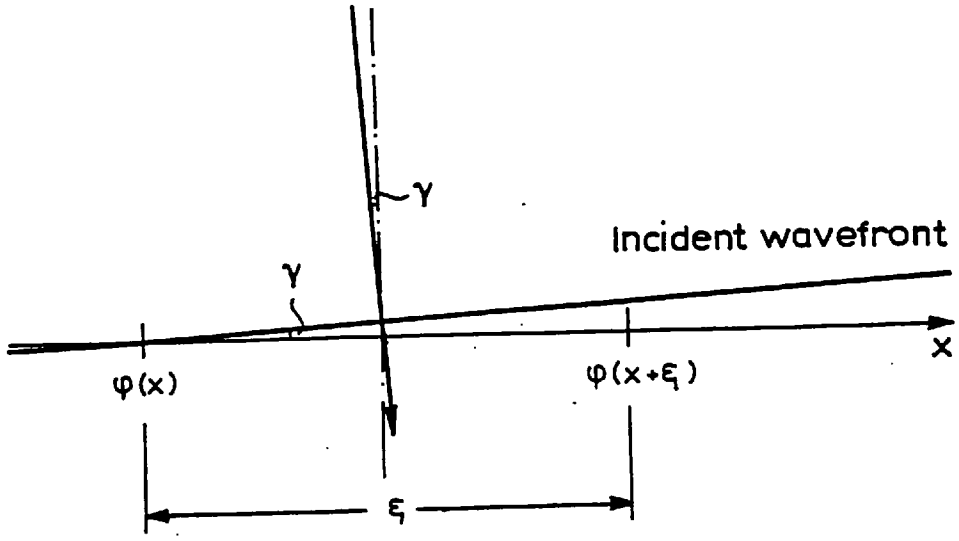

$$\gamma \simeq \frac{\Delta\phi}{k \cdot \xi}$$

and hence:-

$$\sigma_\gamma^2 \simeq \frac{1}{(k \cdot \xi)^2} \cdot \sigma_{\Delta\phi}^2 \qquad (8.7)$$

For a wave length of 8 millimetres, i.e. k = 785, the fluctuations in the angle-of-arrival may be seen to be very small.

Fig. 8.11 shows the variation of $\sigma_{\Delta\phi}$ as a function of the medium scale-size ξ_0, with the receiver spacing as a variable parameter. It is interesting to note that a certain $\sigma_{\Delta\phi}$ measured at a fixed receiver separation may possibly arise from two different scale-sizes. This ambiguity is more apparent at the larger receiver separations. However, this ambiguity may be resolved by carrying the measurements out at different separations.

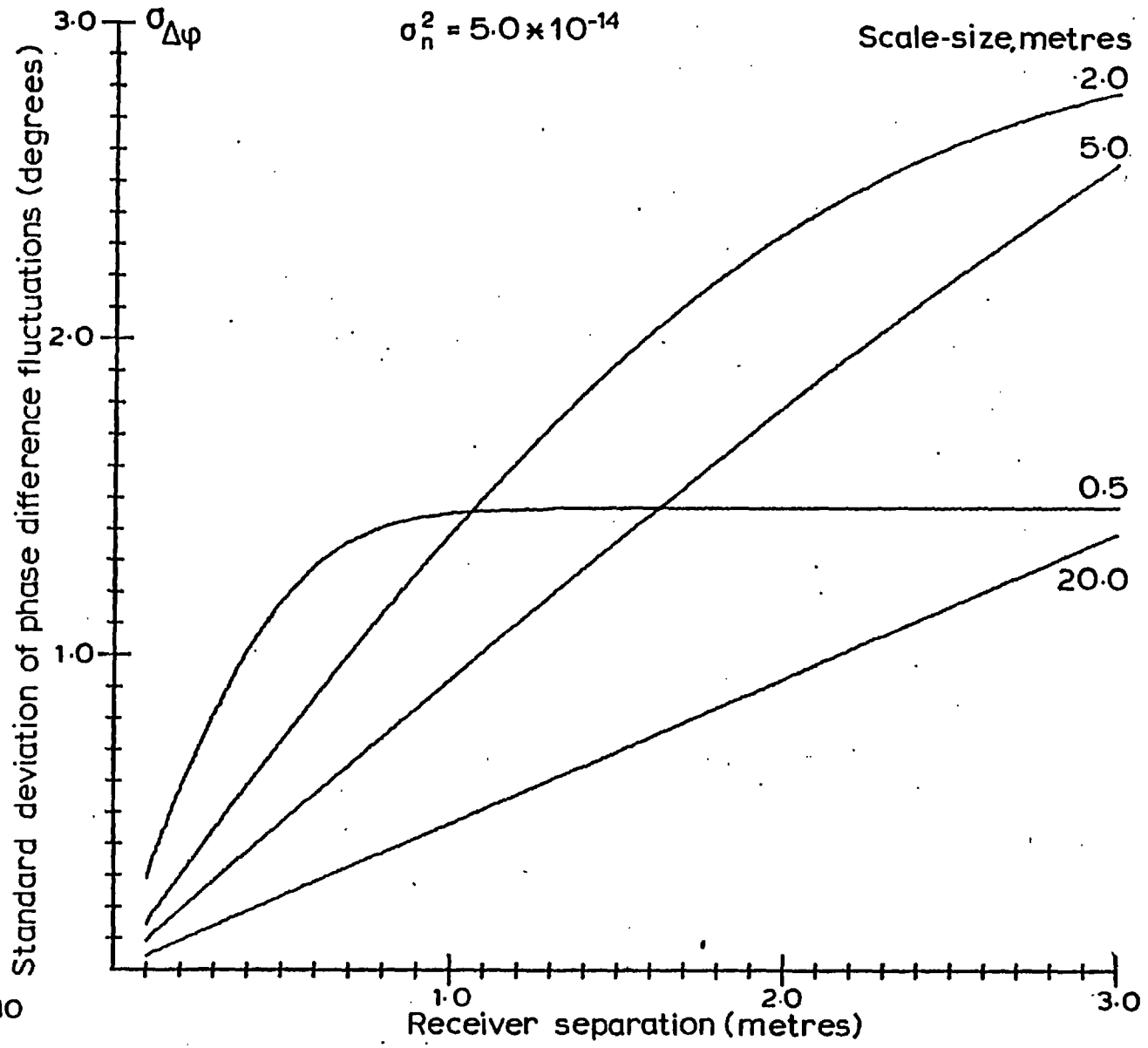
$\sigma_{\Delta\varphi}$
$\sigma_n^2 = 5.0 \times 10^{-14}$
Scale-size, metres
2·0
5·0
0·5
20·0
3·0
2·0
1·0
Standard deviation of phase difference fluctuations (degrees)
1·0
2·0
3·0
Receiver separation (metres)

Fig. 8·10

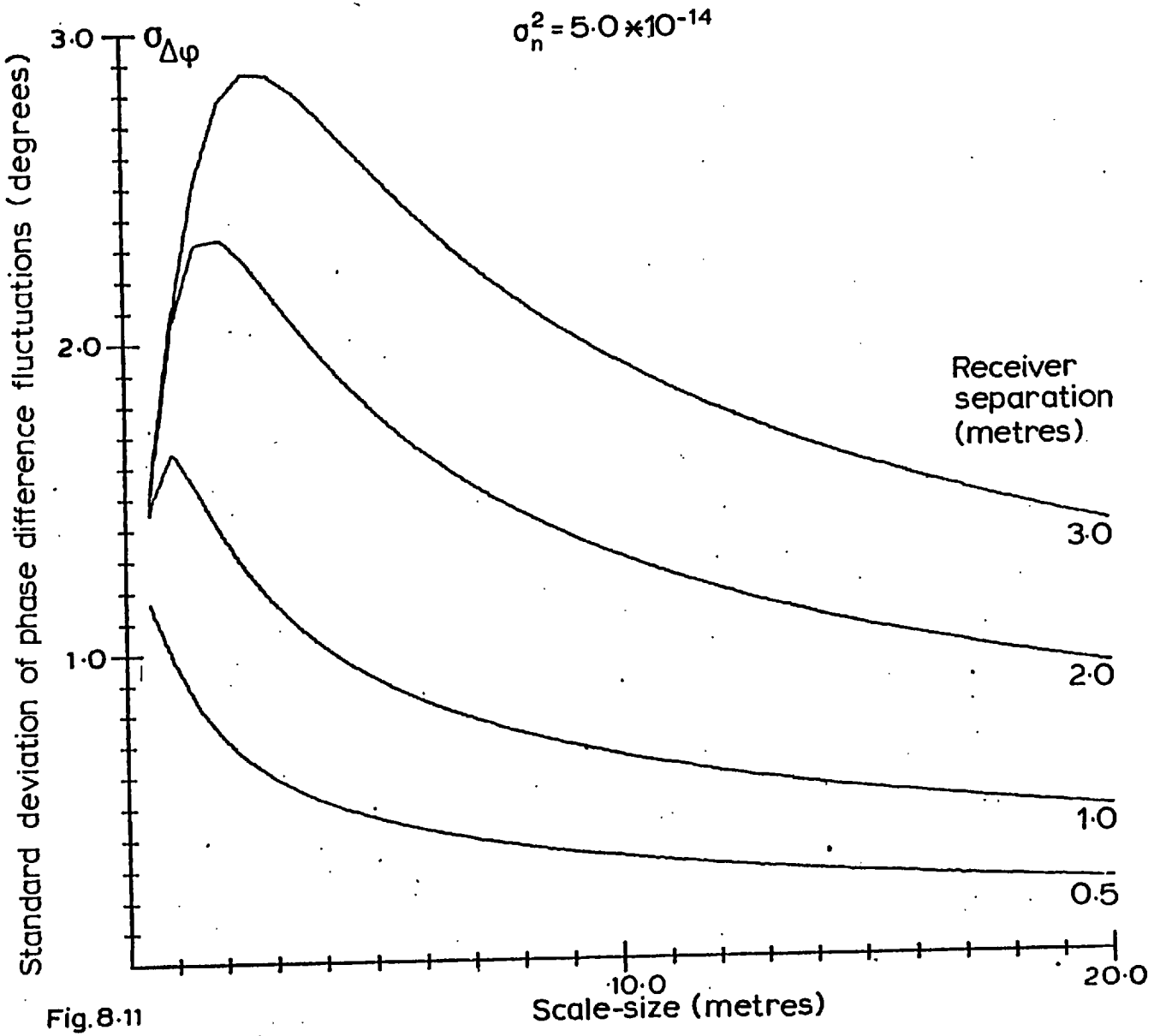
$\sigma_{\Delta\varphi}$
$\sigma_n^2 = 5{\cdot}0 \times 10^{-14}$
3·0
2·0
1·0
Standard deviation of phase difference fluctuations (degrees)
Receiver separation (metres)
3·0
2·0
1·0
0·5
10·0
20·0
Scale-size (metres)

Fig. 8·11

8.2.1 Magnitude of the Phase Difference Fluctuations Under Different Atmospheric Conditions

In this section, some examples of the phase difference fluctuations will be given together with their probability density functions. The examples are chosen such that they cover a cross-section of the observed fluctuations. The receiving antennas in the examples shown were the 0.25 metre diameter dishes. The receiver separation was fixed at 3.0 metres.

The relevant atmospheric conditions pertaining to the examples shown are given in Table 8.4 together with the cross-correlation coefficient between the amplitude and phase-difference fluctuations to give an indication of angle-of-arrival effects on the amplitude variations.

It may be seen from the following figures that the phase difference fluctuations range from ± 1 degree to ± 30 degrees, which was the highest observed fluctuation. Due to the apparent lack of correlation of $\sigma_{\Delta\phi}$ with the measured atmospheric parameter, the underlying mechanism mainly affecting the fluctuations is not readily obvious.

However, the scale-sizes of the distortions in the incident wave front may be deduced from the predicted curves in Figs. 8.10 and 8.11. This may be done by estimating the variance of the refractive index fluctuations σ_n^2 and by noting the variation of $\sigma_{\Delta\phi}$ with receiver separation. From the various observations made, it may be predicted that the effective scale-sizes range from less than 0.5 metres to approximately 10 metres. However, no definite conclusion can be made due to the unknown variations in σ_n^2 which were not monitored during the period of the experiment.

An interesting phase difference fluctuation which was observed

TABLE 8.4

Figure	Time of Meas.	$\sigma_{\Delta\phi}$ Deg.	$r_{A,\ \Delta\phi}$	Sky Condition	Wind Velocity m/sec		Temp. ^{o}C
					Total	Normal	
8.12	18.50	0.28	- 0.16	Sunny and clear	3.7	1.3	20
8.13	16.00	3.54	0.12	Sunny	4.3	4.3	26
8.14	08.50	6.60	0.95	Sunny	2.5	0.7	20
8.15	10.20	0.92	0.03	Drizzle			

at 0850 hours is shown in Fig. 8.14. Measurements made within a short period of time at a smaller separation (0.8 metres) and resulting in a much smaller $\sigma_{\Delta\phi}$ (1.6 versus 6.6 degrees), confirmed the presence of large scale angle-of-arrival fluctuations. This is further confirmed by the high cross-correlation coefficient (0.95) with the amplitude fluctuations. The other measurements shown have not displayed any of the angle-of-arrival effects mentioned above.

The probability density functions are all seen to be quite symmetrical. For small scale-size phase distortions as confirmed by non-decreasing $\sigma_{\Delta\phi}$ at smaller separations, it may be assumed that the individual phase fluctuations at each receiving aperture are uncorrelated. Hence in those situations which are shown in Figs. 8.12, 8.13 and 8.15, the probability density function of the phase fluctuations is likely to be equivalent to those of the phase difference fluctuations. The probability density functions appear to be quite close to a Gaussian distribution. This is in agreement to the prediction made in Chapter 3, Section 3.4.2, where the phase fluctuations due to a Gaussian refractive index autocorrelation function were predicted to be Gaussian distributed.

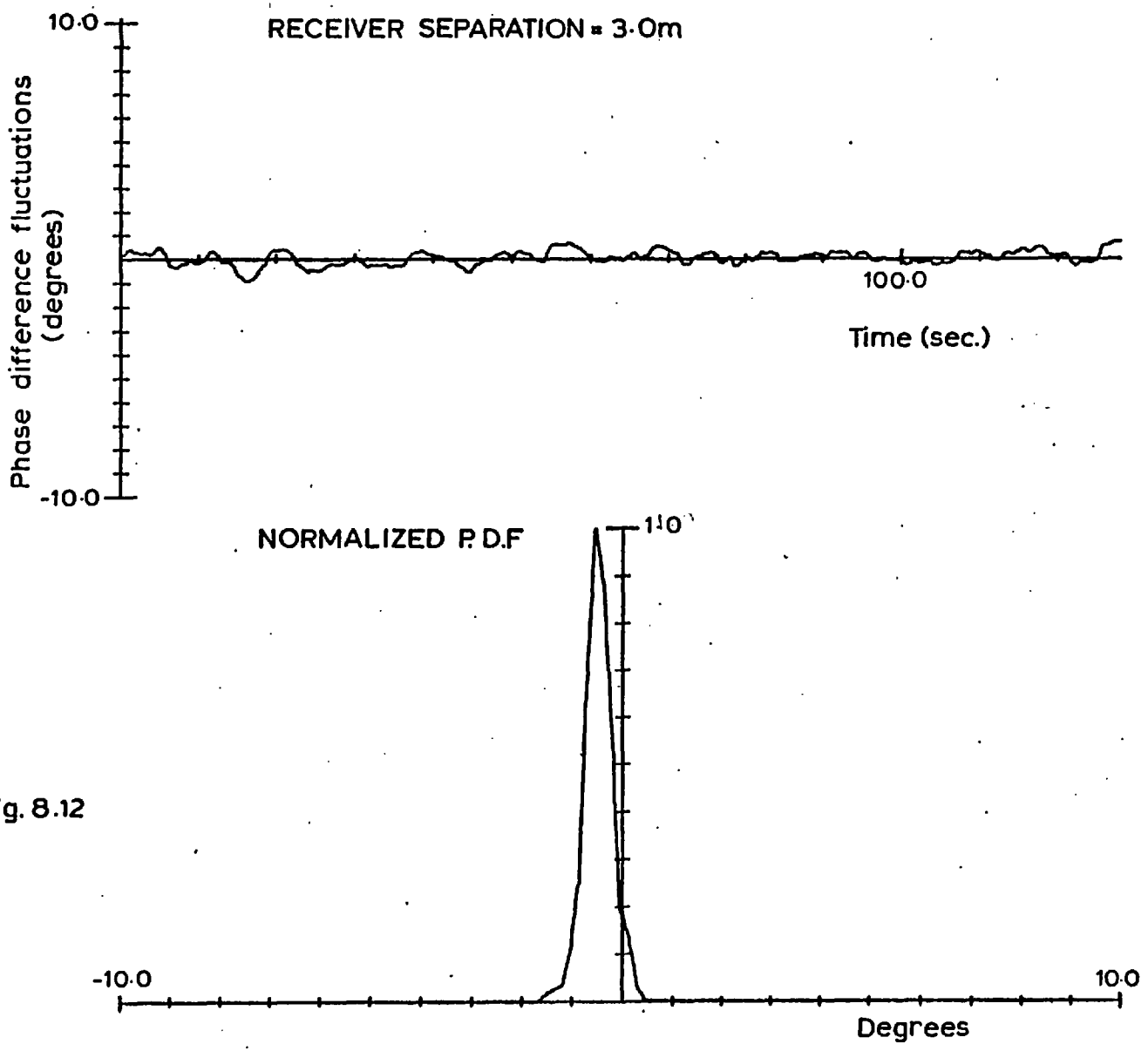
RECEIVER SEPARATION = 3·0m
10·0
-10·0
Phase difference fluctuations (degrees)
100·0
Time (sec.)
NORMALIZED P.D.F
1·0
-10·0
10·0
Degrees

Fig. 8.12

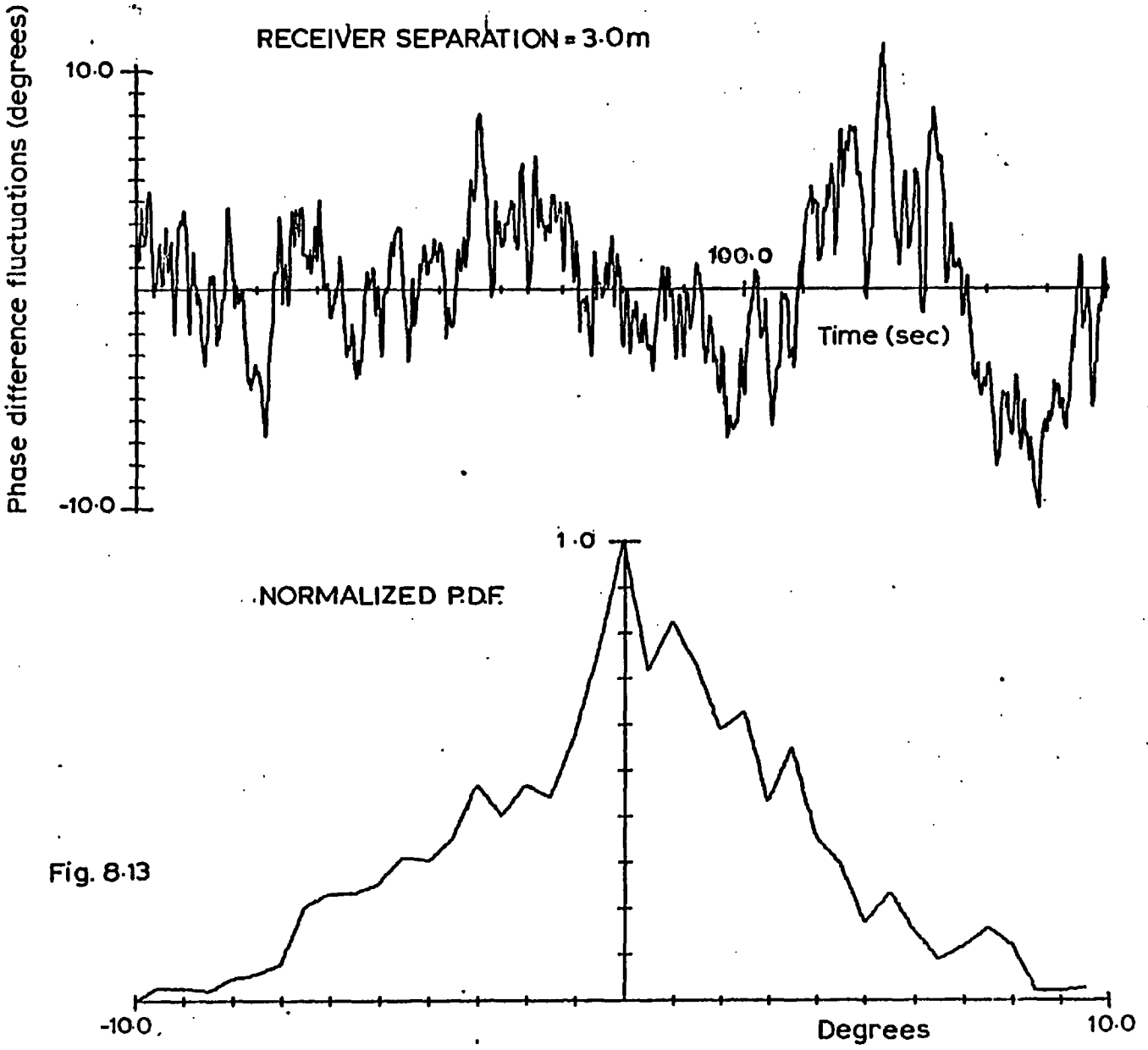
RECEIVER SEPARATION = 3·0m
Phase difference fluctuations (degrees)
10·0
-10·0
100·0
Time (sec)
NORMALIZED P.D.F.
1·0
-10·0
Degrees
10·0

Fig. 8·13

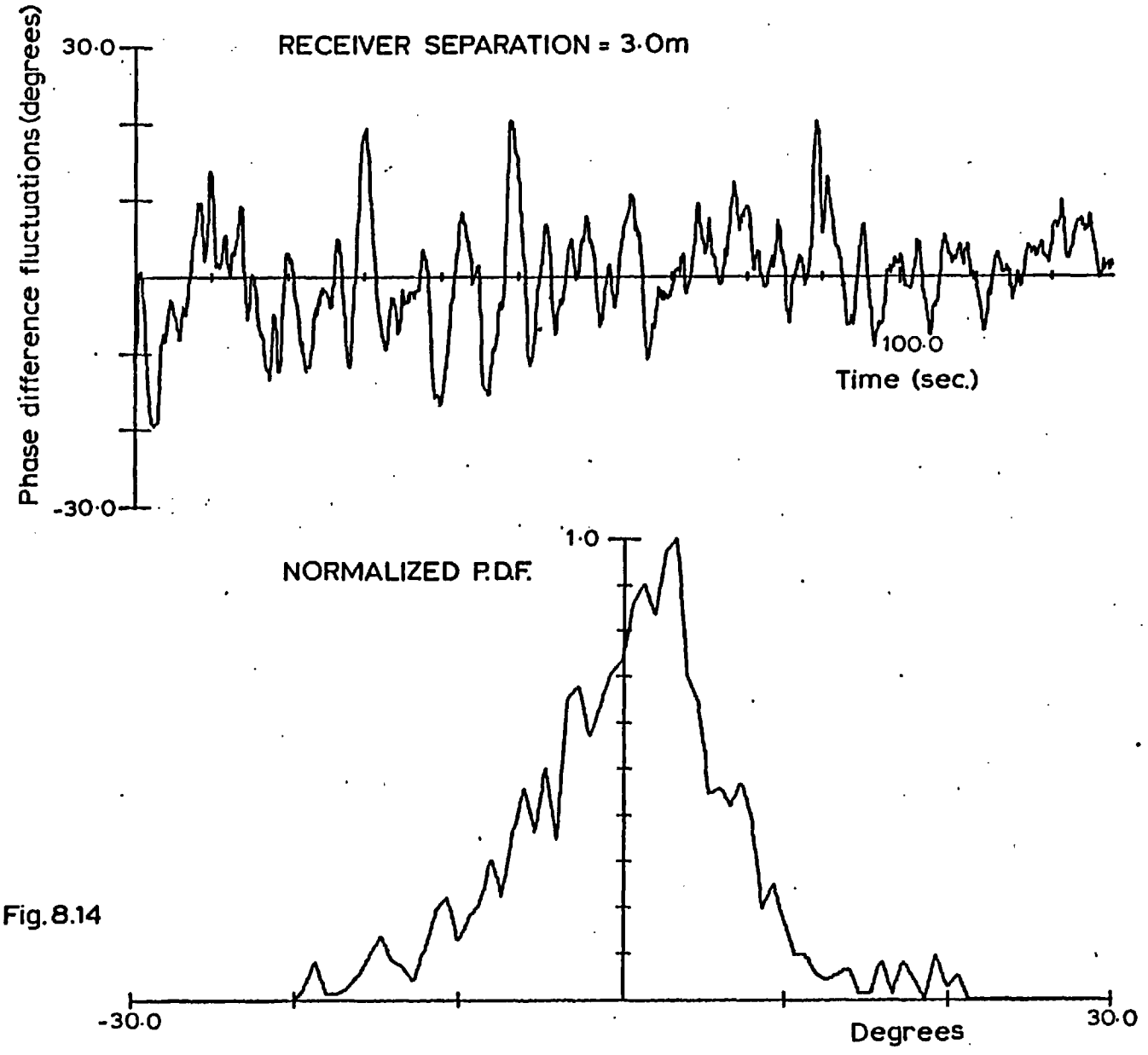
RECEIVER SEPARATION = 3·0m
Phase difference fluctuations (degrees)
30·0
-30·0
100·0
Time (sec.)
NORMALIZED P.D.F.
1·0
-30·0
30·0
Degrees

Fig. 8.14

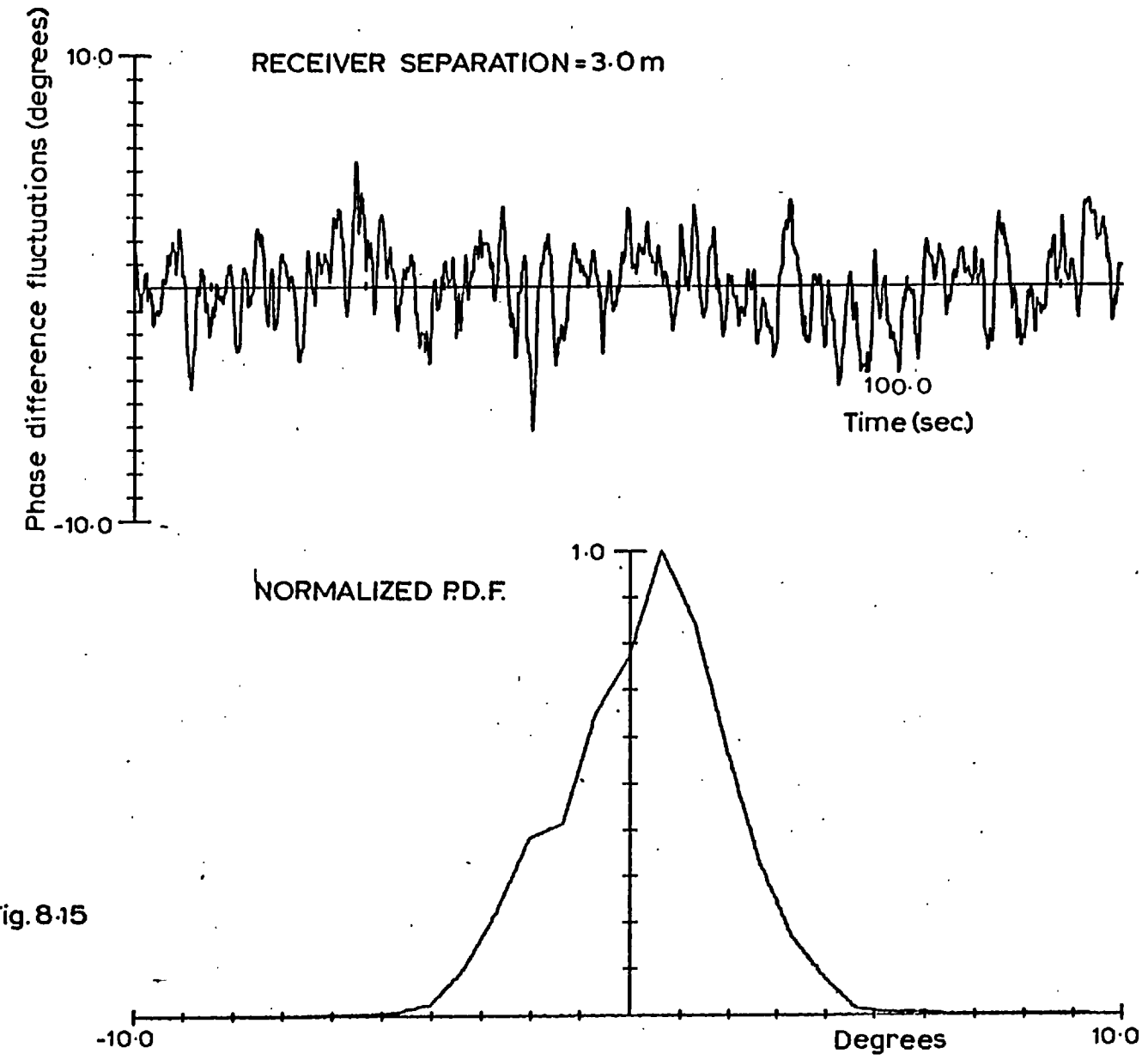
RECEIVER SEPARATION = 3·0 m
Phase difference fluctuations (degrees)
10·0
-10·0
100·0
Time (sec)
NORMALIZED P.D.F.
1·0
-10·0
Degrees
10·0

Fig. 8·15

8.2.2 Investigating the Presence of Large Scale Angle-of-Arrival Fluctuations

In order to determine the lateral scale-size of the phase distortions of the wave incident at the receiver site, the phase difference was measured at different separations within a short period of time. Fig. 8.16 shows the results for the variation of $\sigma_{\Delta\phi}$ as a function of receiver separations. Points joined by straight lines were measured within a period of ten to fifteen minutes, which was the time taken to separate both receivers and to restabilize the receiver for accurate measurements.

It may be seen from the examples shown that for the majority of the observed cases, $\sigma_{\Delta\phi}$ does not appreciably increase as the receiver separation is increased. This indicates that the dominant lateral scale-size of the phase variations is probably less than the largest receiver separation, i.e. 3 metres.

An interesting case, which was discussed in the previous section, is shown where $\sigma_{\Delta\phi}$ increases from 1.6 degrees at a separation of 0.8 metres to 6.6 degrees at a separation of 3.0 metres. The presence of large scale phase variations is probable for this particular case, due to the high correlation coefficient measured between the amplitude and phase fluctuations (0.95). Hence the effect of the angle-of-arrival fluctuations on the amplitude fluctuations is quite evident. For the other sets of phase difference measurements, the cross-correlation coefficient was negligible.

A series of experiments devised to detect the effect of angle-of-arrival fluctuations, however minute, on the amplitude fluctuations were then conducted. The experiment consisted of using two relatively narrow beam receiving apertures (the 0.25 metre diameter dishes with a beam width of ± 2.5 degrees) pointing off their main axis. Therefore,

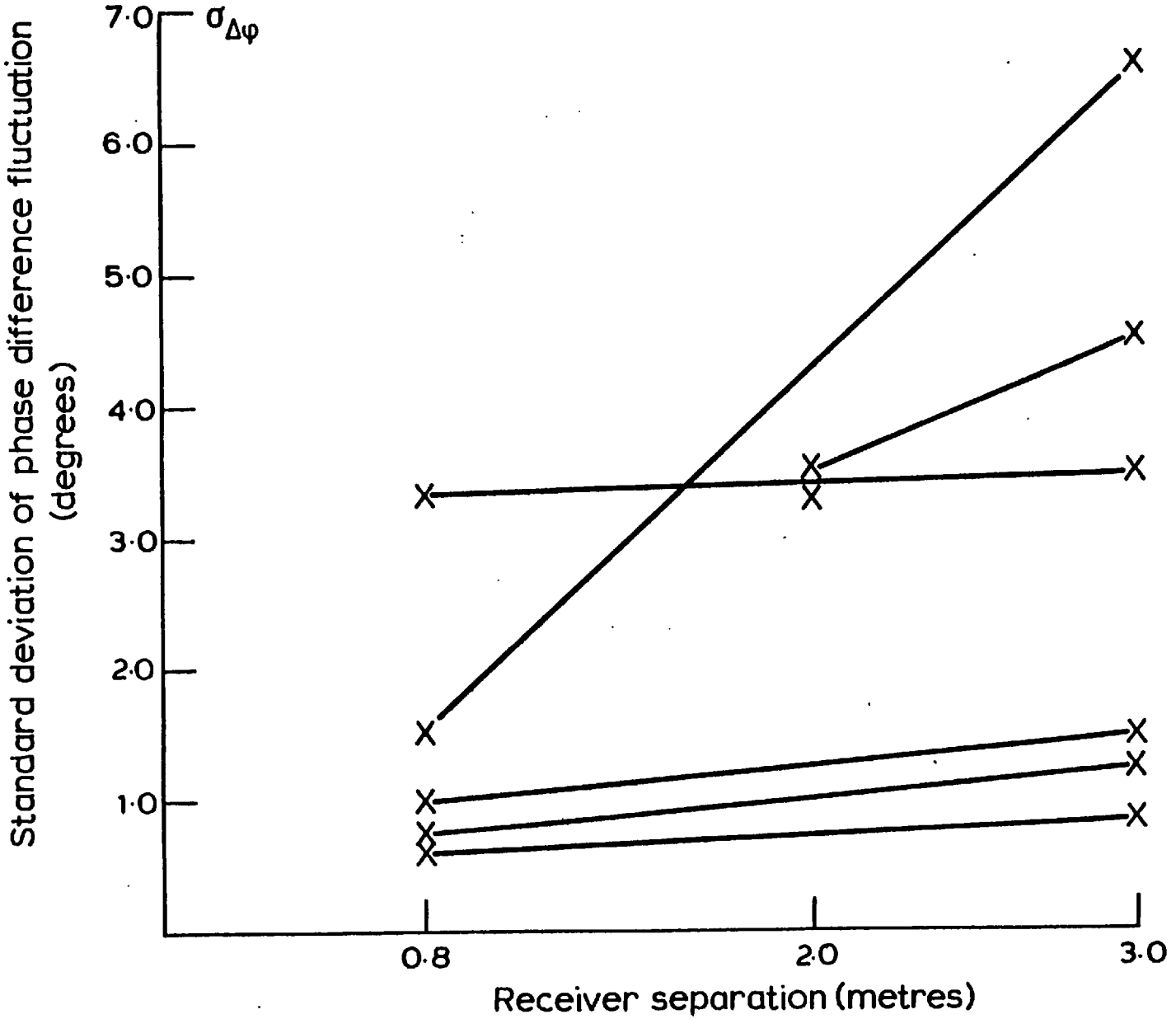
7·0
$\sigma_{\Delta\varphi}$
6·0
5·0
4·0
3·0
2·0
1·0
Standard deviation of phase difference fluctuation (degrees)
0·8
2·0
3·0
Receiver separation (metres)

Fig. 8·16

in effect the interferometer was used as a monopulse system. The antennas were misaligned in such a manner that a variation of one degree in the angle-of-arrival γ would produce a 10 decibel change in the received power.

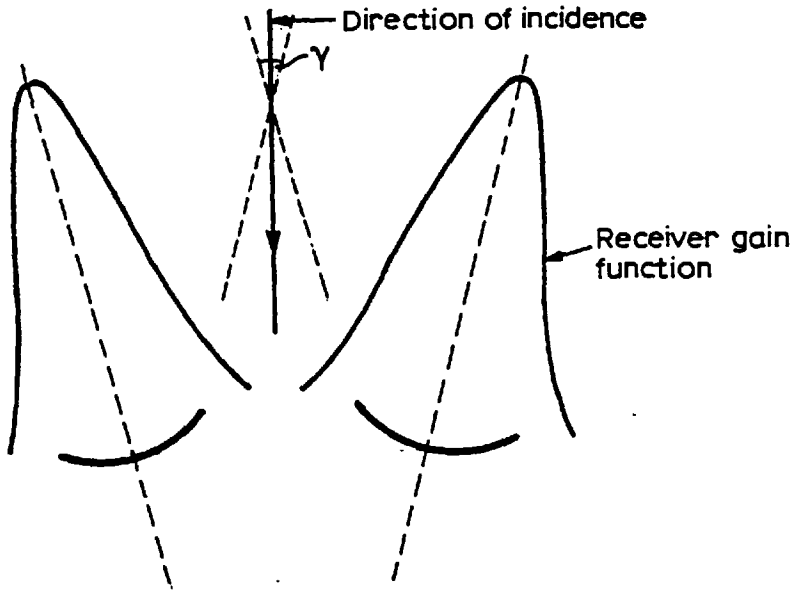

With the interferometer system set as shown above, the amplitude of the received signal would be very sensitive to fluctuations in the angle-of-arrival γ. Therefore, for any effective angle-of-arrival fluctuations, the amplitudes received by both off-axis receivers would be negatively correlated. However, the results obtained do not show such negative correlation even on long term fluctuations. This seems to indicate that the angle-of-arrival effects on amplitude fluctuation are extremely rare, even for accidently misaligned antennas.

8.2.3 Examples of the Frequency Power Spectra of the Phase Difference Fluctuations

The examples of the frequency power spectra of the phase difference fluctuations are shown in Figs. 8.17a, b, c and d. The phase difference fluctuations under consideration were measured at a receiver separation of 3.0 metres; the apertures used were the two 0.25 metres diameter dish.

The spectra shown here were calculated for the phase difference fluctuations measured simultaneously with the amplitude fluctuations. The corresponding amplitude spectra are shown in the same order in Figs. 8.4a, b, c and d. Hence the relevant atmospheric conditions are shown in Table 8.2.

The phase difference spectra have been predicted[58] to have two distinct slopes. The first slope being - m + 1, and second - (m + 1) where m is the slope of the spectra of the corresponding refractive index fluctuations. Hence the difference between both slopes is predicted to be 2 and the slope of the higher portion of the spectra is predicted to be equivalent to that of the corresponding amplitude fluctuations. The break point between both slopes is predicted to be at some frequency greater than v_n/ξ_0, where v_n is the mean value of the prevailing normal wind component and ξ_0 is the separation between both receiving apertures.

It may be seen that the slopes of the spectra of the phase-difference fluctuations are - 3.4 (- 10.2/3), - 3.7 (- 11.1/3), - 3.2 (- 9.6/3) and - 3.1 (- 9.3/3) decibels/Hz for Figs. 8.17a, b, c and d respectively. The corresponding slopes of the amplitude spectra as previously shown are - 3.3 (- 9.9/3), - 3.7 (- 11.1/3), - 2.7 (- 8.1/3) and - 3.4 (- 10.2/3) decibels/Hz respectively. It may be seen that both slopes are indeed very close which agrees with the theoretical predictions. However, the existence of two distinct slopes for the

phase difference spectra are not obvious enough to make any confident comments. However, the spectrum shown in Fig. 8.4b does show two distinct slopes, the first being - 1.7 (- 5.1/3) and second is - 3.7 (- 11.1/3) decibels/Hz. The difference between both slopes is 2 which is in perfect agreement with the theoretical prediction. However, the break point between both slopes is approximately at a frequency of 0.5 Hz. Noting that v_n was 4.3 metres/second and hence the theoretically predicted break point is 4.3/3 = 1.43 Hz, therefore, there is some disagreement with the theoretical prediction.

It is interesting to note that the steepest slope, - 3.7 (- 11.1/3), shown in Fig. 8.17a corresponds to the largest phase difference fluctuation shown in Fig. 8.14. The width of this spectrum is also the narrowest one. This indicates that the scale-sizes involved are considerably larger than in the other examples shown and, hence, the corresponding angle-of-arrival effects previously discussed.

Comparison of the Vertical and Horizontal Phase Difference Fluctuations

For a brief period of time, on July 27, 1978, the phase-difference fluctuations wer measured for vertical and horizontal receiver separations. The apertures used were the two 35.25 mm horns. The antenna separation was 0.7 metres in both cases. The prevailing weather conditions were sun and some cloud with a moderate breeze.

Figs. 8.18a and 8.18c show the probability density function and the frequency power spectrum of the phase-difference fluctuations respectively for the vertical separation measured at 1800 hours. The standard deviation was found to be 0.95 degrees. Figs. 8.18b and 8.18d show the same quantities measured for a horizontal separation 20 minutes later. The standard deviation in this case was 1.41 degrees.

POWER SPECTRA OF THE PHASE DIFFERENCE FLUCTUATIONS

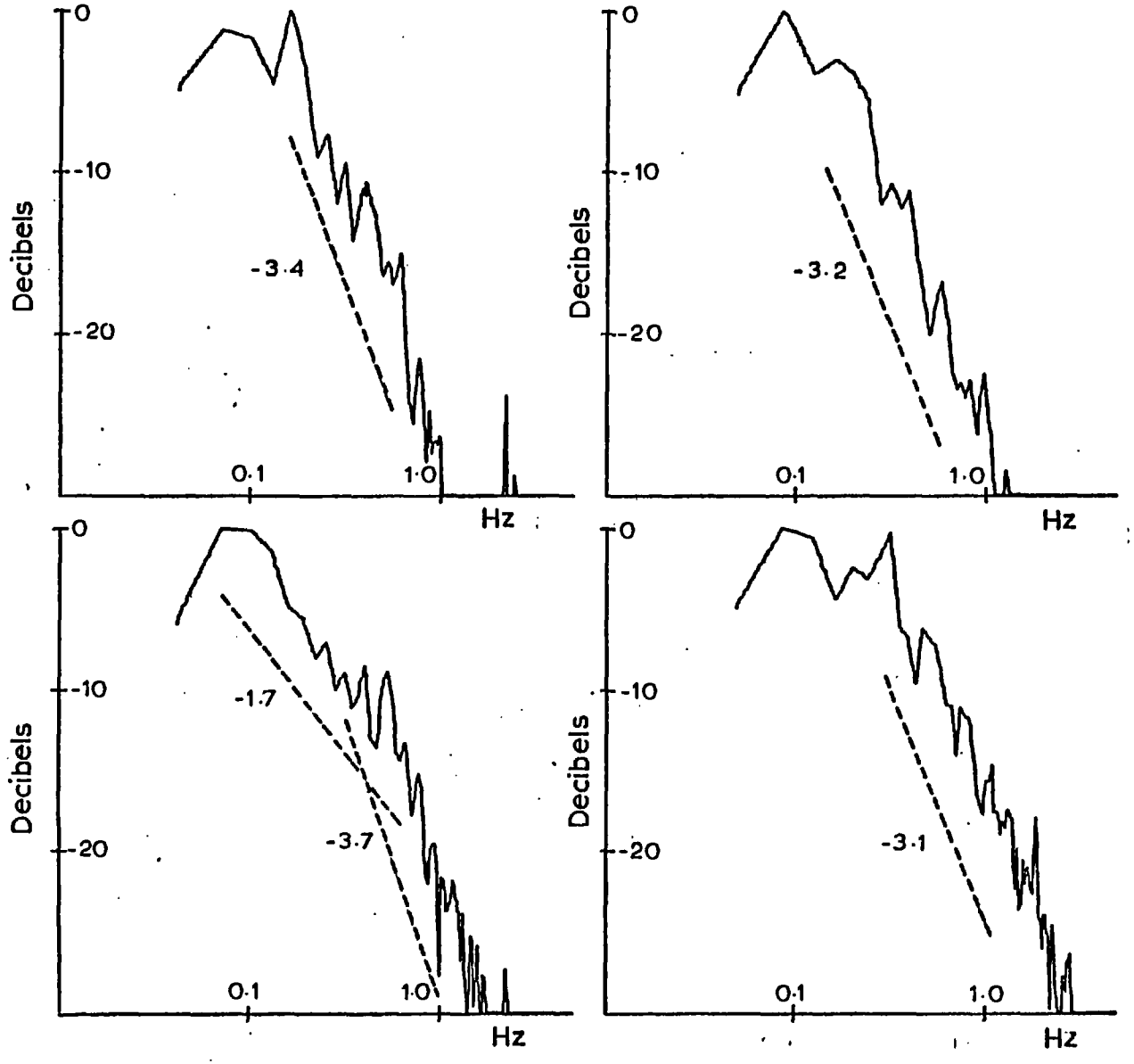

Fig.8·17a

Fig.8·17c

Fig.8·17b

Fig.8·17d

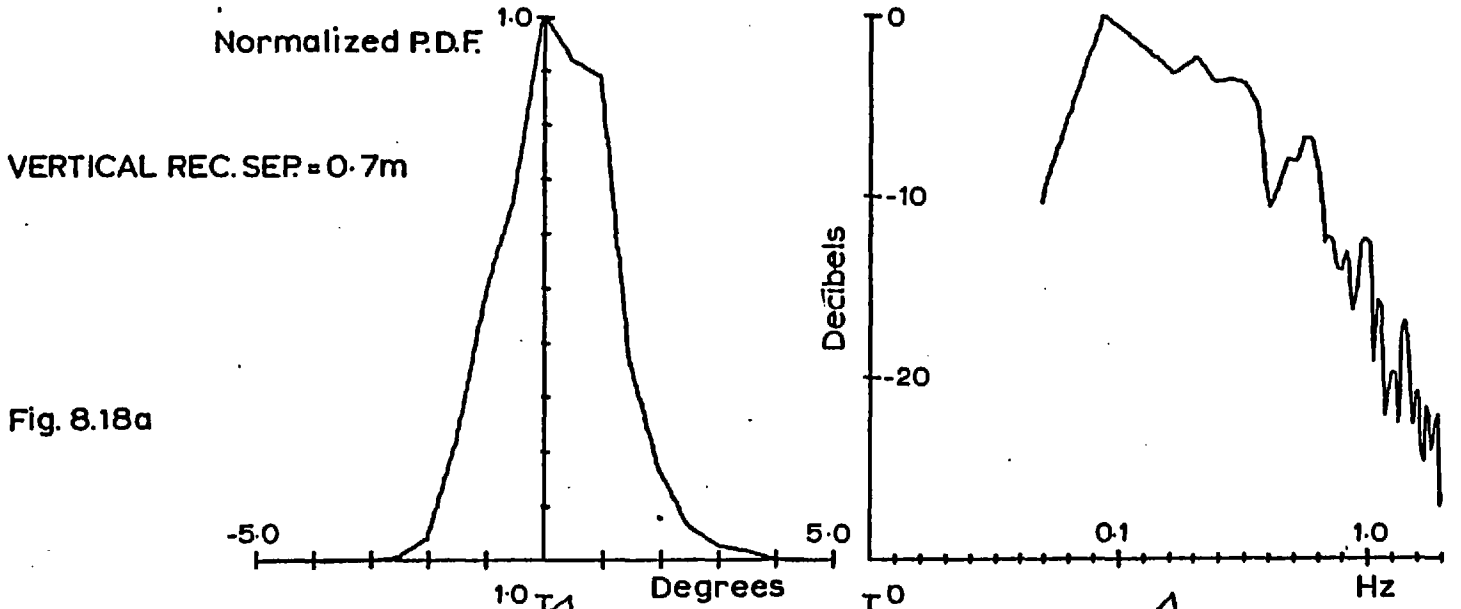

Fig. 8.18a

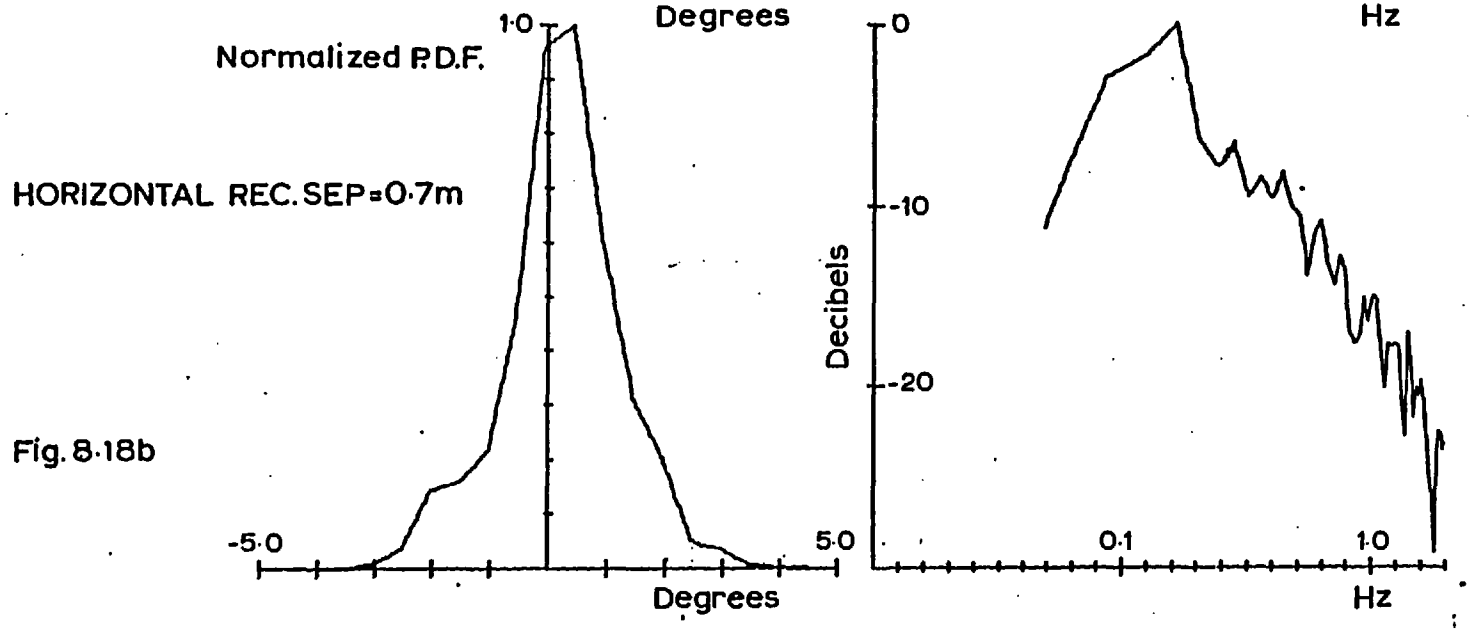

Fig. 8·18b

It may be seen from the close similarity of both the probability density functions and the frequency power spectra and bearing in mind the possible non-stationarity of the phase difference fluctuations over a period of 20 minutes, that under typical atmospheric conditions, the structure of the phase distortions is more or less similar in the vertical and horizontal directions.

8.3 Investigating the Response of Different Size Apertures Under Turbulent Conditions

It has been shown in Chapter 5 that increasing the receiving aperture size possibly causes an increase in the system signal-to-noise ratio and a decrease in the system efficiency. The possibility arises under certain previously discussed turbulence conditions with large transmitting aperture sizes.

An experiment was conducted using different size receiving apertures, to investigate the variation of the system signal-to-noise ratio and efficiency as a function of the receiving aperture size under different turbulent conditions. Another aspect investigated separately was the difference in the power spectra of the amplitude fluctuations observed by different apertures.

Following is a brief description of the experimental procedure carried out to simultaneously investigate the variation of the relative efficiency and signal-to-noise ratio observed by two receiving apertures.

8.3.1 A Practical Method to Investigate the Relative Variation in Efficiency and Signal-to-Noise Ratio

An experimental investigation of the absolute drop in free space gain and hence the loss of efficiency of a receiving aperture is impossible. This is due to the long-term variations in the level of the

incident signal, either due to long-term medium variation, or long-term variations in the transmitter and local oscillator power levels. The possible reduction in gain being of the order of a fraction of one decibel adds to the complexity of the problem. Similarly a measure of the absolute signal-to-noise ratio is practically impossible.

The method proposed is to compare the mean values of the signals observed by two different size apertures within a short period of time and hence obtain a value for the relative efficiency and observe its variation under different atmospheric conditions. Similarly a ratio of the percentage fluctuations observed by the two apertures gives an indication of the variation of the system signal-to-noise ratio as a function of receiver aperture size under different atmospheric conditions.

The experimental setup is shown below in Fig. 8.19. The apertures used were the 0.25 metre diameter dish and the 35.25 mm rectangular horn. Both antennas were clamped to the test rig, thus errors resulting from misalignment which give rise to variations in the mean signal level are eliminated.

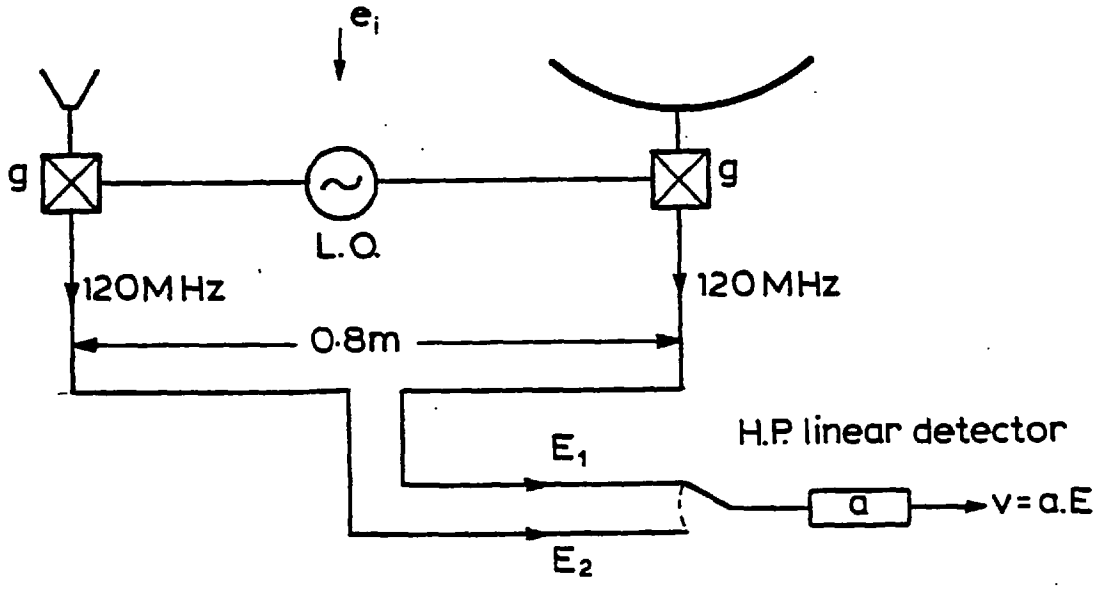

Fig. 8.19

The I.F. signal from each channel was monitored for a period of two minutes by means of a Hewlett-Packard linear detector. The detector output was sampled at a rate of two samples per second and fed into an A/D convertor then into a Tektronix programmable calculator which calculated the mean and variance of the signal. After the two minute period, the detector was switched instantaneously to the next channel for a similar period of time. A two minute sampling period per measurement was chosen so that the first and second order statistics of the incident field e_i, may be assumed to be more or less constant during both measurements.

The detector output voltage is $v_{1,2}$ where the suffix 1 refers to the first channel with the 0.25 m dish, and the suffix 2 refers to the second channel with the 35.25 mm horn antenna.

The random incident field e_i may be presumed to consist of a small incoherent part together with a reduced free-space coherent portion. The magnitude and angular spread of the incoherent portion are assumed to be constant over both data records. For equal mixer gains g and the linear detector response factor a held constant, it follows from the considerations of Section 5.3.1 on antenna efficiency, that the ratio of the averages of the sequential outputs from the detector is given ideally by:-

$$V = \frac{\langle v_1 \rangle}{\langle v_2 \rangle} = \sqrt{\frac{\eta_1 \cdot G_1}{\eta_2 \cdot G_2}} \qquad (8.8)$$

where: $v_{1,2}$ is the output of the linear detector for channels 1 and 2.

$\eta_{1,2}$ is the aperture efficiency for the dish and horn.

$G_{1,2}$ is the free-space gain of the dish and horn.

Hence V^2 is a measure of the ratio of the effective gains of

the two apertures and is thus a measure of the relative efficiencies. Therefore, any variation in V^2, under different atmospheric conditions, could indicate a variation in the efficiency of one aperture with respect to the efficiency of the other aperture.

As defined above, V is independent of long-term variations in the signal level due to variations in either oscillator output. Short-term variations of the order of a few minutes over which each set of measurements were carried out, have not occurred during laboratory tests for either the transmitter or receiver local oscillator.

The criterion for the relative variations of the signal-to-noise ratio under different atmospheric conditions, will be taken as the ratio of the percentage amplitude fluctuations observed by the dish to those observed by the horn. Assuming this ratio to be R, therefore:-

$$R = \frac{\sigma_{E_1}}{\langle E_1 \rangle} \Big/ \frac{\sigma_{E_2}}{\langle E_2 \rangle} = \frac{\sigma_{E_1}}{\sigma_{E_2}} \cdot \frac{\langle E_2 \rangle}{\langle E_1 \rangle} \qquad (8.9)$$

Therefore, values of $R < 1$ indicate that the signal-to-noise ratio of the system with the dish as the receiving aperture are higher than that with the horn as the receiving aperture. The opposite is true for value of $R > 1$. In the latter case, there is no receiver aperture averaging and the percentage amplitude fluctuations tend to increase as the receiver aperture size is increased.

8.3.2 Results for the Relative Efficiency and Signal-to-Noise Ratio Experiments

Fig. 8.20 shows the variation of relative gain and signal-to-noise ratios of the apertures used. The relative gain is given by 20 log (V) where V is defined in Equation (8.8). The free space difference

in gain between the 0.25 metre dish and the 35.25 mm horn is approximately 15 decibels. However, mismatch, cable losses and different I.F. amplifier gains probably reduce the gain difference. It must be emphasized that the main concern in this experiment is to observe the variation in the gain difference, and not the absolute value. Hence a relative drop in the gain difference under different atmospheric conditions, indicates that the efficiency of the larger aperture has dropped relative to the smaller one and vice versa.

The relative signal-to-noise ratio is given by log (R) with R defined by Equation (8.9). Hence value of log (R) > 0 indicate that the larger aperture produces more percentage fluctuations, i.e. less signal-to-noise, than the smaller one and vice versa.

The results shown are for observations over a four-day period. The data points for each day are joined by solid lines. The times of the observation and the sky condition are indicated along the horizontal axis.

It may be seen that 50% of the observation show a positive signal-to-noise ratio and 50% have a negative one. Therefore, it may be safely concluded that on the average, the 0.25 metre dish does not exhibit any smoothing properties in comparison to the 35.25 mm horn.

Similarly the variation of the gain difference appears to be random and uncorrelated to the variation in the signal-to-noise ratio. The variation of the difference in gain may possibly be attributed to the non-stationarity of the received signal. Hence it may also be concluded that the efficiency of the larger aperture is more or less similar to that of the smaller one.

The above conclusion seems to agree with the theoretical predictions made in Chapter 5 where it may be seen from Figs. 5.3a and 5.3b that for a relatively small transmitting aperture (a 1.0 metre

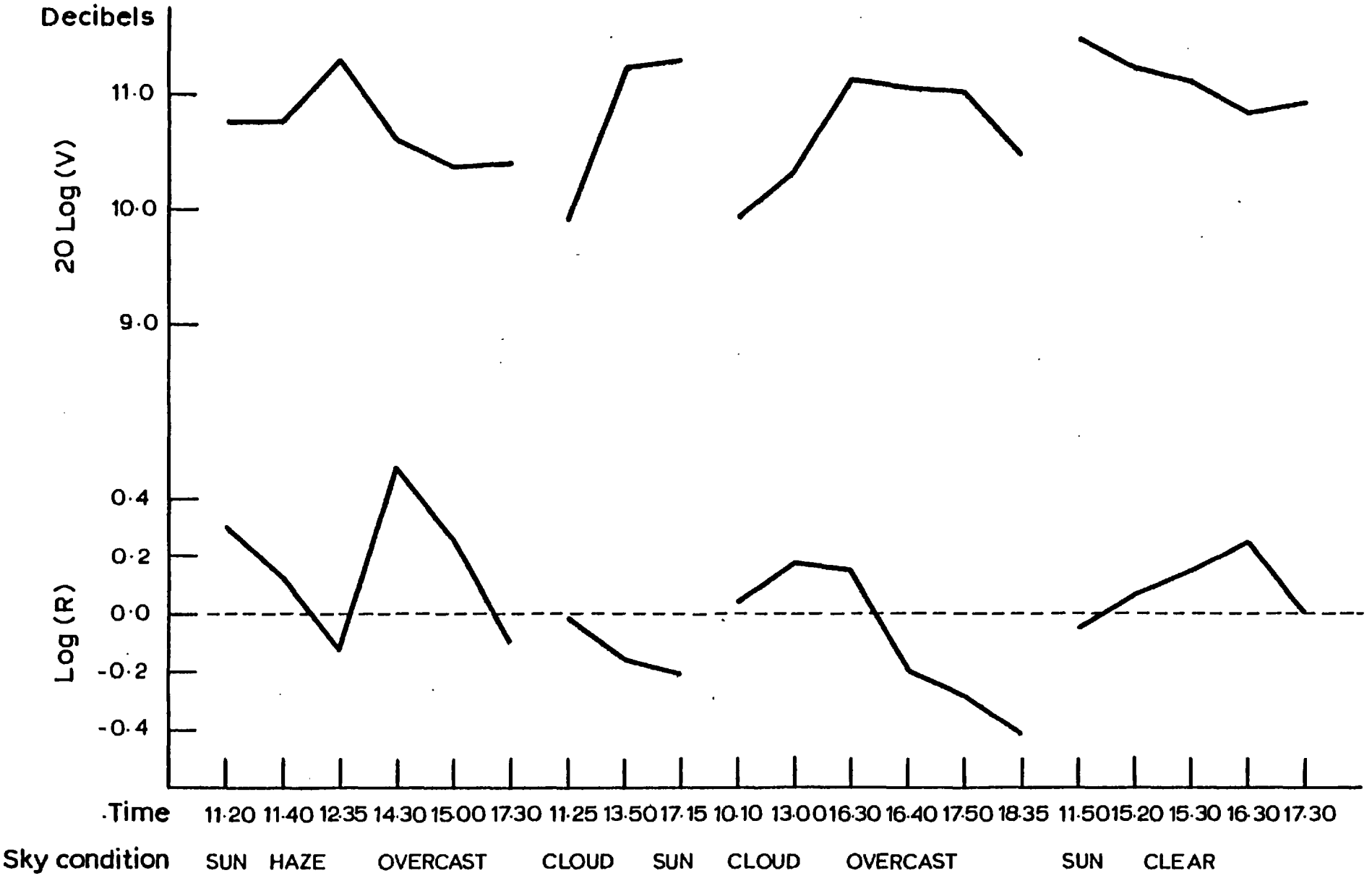
Decibels
20 Log (V)
11·0
10·0
9·0
Log (R)
0·4
0·2
0·0
-0·2
-0·4
Time
11·20 11·40 12·35 14·30 15·00 17·30 11·25 13·50 17·15 10·10 13·00 16·30 16·40 17·50 18·35 11·50 15·20 15·30 16·30 17·30
Sky condition
SUN HAZE OVERCAST CLOUD SUN CLOUD OVERCAST SUN CLEAR

Fig. 8·20

diameter dish), the variation of the receiving aperture size has no effect on the system efficiency and signal-to-noise ratio.

The above results also agree with the predictions of Tatarskii[58] and Fanté[19] which show that the averaging effect of an 0.25 metre dish are negligible, whatever the degree of turbulence.

8.3.3 Effect of the Receiver Aperture Size on the Spectral Characteristics of the Amplitude Fluctuations

Another aspect of the coupling of a perturbed wave front to different size receiving apertures is the variation of the spectral characteristics of the amplitude fluctuations. The dependence of the spectral characteristics on the aperture size may be understood by a brief but intuitive interpretation of the refractive index wave number energy spectrum. Shown below is a sketch of the energy spectrum as proposed by Kolmogoroff[72] where energy is drawn as a function of the wave number k, where $k = 2\pi/\ell$ and ℓ is the scale size of the refractive-index irregularities. The suffixes i and o refer to the inner and outer scale sizes respectively.

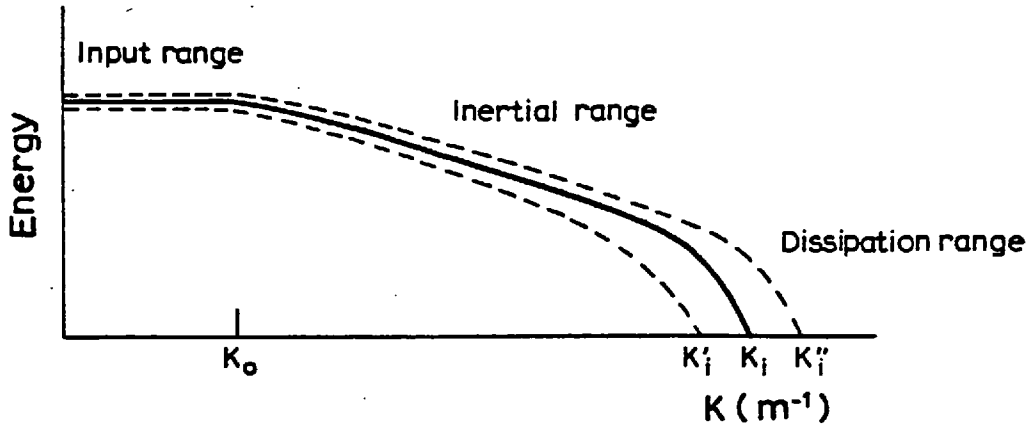

Wave number energy spectrum for the refractive index fluctuations

The shape of the energy spectrum varies according to the amount of energy introduced and hence dissipated. It might be worthwhile to note here that the magnitude and rate of energy introduced is quite different from the magnitude and rate of its dissipation, i.e. energy is introduced in large quantities at a slow rate and is dissipated in smaller packets at a faster rate. The reason for this has been shown to be[9] that energy in the atmosphere is introduced mainly by wind shear and convective heating from the ground. These may be assumed to be slowly varying processes. In physical terms, the energy dissipation process may be explained by the fact that the smaller eddies are formed by the motion of the larger ones and energy is transferred from one scale-size to the next and is finally dissipated by a repetition of this process several times. The shape and behaviour of the tail of the energy spectrum, i.e. in the dissipation region, is not fully understood. However, it is generally known to fall more rapidly in this region. Thus the inner or smaller scale-sizes attributed to the dissipation region are likely to vary quite rapidly for small variations in the dissipation mechanism. Therefore, it may be assumed that although the smaller scale-sizes in the order of millimetres contain far less energy than the larger ones, their rate of fluctuation is much faster.

The relatively rapid rate of fluctuations of the small medium scale-sizes is, in turn, reflected in the presence of relatively fast, small scale-size amplitude fluctuations. However, due to the small energy content of the small medium scale-sizes, the magnitude of the rapidly varying small scale-size amplitude fluctuations is likely to be much smaller than the slowly varying large scale-sizes.

In situations where rapidly varying small scale-sizes are present, a large receiving aperture would tend to "filter" out the rapid fluctuations. Hence the aperture averaging effect is exhibited.

Therefore, it may be assumed that in the situations where a large aperture would average out the amplitude fluctuations, it is likely that the corresponding frequency power spectrum would contain less high frequency spectral components than that corresponding to a smaller receiving aperture.

Figs. 8.21a and 8.21b show the power spectra of the amplitude fluctuations observed simultaneously by an 0.25 metre diameter dish and an open waveguide (4.0 millimetres across) respectively. The receivers were 3.0 metres apart and the measurements were carried out on a calm and clear day. It may easily be seen that the signal received by the open waveguide contains higher spectral components. Similarly, Figs. 8.21c and 8.21d show the power spectra of the amplitude fluctuations observed simultaneously by an 0.25 metre dish and a 35.25 mm horn respectively. The measurements were carried out under light rain conditions and, hence, small medium and amplitude variation scale-sizes are likely to occur. Again it may also be seen that the signal received by the smaller aperture contains higher frequency components.

An interesting result that may be drawn from the above experiments is the dependence of the frequency content and hence the slope of the power spectrum on the size of the receiving aperture used. Therefore, under certain atmospheric conditions, care must be taken in determining the slope of the power spectrum. This becomes especially important as the aperture size is much larger than the scale-sizes involved. For this particular experiment, the difference in the spectral content of the signals received by the different apertures used was negligible except on rare occasions.

8.4 Summary and Conclusions

The various examples shown in this chapter and the analysis

POWER SPECTRA OF THE AMPLITUDE FLUCTUATIONS OBSERVED BY DIFFERENT APERTURES

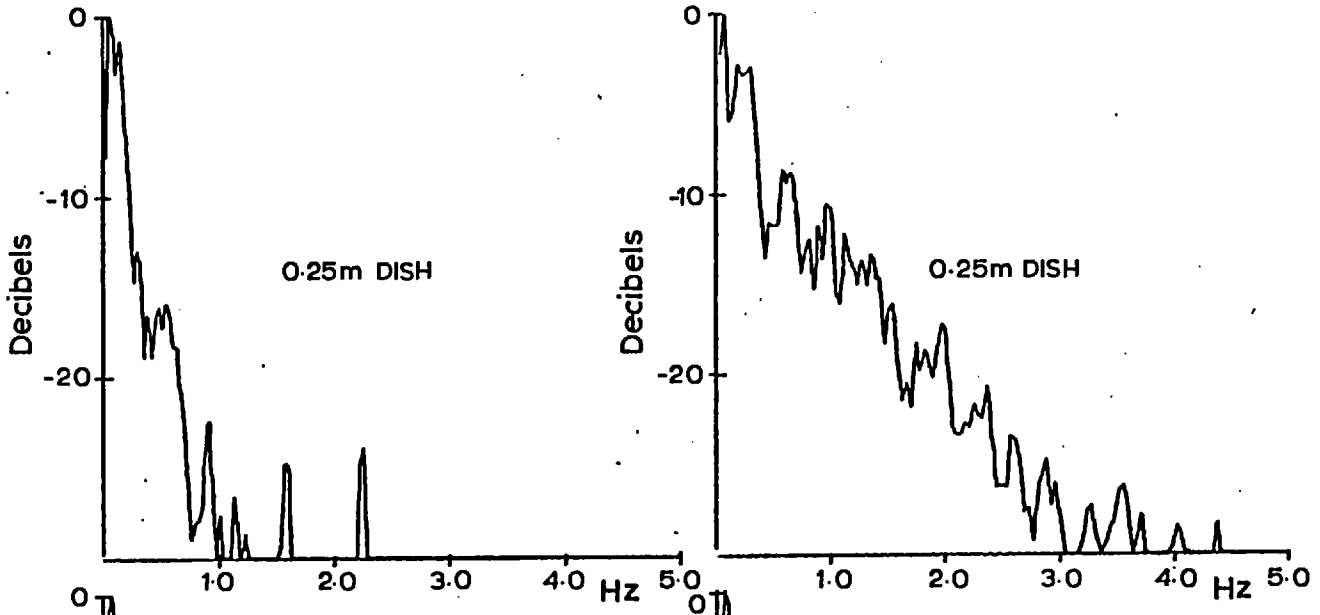

Fig. 8·21a

Fig. 8·21c

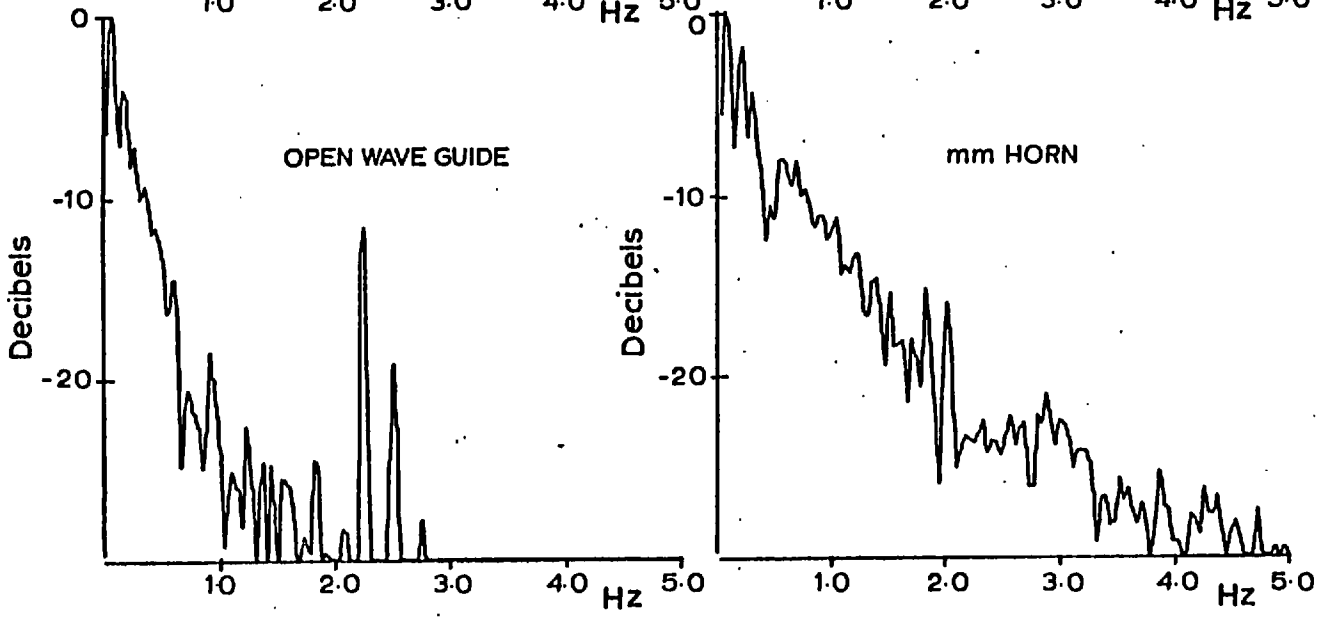

Fig. 8·21b

Fig. 8·21d

carried out indicate that the short-term amplitude fluctuations are very small. The maximum fluctuations occurred on clear days with light to moderate winds and under light rain conditions. There is some evidence of diurnal variations with fluctuations increasing at mid-day and decreasing in the early morning or evening. The small fluctuation level, generally found to be in the region of 1% relative to the mean value, is probably attributed to the small variations of the refractive index. For the brief periods where the refractive index was measured, the variance σ_n^2 has been observed to be of the order of 1.0×10^{-14} n^2-units. Since the effective scale-sizes of the refractive index irregularities lie within the region of $\sqrt{\lambda L}$, where L = 11.6 kilometres and λ = 8 millimetres, hence $\sqrt{\lambda L}$ = 9.6 metres. Therefore, the percentage fluctuations predicted by the coupling Equation (8.1) and shown in Fig. 8.1 are quite close to the observed fluctuation levels.

On investigating the lateral distribution of the amplitude fluctuations, Taylor's "frozen turbulence" hypothesis has been shown to a certain extent to be valid. This is particularly obvious when the cross-wind velocity is steady over the observation period. Based on the validity of this hypothesis, the dominant lateral scale-sizes of the amplitude fluctuations have been shown to be of the order of ten to thirty metres, whereas under slight rain conditions, the dominant scale-size is approximately 1 metre.

Although the amplitude variations lateral scale-sizes are relatively large on clear days, the lateral correlation distance is quite small, which is the distance at which the amplitude cross-correlation coefficient is larger than, say, 0.6 and has been rarely found to exceed 3.0 metres. This is due to the smaller scale-size crinkles superimposed on the larger scale-sizes, thus effectively decreasing the measured cross-correlation coefficient. Hence the measured lateral

correlation lengths are different from the theoretically predicted ones[19].

The spectra of the amplitude fluctuations appear to be closely related to those of the refractive index fluctuations, with the slopes behaving as theoretically predicted. However, no obvious relationship has been observed between the amplitude spectral slopes and the prevailing atmospheric conditions.

Brief measurements of vertical and horizontal spectra and cross-correlation coefficients of the amplitude fluctuations have been carried out. These indicate that the lateral amplitude distortions are quite similar across the vertical and horizontal directions, at least over a separation of 0.7 metres.

The phase difference fluctuations have also been found to be very small, i.e. normally within ± 10 degrees, although phase difference fluctuations as low as ± 1 degree and as high as ± 30 degrees have been observed, the latter occurring under calm and warm weather conditions. Light rain has not been found to have an increased effect on the phase difference fluctuation, e.g. ± 7 degrees peak-to-peak fluctuations.

Measurements have also been made to detect the variation of the standard deviation of the phase difference fluctuation $\sigma_{\Delta\phi}$ as a function of the receiver separation. These have shown that for the majority of the cases observed, $\sigma_{\Delta\phi}$ does not appreciably increase as the separation increases. Hence large scale angle-of-arrival fluctuations are rare. Thus the cross-correlation coefficient between amplitude and phase difference fluctuations has been found to be negligible. Except in the cases where $\sigma_{\Delta\phi}$ increases with the receiver separation and the fluctuations are quite large, the cross-correlation coefficient has been found to be quite large.

Therefore, under typical weather conditions, the lateral scale-size of the phase fluctuations is less than the largest receiver

separation, i.e. less than 3.0 metres.

Calculations of the phase difference spectra show that the slopes are very close to those of the corresponding amplitude fluctuations, which again is in agreement with the theoretical predictions[58].

Similarity between vertical and horizontal phase difference measurements at antenna separations of 0.7 metres has been observed. This leads to the assumption that the structure of the phase distortions across the vertical and horizontal directions are quite similar.

Measurements were carried out to examine the differences in response between two different-size receiving apertures. The results indicate that the 0.25 metres diameter does not consistently exhibit an averaging effect when compared to a smaller 35.25 mm aperture. Simultaneous measurements of the gain difference variations did not show any correlation with the relative aperture averaging factor and were quite random in nature. Hence a variation in the relative efficiency of both receiving apertures was not evident. The similarity of the relative efficiencies and aperture averaging factors of both apertures is also predicted by the coupling formula in Chapter 5.

Frequency power spectra of the amplitude fluctuations of different receiving aperture sizes have usually been found to be similar. However, there is some variation under situations where the effective medium scale-sizes are very small. In such cases, the spectra obtained from a smaller aperture contain higher frequency components. Hence the spectral slopes under such conditions may be dependent on the receiver aperture size.

CHAPTER 9

CONCLUSIONS

Some aspects of the propagation of radio waves with a finite angular spread through a medium with refractive index variations have been studied both theoretically and experimentally. A summary and a brief review of the conclusions drawn from the theoretical and experimental investigations is given below. This is followed by some suggestions for future investigations.

9.1 Summary and Conclusions of the Theoretical Investigations

The effects of two different types of refractive index variations within the propagation medium have been studied. The medium first considered was one characterised by a square-law variation in the refractive index vertical profile across all or part of the path length. The approximate solution considered for the wave equation in a medium with weak large-scale refractive-index variations is the so-called Parabolic Equation solution, which has been shown to allow for the representation of the random medium by a random phase-screen. For long path lengths with strong refractive index variations, or for media with localised variations, the path length is divided into a number of regions, each represented by its characteristic phase screen.

A computer-adaptable recursive formula has been obtained to determine the width and radius of curvature of a Gaussian beam propagating through a number of consecutive phase screens representing a medium with a square-law variation in the refractive index vertical profile. The induced signal gain or loss due to the focussing or defocussing effects of the continuous lens-like medium have been predicted. For example, a refractive index profile with a parabolic gradient of $+ 3 . . 10^{-9}$ is

predicted to produce an increase of 1.3 decibels in the signal level. Large spherical blobs of varying refractive index have been shown to be approximately represented by a region with a square-law refractive index profile. The effect of the position of isolated lens-like regions with respect to the transmitter and receiver aperture planes has also been studied. For the particular example of an 8 millimetre, 12 kilometre path, the mid-path location of a square-law region has been found to have the maximum focussing effect.

The other type of propagation medium considered was one interspersed with refractive index blobs of randomly varying magnitude and scale-size. In this case the medium is also represented by a random phase-modulating screen. The depth of modulation and lateral scale-sizes of the phase screen are determined by the characteristics of the medium. Substituting the transmitter aperture field by a set of elementary Huygens sources and superimposing a characteristic random phase modulation, provided detailed statistics for the fluctuating on-axis near and far-fields. These statistics were obtained as a function of the system and medium parameters. An optimum transmitter aperture size has been observed, where the on-axis field fluctuations are at a minimum. This transmitter aperture-averaging effect is probably due to the presence of two fluctuation-causing mechanisms, namely, scattering and beam wandering.

An investigation of the variances of the real and imaginary components of the random on-axis electric field, provides information required to determine the probability density function of the fluctuating electric field.

It has been found that close to the transmitter aperture plane, the variances of the real and imaginary components, v_1 and v_2 respectively are equal. As the propagation distance d, increases, it

has been found that v_2 becomes much larger than v_1 as shown in the figure below:-

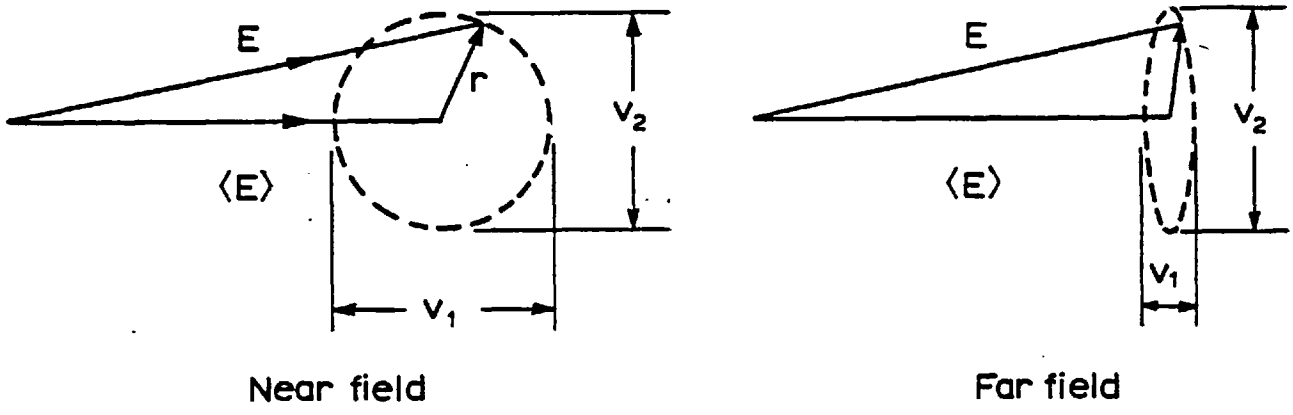

Therefore, under the assumption that the random component r lies equally probably between 0 and 2π, the probability density function of E as shown above has a Rice-Nakagami distribution[73, 74, 75]. The relationship between <E>, v_1 and v_2 has been determined, Sections 3.4.1 and 3.4.2, for various system and medium parameters. Curves of the probability density function as a function of <E>, v_1 and v_2 may be found in Beckmann[40].

The above analysis also yields information for the phase fluctuations of the on-axis field. Since the mean value of the random field has been found in practice to be much larger than the fluctuating real and imaginary components, therefore, the phase fluctuations may be considered to be approximately Gaussian distributed with a zero mean value. The magnitude of the phase fluctuations has been found to be very small, e.g. ± 8 degrees under moderate turbulence conditions, and over a path length of 12 kilometres. This prediction has been found to

be in agreement with the experimentally observed phase fluctuations.

An angular-spectrum lateral-coherence function approach was used to investigate the problem of beam propagation through a strongly random medium. The propagation of the coherent and incoherent portions of the lateral coherence function through a series of random phase screens was investigated. For a homogeneous medium, and considering single-scattered field components only, it has been shown that the effects of the multiple phase screens may be combined into one phase screen, the phase contribution of which is the summation of the phase contributions of the individual phase screens.

The coupling of the coherent and incoherent angular powers to a finite receiving aperture was calculated. Thus a general transmitter-to-medium-to-receiving-aperture coupling formula was obtained as a function of the system and medium parameters. A system efficiency and signal-to-noise ratio have also been defined in terms of the above parameters. Investigation of the interaction of the transmitter and receiver apertures with the refractive index blobs has produced some interesting predictions. For example, increasing the receiver aperture size for relatively small transmitter apertures does not provide an increase in the system-signal-to-noise-ratio , neither does it affect the efficiency. However, under certain atmospheric conditions, outlined in Section 5.4, and for large receiving apertures, an increase in the transmitter aperture is predicted to result in a drop in the overall system efficiency of up to 11%, whereas the signal-to-noise ratio is increased by approximately 2 decibels as shown in Figs. 5.6a and 5.6b. Such an increase in the signal-to-noise ratio is predicted to provide an improvement in the bit-error probability for digital transmission systems by a factor of 100 as shown in Fig. 1.3.

The coupling formula has been tested to a limited degree by

the data available from the 12 kilometre experimental link. The experimentally observed fluctuations have been found to agree with those predicted by the coupling formula. However, lack of detailed knowledge of the medium characteristics makes it difficult to make any confident assessment.

The availability of a general coupling formula should prove to be useful in the optimum design of radio systems and a prediction of their performance. A particularly useful application is for earth-satellite communication systems. The earth's atmosphere may appropriately be represented by a phase-changing screen. The necessity for optimizing the aperture sizes for maximum reception, i.e. higher efficiency, and for minimum noise, i.e. higher signal-to-noise ratio, is obvious due to the weight limitations and long distances involved. Since the formula is not limited to circularly symmetrical antennas, therefore, different beam shapes may be considered, e.g. elliptical or fan-shaped beams, which are quite common in satellite communication systems.

The results obtained from the different analytical models summarised above may be applied to predict the performance of wave propagation in a medium with refractive index variations. The condition for the application of the results obtained is that the wavelength of the propagating wave must be smaller than the scale-size of the medium irregularities. This is the case for underwater sound propagation systems, where ducting due to a square-law velocity profile is quite common, and propagation of optical beams through the atmosphere or any medium with refractive index variations.

9.2 Summary and Conclusions of the Experimental Investigations

Atmospheric effects on an 8 mm continuous-wave narrow-beam

signal propagating over an urban environment for 12 kilometres have been experimentally investigated. An interferometer receiver system was set-up to monitor the amplitude and phase-difference fluctuations under different atmospheric conditions. An off-line data recording and processing procedure was developed to analyse the radio-link data in a number of different ways and to extract as much information as possible from the available data.

The magnitude of the amplitude fluctuations was observed to be very low, e.g. 1% to 2%, with the maximum fluctuations occurring at mid-day. For such a range of fluctuation levels and under moderate turbulence conditions in a homogeneous medium, the scale-sizes predicted by the coupling formula lie in the range of 10 metres. Such a value of predicted medium scale-sizes agrees with that deduced from a 36 GHz, 4 kilometre link over Central London[76].

Measurements of the amplitude cross-correlation coefficients indicate that the correlation distance is quite small. This is the distance beyond which the cross-correlation coefficient is less than say 0.6 and for the majority of the observations was less than 3.0 metres. The dominant lateral scale-size of the amplitude distortions across the receiver plane was found to lie in the range of 10 metres. However, the lack of correlation is due to the smaller scale-size crinkles superimposed on the larger lateral amplitude distortions. These crinkles are caused by the medium inner scale-sizes, which have been predicted to be of the order of 0.1 m, whereas the outer scale-sizes are predicted to be of the order of 10 to 30 metres over Central London[76]. Therefore, the medium scale-sizes are of the same order of magnitude as the scale-sizes of the lateral amplitude distortions. This has also been predicted by a computer simulation model developed by Inggs[60].

The magnitude of the phase difference fluctuations has been found to be quite small, e.g. ± 10 degrees, peak-to-peak, at a receiver separation of 3 metres. The maximum fluctuations have been found to occur on calm clear days, with minimal fluctuations observed on overcast days. Similar results with the same order of magnitude of the phase fluctuations have been observed over a 3.2 mm, 19 kilometre link[77].

The spectra of the phase difference and amplitude fluctuations have been found to be closely related, which is in agreement with the theoretical predictions.

Phase difference measurements at various receiver separations within a short period of time have shown that for the majority of the observations, the phase structure constant does not appreciably increase with increased receiver separation. Therefore, it may be deduced that large-scale angle-of-arrival fluctuations do not occur for such a radio-link. Hence for the majority of the cases, the scale-size of the lateral phase distortions is less than the maximum receiver separation, i.e. less than 3.0 metres.

Experiments using different-size receiving apertures have shown that a 0.25 m diameter dish does not exhibit any obvious averaging properties or loss in efficiency when compared to a 35.25 mm horn. This is in agreement with the predictions obtained from the coupling formula derived in Chapter 5.

The tails of the spectra of the amplitude fluctuations has been observed, in some cases, to be a function of the receiver aperture size. This is due to the presence of small scale-size crinkles in the incident wavefront, which are probably smaller than the relatively large aperture under consideration and hence are smoothed out.

The experimental data produced by the experimental link should

add confidence to millimetre-wave radio system designers. The major cause for concern at such a frequency band is absorption due to precipitation. This has been observed to cause a total loss in the signal, 40 decibels, at rain rates exceeding say 20 mm/hour.

Signal fluctuations under clear air conditions have been found to be very small. However, an increase in the system reliability may be achieved by using spatial diversity techniques. Suitable receiver separations for such systems have been found to be of the order of 3 metres, which is a convenient separation. Experimental evidence, though admittedly scanty, has shown that the structure of the wave-front distortions are more or less similar in the vertical and horizontal directions. Therefore, provided that the propagation axis is elevated sufficiently above the ground and narrow-beam apertures are used, thus greatly reducing surface-caused multipath fluctuations, horizontal or vertical spatial diversity should produce equivalent results.

Signal fluctuations due to angle-of-arrival fluctuations should not pose any serious problems. This is particularly true for terrestrial links. The use of relatively large and cumbersome antennas is not necessary to obtain a high signal-to-noise ratio. Small horn-type antennas have been seen to produce a comparable signal-to-noise ratio. Therefore, in situations where the fade-margin is not a crucial factor, horn antennas are perfectly adequate, especially for portable radio-systems operating under clear air conditions.

9.3 Suggestions for Future Research and Investigations

The investigations reported in this thesis may possibly lead to further developments in the understanding of the adverse effects of a random medium on propagating beam. Some of the points which may be

taken up and which could prove to be useful in communcations systems design, are briefly discussed below.

Detailed statistics of the fluctuations of the field, radiated by a finite aperture, have been determined at an on-axis observation point. However, the response of a non-linear receiving device to such a fluctuating field remains to be investigated. Cable[78] has investigated this problem for underwater sound, and has obtained expressions for the n'th moment of a randomly scattered field. These expressions have been obtained under the assumption of plane-wave propagation and could be extended in conjunction with the Huygens source approach developed in Chapter 3, to incorporate the practical case of narrow diffracting beams.

The Huygens-Parabolic Equation approach that has been applied to study the field fluctuations at an on-axis point may, in principle, be used to determine the field fluctuations at different points across an observation plane. Hence the lateral distribution of the random amplitude and phase of the electric field may be estimated. The dominant fluctuation-causing mechanism, i.e. beam wandering or scattering, may be determined through the knowledge of the lateral field distribution. Such knowledge is useful if compensation systems such as beam-steering aperture arrays are to be considered.

The different aspects of signal coupling to a receiving aperture have been studied for the particular example of Gaussian aperture field distributions. The variations of the signal-to-noise ratio and system efficiency should be investigated for arbitrary aperture field distributions. Since the coupling formula, Equation (5.10), was obtained in a three-dimensional form, the behaviour of non-symmetrical beams, e.g. elliptical or fan-shaped, in a medium with non-isotropic irregularities, may also be studied.

Predictions for the performance of radio systems are more readily appreciated if based on experimental evidence. The greatest potential for millimetre wave radio systems is wide-band, high-bit-rate digital transmission. Hence experiments have been carried out to assess the performance of such systems. For example, variations of the bit error rate versus channel signal-to-noise ratio were obtained in 1968 for a 40 GHz, 32 kilometre system with a data rate of 50 Mb/sec and using a digital phase shift keying modulation scheme[79]. Nowadays much higher data rates are contemplated, e.g. 274, 176 Mb/sec[80] and using various modulation schemes, which may be drastically affected by atmospheric scattering. An example of such a modulation scheme is direct amplitude modulation or On-Off keying which is popular due to its simplicity and available hardware at millimetre wave frequencies. Pulse propagation systems are also widely used in radar and sonar detection systems. The scattering effects of the medium on the shape of a propagating pulse have been theoretically investigated to some extent by Uscinskii[33].

The variation of the efficiency and smoothing characteristics of large apertures may be accurately investigated by using large array antennas. Large and small apertures may thus be realised from the same array by using appropriate feed arrangements. Hence simultaneously received signals by different size apertures may be compared.

Propagation over varying types of terrain and under different atmospheric conditions should be carried out. This is necessary since results obtained over urban or country terrains in northern climates probably would not resemble results obtained under more adverse propagation conditions. Experiments over desert terrains or in humid coastal areas should be performed to provide the necessary information for the rapidly increasing intercontinental communication networks.

The availability of relatively cheap and powerful microprocessors should prove to be very useful in the analysis and handling of available experimental data. Microprocessors may also be used in the control of various experimental settings, such as aperture dimensions determined by appropriate array feeds, or bit-rate settings in digital transmission systems.

APPENDIX I

DETERMINATION OF THE VARIANCES OF THE REAL AND IMAGINARY COMPONENTS OF A RANDOM COMPLEX ELECTRIC FIELD IN THE FRESNEL REGION

To determine the variance of the real and imaginary field components, E_R and E_I respectively, where they are given by:-

$$E_R = \frac{b}{\sqrt{\lambda d}} \int_{-\infty}^{+\infty} e^{-\xi^2/w^2} \cdot \cos\left[\frac{k\xi^2}{2d} - \phi\right] d\xi \qquad (I.1)$$

$$E_I = -\frac{b}{\sqrt{\lambda d}} \int_{-\infty}^{+\infty} e^{-\xi^2/w^2} \cdot \sin\left[\frac{k\xi^2}{2d} - \phi\right] d\xi \qquad (I.2)$$

First the variance of the real component σ_R^2 will be determined:-

$$\sigma_R^2 = \langle E_R^2 \rangle - \langle E_R \rangle^2 \qquad (I.3)$$

where:-

$$E_R^2 = \frac{b^2}{\lambda d} \cdot \int_{-\infty}^{+\infty} \int_{-\infty}^{+\infty} e^{-\xi^2/w^2} \cdot e^{-\xi_1^2/w^2} \cdot \cos\left[\frac{k\xi^2}{2d} - \phi\right] \cdot \cos\left[\frac{k\xi_1^2}{2d} - \phi_1\right] d\xi \cdot d\xi_1 \qquad (I.4)$$

where $\xi_1 = \xi + u$, and u is a variable separation along the ξ-axis with $\phi = \phi(\xi)$ and $\phi_1 = \phi(\xi + u)$.

Since $\phi(\xi)$ and $\phi(\xi + u)$ are both assumed to be zero mean Gaussian random variables, therefore, their sum ϕ_s and difference ϕ_d are both Gaussian random variables with zero mean:-

$$\phi_s = \phi(\xi) + \phi(\xi + u) \tag{I.5}$$

$$\phi_d = \phi(\xi) - \phi(\xi + u) \tag{I.6}$$

Therefore, for ϕ_s and ϕ_d Gaussian:-

$$\langle e^{j\phi_s} \rangle = e^{-\sigma^2_{\phi_s}/2} \quad \text{and} \quad \langle e^{j\phi_d} \rangle = e^{-\sigma^2_{\phi_d}/2} \tag{I.7}$$

where $\sigma^2_{\phi_s}$ and $\sigma^2_{\phi_d}$ are the variances of the sum and difference phases respectively and are given by:-

$$\sigma^2_{\phi_s} = \langle \left[\phi(\xi) + \phi(\xi + u) \right]^2 \rangle \tag{I.8}$$

and:-

$$\sigma^2_{\phi_d} = \langle \left[\phi(\xi) - \phi(\xi + u) \right]^2 \rangle \tag{I.9}$$

for:-

$$\sigma^2_{\phi(\xi)} = \sigma^2_{\phi(\xi + u)} = \sigma^2_{\phi}$$

and:-

$$\langle \phi(\xi) \cdot \phi(\xi + u) \rangle = \sigma^2_{\phi} \cdot r_{\phi}(u) \tag{I.10}$$

where $r_{\phi}(u)$ is the normalized phase autocovariance function and has previously been assumed to be Gaussian and of the form:-

$$r_\phi(u) = e^{-u^2/\xi_0^2} \tag{I.11}$$

Therefore:-

$$\sigma_{\phi_s}^2 = 2\sigma_\phi^2 \left[1 + r_\phi(u)\right] \tag{I.12}$$

and:-

$$\sigma_{\phi_d}^2 = 2\sigma_\phi^2 \left[1 - r_\phi(u)\right] \tag{I.13}$$

Substituting Equations (I.12) and (I.13) in Equation (I.7) and using De Moivres formula, therefore:-

$$\langle\cos(\phi_s)\rangle = \langle\cos\left[\phi(\xi) + \phi(\xi + u)\right]\rangle = e^{-\sigma_\phi^2\left[1 + r_\phi(u)\right]} \tag{I.14}$$

and:-

$$\langle\cos(\phi_d)\rangle = \langle\cos\left[\phi(\xi) - \phi(\xi + u)\right]\rangle = e^{-\sigma_\phi^2\left[1 - r_\phi(u)\right]} \tag{I.15}$$

Expanding Equations (I.14) and (I.15) and for $\sigma_\phi^2 \ll 1$, the following expressions are obtained:-

$$\left.\begin{aligned} &\langle\cos\,\phi(\xi)\,.\,\cos\,\phi(\xi + u)\rangle \simeq 1 - \sigma_\phi^2 \\ &\langle\cos\,\phi(\xi)\,.\,\sin\,\phi(\xi + u)\rangle = 0 \\ &\langle\sin\,\phi(\xi)\,.\,\cos\,\phi(\xi + u)\rangle = 0 \end{aligned}\right\} \tag{I.16}$$

$$\langle \sin \phi(\xi) \cdot \sin \phi(\xi + u) \rangle = \sigma_\phi^2 \cdot r_\phi(u) \qquad \text{(I.16) (Continued)}$$

Therefore, Equation (I.4), after the appropriate expansions and substitutions from Equation (I,.6) gives:-

$$E_R^2 = \frac{b^2}{\lambda d} \cdot \left[I_{1R} + I_{2R} \right] \qquad \text{(I.17)}$$

where:-

$$I_{1R} = (1 - \sigma_\phi^2) \cdot \int_{-\infty}^{+\infty} e^{-2\xi^2/w^2} \cdot \cos \frac{k\xi^2}{2d} \int_{-\infty}^{+\infty} e^{-2\xi u/w^2} \cdot e^{-u^2/w^2} \cdot$$

$$\cdot \cos \frac{k}{2d} (\xi + u)^2 \cdot du \cdot d\xi \qquad \text{(I.18)}$$

and:-

$$I_{2R} = \sigma_\phi^2 \cdot \int_{-\infty}^{+\infty} e^{-2\xi^2/w^2} \cdot \sin \frac{k\xi^2}{2d} \int_{-\infty}^{+\infty} e^{-2\xi u/w} \cdot e^{-\left(\frac{1}{w^2} + \frac{1}{\xi_0^2}\right) \cdot u^2} \cdot$$

$$\cdot \sin \frac{k}{2d} (\xi + u)^2 \, du \cdot d\xi \qquad \text{(I.19)}$$

Using a standard integral[41] and after performing some algebraic manipulations, I_{1R}, after the double integration, becomes:-

$$I_{1R} = (1 - \sigma_\phi^2) \cdot \frac{\pi}{4\sqrt{\left(\frac{1}{w^2}\right)^2 + \left(\frac{k}{2d}\right)^2}} \cdot \cos^2 \left[\frac{1}{2} \tan^{-1} \left(\frac{kw^2}{2d} \right) \right] \qquad \text{(I.20)}$$

Similarly, the integral (I.19) for $r_\phi = \exp(-u^2/\xi_0^2)$ yields:-

$$I_{2_R} = \sigma_\phi^2 \cdot \frac{\pi}{2} \cdot \frac{1}{4\sqrt{\beta}} \cdot$$

$$\cdot \left[\frac{1}{4\sqrt{\left(\frac{2}{w^2} - \frac{\gamma}{\beta}\right)^2 + \left(\frac{k}{2d}\right)^2 \left(1 - \frac{1}{\beta\xi_0^4}\right)^2}} \cdot \cos \left[\frac{1}{2} \tan^{-1} \frac{\frac{k}{2d}\left(1 - \frac{1}{\beta\xi_0^4}\right)}{\left(\frac{2}{w^2} - \frac{\gamma}{\beta}\right)} - \alpha \right] - \right.$$

$$\left. - \frac{1}{4\sqrt{\left(\frac{2}{w^2} - \frac{\gamma}{\beta}\right)^2 + \left(\frac{k}{2d}\right)^2 \left(1 + \frac{1}{\beta\xi_0^4}\right)^2}} \cdot \cos \left[\frac{1}{2} \tan^{-1} \frac{\frac{k}{2d}\left(1 + \frac{1}{\beta\xi_0^4}\right)}{\left(\frac{2}{w^2} - \frac{\gamma}{\beta}\right)} + \alpha \right] \right] \qquad \text{(I.21)}$$

where:-

$$\left.\begin{aligned} \alpha &= \frac{1}{2} \tan^{-1} \frac{k/2d}{\left(\frac{1}{w^2} + \frac{1}{\xi_0^2}\right)} \\ \beta &= \left(\frac{1}{w^2} + \frac{1}{\xi_0^2}\right)^2 + \left(\frac{k}{2d}\right)^2 \\ \gamma &= \left(\frac{1}{w^2}\right)^2 \left(\frac{1}{w^2} + \frac{1}{\xi_0^2}\right) + \left(\frac{k}{2d}\right)^2 \left(\frac{1}{w^2} - \frac{1}{\xi_0^2}\right) \end{aligned}\right\} \qquad \text{(I.22)}$$

Therefore:-

$$\sigma_R^2 = \frac{b^2}{\lambda d} \left(I_{1_R} + I_{2_R}\right) - \langle E_R \rangle^2 \qquad \text{(I.23)}$$

However, from Equation (3.22) and for $\sigma_\phi^2 << 1$, it may be seen that:-

$$\langle E_R \rangle^2 = \frac{b^2}{\lambda d} \cdot I_{1_R} \tag{I.24}$$

Therefore, the variance of the real component is given by:-

$$\sigma_R^2 = \frac{b^2}{\lambda d} \cdot I_{2_R} \tag{I.25}$$

where I_{2_R} is given by Equation (I.21).

Similarly for the variance of the imaginary component and after some manipulations:-

$$\sigma_I^2 = \frac{b^2}{\lambda d} (I_{1_I} + I_{2_I}) - \langle E_I \rangle^2 \tag{I.26}$$

where I_{1_I} is found to be for $\sigma_\phi^2 << 1$:-

$$(1 - \sigma_\phi^2) \frac{\pi}{\sqrt{\left(\frac{1}{w^2}\right)^2 + \left(\frac{k}{2d}\right)^2}} \cdot \sin^2 \left[\frac{1}{2} \tan^{-1} \frac{kw^2}{2d}\right] \tag{I.27}$$

and I_{2_I} is given by:-

$$I_{2_I} = \sigma_\phi^2 \cdot \frac{\pi}{2} \cdot \frac{1}{4\sqrt{\beta}} \cdot$$

$$\left\{ \frac{1}{4\sqrt{\left(\frac{2}{w^2} - \frac{\gamma}{\beta}\right)^2 + \left(\frac{k}{2d}\right)^2 \left(1 - \frac{1}{\beta \xi_0^4}\right)^2}} \cdot \cos \left[\frac{1}{2} \tan^{-1} \frac{\frac{k}{2d}\left(1 - \frac{1}{\beta \xi_0^4}\right)}{\left(\frac{2}{w^2} - \frac{\gamma}{\beta}\right)} - \alpha\right] + \right.$$

$$+\frac{1}{4\sqrt{\left(\frac{2}{w^2}-\frac{\gamma}{\beta}\right)^2+\left(\frac{k}{2d}\right)^2\left(1+\frac{1}{\beta\xi_0^4}\right)^2}}\cdot\cos\left[\frac{1}{2}\tan^{-1}\frac{\frac{k}{2d}\left(1-\frac{1}{\beta\xi_0^4}\right)}{\left(\frac{2}{w^2}-\frac{\gamma}{\beta}\right)}+\alpha\right]\Bigg] \qquad (I.28)$$

where α, β and γ are given in Equation (I.22).

From Equation (3.23) it may be seen that:-

$$\langle E_I\rangle^2 = \frac{b^2}{\lambda d}\cdot I_{1_I} \qquad (I.29)$$

and, therefore, the variance of the imaginary component of the random complex electric field is given by:-

$$\sigma_I^2 = \frac{b^2}{\lambda d}\cdot I_{2_I} \qquad (I.30)$$

with I_{2_I} given by Equation (I.28).

APPENDIX II

PROPAGATION OF THE LATERAL COHERENCE FUNCTION BEYOND A RANDOM PHASE SCREEN

The concept of collapsing the random medium into a characteristic phase screen situated at the transmitter plane has been discussed in Chapter 3. The effect of such a screen on the propagation characteristics of the lateral coherence function will be discussed below.

The two-dimensional case will be considered with an aperture field distribution $E_0(x)$. The random contribution by the phase screen will be taken as $\phi(x)$. Therefore, the field distribution just after the phase screen is E(x) where:-

$$E(x) = d(x) \cdot r(x) \tag{II.1}$$

d(x) is the deterministic part and is by definition $E_0(x)$.

r(x) is the random part of the electric field and is equal to $e^{j\phi(x)}$.

The angular spectrum radiated is thus given by Equation (4.2):-

$$F(S) = \frac{1}{\lambda} \int_{-\infty}^{+\infty} d(x') \cdot r(x') \cdot e^{jkx'S} \, dx' \tag{II.2}$$

and:-

$$F^*(S) = \frac{1}{\lambda} \int_{-\infty}^{+\infty} d^*(x) \cdot r^*(x) \cdot e^{-jkxS} \, dx \tag{II.3}$$

Thus the angular power spectrum is given by:-

$$|F(S)|^2 = \frac{1}{\lambda^2} \cdot \int_{-\infty}^{+\infty} \int_{-\infty}^{+\infty} d(x') \cdot d^*(x) \cdot r(x') \cdot r^*(x) \cdot e^{jk(x' - x)S} \cdot dx' \cdot dx \qquad (II.4)$$

where $x' - x$ is a variable lateral separation which will be taken as ξ, i.e. $\xi = x' - x$ and, hence, the mean angular power spectrum is given by:-

$$\langle |F(S)|^2 \rangle = \frac{1}{\lambda^2} \cdot \int_{-\infty}^{+\infty} \int_{-\infty}^{+\infty} d(x + \xi) \cdot d^*(x) \cdot \langle r(x + \xi) \cdot r^*(x) \rangle \cdot e^{jk\xi S} \cdot d\xi \cdot dx \qquad (II.5)$$

If the random process $r(x)$ is stationary, i.e. independent of position and hence is a function of ξ only, therefore:-

$$\Gamma_r(\xi) = \langle r(x + \xi) \cdot r^*(x) \rangle \qquad (II.6)$$

where $\Gamma_r(\xi)$ is the lateral autocorrelation function of the random part of the field and is a function of ξ only.

Therefore, substituting in Equation (II.5):-

$$\langle |F(X)|^2 \rangle = \frac{1}{\lambda^2} \cdot \int_{-\infty}^{+\infty} \int_{-\infty}^{+\infty} d^*(x) \cdot d(x + \xi) \cdot \Gamma_r(\xi) \cdot e^{jk\xi S} \cdot d\xi \cdot dx \qquad (II.7)$$

The lateral autocorrelation function of the deterministic part of the electric field is given by $\Gamma_d(\xi)$ where:-

$$\Gamma_d(\xi) = \int_{-\infty}^{+\infty} d^*(x) \cdot d(x + \xi)\, dx \qquad (II.8)$$

Therefore Equation (II.7) reduces to:-

$$\langle |F(S)|^2 \rangle = \frac{1}{\lambda^2} \cdot \int_{-\infty}^{+\infty} \Gamma(\xi) \cdot e^{jk\xi S} \cdot d\xi \qquad \text{(II.9)}$$

where:-

$$\Gamma(\xi) = \Gamma_d(\xi) \cdot \Gamma_r(\xi) \qquad \text{(II.10)}$$

$\Gamma(\xi)$ is the lateral coherence function of the randomly phase modulated aperture field.

According to the Van Cittert-Zernike theorem[46], the mean angular power spectrum is the Fourier transform of the lateral coherence function, i.e.:-

$$\langle |F(S)|^2 \rangle \longleftrightarrow \Gamma(\xi)$$

and by inverting:-

$$\Gamma(\xi) = \frac{1}{\lambda} \cdot \int_{-\infty}^{+\infty} \langle |F(S)|^2 \rangle \cdot e^{-jk\xi S} \cdot dS \qquad \text{(II.11)}$$

The angular spectrum F(S) at a distance L from the transmitter plane is given by:-

$$F(S)\Big|_{z=L} = F(S)\Big|_{z=0} \cdot e^{-jkLC} \qquad \text{(II.12)}$$

i.e:-

$$|F(S)|\Big|_{z = L} = |F(S)|\Big|_{z = 0}$$

and hence the lateral coherence function over the new plane at z = L is:-

$$\Gamma(\xi;L) = \frac{1}{\lambda} \cdot \int_{-\infty}^{+\infty} \langle|F(S)|^2\rangle\Big|_{z = L} \cdot e^{-jk\xi S} \cdot dS = \Gamma(\xi;0) \qquad \text{(II.13)}$$

Therefore, the lateral coherence function propagates in the forward direction without change.

APPENDIX III

LINEAR FIELD STRENGTH DETECTOR

To complement the dual channel receiver, a second field detector was built. The circuit diagrams of the detector-amplifier module are shown in Figs. III.1 and III.2. The 120 MHz first I.F. is mixed with a 128 MHz local oscillator output, producing an 8 MHz second IF signal. The mixer used was a Hewlett-Packard 5082-9200 single balanced printed circuit mixer with a common RF/IF port. The 8 MHz second IF is obtained through a tunable low-pass filter. This is then amplified by an MC1350P variable gain IF amplifier, with a 500 KHz bandwidth.

The detector used was an envelope detector, SG1402. The field strength was obtained from the product of the 8 MHz variable amplitude signal and a limited version of it. The limited signal was obtained from a CA3043 high gain limiter/amplifier. The limited output was also used as a constant amplitude output to the phase difference detector. This output was first converted to TTL form.

The balanced field strength signal obtained from the envelope detector was then amplified to a suitable recording level by a d.c. amplifier.

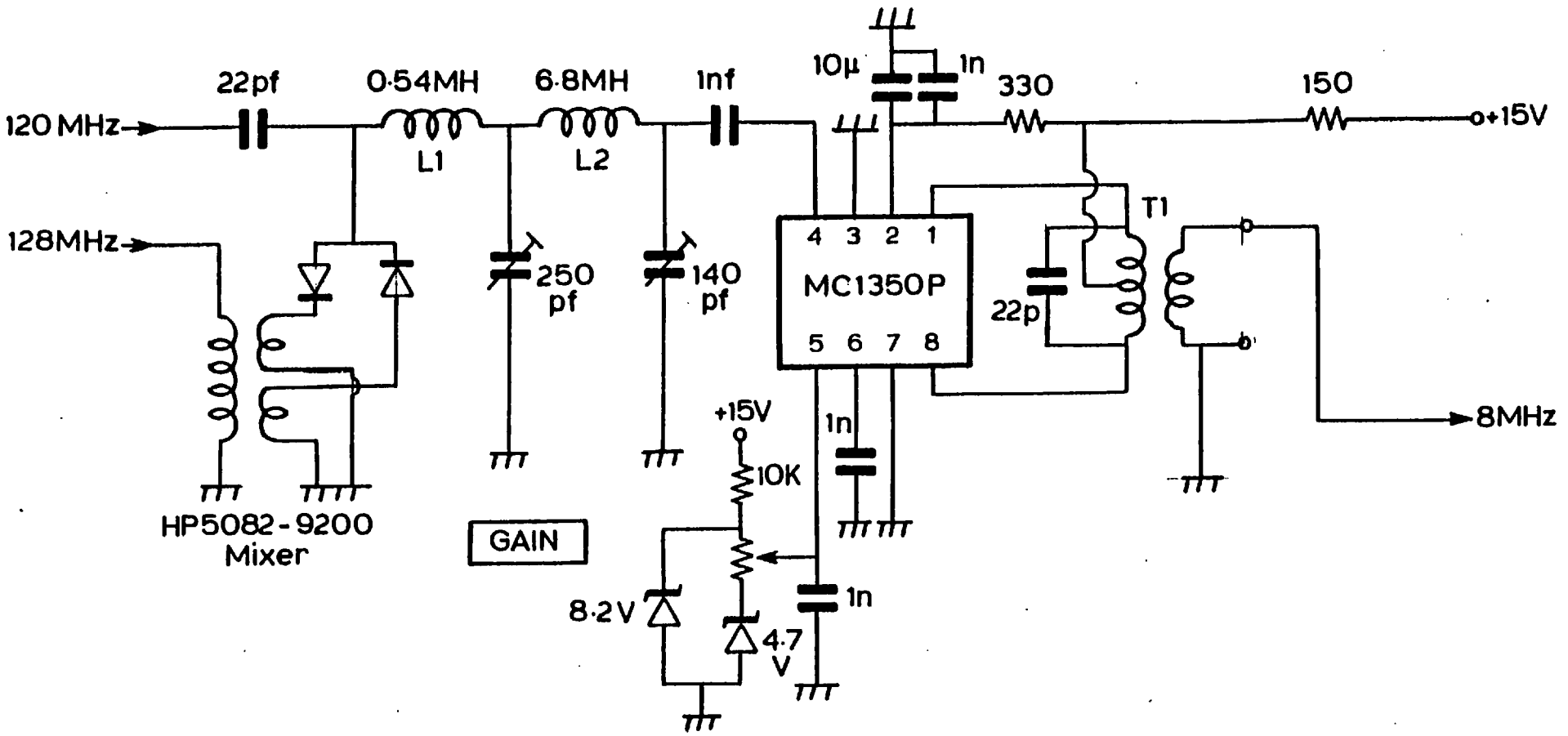

L1 : 10 turns on 1/4" former

L2 : 15 turns on LA2962 ferrite core

T1 : Primary: 18 turns centre tapped

Secondary: 1 turn on LA2962 ferrite core

Fig. 111·1 2nd. I.F. mixer and amplifier

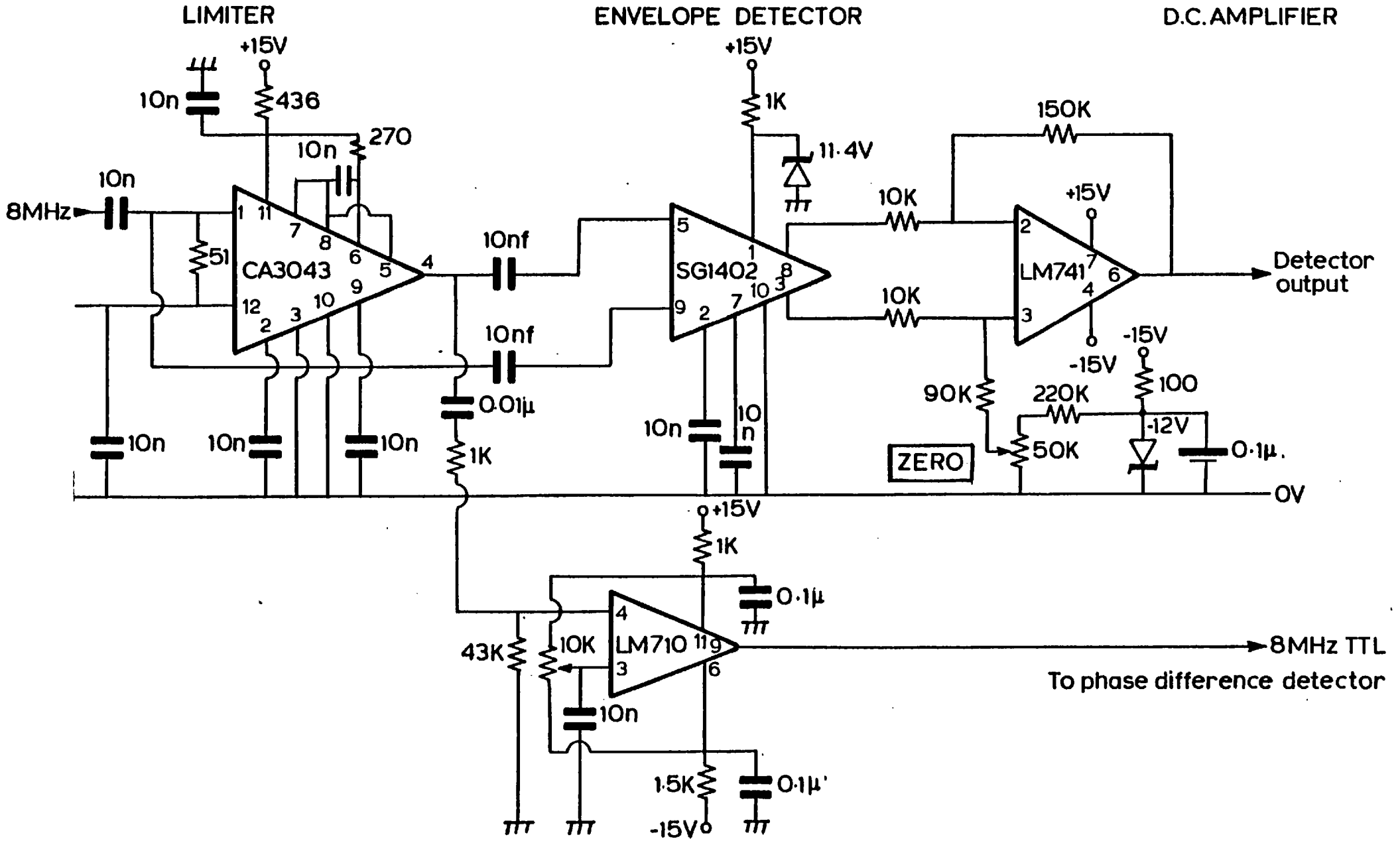

Fig.111·2 Field strength detector

APPENDIX IV

PHASE DIFFERENCE DETECTOR

The principle used to obtain the phase difference was that of a product detector. As previously mentioned, a frequency division by 10 was used to obtain an extended range of $\pm 900^{o}$. Since the signals were in TTL form, the division was obtained by an SN7490A decade counter.

The multiplier used was an MC1595 linear multiplier. The response of the mutiplier as a function of the phase difference between the two input signals was of the form:-

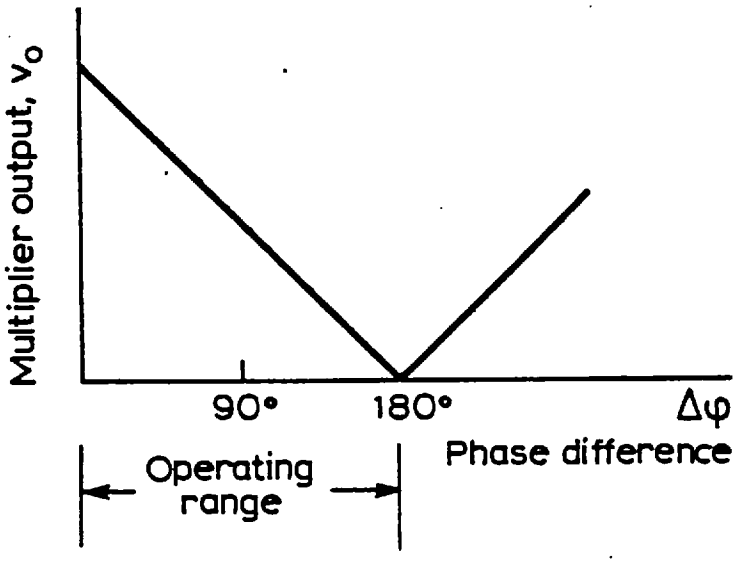

To obtain a range of $\pm 90^{o}$ ($\pm 900^{o}$) with zero output at zero degrees, a phase shift of 90^{o} was imposed on the first channel. An additional phase shift was also required to offset any constant system phase shifts between the two received signals. This offset was provided by an externally variable pulse width monostable. The procedure may be understood from the figure shown below.

The offset circuit provides a phase shift of $90^{o} + \theta$, where θ may be varied from 0^{o} to 180^{o}. After the phase offsetting, two monostables provided precise 50% duty cycle pulses to the multiplier inputs.

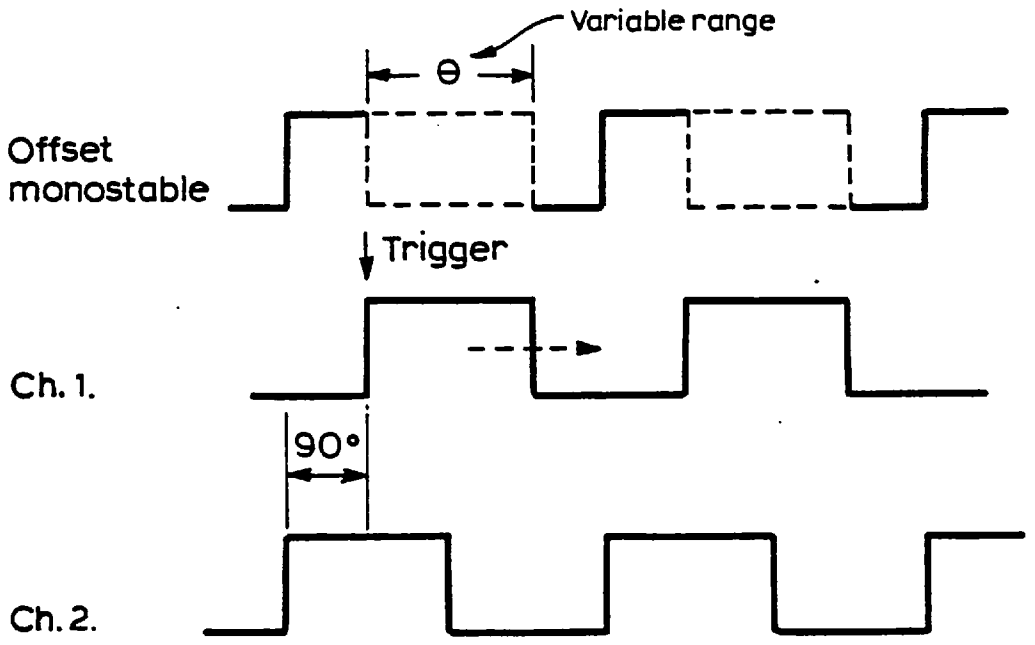

The multiplier was linearized and stabilized by a resistor network. The output was filtered and then amplified to a suitable level for meter display and recording.

Figs. IV.1 and IV.2 show the detailed circuitry of the phase-difference detector described above.

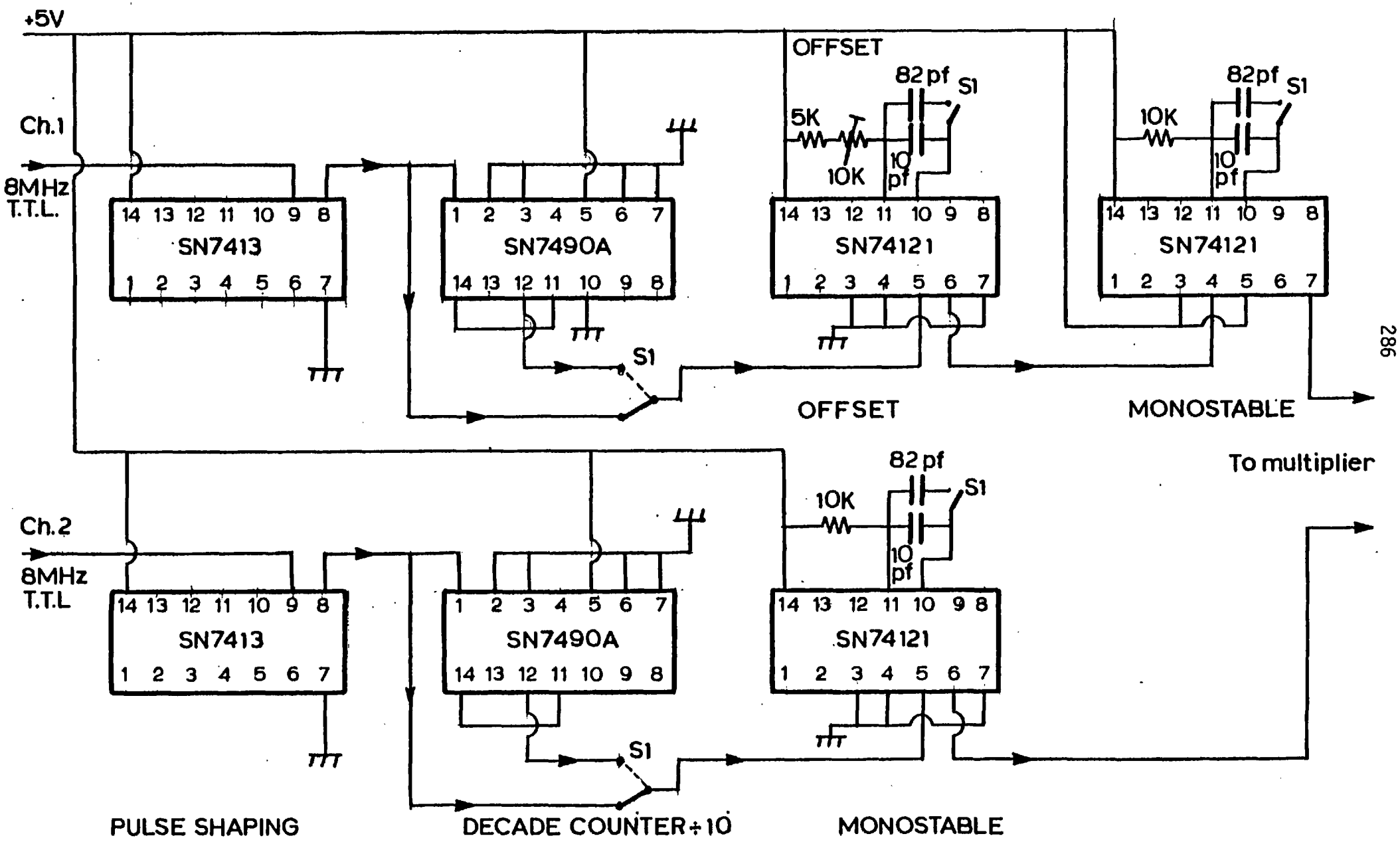

Fig IV·1 Phase detector pulse shaping and offset circuit

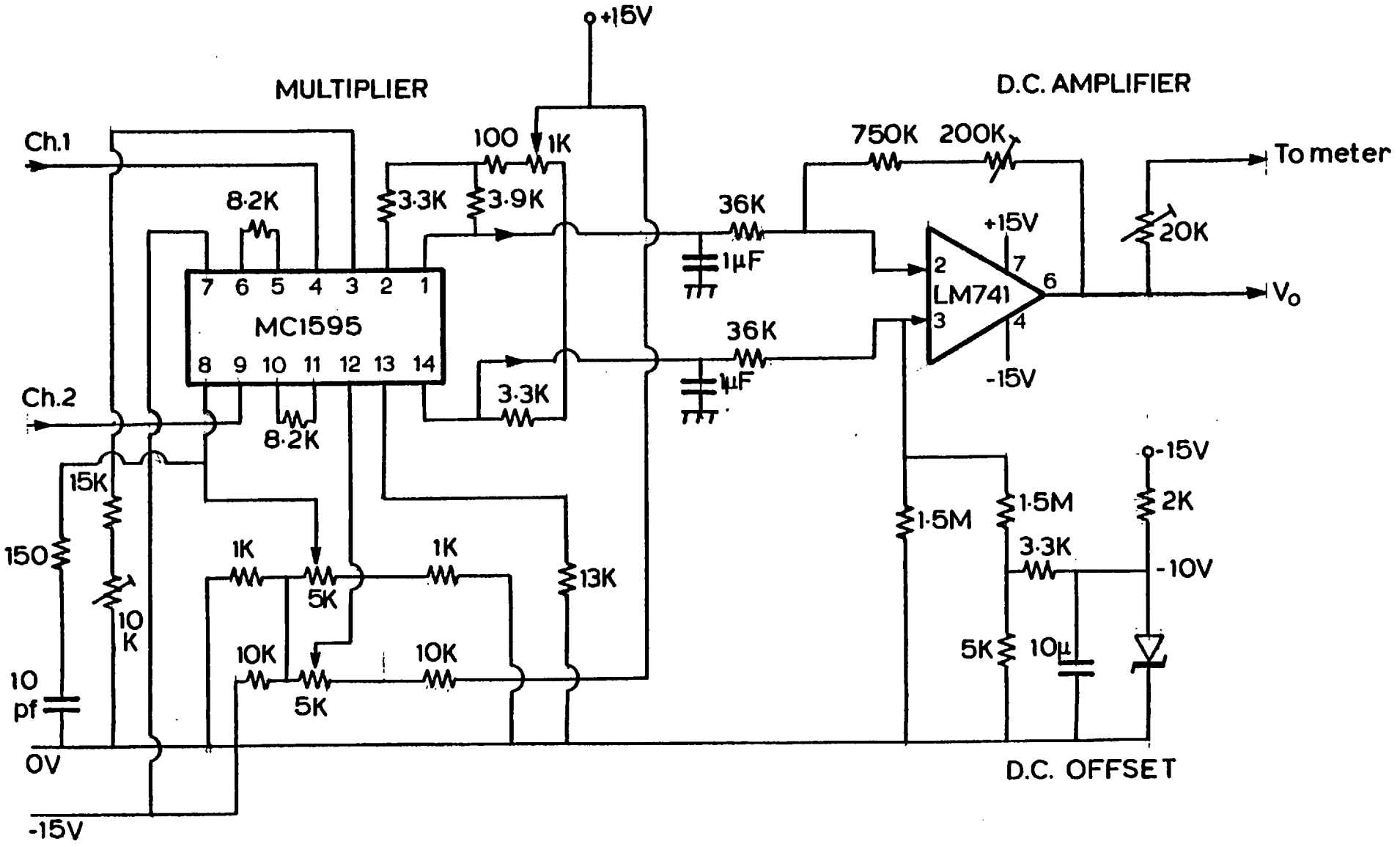

Fig IV·2 Phase detector multiplier and offset amplifier circuit

APPENDIX V

DIGITAL NOTCH FILTER

The necessity of a digital filter basically arises in the processing of digitized data. The analogue-to-digital conversion and subsequent mass storage may introduce a level of noise. The only method available to filter out such noise is through the use of a digital filter. A digital filter may also be used to test the properties of a signal after eliminating undesired frequency components. For example, two signals may be correlated in their low frequency fluctuations only, hence a removal of the higher frequency components is necessary to extract such a trend and vice versa.

Thus the availability of a band-stop notch filter was thought to be convenient in processing the link data on the PDP-15 computer. The synthesis of the filter used was based on one designed by Constantinides[81]. The basic properties of the filter may be outlined as follows:-

1. Second-order notch filter.
2. Recursive.
3. Adjustable notch frequency, w_0.

The transfer function in the z-domain is given by:-

$$\frac{\text{Output of the z-transform}}{\text{Input of the z-transform}} = \frac{V(z^{-1})}{U(z^{-1})} = G(z^{-1}) =$$

$$= \frac{z^{-2} - 2\cos w_0 T\, z^{-1} + 1}{(1-k)\, z^{-2} - 2\cos w_0 T\, z^{-1} + (1+k)} \qquad (V.1)$$

where w_0 is the variable notch angular frequency.

The response of the filter may be schematically shown as follows:-

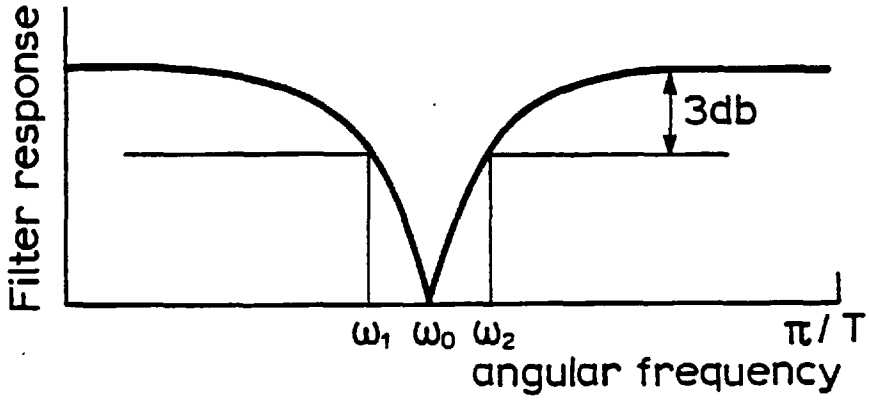

T is the sampling period = $1/f_s$, f_s is the sampling frequency.

w_1 and w_2 are the 3 db lower and upper angular frequencies respectively.

$$k = \frac{2}{1 + \cos w_0 T} \cdot \tan \left[\frac{w_2 - w_1}{2} \right] T \qquad (V.2)$$

and:-

$$\cos w_0 T = \frac{\cos \left[\frac{w_2 - w_1}{2} \right] T}{\cos \left[\frac{w_2 - w_1}{2} \right] T} \qquad (V.3)$$

Therefore, it may be seen from Equations (V.1), (V.2) and (V.3) that the filter has a variable notch frequency w_0 and a variable 3 db band width $(w_2 - w_1)$. The band width is defined by defining either the upper or lower 3 db frequency.

Inverting the z-transform, Equation (V.1), and transferring the variables, the filter recursive formula is thus given by:-

$$v_n = \frac{1}{1+k}\left[u_n - 2\cos w_o T\, u_{n-1} + u_{n-2} + 2\cos w_o T\, v_{n-1} - (1-k)\, v_{n-2}\right] \tag{V.4}$$

where v_n and u_n are the n'th output and input data points respectively.

A subroutine BSF has been written on the basis of the recursive formula (V.4). This subroutine has been tested by applying it to oscillator produced frequencies and looking at the plotted temporal output.

```
C       ***** DIGITAL NOTCH FILTER PROGRAM *****
C
C          S: INPUT-OUTPUT ARRAY(256 POINTS)
C          FO:NOTCH FREQUENCY
C          NF:3*SAMPLING FREQUENCY
C          BW:HALH THE 3-DB BANDWIDTH
        SUBROUTINE BSF(S,FO,NF,BW)
        DIMENSION S(258),P(258)
        PI=4.0*ATAN(1.0)
        WO=2.0*PI*FO
        FMAX=FLOAT(NF)/3.0
        T=1.0/(FMAX)
100     FORMAT(F8.4)
        F2=FO+BW
        W2=2.0*PI*F2
        TAN=(SIN(W2*T/2.0))/(COS(W2*T/2.0))
        TAN=ABS(TAN)
        C=(1.0-COS(WO*T))/((1.0+COS(WO*T))*TAN)
        B=ATAN(C)
        W1=2.0*B/T
        F1=W1/(2.0*PI)
        WRITE(5,1)F1
1       FORMAT(3X,'LOWER 3DB. FREQ. IS: ',F8.4)
        A=SIN(T*(W2-W1)/2.0)/COS(T*(W2-W1)/2.0)
        A1=1.0/(1.0+A)
        A2=1.0-A
        P(1)=0.0
        P(2)=0.0
        DO3I=1,256
        P(I+2)=A1*(S(I)-2.0*COS(WO*T)*S(I+1)+S(I+2))
        1+2.0*COS(WO*T)*A1*P(I+1)-A2*A1*P(I)
3       CONTINUE
5       FORMAT(3X,'S= ',F8.4,4X,'P= ',F8.4)
        DO4I=3,258
        L=I-2
4       S(L)=P(I)
        RETURN
        END
```

REFERENCES

1. HEMPEL, R.
"United States Frequency Allocations".
Microwave Systems News, Vol. 6, No. 4, p. 96, 1976.

2. IEEE STANDARD DEFINITIONS OF TERMS FOR RADIO WAVE PROPAGATION.
IEEE Trans. A & P, Vol. 17, p. 271, 1969.

3. C.C.I.R. RECOMMENDATIONS.
Rec. No. 309, Los Angeles, 1959.

4. MATTHEWS, P. A.
"Radio Wave Propagation V.H.F. and Above".
Chapman and Hall Ltd., London, 1965.

5. DU CASTEL, F.
"Tropospheric Radiowave Propagation Beyond the Horizon".
Pergamon Press, London, 1966.

6. BEAN, B. R. and THAYER, G. D.
"Models of the Atmospheric Radio Refractive Index".
Proc. I.R.E., Vol. 47, p. 740, 1959.

7. WHITE, R. F.
"Engineering Considerations for Microwave Communications System".
GTE Lenkurt, Los Angeles, 1975.

8. VAN MIEGHEM, J.
"Atmospheric Energetics".
Clarendon Press, Oxford, 1973.

9. SCORER, R. S.
"The Causes of Atmospheric Inhomogeneities".
Extract from: "Bulletin Astronomique", Vol. XXIV, p. 216.

10. BRUNT, D.
"Physical and Dynamical Meteorology".
Cambridge University Press, 2nd. Edition, 1939.

11. SCORER, R. S. and LUDLAM, F. H.
"Bubble Theory of Penetrative Convection".
Quart. J. Roy. Met. Soc., Vol. 79, p. 94, 1953.

12. SCORER, R. S. and RONNE, C.
"Experiments with Convective Bubbles".
Weather, No. 11, p. 151, 1956.

13. NICOLAIDES, M.
"An Experimental Investigation and Laboratory Simulation of Atmospheric Fading on a 900 MHz Transhorizon Radio-Link".
Ph.D. Thesis, Imperial College, University of London, 1979.

14. WULFSON, N. I.
"Investigation of Convective Motion in the Free Atmosphere".
Izd. Akad. Nauk., USSR, 1961.

15. TAYLOR, G. I.
"Statistical Theory of Turbulence".
Proc. Roy. Soc., Part 1 - 4, Vol. 151, p. 421, 1935.

16. KOLMOGOROFF, A. N.
"The Local Structure of Turbulence in Incompressible Viscous Fluid for Very Large Reynolds Numbers".
and:-
"On Degeneration of Isotropic Turbulence in an Incompressible Viscous Fluid".
Turbulence : Classic Papers on Statistical Theory, Interscience Publishers Inc., New York, p. 151, 1961.

17. GARNER, W. J.
"Bit Error Probabilities Related to Data-Link S/N".
Microwaves, p. 101, November, 1978.

18. BURROWS, W. G.
"Degradation in the Efficiency of Medium-Size Parabolic Antennas with Propagation Conditions".
The Radio and Electronic Engineer, Vol. 47, No. 11, p. 529, 1977.

19. FANTE, R. L.
"Electromagnetic Beam Propagation in Turbulent Media".
Proc. IEEE, Vol. 63, No. 12, p. 1669, 1975.

20. SKOLNIK, M. I.
"Introduction to Radar Systems".
McGraw-Hill, 1962.

21. KERR, J. R. and DUNPHY, J. R.
"Experimental Effects of Finite Transmitter Apertures on Scintillations".
J. Opt. Soc. Am., Vol. 63, No. 1, p. 1, 1973.

22. MAVROKOUKOULAKIS, N. D., HO, K. L. and COLE, R. S.
"Temporal Spectra of Amplitude Scintillations at 110 GHz and 36 GHz".
IEEE Trans. A & P, Vol. 26, No. 6, 1978.

23. KERR, D. E.
"Propagation of Short Radio Waves".
M.I.T. Radiation Laboratory Series, McGraw-Hill, 1951.

24. PAPPAS, C. F., VOGLER, L. E. and RICE, P. L.
"Graphical Determination of Radio Ray Bending in an Exponential Atmosphere".
J. Res. of N.B.S., Vol. 65D, No. 2, p. 175, 1961.

25. BEAN, B. R. and DUTTON, E. J.
"Radio Meteorology".
Dover Publication, New York, 1968.

26. GOSSARD, E. E.
"Refractive Index Variance and its Height Distribution in Different Air Masses".
Radio Science, Vol. 12, No. 1, p. 89, 1977.

27. KOGELNIK, H.
"On the Propagation of Gaussian Beams of Light Through Lens-Like Media Including Those with a Loss or Gain Variation".
Applied Optics, Vol. 4, No. 12, p. 1562, 1965.

28. TIEN, P. K., GORDON, J. P. and WHINNERY, J. R.
"Focussing of a Light Beam of Gaussian Distribution in Continuous and Periodic Lens-Like Media".
Proc. IEEE, Vol. 53, p. 129, 1965.

29. MARCUSE, D.
"Light Transmission Optics".
Van Nostrand Reinhold Co., 1972.

30. CLARKE, R. H.
"Acoustic and Electromagnetic Waves Propagating in a Tenuous Random Medium".
Published in: "Aspects of Signal Processing", Ed. G. Tacconi, NATO Advanced Study Institutes Series, D. Reidel Publishing Co., Boston, 1977.

31. TAPPERT, F. D. and HARDIN, R. in C. W. SPOFFORD
"A Synopsis of the AESD Workshop on Acoustic-Propagation Modelling by Non Ray-Trading Techniques".
AESD, Arlington, Va., May, 1973.

32. SIEGMAN, A. E.
"An Introduction to Lasers and Masers".
McGraw-Hill, 1971.

33. USCINSKI, B. J.
"The Elements of Wave Propagation in Random Media".
McGraw-Hill, 1977.

34. CLARKE, R. H.
"Theory of Acoustic Propagation in a Variable Ocean".
SACLANTCEN Mem SM-28, ASW Ros. Centre, October, 1973.

35. BORN, M. and WOLF, E.
"Principles of Optics".
Pergamon Press, 5th Edition, 1975.

36. PAPOULIS, A.
"Probability, Random Variables and Stochastic Processes".
McGraw-Hill, 1965.

37. FEJER, J. A.
"The Diffraction of Waves in Passing Through an Irregular Refracting Medium".
Proc. Roy. Soc., A220, p. 455, 1953.

38. BRAMLEY, E. N.
"The Diffraction of Waves by an Irregular Refracting Medium".
Proc. Roy. Soc., A225, p. 515, 1954.

39. CLARKE, R. H.
"Theoretical Characteristics of Radiation Reflected Obliquely from a Rough Conducting Surface".
Proc. IEE, Vol. 110, No. 1, p. 91, 1963.

40. BECKMANN, P. and SPIZZICHINO, A.
"The Scattering of Electromagnetic Waves from Rough Surfaces".
Pergamon Press, New York, 1963.

41. GRADSHTEYN, I. S. and RHYZIK, I. M.
"Table of Integrals, Series, and Products".
Academic Press, 4th Edition, 1965.

42. BOOKER, H. G. and CLEMMOW, P. C.
"The Concept of an Angular Spectrum of Plane Waves and its Relation to that of Polar Diagram and Aperture Distribution".
Proc. IEEE, Vol. 97, Part III, p. 11, 1950.

43. BOOKER, H. G., RATCLIFFE, J. A. and SHINN, D. H.
"Diffraction from an Irregular Screen with Applications to Ionospheric Problems".
Phil. Trans. Roy. Soc., Series A, Vol. 242, p. 579, 1950.

44. LALOR, E.
"Conditions for the Validity of the Angular Spectrum of Plane Waves".
J. Opt. Soc. Am., Vol. 58, No. 9, p. 1235, 1968.

45. ZERNIKE, F.
"The Concept of Degree of Coherence and its Application to Optical Problems".
Physica V, No. 8, p. 785, 1938.

46. RATCLIFFE, J. A.
"Some Aspects of Diffraction Theory and Their Application to the Ionosphere".
Rep. Prog. Phys., Vol. 19, p. 188, 1956.

47. BROWN, J.
"A Generalized Form of the Aerial Reciprocity Theorem".
Proc. IEE, Mon. No. 301R, p. 472, 1958.

48. RUZE, J.
"Antenna Tolerance Theory - A Review".
Proc. IEEE, Vol. 54, No. 4, p. 633, 1966.

49. JAIRAM, H.
"The Effect of Manufacturing Errors on the Performance of Parabolic Antennas".
M.Sc. Thesis, Imperial College, University of London, 1976.

50. BRAMLEY, E. N.
"The Accuracy of Computing Ionospheric Radio-Wave Scintillation by the Thin-Phase-Screen Approximation".
J. Atm. and Terr. Phys., Vol. 39, p. 367, 1977.

51. HEWISH, A.
"The Diffraction of Radio Waves in Passing Through a Phase-Changing Ionosphere".
Proc. Roy. Soc., Vol. 209A, p. 81, 1951.

52. BROWN, J.
"A Theoretical Analysis of Some Errors in Aerial Measurements".
Proc. IEE, Mon. No. 285R, p. 343, 1958.

53. CHU, T. S.
"An Approximate Generalization of the Friis Transmission Formula".
Proc. IEEE, Vol. 53, No. 3, p. 296, 1965.

54. HALL, M. P. M. and MISME, P.
"Gain Degradation of a 25 m Paraboloidal Aerial on 2 GHz Trans-horizon Radio Paths".
Proc. IEE, Vol. 122, No. 4, p. 358, 1975.

55. D'AURIA, G. and SOLIMINI, D.
"Performance of Antennas in Random Fields".
IEEE Trans. A & P, Vol. 20, No. 5, p. 577, 1972.

56. BARZILAI, G.
"Research on Statistical Aspects of Tropospheric Propagation".
Radio Science, Vol. 10, No. 7, p. 745, 1975.

57. D'AURIA, G. and COLAVITO, C.
"Efficiency of Large Aperture Antennas and Reflectors".
Alta Frequenza, Vol. XXXV, No. 11, p. 866, 1966.

58. TATARSKII, V. I.
"The Effects of the Turbulent Atmosphere on Wave Propagation".
Israel Program for Scientific Translations, 1971.

59. FRIED, D. L.
"Optical Heterodyne Detection of an Atmospherically Distorted Signal Wave Front".
Proc. IEEE, Vol. 55, No. 1, p. 57, 1967.

60. INGGS, M. R.
"The Propagation of Millimetric Radio Wave Through the Clear Atmosphere".
Ph.D. Thesis, Imperial College, University of London - to be published.

61. BRAUN, E. H.
"Some Data for the Design of Electromagnetic Horns".
I.R.E. Trans. A & P, Vol. 4, No. 1, p. 29, 1956.

62. OLSEN, R. L. et al
"The aR^b Relation in the Calculation of Rain Attenuation".
IEEE Trans. A & P, Vol. 26, No. 2, p. 318, 1978.

63. SKELTON, T.
"A Transistor Atmospheric Temperature Sensor".
B.Sc. Project, Imperial College, 1976.

64. ASPINALL, C. R.
"The Development of a Digital Recording System".
B.Sc. Project, Imperial College, 1977.

65. PDP-15 MACRO-15 MACRO-ASSEMBLER PROGRAM REFERENCE MANUAL.
DEC, Maynard, Mass., 1974.

66. BENDAT, J. S. and PIERSOL, A. G.
"Random Data : Analysis and Measurement Procedures".
Wiley-Interscience, 1971.

67. OTNES, R. K. and ENOCHSON, L.
"Digital Time Series Analysis".
John Wiley & Sons, New York, 1972.

68. RICHARDS, P. J.
"Computing Reliable Power Spectra".
IEEE Spectrum, Vol. 4, p. 83, 1967.

69. BERGLAND, G. D.
"A Guided Tour of the Fast Fourier Transform".
IEEE Spectrum, Vol. 6, p. 41, 1969.

70. RAMIREZ, R. W.
"The FFT : Fundamentals and Concepts".
Published by Tektroniks Inc., Oregon, USA, 1975.

71. HO, K. L., COLE, R. S. and MAVROKOUKOULAKIS, N. D.
"The Effect of Wind Velocity on the Amplitude Scintillations of Millimetre Radio Waves".
J. Atmos. & Terr. Phys., Vol. 40, No. 140, p. 443, 1978.

72. STROHBEHN, J. W.
"Line-of-Sight Wave Propagation Through the Turbulent Atmosphere".
Proc. IEEE, Vol. 56, No. 8, p. 1301, 1968.

73. NORTON, K. A. et al.
"The Probability Distribution of the Amplitude of a Constant Vector Plus a Rayleigh-Distributed Vector".
Proc. I.R.E., Vol. 43, No. 10, p. 1354, 1955.

74. BECKMANN, P.
"Probability in Communication Engineering".
Harcourt, Brace & World, 1967.

75. STROHBEHN, J. W., WANG, T. and SPECK, J.
"On the Probability Distribution of Line-of-Sight Fluctuations of Optical Signals".
Radio Science, Vol. 10, No. 1, p. 59, 1975.

76. VILAR, E. and MATTHEWS, P. A.
"Summary of Scintillation Observations in a 36 GHz Link Across London".
IEE Conf. on A & P, Publ. No. 169, 1978.

77. ETCHEVERRY, R. D. et al.
"Measurements of Spatial Coherence in 3.2-mm Horizontal Transmission".
IEEE Trans. A & P, Vol. 15, No. 1, p. 136, 1967.

78. CABLE, P. G.
"Statistics of Surface Scattered Signals".
Conf. Inst. of Acous., Underwater Acous. Group, Imperial College, London, 1978.

79. ROCHE, J. F. et al.
"Radio Propagation at 27 - 40 GHz".
IEEE Trans. A & P, Vol. 18, No. 4, p. 452, 1970.

80. BECKERICH, J. F.
"Digital Communication Fundamentals".
Digital Microwave Transmission Eng. Symposium III, published by Rockwell Int., September, 1978.

81. CONSTANTINIDES, A. G.
"Digital Notch Filters".
Electronics Letters, Vol. 5, No. 9, 1969.